Mechanics of Deformation of Carbon Nanotubes

by

Mohit Garg

A.A.Sc. Computer Graphics and Design
Tarrant County College, 2001

B.Sc. Aerospace Engineering
University of Texas, Austin, 2003

SUBMITTED TO THE DEPARTMENT OF MECHANICAL ENGINEERING IN PARTIAL FULFILLMENT OF THE REQUIREMENTS FOR THE DEGREE OF

MASTER OF SCIENCE IN MECHANICAL ENGINEERING
AT THE
MASSACHUSETTS INSTITUTE OF TECHNOLOGY

JUNE 2005

Signature of Author: _____
Department of Mechanical Engineering
May 9, 2005

Certified by: _____
Dr. Mary C. Boyce
Kendall Family Professor of Mechanical Engineering

Accepted by: _____
Dr. Lallit Anand
Chairman, Department Committee on Graduate Students

Mechanics of Deformation of Carbon Nanotubes

by

Mohit Garg

Submitted to the Department of Mechanical Engineering
on May 9, 2005, in partial fulfillment of the
requirements for the degree of
Master of Science in Mechanical Engineering

ABSTRACT

The deformation mechanics of multi-walled carbon nanotubes (MWCNT) and vertically aligned carbon nanotube (VACNT) arrays were studied using analytical and numerical methods. An equivalent orthotropic representation (EOR) of the mechanical properties of MWCNTs was developed to model the anisotropic mechanical behavior of these tubes during various types of deformation. Analytical models of the micro-mechanical contact and deformation during nano-indentation and scratching of VACNTs were developed. The EOR model was developed based on finite element (FE) nested shell structural representation of MWCNTs. The EOR was used together with the FE method to simulate bending, axial compression and lateral compression. Results were compared with those of the nested shell model for 4-, 8-, 9-, 14-, and 19-walled carbon nanotubes. The comparison of axial and lateral compression results indicated that although MWCNTs have high strength and stiffness in the axial direction, they can exhibit significant radial deformability owing to their relatively compliant interwall normal and shear behaviors. The EOR results provide an improvement in computational efficiency as well as a successful replication of the overall deformation behavior including the initial linear elastic behavior and the onset of buckling of MWCNTs and the post-buckling compliance. The post-buckling progression in wavelength (a doubling of wavelength as deformation progresses) was not captured by the EOR model. Analytical predictions of the force-penetration depth during nano-indentation with a three-sided pyramidal shaped indentor tip were compared with results from macro-scale experiments, FE simulations and nano-indentation of VACNT forests. These comparisons indicated that the proposed nano-indentation micro-mechanical contact model captures effectively both the nonlinear deformation mechanics and buckling effects of MWCNTs. The effective bending modulus of two VACNT forest samples was found to be 1.10 *TPa* and 1.08 *TPa*. Similarly, results from the micro-mechanical contact model for nano-scratching were compared with the results from macro-scale experiments with a sharp tip and FE simulations with both sharp and Bekovich tips. The comparison of these results indicated that the proposed contact model is able to capture remarkably well the variation in vertical force with lateral indentor tip displacement. The proposed FE and analytical models offer computationally efficient methods for simulating large and complex systems of MWCNTs with a small penalty in precision.

Thesis Supervisor: Dr. Mary C. Boyce
Title: Kendall Family Professor of Mechanical Engineering

Acknowledgements

I would like to thank my advisor Prof. Mary C. Boyce for her invaluable advice and support during my masters study and research at MIT; I appreciate her pushing me to my limit, then pushing me more. I would like to express my appreciation to the help and cooperation from the Cambridge MIT alliance and DURINT group members, and especially Post Doctorates H. J. Qi and A. Pantano for their valuable discussion on their nano-indentation and nested shell models; a special thanks to Yuto Shinagawa, for his undivided attention in helping me edit my thesis.

I also thank my family (Mom, Priya Agrawal, Monica Shangle, Dad, Atul Agrawal, Prashant Shangle, Rohit Garg, and my lovely two nieces [Sezal Agrawal and Trisha Shangle] and three nephews [Suvansh Agrawal, Sahil Shangle and Suvan Shangle]) for their support, and friends (Melis Arslan, Regina Cheung, Kristin Myers, Nuo Sheng Anastassia P. Apaskaleva, Nicoli M. Ames, Sabine Cantournet, Saisarva, Cathal J. Kearney, Franco Capaldi, Mats Danielsson, Ethan Parsons, Jin Yi, Adam D. Mulliken, Timothy P. M. Johnson, Jeffery Palmer, Rajdeep Sharma, Yugie Wei, Theodora Tzianetopoulou, Una Sheehan, Ray Hardin, Pierce Hayward, Leslie Regan and Joan Kravit) for making everything a little easier. I will always be grateful for their positive influence, and will get even for their negative ones☺.

Table of Contents

Chapter 1

In 1985, Kroto et al., (2005) discovered the C_{60} molecule known as fullerene, Buckminsterfullerene, or buckyball, as shown in Figure 1.1. Subsequently, Iijima (1991) discovered carbon nanotubes, CNT, as shown in Figure 1.2. Ever since the discovery of CNTs, researchers throughout the scientific community have been investigating the nearly perfect structure and properties of this one-dimensional structure. CNTs are usually classified into two main categories: single-walled carbon nanotubes (SWCNT) and multi-walled carbon nanotubes (MWCNT), as shown in Figure 1.2. A SWCNT is composed of a single tubular structure formed by rolling a graphene sheet, whereas a MWCNT is comprised of concentric nested tubes of different radii separated by an interwall distance controlled by van der Waal interactions between the atoms. The diameter of CNTs is anywhere from 0.3 nm (Zhao et al., 2004) for the smallest SWCNT to 200 nm for the largest MWCNT.

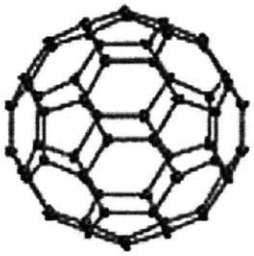

Figure 1.1: Schematic diagram of a C_{60} fullerene (Cui et al., 2004).

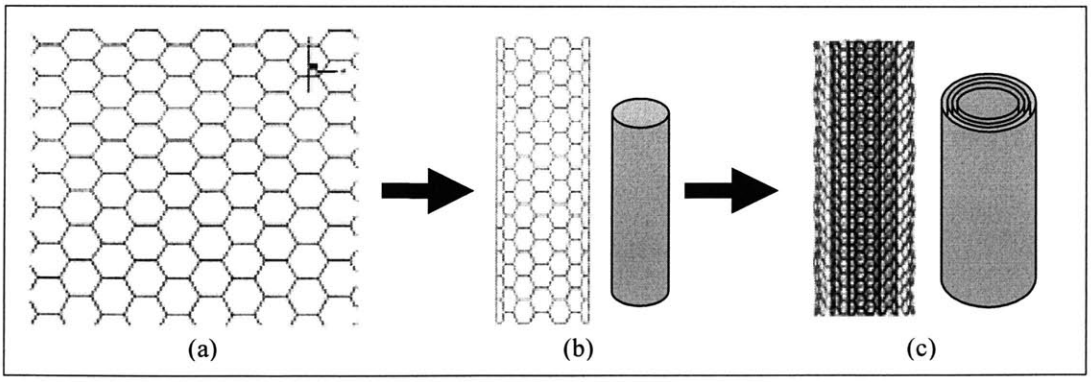

Figure 1.2: Schematic diagram showing how a hexagonal graphite sheet (Dresselhaus et al., 2000) (a) is rolled to form a SWCNT (Tserpes and Papanikos, 2005) (b) and a MWCNT (Liew et al., 2004) (c).

Performing experiments on such nano-scale structures is extremely challenging. Therefore, researchers have been working to develop experimental techniques to quantitatively measure properties and to predict the properties of CNTs with theoretical models. Assuming a perfect atomic structure, theoretical and computational studies have found CNTs to possess favorable mechanical, electric, thermal and chemical properties. These properties make them attractive for many applications in nano-electro-mechanical systems (NEMS) (e.g., Ke et al., 2005; Kang et al., 2005), micro-electro-mechanical systems (MEMS) devices (e.g., Kang et al., 2005) and even in material reinforcements for fiber composites. Theoretical and experimental results both indicate that mechanically, CNTs have high strength and stiffness in the axial direction and are resilient. Electronically, CNTs can be metallic or semiconducting depending on the chirality (see Section 1.1) of their structure and show remarkable logic and amplification functions (Qian et al., 2002). Thermally, CNTs are highly conductive while chemically, they resist degradation in many chemicals. These properties have led researchers to find biomedical applications in addition to the more obvious NEMS, MEMS, and composite material uses. Researchers believe that these properties can be tailored according to the required application.

In this introductory chapter, a discussion of the molecular structure of CNTs is first reviewed followed by the synthesis of SWCNTs and MWCNTs and investigation of elastic properties of CNTs via experimental, theoretical, and computational analyses.

1.1 Molecular Structure

In general, a SWCNT is a cylindrical structure that can be formed conceptually by rolling a graphene sheet. This graphene sheet consists of a periodically repeating hexagonal pattern in space, as shown in Figure 1.2. The planar hexagonal pattern is composed of carbon atoms bonded together with strong in-plane sigma bonds. On the other hand, MWCNT consists of several concentric SWCNTs where each wall interacts with its neighboring walls through weak van der Waals forces (Qian et al., 2002). In the

following two sub-sections, we first look at the basic bond structure of the graphene sheet and subsequently, the SWCNT and MWCNT structures.

1.1.1 Bond Structure

The planar hexagonal pattern consists of six carbon atoms that interact with one another through strong in-plane covalent sigma bonds to form graphite. Because of periodicity, each carbon atom is bonded in a plane to three neighboring carbon atoms and separated by a *C-C* bond ($l_{c\text{-}c}$) length or sigma bond length of 0.1421 *nm* and by an angular separation of 120°, as shown in Figure 1.3. The final width of the hexagonal pattern is about 0.246 *nm* (Harik, 2001). These in-plane sigma bonds result in the CNT's extraordinary stiffness and strength in the axial direction.

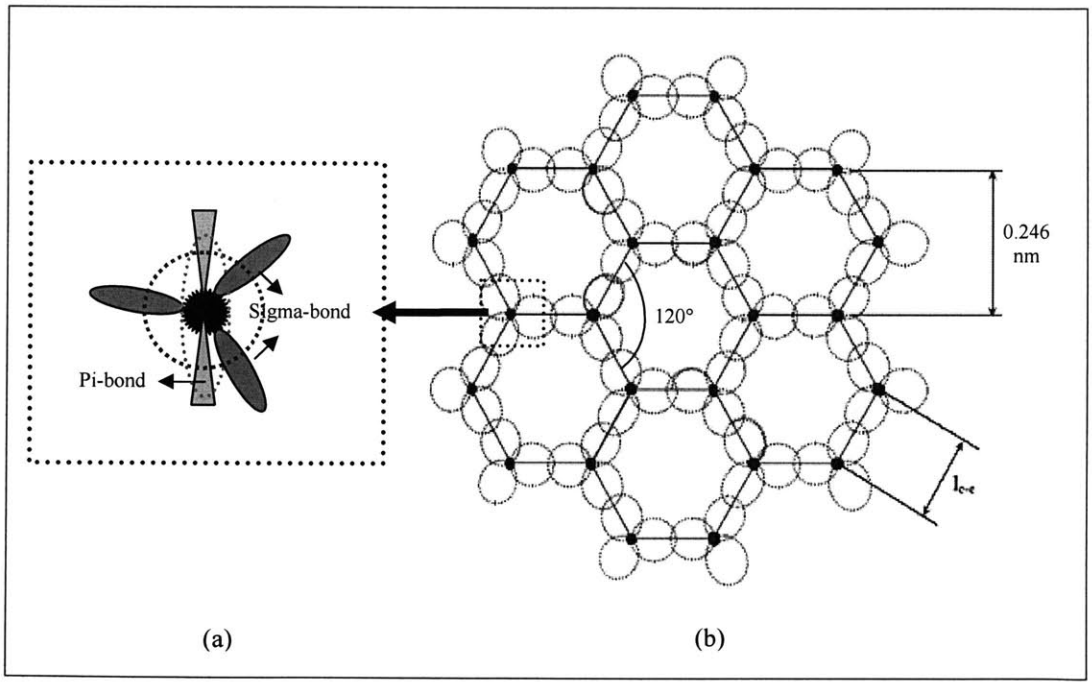

Figure 1.3: Carbon atom (sphere) with in-plane sigma-bonds (oval) and out-of-plane pi-bonds (triangular) (a). Carbon atom attachment in a graphene sheet (b). The black dots are the carbon atoms, dotted circles are the sigma bonds and solid line shows the hexagonal pattern (Harik, 2001).

The additional out-of-plane pi-bonds that result because of sp^2 hybridization interact with adjacent carbon atoms on a separate sheet to form the interlayer force in MWCNTs. The sp^2 hybridization occurs when carbon atoms come together to form graphite (Qian et al., 2002). The interaction between the out-of-plane pi-bonds (also known as van der Waals force) result in an equilibrium separation of ~0.34 *nm* between the nested shell (coaxial cylindrical geometry) structure of the MWCNTs (Saito and Yoshikawa, 1993; Qian et al., 2002). Contrary to sigma-bonds, the pi-bonds make the CNT radial direction relatively compliant compared to the axial and tangential direction.

1.1.2 Single- and Multi-Walled Carbon Nanotube Structure

As shown in Figures 1.2 and 1.3, the hexagonal lattice structure forms a graphene sheet. This graphene sheet can be rolled in different directions to form the cylindrical tube known as SWCNT. The direction of the CNT axis is the defined as the translational vector ***T,*** and the direction perpendicular to vector ***T*** or the roll-up direction of the graphene sheet is defined as the roll-up or chiral vector $\boldsymbol{C_h}$, as shown in Figure 1.4. The vector $\boldsymbol{C_h}$ can be defined as a linear combination of base vectors $\boldsymbol{a_1}$ and $\boldsymbol{a_2}$ (Figure 1.4) of the hexagonal lattice as,

$$\mathbf{C}_h = n\mathbf{a}_1 + m\mathbf{a}_2 \tag{1.1}$$

$$\mathbf{C}_h \cdot \mathbf{T} = 0 \tag{1.2}$$

with n and m being integers. A particular SWCNT is thus described to fall into one out of three categories which are associated with an integer pair (n, m),

$\theta = 0°$ or $m = 0$ --- (n,0) -- Zigzag (1.3a)

$0° < \theta < 30°$ or other --- (n,m) -- Chiral (1.3b)

$\theta = 30°$ or $n = m$ --- (n,n) -- Arm Chair (1.3c)

where the diameter d and the chiral angle θ of the CNT can be found from (Saito et al., 2001)

$$d = 0.0783\sqrt{n^2 + n.m + m^2} \quad nanometer \tag{1.4}$$

$$\theta = \sin^{-1}\left[\frac{\sqrt{3}m}{2\left(n^2 + nm + m^2\right)}\right] \quad radians. \tag{1.5}$$

When several concentric SWCNTs of increasing radius form a nested shell structure, they form a MWCNT, as shown in Figure 1.2. The separation between the concentric walls can vary from 0.34 *nm* to 0.39 *nm* and is inversely proportional to the number of layers and directly proportional to the curvature (Kiang et al., 1998).

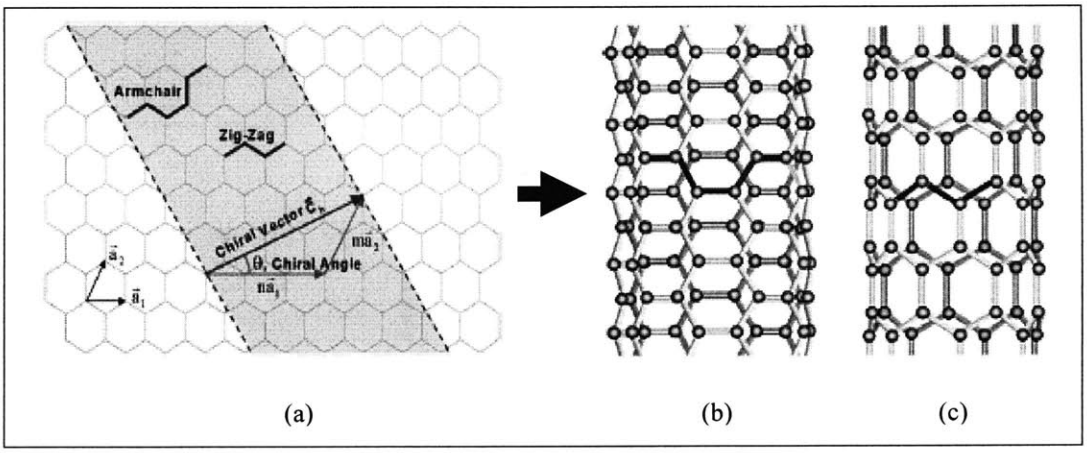

Figure 1.4: Schematic diagram showing how a hexagonal graphite sheet is rolled to form a carbon nanotube (a). The atomic structure of an armchair (*n, n*) (b) and a zig-zag (*n, 0*) nanotube (c) (Thostenson et al., 2001).

The closed shell cylinder configuration in a SWCNT or MWCNT is more stable than the flat graphene sheet because of the total energy reduction due to the elimination of the dangling-bonds at the edge of the sheet. However, the energy per carbon atom within a closed shell increases as tube radius decreases, and is found to increase in proportion to the curvature of the tube wall (Ebbesen, 1997). Many researchers use this notion of energy in their analysis in order to estimate the elastic properties of CNTs.

1.2 Synthesis of Carbon Nanotubes

The possible applications of carbon nanotubes in various fields demand tailoring of CNTs, and have consequently sparked research in the synthesis of these nano-wonders. In the following subsections, the reader will find a brief summary of the main synthesis techniques used in the production of CNTs.

1.2.1 Electric-Arc-Discharge Technique

The CNTs discovered by Iijima (1991) were in the soot of an arc-discharge generator (Dresselhaus et al., 2000). The Electric-arc-discharge technique is used to process high quality SWCNTs and MWCNTs in gram quantities; see Figure 1.5.

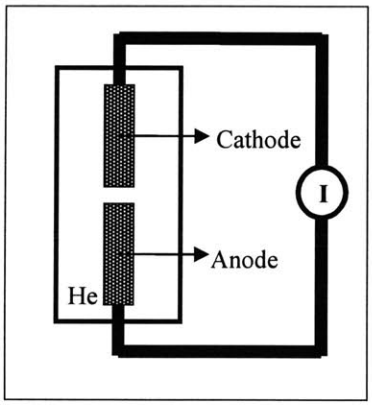

Figure 1.5: Schematic illustration of *Electric-Arc-Discharge* generator (Dresselhaus et al., 2000).

Usually two high purity graphite rod electrodes of 5-20 *mm* diameter separated by about 1 *mm* are used as cathode and anode. The synthesis of CNTs requires a direct current (DC) of about 50-120 *A* and a voltage difference of about 20-25 *V* across the electrodes. Stable arcing occurs in a helium atmosphere at approximately 500 *torr* flowing at a rate of 5-15 $ml.s^{-1}$ (Saito et al., 2001). A carbon deposit forms on the cathode as the anode is consumed during arcing. Throughout the arcing process, the gap between the electrodes is maintained at the initial value. The CNTs form near the center region of the cathode where the temperature is about 2500-3000 *°C* and aligned in the direction of the current flow. To synthesize isolated SWCNTs, the electrodes are doped with a small

amount of a transition metal such as *Co* or *Ni*, whereas processing of MWCNTs, in the form of bundles bound together by van der Waals force, does not require any catalyst. The growth mechanism in this technique is believed to occur at the open ends of the CNTs (Saito et al., 2001).

The average SWCNT synthesized in an arc-discharge technique has an average diameter of ≤ 1.5 *nm* and a length of about 1 μm. On the other hand, the MWCNT diameter ranges from 5-30 *nm* with a length of about 10 μm. The CNTs processed from this technique have fewer structural defects that give them their exceptional properties and makes them highly desirable for various applications. Since the fullerenes and other graphite particles form along with the CNTs, a purification process is required to isolate the nanotubes from other by-products (impurities) (Dresselhaus et al., 2000).

1.2.2 Laser-Ablation Technique

Thess et al., (1997) synthesized SWCNTs of high purity at a 1-10 *g* scale and with a high yield of about 70% with a Laser-Ablation Technique. In this processing technique, a graphite target doped with the catalyst *Ni* and *Co* is ablated (vaporized) with laser pulses in a growth chamber. The ablation of the target is performed inside a furnace, which is maintained at about 1200 *°C* and in the presence of a flowing inert gas such as argon. Thereafter, the condensed material from the ablation is collected downstream of the gas flow on a water cooled surface known as cold finger, see Figure 1.6.

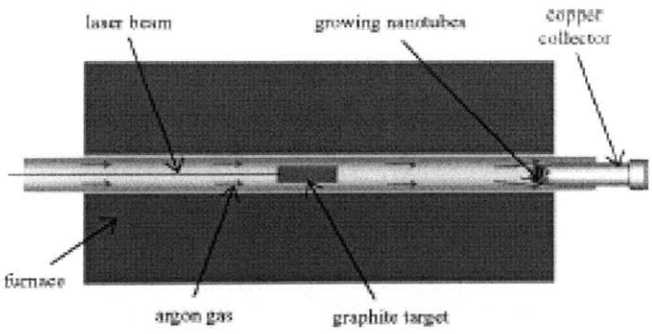

Figure 1.6: Schematic illustration of *Laser-Ablation* technique (Thostenson et al., 2001).

The laser-ablation technique allows the growth of SWCNTs with remarkably uniform diameters and hundreds of μm length. However, these SWCNTs are found in bundles (ropes) bound together with van der Waals forces and are highly tangled. Like the electric-arc-discharge technique, a purification process is required to isolate the tangled SWCNTs from other by products from the process (Popov et al., 2000).

1.2.3 Chemical Vapor Deposition (CVD) Technique

Another promising CNT synthesis method is the chemical vapor deposition (CVD) technique. High quality MWCNTs as well as SWCNTs can be processed by CVD. Here a catalyst material such as Ni in the form of a thin film on a substrate is heated to high temperatures in a tube furnace with a flowing hydrocarbon gas (usually ethylene or acetylene) as the carbon feedstock that remains in the tube reactor for a period of time; see Figure 1.7. The hydrocarbon gas, catalyst and growth temperatures are the key parameters that control the growth process. An optimum set of these parameters can synthesize a vertical array of CNTs with controlled diameter and length.

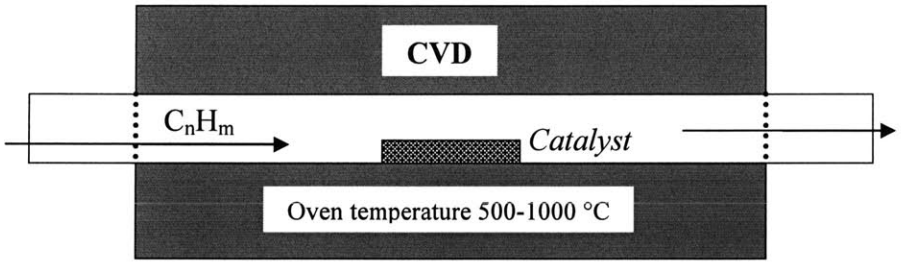

Figure 1.7: Schematic illustration of Chemical Vapor Deposition (CVD) technique (Dresselhaus et al., 2000).

Such optimization has been achieved by Plasma Enhanced Chemical Vapor Deposition (PECVD) where plasma is excited by a DC or microwave source. In this process, the diameter of the CNTs can be adjusted by controlling the thickness of the catalyst on the sample surface; the length can be controlled by regulating vaporization time or the temperature inside the oven; and the direction of the CNTs is controlled by the DC plasma (Saito et al., 2001).

The drawback of the CVD technique when compared to the previous techniques is that the CNTs may have defects on their surface. However, a nearly continuous supply of CNTs in prescribed patterns and uniform distribution over a surface is possible without any purification process. Moreover, if needed, tangled, spaghetti-like CNTs with little length, diameter, and structure consistency can be produced in large quantities and low cost by a regular CVD process (Thostenson et al., 2001).

1.3 Elastic Properties

Before elastic properties of CNTs are discussed, it is important to note that the concept of Young's modulus and elastic constants belong to the framework of continuum elasticity, and that an estimate of these material parameters for CNTs requires a continuum assumption. The thickness of a SWCNT is valid only when it is given on the continuum assumption (Qian et al., 2002). There is no direct technique to measure the elastic properties of CNTs and as a result, most experimentalists estimate the effective elastic properties of the CNT by comparing experimental data with simple dynamic and static solid beam models. Theorists on the other hand, estimate the effective elastic properties of the CNT by applying atomistic, molecular, or continuum mechanics models.

1.3.1 Experimental Analysis

A first attempt to experimentally measure the mechanical properties of CNTs was made by Treacy et al., (1996). In the experiment, they measured the amplitude of thermal vibrations induced on anchored isolated MWCNTs within a Transmission Electron Microscopy (TEM). Assuming a solid homogenous cylindrical beam and using classical vibration theory for elastic rods, an effective Young's modulus value was found to range between 0.4 - 4.15 *TPa* with 1.8 *TPa* as an average value. Krishnan et al., (1998) conducted similar experiments on SWCNTs and found the effective Young's modulus of the tube to be 1.3 ± 0.5 *TPa*. In a different experimental attempt, Wong et al., (1997) used an Atomic Force Microscope (AFM) tip to laterally deflect MWCNTs at were fixed on

one end to square pads of SiO. Thereafter, by assuming a solid beam and applying simple beam theory to reduce the lateral force-displacement data, an effective Young's modulus was found to be 1.28 ± 0.59 *TPa*. Recently, Qi et al., (2003) used classic beam theory and applied it to indentation of vertically aligned carbon nantoube (VACNT) forests to estimate the statistical effective bending, axial, and wall modulus of the CNTs. In another experiment, Salvetat et al., (1999) deposited MWCNTs on a polished ultra-filtration membrane containing pores. On CNTs that would occasionally land over and across these pores, nano-indentations with an AFM tip revealed the effective bending modulus to be 0.81 ± 0.41 *TPa*. In a similar experiment, Tombler et al., (2000) found the effective bending modulus of SWCNTs to be ~1.2 *TPa*. Lourie et al., (1998) used Raman spectroscopy to measure the compressive deformation of a CNT embedded in an epoxy matrix. The effective Young's modulus for a SWCNT was found to be in the range 2.8 – 3.6 *TPa*, while for a MWCNT, in the range of 1.7 – 2.4 *TPa*. Poncharal et al., (1999) in a test simlar to that of Treacy et al., (1996) induced vibrations using electromechanical excitation instead of thermal effects to probe the resonant frequencies of MWCNTs. CNTs of less then 12 *nm* diameter were found to have a Young's modulus ~ 1.0 *TPa*. However, for larger MWCNTs, the effective bending modulus was found to drop from 1 to 0.1 *TPa* with increases in the CNT's diameter from 8 to 40 *nm*.

While performing the above bending experiments, Poncharal et al., (1999) noticed the reversible wavelike distortion (rippling) of the MWCNTs on the compressive side of the bend. These ripples were further studied by Falvo et al., (1997) and Hertel et al., (1998). They used an AFM tip to bend MWCNTs through large angles repeatedly without causing any permanent damage. This local elastic buckling occurs in both SWCNTs and MWCNTs in a rippling bending mode. The ripple pattern penetrates to the inner walls while maintaining the inter-wall spacing, see Figure 1.8.

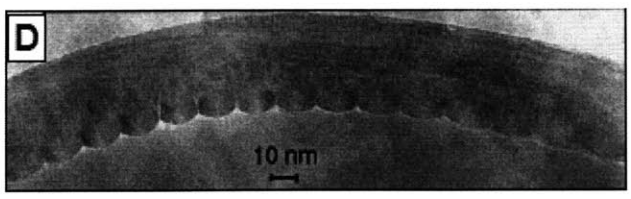

Figure 1.8: Characteristic wave like distortion on the bent side of a MWCNT was observed in HRTEM image (Poncharal et al., 1999).

Iijima et al., (1996) conducted both experimental and theoretical analysis of SWCNT and double-walled CNTs (DWCNT) and found that CNTs can be bent to about 120° without causing any permanent structure damage (bond breakings). They also reported that the kinking or local bucklings seem to become more complex as the number of concentric tube walls in a CNT increases. The buckling occurs not only upon the bending of a CNT, but also upon compression and twisting. When a CNT is twisted, a flattening or collapse of the cross-section occurs (Yakobson et al., 1996).

In addition to axial and bending deformations, researchers have also studied the lateral or radial deformation of CNTs. Ruoff et al., (2003) were among the first to study the radial deformability of CNTs. CNTs (MWCNTs) were aligned to be adjacent to one another and the deformation was subsequently observed under a TEM. The partially deformed MWCNTs suggested the presence of van der Waals forces along the contact region of the two CNTs (Qian et al., 2002) causing distortion of the tube cross-section. Later, in a different experiment, Lordi and Yao (1998) used High-Resolution TEM (HRTEM), in tandem with molecular dynamics simulations to study the response of tubes to asymmetrical radial compressive forces. They related the elasticity and resilience of the walls directly to the tube radius and indirectly to the number of layers in a CNT, as shown in Figure 1.9.

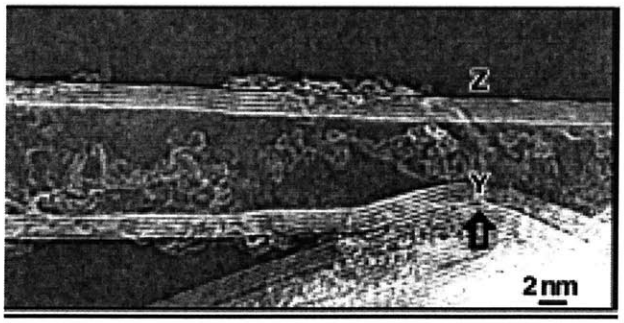

Figure 1.9: Reverse-contrast HRTEM images of asymmetrical radial compression of a MWCNT. A five-layered CNT is essentially experiencing a point force at Y (Lordi and Yao, 1998).

Shen et al., (2000) took a different approach in their experiment. They performed radial indentation of a ~10 *nm* diameter MWCNT with Scanning Probe Microscopy (SPM) in the indentation / scratch mode. They were able to estimate the radial

compressive elastic modulus of an MWCNT by subjecting it to radial compression (asymmetric radial compression). The radial compressive strength thus found was well beyond 5.3 *GPa*. In a separate experiment, Yu et al., (2000-a) indented an MWCNT with an AFM tip after scanning it in tapping mode. They were able to show the reversible radial deformability to be up to 40%. The MWCNTs were indented at five different locations along the length, and the data for force versus strain were obtained. The estimated effective elastic modulus of several sections of the MWCNTs in the radial direction ranged between 0.3 – 4.0 *GPa*.

1.3.2 Theoretical Analysis

In addition to the experimental investigations, the discovery of CNTs has also motivated numerous theoretical and numerical studies in order to better understand the physics and to validate experimental results. Xiao et al., (2005) splits the modeling studies into two categories: *bottom up* and *top down*. The bottom up is based on atomistic (or ab initio), classical molecular dynamics (MD) analysis and the top down covers the structural, continuum mechanics, and Finite Element (FE) analyses. Researchers mainly focus on one of the two categories. A brief description of different modeling approaches are explained in the following sub-sections.

1.3.2.1 Quantum Mechanics (ab initio) Analysis

Generally, to understand the physics of a system, atomistic or ab initio analyses provide the most detailed results when compared to other methods. However, this approach is computationally very expensive. Because of the computational expense, atomistic analysis is used when experimental data are either unavailable or very difficult to obtain – for example, when the characterization of electronic properties of CNTs is required (e.g., Ghosh et al., 2005).

In this analysis, the state of a particle is defined by a wave function in which the energy associated with each electron (particle) in an atom comprising the CNT is added together. Thereafter, using either the Hartree-Fock (e.g., Ghosh et al., 2005), local density

approximation (LDA), or Tight-Binding (TB) (e.g., Hernandez et al., 1998) methods, an approximate solution is obtained to solve the Schrodinger equation

$$H\psi = E\psi\,, \tag{1.6}$$

where H is the Hamiltonian operator of the quantum mechanical system, and ψ is the energy eigenfunction corresponding to the energy eigenvalue E (Qian et al., 2002).

1.3.2.2 Classical Molecular Dynamics (MD) Analysis

Following ab initio analyses, MD analyses are the next most widely used method in the theoretical study of the physical behavior of CNTs. Applying MD mechanics, the physical as well as the chemical properties of CNTs at the atomic-scale can be simulated quite precisely. Though computationally more efficient than atomistic analysis, a maximum number of about 10^9 atoms (Wang and Wang, 2004) and 1^{-15} second time step (Lau et al., 2004) still limits MD simulation capabilities.

CNTs can be thought of as a single large molecule consisting of carbon atoms (Tserpes and Papanikos, 2005). Analytically, in this approach Newton's second law is applied to solve the governing equations of particle dynamics, i.e.,

$$m_i \frac{d^2 r_i}{dt^2} = -\nabla V\,, \tag{1.7}$$

where m_i and r_i are the mass and spatial coordinates of the i^{th} atom, respectively. V is the empirical potential for the system, and ∇ denotes the spatial gradient (Qian et al., 2002). The several methods by which the empirical potential for the system is calculated falls under one of the three categories in the literature and are explained briefly.

a. Force field Method

The force field method provides a simple and effective approach for describing the atomic potential of interacting atoms in a system. The force field is calculated by summing the individual energy contributions from each degree of freedom (bond

stretching, bond angle bending, bond torsion, and non-bonded interactions) of the individual carbon atoms in a CNT (Valavala and Odegard, 2005). Allinger et al., (1977) developed molecular mechanics force field models, *MM2 and MM3*, that can be used for both organic and inorganic systems. The *MM2* force field is based on bond stretching and angle bending that has "catastrophic" bond lengthening and angle-bending. In the *MM3* force field version, Allinger et al., (1989) fixed the bond lengthening and the angle bending issues by including a quartic term in his formulations. Sears and Batra (2004) recently used the *MM3* model and compared results with the other bond order methods in deriving macroscopic properties of SWCNTs. In an another generic force field model by Mayo et al., (1990), bond length, angle bend, and torsion terms are considered in the formulation of the potential function.

b. Bond Order Method

Abell (1985) originally introduced the Morse pair potential where universality in bonding of similar elements was explored. Tersoff and Ruoff (1994) modified the Morse type potential for carbon atoms. The subsequent Abell-Tersoff method is another improvement where the energy of each bond and the angular dependency due to the bond angles is considered in the formulation of the potential. Brenner later modified the Tersoff potential by including formation and breaking of the bonds (Qian et al., 2002). An improved version, the Tersoff-Brenner potential, is now available where the analytic functions for the intra-molecular interactions and an expanded fitting database are included in the previous version (Brenner et al., 2002).

c. Semi-Empirical Method

Pettifor and Oleinik (1999) have proposed an analytical form derived directly from a TB model and successfully modeled the structural differentiation and radical formation. Since this method includes explicit angular interactions and is somewhat less empirical then the empirical bond-order form proposed by Tersoff in the previous section. Qian et al., (2002) referred it as semi-empirical method. This method was used by Zhou et al., (2000).

Besides the above potential functions in the study of CNTs, another important aspect is the interlayer interaction. A widely used form of the inverse power model – the Lennard-Jones (LJ) potential for atomic interactions – was modified by Zhao and Spain (1989) as a pressure/inter-layer-distance relation

$$P = \frac{\Psi}{6}\left[\left(\frac{c_0}{c}\right)^{10} - \left(\frac{c_0}{c}\right)^{4}\right]. \tag{1.8}$$

In Equation 1.8, P is the pressure, c is inter-layer distance, c_0 = 0.341 nm is the equilibrium distance, and Ψ = 36.5 GPa. Zhao and Spain (1989) obtained the relation in Equation 1.8 by modifying the LJ potential energy relation in Equation 1.9 for a carbon system modified by Girifalco and Lad (1956)

$$\phi_i = \frac{A}{\sigma^6}\left[\frac{1}{2}y_0^6\frac{1}{(r_i/\sigma)^{12}} - \frac{1}{(r_i/\sigma)^6}\right]. \tag{1.9}$$

In Equation 1.9 the C-C bond length σ = 0.142 nm, A and y_0 are 24.3E-79 $J.m^6$ and 2.7, respectively, and r_i is the distance between the i^{th} atom pair. Recently, Pantano et al., (2003, 2004-a, 2004-b) and Guo et al., (2004) used this interlayer relation in their continuum shell model and MD simulations, respectively.

The other functional form of the interlayer interaction is the Morse function model. Based on Local Density Approximations (LDA), Wang et al., (1991) derived the Morse potential function for carbon systems; it is given by

$$U(r) = D_e\left[\left(1 - e^{-\beta(r-r_e)}\right)^2 - 1\right] + E_r e^{-\beta' r}, \tag{1.10}$$

where D_e = 6.50E-3 eV is the equilibrium binding energy, E_r = 6.94E-3 eV is the hard-core repulsion energy, r_e = 4.05 Å is the equilibrium distance between two carbon atoms, β = 1.00 $Å^{-1}$ and β' = 4.00 $Å^{-1}$ (Qian et al., 2002). Recently, a modified form of the Morse

potential has been used by Xiao et al., (2005) in their analytical molecular structural model and by Sun and Zhao (2005) to model the breakage of a *C-C* chemical bond.

1.3.2.3 Structural Mechanics Analysis

Odegard et al., (2002) have used a truss model as a bridge between the molecular and continuum models in a manner analogous to a TB model that acts as a bridge between the ab initio and MD analysis. Li and Chou (2003a, 2003b), Shen and Li (2004), Tserpes and Papanikos (2005), and Xiao et al., (2005) later used the equivalent truss model to study the mechanical behavior of CNTs having different diameters and chiralities.

Here, the geometry of the molecular structure is used to define an equivalent truss structure. The stiffness (*EI*) of the truss elements is determined such that the total potential energy of the molecular model and the strain energy of the equivalent truss are equal for the same loading (Odegard et al., 2002). The three dimensional members in a truss structure are pin-jointed with three displacement degrees of freedom at each end. The nodes (pin-joints) represent the location of the carbon atoms in a CNT; see Figure 1.10.

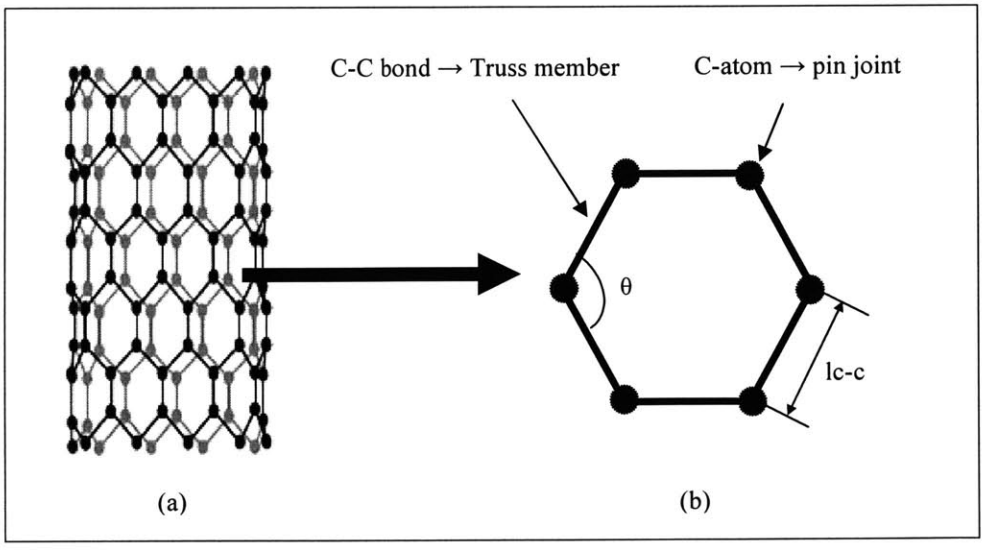

Figure 1.10: Equivalent truss structure of a CNT (a). Hexagonal pattern made of carbon atoms and truss members that make the molecular structure of a CNT (b) (Tserpes and Papanikos 2005; Xiao et al., 2005).

Besides the truss elements to model the sigma bonds, Li and Chou (2003b) used nonlinear truss rod elements to take into consideration the van der Waals interactions that act between individual carbon atoms located on the neighboring layers in an MWCNT. The equivalent truss structure approach seems to work well in visualizing and finding differences in elastic properties of CNTs having different chiralities.

1.3.2.4 Continuum Mechanics Analysis

Theoretical analysis using ab initio or MD methods give extremely good results for the study of the physics behind SWCNT and MWCNT, but are typically limited to the simulation of four concentric CNTs (Liew et al., 2004). However, if the purpose of the theoretical analysis is to investigate the global responses of individual SWCNTs or MWCNTs or CNT-based composites, such as deformations, effective stiffness, or load transfer mechanisms in the nanocomposites, then the continuum mechanics approach can be applied safely to provide needed results effectively and efficiently (Liu and Chen, 2003). Solid and nested shell models have been used as equivalent continuum models with average material properties of CNTs to study their mechanics. Harik (2001) adopted an approach using non-dimensional ratios of geometric parameters to find ranges of validity for the continuum beam model. To check the applicability of the beam assumption for CNTs, he laid the following three criteria for a continuum beam,

* homogenization criteria - $L_{NT} / a_1 > 10$

* aspect ratio criteria - $L_{NT} / d_{NT} > 10$

* linearity of strains criteria - $\left(L_{NT} - L_{NT_0}\right) / L_{NT_0} << 1$. (1.11)

In Equation 1.11, L_{NT}, L_{NT0} and d_{NT} are the final length, initial length and diameter of the CNT, respectively, and a_1 is the width of the carbon ring – about 0.24 *nm*.

Large ambiguities in the properties of CNTs exist as a result of the application of continuum models. Nonetheless, high computational efficiency at the cost of this ambiguity and loss of accuracy seems to be accepted by the researchers.

a. Equivalent Solid model

Treacy et al., (1996), Wong et al., (1997), Krishnan et al., (1998), Poncharal et al.,(1999), Salvetat et al., (1999), and Qi et al. and many others applied beam theory to isotropic solid cylindrical beam models to estimate the effective mechanical properties of individual CNTs. The application of the solid beam model has been somewhat successful for calculating the static and dynamic responses of the CNTs. However, the ambiguity in the estimated properties such as effective bending modulus ($0.81 - 1.8$ *TPa*) can be seen when Euler beam theory is applied to analyze the experimental data. Recent investigations by Liu et al., (2001, 2003), Wang and Wang (2004), Wang et al., (2004), and Wang et al., (2005) have taken the anisotropic nature of CNT into account in their 2D (e.g., Liu et al., 2001, 2003) and 3D (e.g., Wang and Wang, 2004; Wang et al, 2004; Wang et al., 2005) solid beam models. Using FE techniques, they were able to capture both pre- and post-buckling effects of a CNT assuming small-strains and large-deflections, and found a highly nonlinear moment-curvature relation; in addition they found a non-dimensional critical curvature for the onset of the rippling bending mode in a CNT. The material properties of basal graphene sheet were adopted to model the anisotropic nature of MWCNTs.

b. Equivalent Shell Model

Yakobson et al., (1996) first compared the results of atomistic modeling for axially compressed buckling of single-walled nanotubes with a simple continuum shell tube that mimics the SWCNT wall. They found that the buckling patterns displayed by MD simulations can also be predicted by the continuum shell. Thereafter, Ru (2000a, 2000b, 2000c, 2001), Wang et al., (2003), He et al., (2005), and others used analytic shell models to capture the nonlinear mechanical behavior of both SWCNTs as well as MWCNTs very well. Researchers however, are not consistent in their effective shell thickness and Young's modulus in that they range from $0.066 - 3.4$ *nm* and $1.0 - 5.5$ *TPa*, respectively. The properties are usually found by equating the total strain energies of the system with that obtained from ab initio or MD analysis under identical loading conditions. Later Pantano et al., (2003, 2004a, 2004b) used Yakobson et al.'s, (1996)

insight to propose a continuum nested structural shell method for modeling CNTs; this method will be discussed in detail in the next chapter.

1.3.2.5 Finite Element (FE) Analysis

Much like MD simulations, FE analyses help researchers verify the analytical solutions and to visualize the experiments that are hard to see at nano scale levels. All continuum models: solid, truss and shell have been used to study CNTs. Liu et al., (2001, 2003), Wang and Wang (2004), Wang et al., (2004), Wang et al., (2005), and current authors have modeled the anisotropic solid beam model using the solid elements (Figure 1.11-a), Tserpes and Papanikos (2005), Li and Chou, (2003a, 2003b) developed a Truss model using beam elements; see Figure 1.11-c. Pantano et al., (2003, 2004a, 2004b), and Arroyo and Belytschko (2003) modeled MWCNTs with the LJ potential as the interlayer force while Sears and Batra (2004) modeled SWCNTs with thin shell elements, see Figure 1.11-b.

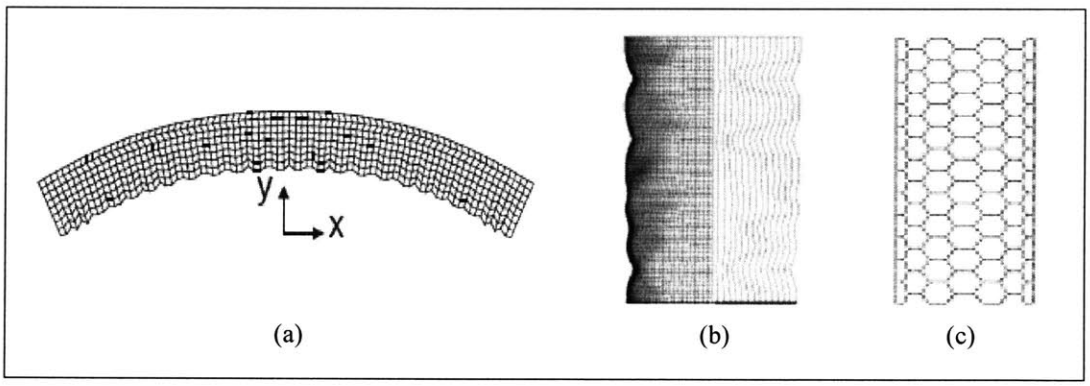

Figure 1.11: Finite Element analysis of CNT using orthotropic solid model (a) (Liu et al., 2001), equivalent nested shell model (b) (Pantano et al., 2003), and truss model (c) (Tserpes and Papanikos, 2005).

The FE-based orthotropic solid models, Liu et al., (2001, 2003), Wang and Wang (2004), Wang et al., (2004), and Wang et al., (2005) adopted basal graphite plane elastic properties to simulate MWCNTs subjected to bending. All the orthotropic solid FE-based models were simulated in a commercial FE software package, *ABAQUS*. The FE-based truss models are usually modeled with beam elements. Li and Chou (2003b) treated

MWCNTs as a single-walled frame like structure and used a nonlinear truss rod model to simulate the LJ potential and represent the interlayer van der Waals forces. The properties were derived in an approach similar to that suggested by Odegard et al., (2002) in Section 1.3.2.3. Lastly, as mentioned in the previous section, Pantano et al., (2004b) modeled the nested shell structure by assuming shell elements to be isotropic having Young's modulus and mechanical wall thickness pair of 4.84 *TPa* and 0.075 *nm*, respectively. The interlayer van der Waals force was also included in the nested shell FE-based model of MWCNTs subjected to bending and axial compression (e.g., Pantano et al., 2003). Using the nested shell FE-based model, Pantano et al., (2003, 2004a, 2004b) were able to study the effect of van der Waals forces on the rippling behavior on MWCNTs subjected to bending (e.g., Pantano et al., 2003) and axial compression (e.g., Pantano et al., 2004a).

In this chapter, we presented a detailed description of the nearly defect-free carbon nanotube structure, and a brief overview of their potential applications. Thereafter, we discussed techniques researchers are currently using to synthesize high quality carbon nanotubes, and also to measure their mechanical properties. Measuring the mechanical properties experimentally is a challenge due to exceptionally small dimensions of the nanotubes; therefore, researchers must simulate the mechanical behavior of these nanotubes using computational techniques, such as MD and FE simulations. Recently, most experimental investigations point to a unified characterization of the mechanical properties of carbon nanotubes; however, theoretical investigations differ in their approach in estimating these properties. MD simulations being the most precise, lack in computational efficiency in modeling multi-walled carbon nanotubes. On the other hand, the less precise FE simulations are more computationally efficient. Theorists have used beam, truss, solid, and shell elements to model carbon nanotubes. Recently, Pantano et al., (2003, 2004a, 2004b) developed the nested shell model in which they used shell elements to model MWCNTs, and user defined interference elements to model interlayer van der Waals forces. With this technique, they were able to successfully capture the complex nonlinear deformation mechanics of both single and multi-wall carbon nanotubes; however, they used small-sized elements that make their model computationally inefficient for large MWCNTs. For FE simulations,

modeling nanotubes with solid elements is the most efficient approach; however, they either fail to capture the complex buckling behavior of MWCNTs or fail to account for the van der Waals force. This motivated us to develop a new FE approach, presented in Chapter 2, which uses computationally efficient solid elements whose properties are derived from nested shell theory (Pantano et al., 2003).

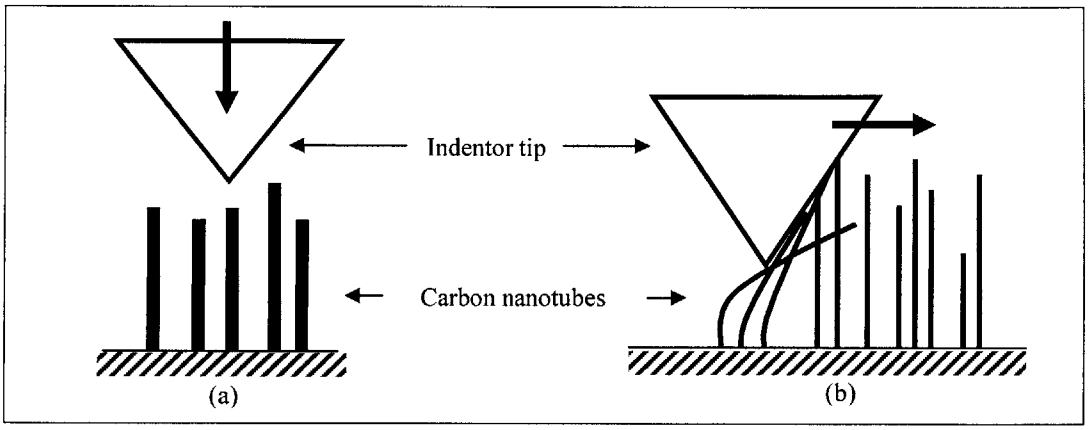

Figure 1.12: Two-dimensional schematic of nano-indentation (a) and nano-scratching (b).

Thereafter in Chapter 3, we will apply the developed FE approach to an analytical contact model first proposed by Qi et al. (2003). The contact model simulates the nano-indentation of vertically aligned carbon nanotube (VACNT) forests, whereby nanotubes are consecutively bent during the penetration of the indentor (AFM tip), as shown in Figure 1.12-a. Using the simulation results obtained from the FE approach in Chapter 2, the contact model will be modified to include the buckling effect observed in MWCNTs. Thereafter, the nano-indentation contact model will be further modified to simulate nano-scratching of beams, as shown in Figure1.12-b. Finally, Chapter 4 concludes the thesis.

Chapter 2

This chapter proposes a method for the representation of the mechanical behavior of an MWCNT by building a linear elastic representation based on the local orthotropy of its nested tube microstructure. We will refer to this as an "equivalent orthotropic representation" (EOR) with the caveat that the tube as a whole is not orthotropic but its microstructure is locally orthotropic. The effectiveness of the EOR model in predicting nonlinear deformations is examined via comparison with the results of the nested structural shell representation (NSSR) developed by Pantano et al., (2004b). The proposed method when applied to the Finite Element Method (FEM) MWCNT models replicates the bending, axial compression and radial compression phenomenon seen in the NSSR model and several experimental investigations. The proposed model was observed to capture the pre- as well as post-buckling, nonlinear structural behavior of MWCNTs within a reasonable amount of deviation from previous predictions. The proposed method is able to provide excellent predictions of such complex deformations, since it directly accounts for the stiff axial behavior of the shell and the compliant radial and shear behavior of the interlayer van der Waals interactions. The proposed model is time efficient and works well for a complicated system of MWCNTs in FEM which is currently impractical if not impossible with Molecular Dynamics (MD) or NSSR techniques.

2.1 Introduction

Investigators have been able to successfully use MD simulations (e.g., Yakobson et al., 1996, Iijima et al., 1996, Tserpes and Papanikos, 2005, Sun and Zhao, 2005, Xiao et al., 2005, Liew et al., 2004) and NSSR modeling (e.g., Pantano et al., 2003, 2004a, 2004b) to simulate the tension, compression and bending of MWCNTs thereby capturing the initial linear elastic behavior of the tube as well as the buckling instabilities and resulting nonlinear behavior. Liew and Wong et al. modeled a maximum of four

concentric tubes with MD simulations, while Pantano et al., (2003) modeled a maximum of nineteen concentric tubes with NSSR technique in FEM including interlayer interactions. Although with the nested shell model approach, Pantano et al., (2003, 2004a, 2004b) are able to simulate a higher number of walls in the MWCNTs, it still becomes impractical for very large MWCNTs containing over 100 walls.

Many of the potential applications for CNTs will utilize MWCNTs (VACNT, CNT-based composites, MEMS devices, and others). Current atomistic modeling and FEM nested structural shell models, while providing detailed insights into the tube structure and deformation, are computationally burdensome for use in actual composite material simulations. This chapter presents an alternative continuum solid model approach that preserves the structural features governing the tube mechanical behavior while offering tremendous improvements in computational cost. The new model takes into account the nested tube structure, the stiff inter-wall van der Waals normal interactions, and the compliant shear interactions between walls that give carbon nanotubes their unique mechanical behavior. The proposed EOR model has the potential to construct several MWCNTs that include the internal van der Waals interactions between walls and external interactions between individual tubes.

This chapter first reviews past models of CNT structure and then presents the new approach. Axial compression, bending and radial compression behaviors from the new model are then presented and compared for different models.

2.2 Review of Prior Modeling Approaches

This section reviews models of the structural and mechanical behavior of nanotubes, including Molecular Dynamics, isotropic continuum solid, and nested structural shell representations.

2.2.1 Molecular Dynamics Model

Molecular Dynamics simulations of defect free cylindrical carbon nanotubes have been performed by several research groups (Yakobson et al., 1996, Iijima et al., 1996, Tserpes and Poponikos, 2005, Xiao et al., 2005, Sun and Zhao, 2005, Liew et al., 2004). MD simulation models can predict CNT behavior at small linear deformations and also beyond the linear response. An analytic approach uses Newton's second law to solve the governing equations of particle dynamics:

$$m_i \frac{d^2 r_i}{dt^2} = -\nabla V, \tag{2.1}$$

where m_i and r_i are the mass and spatial coordinates of the i^{th} atom, respectively. V is the empirical potential for the system, and ∇ denotes the spatial gradient (Qian et al., 2002). The empirical potential for the system is defined by one of force field, bond-order or semi-empirical methods, as discussed earlier in Chapter 1. The interlayer interactions in MWCNT are usually taken into account by either of two available potentials: Lennard-Jones (LJ) (Girifalco and Lad, 1956) or Morse potential (Wang et al., 1991).

Yakobson et al., (1996) used the Tersoff-Brenner potential in their MD simulations of SWCNTs for modeling interactions between carbon atoms (bond-order empirical potential); the SWCNTs modeled had different diameters, helicities and lengths. They subjected these SWCNTs to axial compression, bending and torsion in their simulations. The results thus obtained were plotted as strain energy of deformation versus axial compression strain, bending angle or torsion angle. A sudden drop in strain energy was observed in simulations upon the initiation of buckling. In a separate research, Iijima et al., (1996) carried out similar MD simulations in bending. Here several SWCNTs and DWCNTs of different diameters and helicities were modeled by applying the Tersoff-Brenner potential. For DWCNTs, the compliant van der Waals interaction between the layers was also taken into account.

In their MD simulations for SWCNT and DWCNT, both Yakobson et al., (1996) and Iijima et al., (1996) found that the strain energy of nanotubes increase quadratically with the bending angle until the onset of buckling and subsequently linearly thereafter.

The quadratic behavior implies that the bending response of a nanotube can be treated as some effective linear elastic continuum beam. However, quadratic behavior appears only before buckling implying that the effective linear elastic beam assumption is valid only prior to the onset of local instabilities, as shown in Figure 2.1.

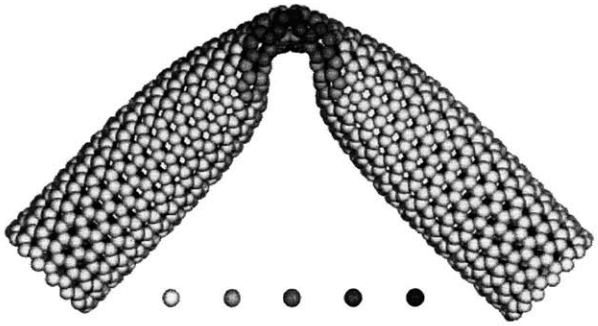

Figure 2.1: Molecular Dynamics simulation of a SWCNT subjected to bending (Iijima et al., 1996). Single kink is visible, which results in the drop in the strain energy curve when plotted with respect to bending angle.

Robertson et al., (1992) found that unloaded SWCNTs possess an internal strain energy per carbon atom that exhibits a $1/R^2$ relationship, where R is the radius of the tube wall. The inverse square relationship in comparison with continuum-level elastic structural mechanics predictions indicated that the single-atom thick tube-wall behaved in a manner mechanically equivalent to that of a thin shell. In classic elasticity theory, the internal energy per unit area or rolling energy, U_R, in a cylindrical tube is given by $U_R = \frac{1}{2}(D/R^2)$, where D is the bending stiffness of the sheet. (Yakobson et al., 1996) supports the Robertson et al., (1992) argument by comparing the internal energy of a SWCNT obtained from ab initio or semi-empirical studies with the energy of a shell. Considering the two-dimensional hexagonal structure of graphite as an isotropic material implies that only two elastic parameters C (the membrane stretching stiffness) and D (the bending stiffness) are required to define the equivalent shell. Taking the data from Robertson et al., (1992), Yakobson et al., (1996) obtained $C = 59\ eV/atom$ and $D = 0.85\ eV$ (= 2.23 eV $\text{Å}^2/atom$ [assuming the occupied area per carbon atom to be $\Omega = 2.62\ \text{Å}^2/atom$]). They also reported the Poisson ratio as 0.19 for the shell, obtained by estimating the reduction

in diameter of a tube subjected to uniaxial tension in a simulation. This value of Poisson ratio also happens to be the value obtained from experimental results for single crystal graphite by Kelly et al., (1981). Then applying classical shell theory, where $C = Yh$ and $D = Yh^3/12(1 - v^2)$, they obtained $E = 5.5$ *TPa* and $h = 0.066$ *nm*, where E and h are the Young's modulus and the thickness of the shell, respectively. Later, Pantano et al., (2003, 2004a, 2004b) used classical shell theory, and the above C and D values to find an equivalent Young's modulus and mechanical wall thickness pair of 4.84 *TPa* and 0.075 *nm*, respectively.

2.2.2 Linear Elastic Beam Model

MD simulation is an excellent technique for capturing CNT mechanics; however, it is computationally expensive. For example, the model of DWCNT is a challenge when simulating from initial small-strain, small-deformation behavior through the structural instabilities. Therefore, linear elasticity theory in various forms has been employed by many investigators to study and interpret various CNT deformations. As mentioned in the previous section, Yakobson et al., (1996) and Iijima et al., (1996) indicated that a CNT can be treated as an effective solid beam because the strain energy of the tube shows a quadratic behavior as a function of curvature for bending simulations before buckling initiates. Harik (2001) using a non-dimensional approach, also supported the Yakobson et al., (1996) theory of treating CNTs of large aspect ratio as nanobeams. Many experimentalists (Wong et al., 1997, Qi et al., 2003, and more) performed bending on CNTs using AFM tips; thereafter, they reduced the data assuming an effective linear elastic beam to find the effective mechanical properties of the tube, such as a bending modulus of CNTs. The bending is limited to small angles prior to any onset of buckling. Here the effective bending stiffness, $(EI)_{Eff}$, of a CNT is given by the classic formula,

$$EI_{Eff} = E_b I_{tube} = E_b \frac{\pi}{4}\left(R_o^4 - R_i^4\right) \tag{2.2}$$

where E_b, I_{tube}, R_o, R_i are the effective bending modulus, moment of inertia, outermost and innermost radius of the effective linear elastic beam, respectively. The E_b found by reducing it from the experimental results usually varies between 0.8 to1.8 *TPa* (Treacy et al., 1996, Wong et al., 1997, Krishnan et al., 1998, Qi et al., 2003). The continuum elastic solid beam is considered to have homogenous isotropic properties.

2.2.3 Discrete Nested Shell Model

A linear elastic isotropic beam model provides an adequate representation of the mechanical behavior of SWCNTs and MWCNTs for small strain deformation behavior prior to any buckling and is time efficient for producing results for even large radius MWCNTs. However, this technique cannot predict the buckling and post-buckling behavior of a CNT. The experimental observations of internal structures during bending, buckling, and telescopic sliding (Cummings and Zettl, 2000) indicate that specific structural features of CNTs make important contributions to nanotube deformation response during some cases of mechanical loading; therefore, such features should be accounted for in any model of a nanotube. Pantano et al., (2004b) used the insights derived from experimental work and atomistic simulations to develop an FEM-based elastic nested shell model approach that considers the internal structural features of a tube. The nested shell model can predict the pre-buckling (linear) mechanics, onset of local versus global buckling and the post-buckling (nonlinear) mechanics of both SWCNTs and MWCNTs, as shown in Figure 2.2.

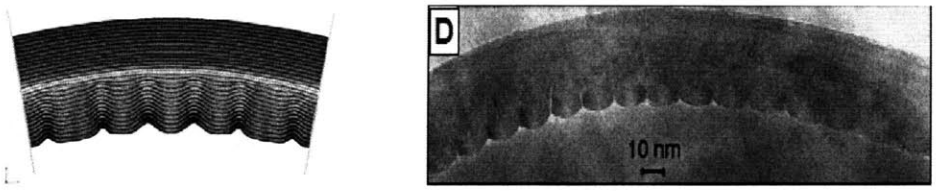

(a) (b)

Figure 2.2: Finite Element bending simulation of a 14-walled CNT using nested shell model (a) (Pantano et al., 2004b). Complex rippling mode is apparent in the figure (b) which is remarkably similar to the HRTEM image taken by Poncharal et al., (1999).

Pantano et al., (2004b) specified four key aspects for modeling a CNT as a continuum shell. First, a Poisson ratio of 0.19 and a specific paring of elastic constants (E_{wall} = 4.84 *TPa*, t_{wall} = 0.075 *nm*) must be assigned to each tube wall such that both the membrane stretching and bending behavior of the wall are captured. Second, an initial stress state that corresponds to the curvature of the tube wall must be assigned. The initial stress state develops because the stress-free planar hexagonal structure wraps into a tubular structure. The initial stress state in the tangential direction, $\sigma_{\theta\theta}$, is inversely proportional to the radius of the tube and can be calculated from the following equation derived using classic elasticity theory,

$$\sigma_{\vartheta\vartheta} = \frac{E_{wall}}{(1-\nu^2)}\left[\frac{r-R}{R}\right], \tag{2.3}$$

where, R is the mean radius of the shell tube, and r is the radial location of a point in the tube. Clearly from Equation 2.3, the magnitude of the initial stress state diminishes as the radius of the MWCNT increases. Third, a strong normal force interaction between the adjacent walls, with other portions of itself, and with like substrates must be incorporated. Pantano et al., (2003, 2004a, 2004b) used the pressure/inter-layer-distance relation which Zhao and Spain (1989) derived from Girifalco and Lad (1956) LJ potential energy model. The pressure/inter-layer-distance relation that Pantano et al., (2004b) used to model the van der Waals interaction pressure-separation behavior is given below:

$$P = \frac{\Psi}{6}\left[\left(\frac{c_0}{c}\right)^{10} - \left(\frac{c_0}{c}\right)^{4}\right], \tag{2.4}$$

where, P is the interlayer pressure, c is the inter-layer distance, c_0 = 0.34 *nm* is the interlayer equilibrium separation distance, and Ψ = 36.5 *GPa*. Fourth, the wall-to-wall shear resistance, taken to be negligible, was observed experimentally to be very compliant and an order of magnitude weaker when compared to the stiff normal wall-to-wall resistance provided by van der Waals interaction. Blakslee et al., (1970) found the shear modulus for Pyrolytic Graphite to be 0.18 to 0.35 *GPa*. In addition, Yu et al.,

(2000b) and Cummings and Zettl (2000) made measurements of tube pull-out force as a function of overlap length between shells, and controlled and reversible telescopic extensions of MWCNTs within a TEM and found average sliding resistance strength of 0.48 *MPa*. The sliding resistance strength thus found for CNTs matches the experimental mean value of the inter-layer sliding resistance strength for crystalline graphite found by Kelly (1981).

In addition to the four key aspects, Pantano et al., (2004b) concluded that the most accurate mechanical behavior for predicting structural instabilities was obtained when with square individual shell elements discretizing the SWCNT, and with a side length of 0.24 nm, which is the same as the height of the hexagonal lattice cell. They (Pantano et al., 2004b) found that smaller elements might erroneously capture a wavelength that cannot be accommodated by the carbon lattice structure and too large an element dimension might miss the buckling wavelength.

The interlayer potential between nested shell structures have been successfully modeled with nonlinear FE method in Pantano et al., (2003, 2004a, 2004b). Results obtained by compressing and bending the FE-based nested elastic shell model for SWCNTs and MWCNTs were compared with MD simulations of SWCNT deformations (Yakobson et al., 1996) and with high-resolution images of bent MWCNTs (e.g., Falvo et al., 1997, Poncharal et al., 1999, Bower et al., 1999). In their simulations with the FE nested shell model, Pantano et al., (2003, 2004a, 2004b) were able to successfully capture the pre- and post-buckling behavior of the CNTs. By setting the square shell element size to that of the carbon lattice spacing (0.24 *nm*) and applying van der Waals interaction within the tube, a single kink similar to that of MD simulations developed in the SWCNTs. However, due to lack of numerical simulation results for MWCNTs, Pantano et al., (2004b) compared the results from the nested shell model with the experimental observations of Lourie et al., 1998, Poncharal et al., 1999, and Bower et al., 1999.

MWCNTs develop a multiple kink pattern (rippling or wrinkling) in the post-buckling regime, as shown in Figure 2.2. From their NSSR model, Pantano et al., (2003) showed this rippling pattern to progress from a shorter initial wavelength (λ) to a "steady-state" longer wavelength as macroscopic loading increased. The predicted steady-state buckling wavelengths were computed for several MWCNTs and compared with the

experimental observations of Lourie et al., 1998 and Bower et al., 1999; the nested shell model showed remarkably good agreement with the experimental observations (Pantano et al., 2003, 2004b). The initial buckling wavelength for the outermost tube in an MWCNT was found to match the value predicted by thin shell theory (Timoshenko, 1936) that not only accounts for the outer wall stress, but also thickness.

$$\lambda = 3.4\sqrt{R_o h}\,, \tag{2.5a}$$

here R_o and h are the outermost radius and the CNT outer wall thickness (= 0.075 *nm*) of the nanotube, respectively. In addition, Pantano et al., (2003, 2004b) showed that the steady state longer wavelength in an MWCNT can be predicted from Equation 2.5b.

$$\lambda = \sqrt{R_o h_t}\,, \tag{2.5b}$$

where $h_t = (R_o - R_i)$ is the total tube thickness and R_i is the innermost tube radius, following that observed by Bower et al., (1999).

2.3 Present Model Design

Here, we propose a new FE-based equivalent orthotropic representation (EOR) model for an MWCNT based upon the nested shell structure of similar CNTs. The EOR model uses a micro-mechanical representation, where the "plane" of orthotropy is aligned with the radial (r), the tangential (θ), and the axial (z) directions of the tube, as shown in Figure 2.3-a and 2.3-b. Unwrapping a local point (Figure 2.3-c), we construct a representative volume element (RVE) of a material point, a radially symmetric layered structure, to predict the equivalent mechanical properties. The EOR model can be thought of as transversely isotropic in nature because of the radially symmetric nature, and therefore requires five independent effective elastic constants to fully define its equivalent mechanical properties. The required five constants that fully capture the

locally transverse isotropic nature of the layered material are determined by the axial/tangential modulus ($E_{zzEff} = E_{\theta\theta Eff}$), the radial modulus ($E_{rrEff}$), the Poisson ratios $\nu_{\theta zEff}$ ($= \nu_{z\theta Eff}$) and $\nu_{r\theta Eff}$ ($= \nu_{rzEff}$), and the shear modulus ($G_{r\theta Eff} = G_{rzEff}$). Note that the Poisson ratio notation used, for example is $\nu_{\theta z} = -\varepsilon_{zz} / \varepsilon_{\theta\theta}$ for axial loading in the θ-direction.

In the following sections, starting with simple rule of mixture (ROM) method, we subject the RVE to four uniform loading conditions: in-plane stress (σ_{zz} or $\sigma_{\theta\theta}$), transverse stress (σ_{rr}), transverse shearing ($\sigma_{r\theta} = \sigma_{rz}$) and in-plane shearing ($\sigma_{\theta z}$). The loading conditions are chosen such as to determine the five constants in terms of the tube wall properties, the interlayer potential and the RVE geometry (interlayer spacing) listed earlier.

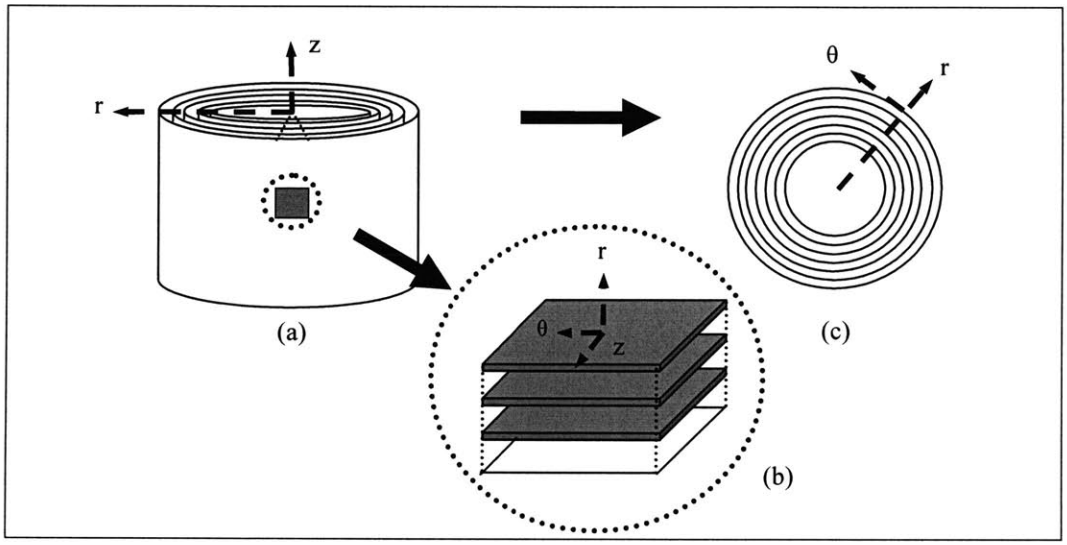

Figure 2.3: *N-walled* CNT with a representative volume element (RVE) (a) at a material point with inset (b). The gray layers represent the graphene sheets and the spaces between the sheets are the spaces where interlayer interactions exist. Top-view of the *N-walled* CNT with cylindrical coordinate system (c).

The condition that $\sigma_{\theta\theta} \neq 0$ and all other $\sigma_{ij} = 0$ will determine $E_{\theta\theta Eff}$ and $\nu_{\theta zEff}$, the condition that $\sigma_{rr} \neq 0$ and all other $\sigma_{ij} = 0$ will determine E_{rrEff} and $\nu_{r\theta Eff}$, the condition that $\sigma_{r\theta} \neq 0$ and all other $\sigma_{ij} = 0$ will determine $G_{r\theta Eff}$ and finally, the condition that $\sigma_{\theta z} \neq 0$ and

all other $\sigma_{ij} = 0$ will determine $G_{\theta zEff}$. The different loadings are applied on an *N-layered* composite RVE taken from an MWCNT wall, as shown in Figures 2.3-a and 2.4-b.

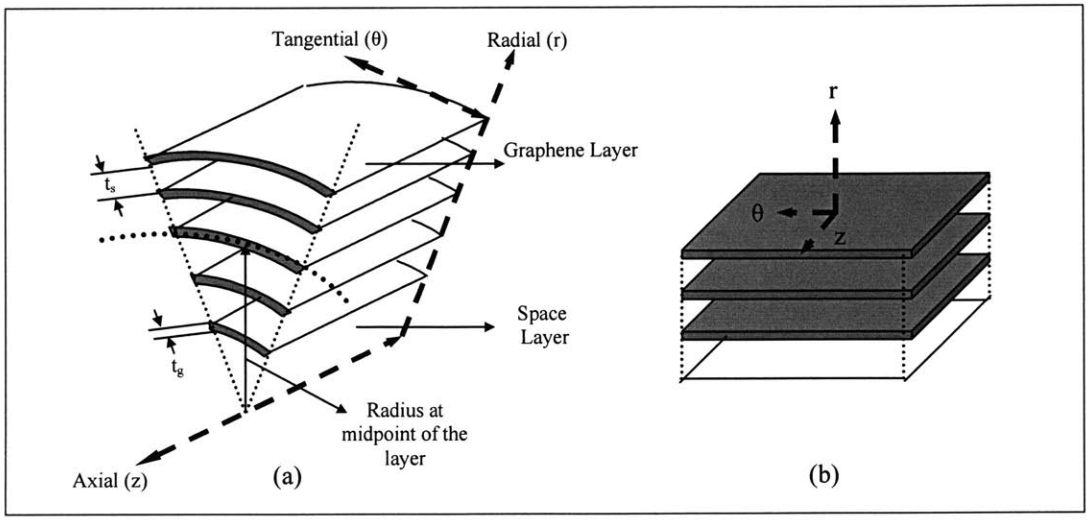

Figure 2.4: Iso-view of the representative volume element for an MWCNT from Figure2.3. Notice the Graphene layers and the Space layers that constitute the RVE in cylindrical coordinate system (a). The *N*-layered planar RVE at a material point used in the analysis along with cylindrical coordinate system (b).

2.3.1 Effective Elastic Orthotropic Properties

The EOR material can be treated as a micro-laminate composite made of alternating layers of graphene sheets and empty space, as shown Figure 2.4-b. Applying the ROM for composites, we can analytically determine the equivalent effective properties for our layered EOR structure. Enforcement of compatibility and equilibrium during the previously stated loading conditions enables us to determine the effective composite properties based on the layer properties and their volume fraction. The volume fraction of a constituent in the RVE is defined as the ratio of the volume of the constituent, V_i ($i = g$ for graphene, $i = s$ for space) to the total volume of the structure, V:

$$V = V_g + V_s \tag{2.6a}$$

$$f_g = \frac{V_g}{V}; \qquad f_s = \frac{V_s}{V} = 1 - f_g \tag{2.6b}$$

$$f_g = \frac{t_g}{t_g + t_s} \tag{2.6c}$$

$$f_g(N) = \left[\frac{2t_g * \sum_i^N R^i}{\left(R_o + \left(\frac{t_g}{2}\right)\right)^2 - \left(R_i - \left(\frac{t_g}{2}\right)\right)^2} \right] \tag{2.6d}$$

$$f_g(R^i) = \left[\frac{2t_g * R^i}{\left(R^i + \left(\frac{t_g}{2}\right)\right)^2 - \left(R^i - t_s + \left(\frac{t_g}{2}\right)\right)^2} \right] \tag{2.6e}$$

where f_g and f_s are the volume fractions of graphene and space layer, respectively; t_g is the thickness of the graphene layer; t_s (= c_o) is the interlayer equilibrium spacing; R_o and R_i are the outermost and innermost tube radius. In addition, R^i and N in Equations 2.6d and 2.6e are the mean radius of the i^{th} tube and the number of concentric tubes, respectively. Equations 2.6c to 2.6e represent three forms of f_g: constant global f_g, global $f_g(N)$ as a function of N, and local $f_g(R^i)$ as a function of R^i. The basic difference in the three forms of f_g is that the $f_g(N)$ and $f_g(R^i)$ takes the curvature of the CNTs into account, while the constant global form assumes layered planar structure. In addition to the curvature of the layers, $f_g(R^i)$ accounts for the variation in volume fraction based on the variation in curvature of the layers within an MWCNT. Therefore, $f_g(R^i)$ obtained from Equation 2.6e offers the most precise value out of the three forms.

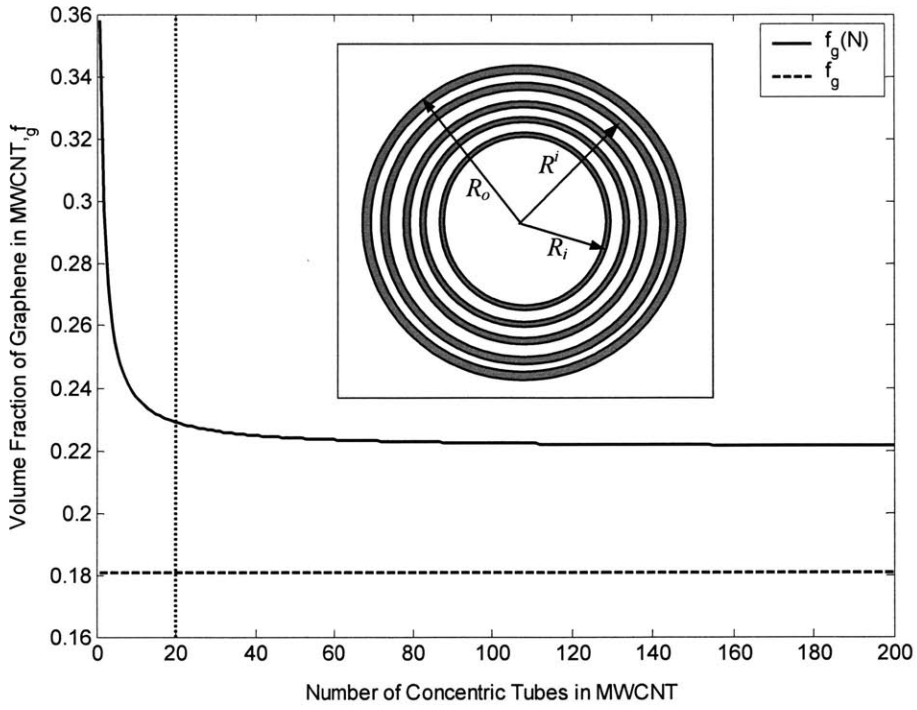

Figure 2.5: Variation of the volume fraction of graphene ($f_g(N)$) with number of layers in an MWCNT (t_g = 0.075 *nm*, t_s=0.34 *nm*). The inset view shows the top-view of MWCNT with specific parameters used in the determination of global volume fraction.

Figures 2.5 and 2.6 are graphical representations of Equations 2.6d and 2.6e obtained by substituting t_g = 0.075 *nm* and t_s = 0.34 *nm*. Similarly, substituting values for t_g and t_s in Equation 2.6c, we find that f_g is a constant value of 0.181 that does not vary with either N or R^i, and represented by a straight dash-line in Figures 2.5 and 2.6. However, substituting similar values of t_g and t_s in Equations 2.6d and 2.6e, we observe that f_g varies with N or R^i, as shown in Figures 2.5 and 2.6, respectively. Simulation results indicated that Equation 2.6d give better results for higher number of coaxial tubes in a MWCNT is considered – higher than 20 concentric tubes, as shown by dash line in Figure 2.5. For MWCNTs having more than five concentric tubes, the right hand term in the denominator can be ignored when compared to that of the left hand term in the denominator in Equation 2.6d and 2.6e. Figure 2.6 shows the variation of the volume fraction of the graphene layer and the adjacent space layer as a function of tubes radial location R^i. We expect to get better simulations results, if in future, material properties

within a MWCNT model can be made to vary as a function of element's location with respect to the axis of the CNT with the help of $f_g(R^i)$.

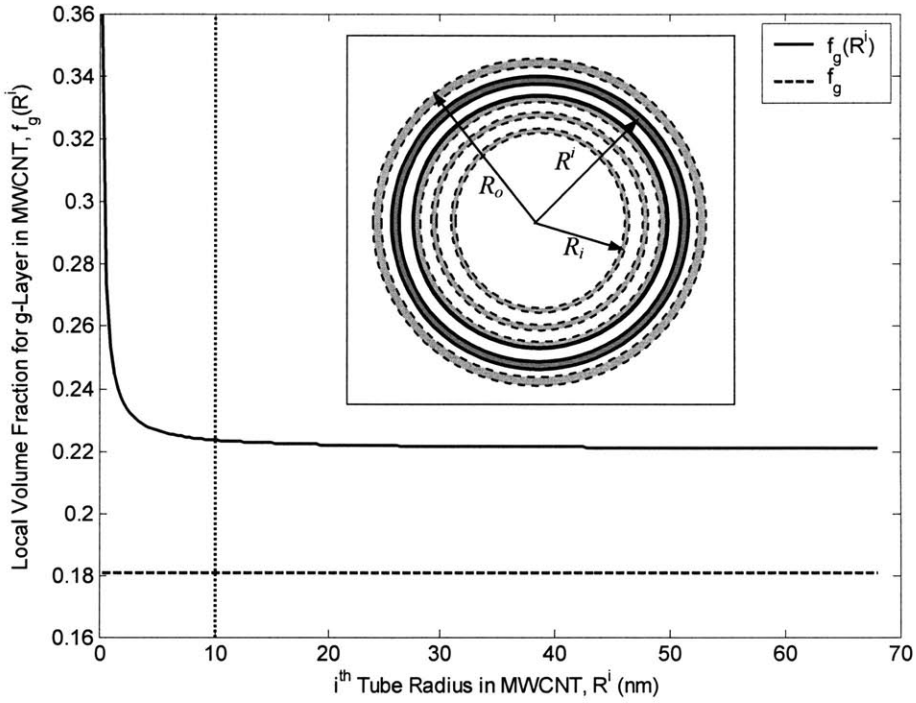

Figure 2.6: Variation of the volume fraction $(f_g(R^i))$ for an individual graphene layer with radial position in an MWCNT (t_g = 0.075 *nm* and t_s=0.34 *nm*). The inset view shows the top-view of MWCNT with specific parameters used in the determination of local volume fraction.

In the subsequent sections, we will revisit the volume fraction issue and its possible role in the in the formulation or the EOR model. Next, we subject the RVE at a material point to each of the four aforementioned uniform stress conditions in order to determine the effective independent elastic constants for the EOR model material. Each constituent layer is taken to be linearly elastic with properties E_g, G_g, v_g and E_s, G_s, v_s defining the effective Young's modulus, shear modulus and Poisson ratio for the graphene and space layers, respectively. By satisfying the equilibrium and compatibility conditions, we can derive the equations that govern the overall composite behavior for each loading condition.

A. RVE Subjected to Macroscopic Normal Stress (θ - direction) ($\sigma_{\theta\theta} \neq 0$ with all other $\sigma_{ij} = 0$)

The effective in-plane Young's modulus ($E_{\theta\theta Eff}$ and E_{zzEff}) and Poisson ratio ($\nu_{\theta zEff}$) of the RVE are calculated by applying a macroscopic stress, $\sigma_{\theta\theta}$, as shown in Figure 2.7. The main assumption in this formulation is that the strains in the θ- and z-directions in the symmetry plane are the same in the graphene (g) and the space (s) layers. This implies that the graphene-space layer bond is perfect.

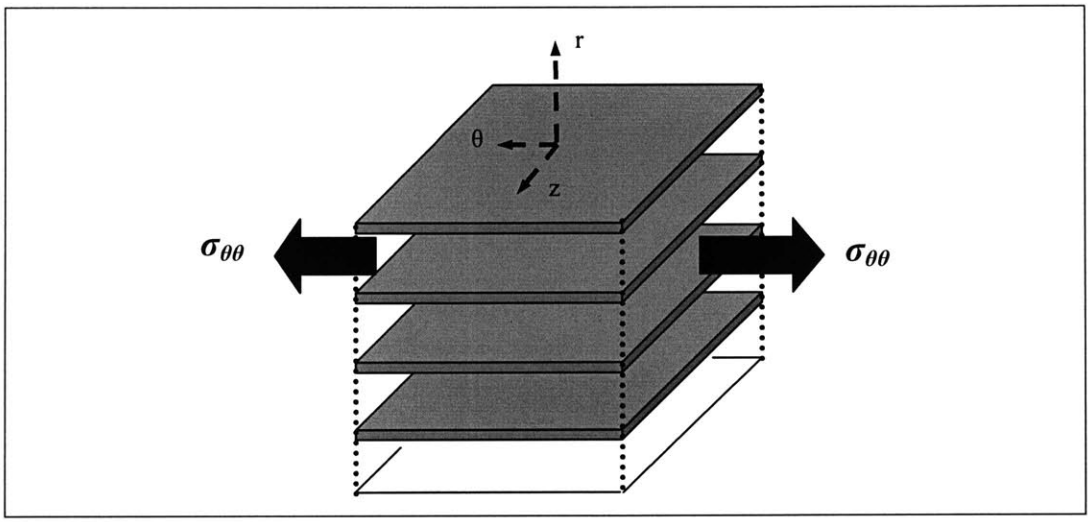

Figure 2.7: Representative volume element from a N-walled CNT is subjected to macroscale normal stress in θ-direction.

1. Equilibrium Equations

$$\sigma_{rrg} = \sigma_{rrs} = \sigma_{rr} = 0 \tag{2.7a}$$

$$\sigma_{\theta\theta g} f_g + \sigma_{\theta\theta s} f_s = \sigma_{\theta\theta} \tag{2.7b}$$

$$\sigma_{zzg} f_g + \sigma_{zzs} f_s = \sigma_{zz} = 0 \tag{2.7c}$$

2. Compatibility Equations

$$\varepsilon_{rrg} f_g + \varepsilon_{rrs} f_s = \varepsilon_{rr} \tag{2.8a}$$

$$\varepsilon_{\theta\theta g} = \varepsilon_{\theta\theta s} = \varepsilon_{\theta\theta} \tag{2.8b}$$

$$\varepsilon_{zzg} = \varepsilon_{zzs} = \varepsilon_{zz} \tag{2.8c}$$

3. Stress-strain Equations

$$\varepsilon_{rrg} = -\left[\frac{\nu_{\theta rg}}{E_{\theta\theta g}}\sigma_{\theta\theta g} + \frac{\nu_{zrg}}{E_{zzg}}\sigma_{zzg}\right] \tag{2.9a}$$

$$\varepsilon_{\theta\theta g} = \left[\frac{1}{E_{\theta\theta g}}\sigma_{\theta\theta g} - \frac{\nu_{z\theta g}}{E_{zzg}}\sigma_{zzg}\right]; \nu_{z\theta g} = \nu_{\theta zg} \tag{2.9b}$$

$$\varepsilon_{zzg} = \left[\frac{1}{E_{zzg}}\sigma_{zzg} - \frac{\nu_{\theta zg}}{E_{\theta\theta g}}\sigma_{\theta\theta g}\right] \tag{2.9c}$$

A similar set of equations are obtained for the *s*-layer in the composite (switch the subscripts '*g*' in Equations 2.9a to 2.9c by '*s*'). Next, multiplying Equation 2.9c by $\nu_{\theta zg}$ and adding the result to Equation 2.9b, we get

$$\sigma_{\theta\theta g} = \frac{E_{\theta\theta g}}{\left(1-\nu_{\theta zg}^2\right)}\left[\varepsilon_{\theta\theta g} + \nu_{\theta zg}\varepsilon_{zzg}\right]. \tag{2.10a}$$

Similarly, multiplying Equation 2.9b by $\nu_{\theta zg}$ and adding the result to Equation 2.9c gives

$$\sigma_{zzg} = \frac{E_{zzg}}{\left(1-\nu_{\theta zg}^2\right)}\left[\varepsilon_{zzg} + \nu_{\theta zg}\varepsilon_{\theta\theta g}\right]. \tag{2.10b}$$

Similar equations for stresses in the *s*-layer are obtained (switch the subscript '*g*' by '*s*' in Equations 2.10a and 2.10b). Next, combining stress-strain equations with the equilibrium and compatibility equations and rearranging, we get

$$\sigma_{\theta\theta} = \left[\frac{E_{\theta\theta g} f_g}{\left(1-\nu_{\theta zg}^2\right)} + \frac{E_{\theta\theta s} f_s}{\left(1-\nu_{\theta zs}^2\right)}\right]\varepsilon_{\theta\theta} + \left[\frac{E_{\theta\theta g} f_g \nu_{\theta zg}}{\left(1-\nu_{\theta zg}^2\right)} + \frac{E_{\theta\theta s} f_s \nu_{\theta zs}}{\left(1-\nu_{\theta zs}^2\right)}\right]\varepsilon_{zz}. \tag{2.11a}$$

Similarly,

$$\sigma_{zz} = \left[\frac{E_{zzg}\nu_{\theta zg} f_g}{\left(1-\nu_{\theta zg}^2\right)} + \frac{E_{zzs}\nu_{\theta zs} f_s}{\left(1-\nu_{\theta zs}^2\right)}\right]\varepsilon_{\theta\theta} + \left[\frac{E_{zzg} f_g}{\left(1-\nu_{\theta zg}^2\right)} + \frac{E_{\theta\theta s} f_s}{\left(1-\nu_{\theta zs}^2\right)}\right]\varepsilon_{zz}; \tag{2.11b}$$

Note that $\sigma_{zz} = 0$, we solve for ε_{zz} in terms of $\varepsilon_{\theta\theta}$ from Equation 2.11b and the substitute the result into Equation 2.11a and rearrange then gives the required effective Young's modulus in axial and tangential direction as

$$E_{\theta\theta Eff} = \frac{\sigma_{\theta\theta}}{\varepsilon_{\theta\theta}} = \left[\frac{E_{\theta\theta g} f_g}{\left(1-\nu_{\theta zg}^2\right)} + \frac{E_{\theta\theta s} f_s}{\left(1-\nu_{\theta zs}^2\right)}\right] - \left[\frac{E_{\theta\theta g} f_g \nu_{\theta zg}}{\left(1-\nu_{\theta zg}^2\right)} + \frac{E_{\theta\theta s} f_s \nu_{\theta zs}}{\left(1-\nu_{\theta zs}^2\right)}\right] \times \left[\frac{E_{zzg}\nu_{\theta zg} f_g\left(1-\nu_{\theta zs}^2\right) + E_{zzs}\nu_{\theta zs} f_s\left(1-\nu_{\theta zg}^2\right)}{E_{zzg} f_g\left(1-\nu_{\theta zs}^2\right) + E_{zzs} f_s\left(1-\nu_{\theta zg}^2\right)}\right]. \tag{2.11c}$$

Now, comparing ε_{zz} from Equation 2.11b and Equation 2.11d below,

$$\varepsilon_{zz} = -\nu_{\theta zEff}\,\varepsilon_{\theta\theta}, \tag{2.11d}$$

and comparing ε_{zz} from Equation 2.11b and Equation 2.11d, we get

$$\nu_{\theta zEff} = \left[\frac{E_{zzg}\nu_{\theta zg} f_g(1-\nu_{\theta zs}^2) + E_{zzs}\nu_{\theta zs} f_s(1-\nu_{\theta zg}^2)}{E_{zzg} f_g(1-\nu_{\theta zs}^2) + E_{zzs} f_s(1-\nu_{\theta zg}^2)}\right]. \tag{2.11e}$$

Substituting Equation 2.11e back into Equation 2.11c, we get

$$E_{\theta\theta Eff} = \frac{\sigma_{\theta\theta}}{\varepsilon_{\theta\theta}} = \left[\frac{E_{\theta\theta g} f_g}{\left(1-\nu_{\theta zg}^2\right)} + \frac{E_{\theta\theta s} f_s}{\left(1-\nu_{\theta zs}^2\right)}\right] - \nu_{\theta zEff}\left[\frac{E_{\theta\theta g} f_g \nu_{\theta zg}}{\left(1-\nu_{\theta zg}^2\right)} + \frac{E_{\theta\theta s} f_s \nu_{\theta zs}}{\left(1-\nu_{\theta zs}^2\right)}\right]. \quad (2.11f)$$

B. RVE Subjected to Macroscopic Normal Stress (r - direction) ($\sigma_{rr} \neq 0$ with all other $\sigma_{ij} = 0$)

The effective transverse Young's modulus (E_{rrEff}) and Poisson ratio ($v_{r\theta Eff}$) of the RVE are calculated by applying a macroscopic transverse stress in the radial-direction, as shown in Figure 2.8. Equilibrium provides the condition that stress in the *r*-direction is the same in the graphene and the space layers.

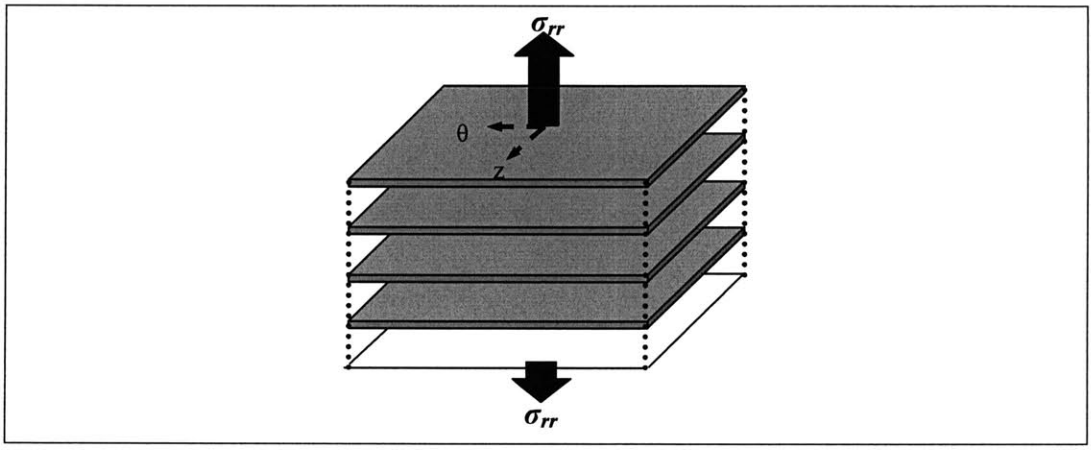

Figure 2.8: Representative volume element from *N*-walled CNT is subjected to macro-scale normal stress in *r*-direction.

1. Equilibrium Equations

$$\sigma_{rrg} = \sigma_{rrs} = \sigma_{rr} \quad (2.12a)$$

$$\sigma_{\theta\theta g} f_g + \sigma_{\theta\theta s} f_s = \sigma_{\theta\theta} = 0 \Rightarrow \sigma_{\theta\theta s} = -\frac{f_g}{f_s}\sigma_{\theta\theta g} \quad (2.12b)$$

$$\sigma_{zzg} f_g + \sigma_{zzs} f_s = \sigma_{zz} = 0 \quad (2.12c)$$

$$\sigma_{zzg} = \sigma_{\theta\theta g}\text{; isotropic plane} \quad (2.12d)$$

2. *Compatibility Equations*

$$\varepsilon_{rrg} f_g + \varepsilon_{rrs} f_s = \varepsilon_{rr} \tag{2.13a}$$

$$\varepsilon_{\theta\theta g} = \varepsilon_{\theta\theta s} = \varepsilon_{\theta\theta} \tag{2.13b}$$

$$\varepsilon_{zzg} = \varepsilon_{zzs} = \varepsilon_{zz} \tag{2.13c}$$

3. *Stress-Strain Equations*

$$\varepsilon_{rrg} = \left[\frac{\sigma_{rrg}}{E_{rrg}} - \frac{\nu_{\theta rg}}{E_{\theta\theta g}} \sigma_{\theta\theta g} - \frac{\nu_{zrg}}{E_{zzg}} \sigma_{zzg} \right] \tag{2.14a}$$

$$\varepsilon_{rrg} = \left[\frac{\sigma_{rrg}}{E_{rrg}} - \left\{ \frac{\nu_{\theta rg}}{E_{\theta\theta g}} + \frac{\nu_{zrg}}{E_{zzg}} \right\} \sigma_{\theta\theta g} \right]; \quad \because \sigma_{zzg} = \sigma_{\theta\theta g} \tag{2.14b}$$

Similarly,

$$\varepsilon_{\theta\theta g} = \left[-\frac{\nu_{r\theta g}}{E_{rrg}} \sigma_{rrg} + \left\{ \frac{1}{E_{\theta\theta g}} - \frac{\nu_{\theta zg}}{E_{zzg}} \right\} \sigma_{\theta\theta g} \right]. \tag{2.14c}$$

Similar strain equations are obtained for the *s*-layer (switch the subscript '*g*' with '*s*' in Equations 2.14b and 2.14c). Next, combining the stress-strain equations with the equilibrium and compatibility equations and rearranging, we get

$$\varepsilon_{rr} = \left[\frac{f_g}{E_{rrg}} + \frac{f_s}{E_{rrs}} \right] \sigma_{rr} - \left[\left\{ \frac{\nu_{\theta rg}}{E_{\theta\theta g}} + \frac{\nu_{zrg}}{E_{zzg}} \right\} - \left\{ \frac{\nu_{\theta rs}}{E_{\theta\theta s}} + \frac{\nu_{zrs}}{E_{zzs}} \right\} \right] f_g \sigma_{\theta\theta g}. \tag{2.15a}$$

Note that $\varepsilon_{\theta\theta g} = \varepsilon_{\theta\theta s}$, and substitute Equations 2.12b and 2.14c in the above equation (similarly for the *s*-layer); then rearrange to get

$$\left[\left\{\frac{1}{E_{\theta\theta g}}-\frac{\nu_{\theta zg}}{E_{zzg}}\right\}\sigma_{\theta\theta g}+\left\{\frac{1}{E_{\theta\theta s}}-\frac{\nu_{\theta zs}}{E_{zzs}}\right\}\left(\frac{f_g}{f_s}\right)\sigma_{\theta\theta g}\right]=\left[\frac{\nu_{r\theta g}}{E_{rrg}}-\frac{\nu_{r\theta s}}{E_{rrs}}\right]\sigma_{rr}\,. \tag{2.15b}$$

Rearrange the above equation to get

$$\sigma_{\theta\theta g}=\frac{\left[\frac{\nu_{r\theta g}}{E_{rrg}}-\frac{\nu_{r\theta s}}{E_{rrs}}\right]}{\left[\left\{\frac{1}{E_{\theta\theta g}}-\frac{\nu_{\theta zg}}{E_{zzg}}\right\}+\left\{\frac{1}{E_{\theta\theta s}}-\frac{\nu_{\theta zs}}{E_{zzs}}\right\}\left(\frac{f_g}{f_s}\right)\right]}\sigma_{rr} \tag{2.15c}$$

After substituting Equation 2.15c into Equation 2.15a and $E_{rr}=\frac{\sigma_{rr}}{\varepsilon_{rr}}$, we get

$$E_{rrEff}=\left[\left\{\frac{f_g}{E_{rrg}}+\frac{f_s}{E_{rrs}}\right\}-\left[\left\{\frac{\nu_{\theta rg}}{E_{\theta\theta g}}+\frac{\nu_{zrg}}{E_{zzg}}\right\}-\left\{\frac{\nu_{\theta rs}}{E_{\theta\theta s}}+\frac{\nu_{zrs}}{E_{zzs}}\right\}\right]f_g\right.$$
$$\left.\times\left\{\frac{\left[\frac{\nu_{r\theta g}}{E_{rrg}}-\frac{\nu_{r\theta s}}{E_{rrs}}\right]}{\left[\left\{\frac{1}{E_{\theta\theta g}}-\frac{\nu_{\theta zg}}{E_{zzg}}\right\}+\left\{\frac{1}{E_{\theta\theta s}}-\frac{\nu_{\theta zs}}{E_{zzs}}\right\}\left(\frac{f_g}{f_s}\right)\right]}\right\}\right]^{-1} \tag{2.16a}$$

Substituting Equations 2.12a, 2.14c, and 2.15c into Equation 2.13b, we get

$$\varepsilon_{\theta\theta}=-\left[\frac{\nu_{r\theta g}}{E_{rrg}}-\left\{\frac{1}{E_{\theta\theta g}}-\frac{\nu_{\theta zg}}{E_{zzg}}\right\}\left\{\frac{\left[\frac{\nu_{r\theta g}}{E_{rrg}}-\frac{\nu_{r\theta s}}{E_{rrs}}\right]}{\left[\left\{\frac{1}{E_{\theta\theta g}}-\frac{\nu_{\theta zg}}{E_{zzg}}\right\}+\left\{\frac{1}{E_{\theta\theta s}}-\frac{\nu_{\theta zs}}{E_{zzs}}\right\}\left(\frac{f_g}{f_s}\right)\right]}\right\}\right]E_{rrEff}\varepsilon_{rr} \tag{2.16b}$$

$$\because\ \varepsilon_{\theta\theta}=-\nu_{r\theta eff}\varepsilon_{rr} \tag{2.16c}$$

$$\nu_{r\theta Eff} = E_{rrEff}\left[\frac{\nu_{r\theta g}}{E_{rrg}} - \left\{\frac{1}{E_{\theta\theta g}} - \frac{\nu_{\theta z g}}{E_{zzg}}\right\}\left\{\frac{\left[\frac{\nu_{r\theta g}}{E_{rrg}} - \frac{\nu_{r\theta s}}{E_{rrs}}\right]}{\left\{\frac{1}{E_{\theta\theta g}} - \frac{\nu_{\theta z g}}{E_{zzg}}\right\} + \left\{\frac{1}{E_{\theta\theta s}} - \frac{\nu_{\theta z s}}{E_{zzs}}\right\}\left(\frac{f_g}{f_s}\right)}\right\}\right] \tag{2.16d}$$

C. RVE Subjected to Macroscopic Shear Stress ($r\theta$ - plane) ($\sigma_{r\theta} \neq 0$ with all other $\sigma_{ij} = 0$)

The effective shear modulus ($G_{r\theta Eff}$) of the RVE is calculated by applying a macroscopic shear stress in the radial-tangential-direction, as shown in Figure 2.9. Equilibrium gives the shear stress in the r-θ-plane to be equal in the graphene and the space layers.

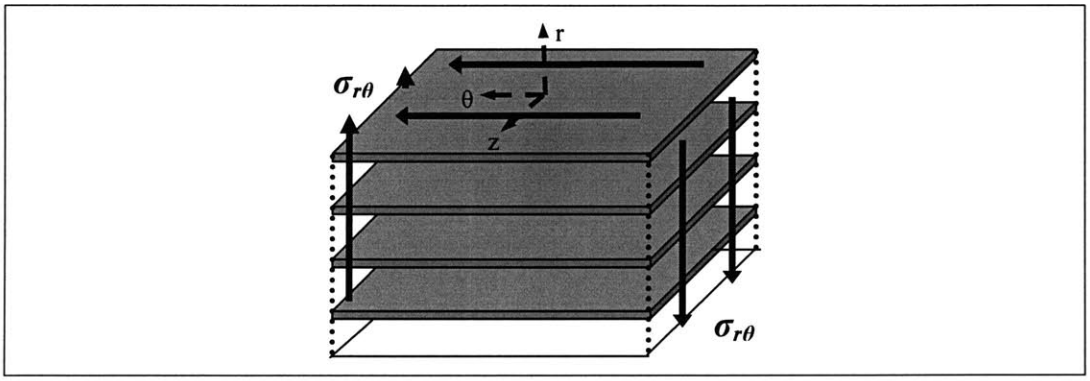

Figure 2.9: Representative volume element from N-walled CNT is subjected to macro-scale shear stress in r-θ-plane.

1. Equilibrium Equation

$$\sigma_{r\theta g} = \sigma_{r\theta s} = \sigma_{r\theta} \tag{2.17}$$

2. Compatibility Equation

$$\varepsilon_{r\theta g} f_g + \varepsilon_{r\theta s} f_s = \varepsilon_{r\theta} \tag{2.18}$$

3. Stress-Strain Equations

$$\varepsilon_{r\theta g} = \frac{1}{2G_{r\theta g}}\sigma_{r\theta g} \tag{2.19a}$$

$$\varepsilon_{r\theta s} = \frac{1}{2G_{r\theta s}}\sigma_{r\theta s} \tag{2.19b}$$

Next, combining stress-strain equations with equilibrium and compatibility equations, we get

$$\varepsilon_{r\theta} = \frac{f_g}{2G_{r\theta g}}\sigma_{r\theta g} + \frac{f_s}{2G_{r\theta s}}\sigma_{r\theta s}. \tag{2.20a}$$

Rearranging Equation 2.20a

$$\varepsilon_{r\theta} = \frac{1}{2}\left[\frac{f_g}{G_{r\theta g}} + \frac{f_s}{G_{r\theta s}}\right]\sigma_{r\theta}, \tag{2.20b}$$

$$\varepsilon_{r\theta} = \frac{1}{2G_{r\theta Eff}}\sigma_{r\theta} \tag{2.20c}$$

$$G_{r\theta Eff} = \left[\frac{f_g}{G_{r\theta g}} + \frac{f_s}{G_{r\theta s}}\right]^{-1}. \tag{2.20d}$$

D. RVE Subjected to Macroscopic Shear Stress (θz - plane) ($\sigma_{\theta z} \neq 0$ with all other $\sigma_{ij} = 0$)

The effective shear modulus ($G_{\theta zEff}$) of the RVE is calculated by applying a macroscopic shear stress in tangential-axial-direction, shown in Figure 2.10. Here equilibrium condition gives the shear strain in the θ-z-plane to be equal in the g- and the s-layers.

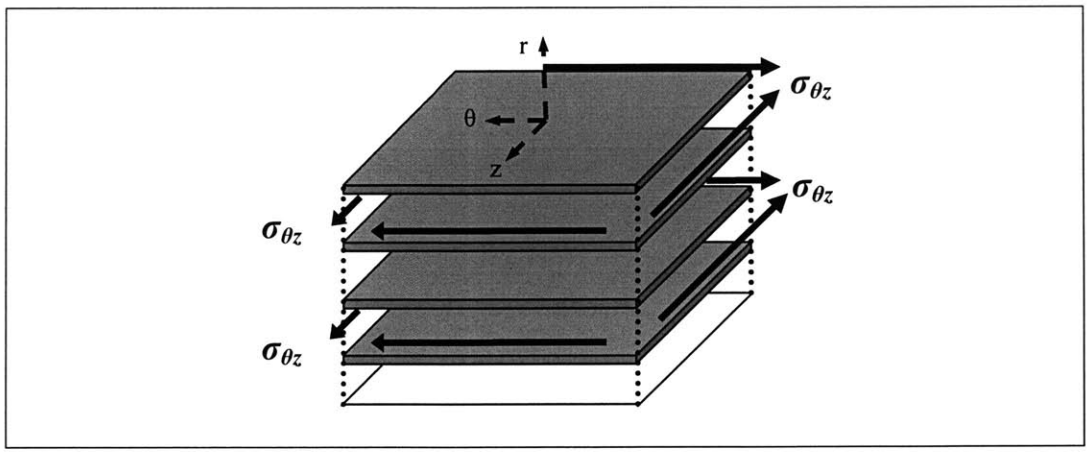

Figure 2.10: Representative volume element from *N*-walled CNT is subjected to macro-scale shear stress in θ-z-plane.

1. Equilibrium Equation

$$\sigma_{\theta z} = \sigma_{\theta zg} f_g + \sigma_{\theta zs} f_s \tag{2.21}$$

2. Compatibility Equation

$$\varepsilon_{zzg} = \varepsilon_{\theta zs} = \varepsilon_{\theta z} \tag{2.22}$$

3. Stress-Strain Equations

$$\sigma_{\theta zg} = 2G_{\theta zg}\varepsilon_{\theta zg} \tag{2.23a}$$

$$\sigma_{\theta zs} = 2G_{\theta zs}\varepsilon_{\theta zs} \tag{2.23b}$$

Combining the stress-strain equations with the equilibrium and compatibility equations, we get

$$\sigma_{\theta z} = 2\left(G_{\theta zg} f_g + G_{\theta zs} f_s\right)\varepsilon_{\theta z} \tag{2.24a}$$

$$\varepsilon_{\theta z} = \frac{1}{2G_{\theta z eff}} \sigma_{\theta z} \tag{2.24b}$$

$$G_{\theta z Eff} = G_{\theta z g} f_g + G_{\theta z s} f_s \tag{2.24c}$$

We can simplify the effective material constant equations (Equations 2.11c, 2.11f, 2.16a, 2.16d, 2.20d and 2.24c) by substituting the conditions satisfied by the isotropic (graphene) and transversely isotropic layers (space). For the isotropic layers, we can use the conditions given in Equations 2.25a to 2.25c, and for the transversely isotropic layers we can use the supplementary conditions given in Equations 2.26a to 2.26d (Solecki and Conant, 2003). Recall that the isotropic and transversely isotropic layer assumption is based on nested shell model (Pantano et al, 2004b).

Isotropic Material

$$E_{ij} = E \tag{2.25a}$$

$$\nu_{ij} = \nu \tag{2.25b}$$

$$G = \frac{E}{2(1+\nu)} \tag{2.25c}$$

Transversely Isotropic Material

$$\frac{\nu_{ij}}{E_{ii}} = \frac{\nu_{ji}}{E_{jj}}, \text{ for } i = r \text{ and } j = \theta \text{ and } z \tag{2.26a}$$

$$\nu_{\theta z} = \nu_{z\theta} \tag{2.26b}$$

$$E_{\theta\theta} = E_{zz} \tag{2.26c}$$

$$G_{\theta z} = \frac{E_{\theta\theta}}{2(1+\nu_{\theta z})} \tag{2.26d}$$

Final Material Constant Equations for the EOR model

$$E_{rrEff} = \left[\left\{ \frac{f_g}{E_g} + \frac{f_s}{E_{rrs}} \right\} - 2f_g \left\{ \left(\frac{\nu_g}{E_g} \right) - \left(\frac{\nu_{r\theta s}}{E_{rrs}} \right) \right\} \left\{ \frac{E_{\theta\theta s} f_s \left(E_{rrs}\nu_g - E_g \nu_{r\theta s} \right)}{E_{rrs} \left\{ \left(1-\nu_g\right) f_s E_{\theta\theta s} + \left(1-\nu_{\theta zs}\right) f_g E_g \right\}} \right\} \right]^{-1} \tag{2.27a}$$

$$E_{\theta\theta Eff} = E_{zzEff} = \left[\frac{E_{\theta\theta g} f_g}{\left(1-\nu_{\theta zg}^2\right)} + \frac{E_{\theta\theta s} f_s}{\left(1-\nu_{\theta zs}^2\right)} \right] - \nu_{\theta zEff} \left[\frac{E_{\theta\theta g} f_g \nu_{\theta zg}}{\left(1-\nu_{\theta zg}^2\right)} + \frac{E_{\theta\theta s} f_s \nu_{\theta zs}}{\left(1-\nu_{\theta zs}^2\right)} \right] \tag{2.27b}$$

$$\nu_{r\theta Eff} = \nu_{rzEff} = \left(\frac{E_{rrEff}}{E_g} \right) \left[\nu_g - \left\{ \frac{E_{\theta\theta s} f_s \left(1-\nu_g\right) \left(E_{rrs}\nu_g - E_g \nu_{r\theta s} \right)}{E_{rrs} \left\{ \left(1-\nu_g\right) f_s E_{\theta\theta s} + \left(1-\nu_{\theta zs}\right) f_g E_g \right\}} \right\} \right] \tag{2.27c}$$

$$\nu_{\theta zEff} = \nu_{z\theta Eff} = \left[\frac{E_g \nu_g f_g (1-\nu_{\theta zs}^2) + E_{\theta\theta s} \nu_{\theta zs} f_s (1-\nu_g^2)}{E_g f_g (1-\nu_{\theta zs}^2) + E_{\theta\theta s} f_s (1-\nu_g^2)} \right] \tag{2.27d}$$

$$G_{r\theta Eff} = G_{rzEff} = \left[\frac{f_g}{G_g} + \frac{f_s}{G_{r\theta s}} \right]^{-1} \tag{2.27e}$$

$$G_{\theta zEff} = G_g f_g + G_{\theta zs} f_s \tag{2.27f}$$

Equations 2.27a to 2.27f give the necessary equivalent material constants for the EOR model; in the following sections, we apply these equations to model MWCNTs with an advanced Finite Element commercial software.

2.3.2 Finite Element Effective Orthotropic Solid Beam Model

The EOR model uses a micro-mechanical representation of the radially symmetric layered structure to predict the equivalent mechanical properties for an effective elastic orthotropic continuum solid; these effective elastic properties were derived in the previous section (Equations 2.27a to 2.27f).

Since the EOR model is based upon the NSSR model, the material properties for the graphene layers are directly adopted from (Pantano et al., 2004b), and are listed in Table 2.1. Recall that MWCNTs consist of layers of graphene sheets with a well-defined inter-sheet equilibrium spacing of 0.34 *nm* – where van der Waals interactions occur; we define this interlayer separation as the thickness of the space layer in our layered structured EOR model. Since the van der Waals interaction can be thought of as effective interlayer space radial modulus $E_{rrs}(\varepsilon_{rr})$ that depend on interlayer separation, we derive the interlayer space modulus from the LJ potential (Equation 2.4). Substituting Equation 2.28 into Equation 2.4 and then taking the derivative of both sides with respect to radial normal strain (ε_{rr}), we get

$$\varepsilon_{rr} = \frac{(c - c_0)}{c_0},$$

$$\therefore c = c_0(1 + \varepsilon_{rr}), \tag{2.28}$$

$$E_{rr_s}(\varepsilon_{rr}) = \left(\frac{\Psi}{6}\right)\left[\left\{\frac{10}{(1+\varepsilon_{rr})^{11}}\right\} - \left\{\frac{4}{(1+\varepsilon_{rr})^{5}}\right\}\right], \tag{2.29}$$

where c and c_o are the current and the equilibrium inter-layer spacing, respectively. The values of constants c_0 and Ψ are 0.34 *nm* and 36.5 *GPa*, respectively. Figure 2.11 is the graphical representation of Equation 2.29 where ε_{rr} ranges between -0.5 to 0.15. In Figure 2.11, zero strain refers to the equilibrium separation distance of 0.34 *nm*.

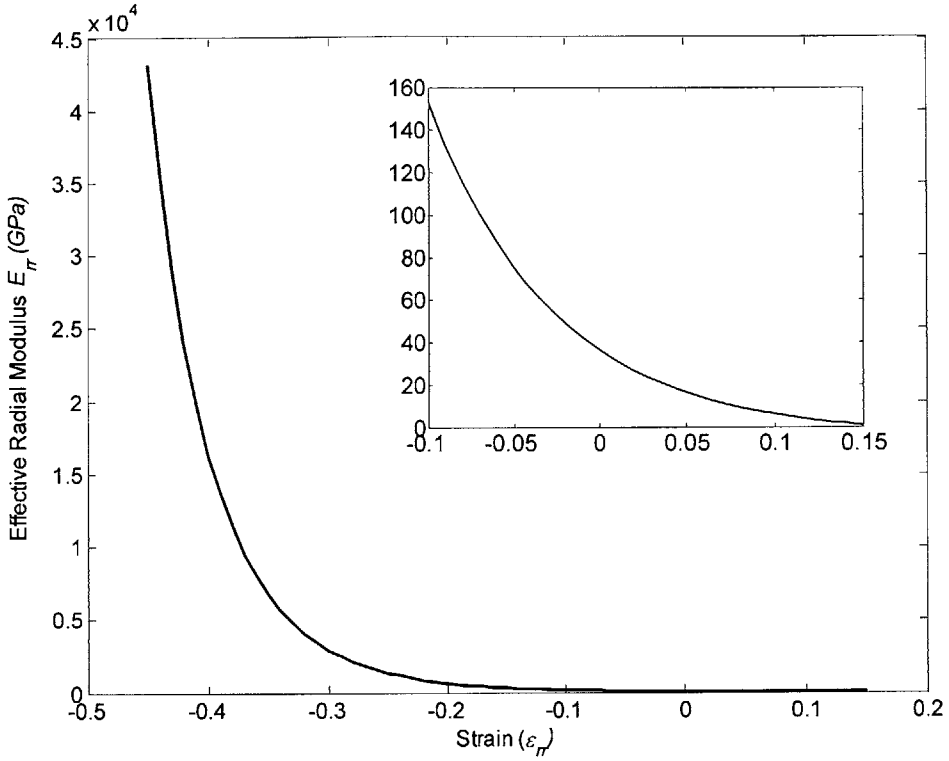

Figure 2.11: Radial modulus versus compressive strain for the s-layer derived from LJ potential.

Since the Poisson ratio is undefined for the space layer, we assume it to be same as that of graphene layer (= 0.19). In addition, the effective shear modulus of the space layer is taken to be 0.48 *MPa*, a negligible value; we assumed a negligible shear modulus value since Pantano et al., (2004b) assumed the shear stiffness and strength to be zero for their NSSR model. The shear modulus values reported in literature ranges from 70 *MPa* to 4.5 *GPa* (e.g., Blakslee et al., 1970; Zhao and Spain, 1989). Pantano et al., (2004b) made the zero shear stiffness assumption based on the experimental studies of Cummings and Zettl (2000) and Yu et al., (2000b). The effective Young's modulus ($E_{\theta\theta} = Ezz$) for the space layer is then calculated via Equaion 2.25c. The final properties thus taken for the layered structured EOR model in the local material coordinate system are listed in Table 2.1.

Table 2.1: Elastic properties used for Equivalent Orthotropic Solid model represented in cylindrical coordinate system. The thickness of the graphene layer t_g = 0.075 *nm* and that for space layer t_s =0.34 *nm*.

Mechanical Properties Constants	***Graphene Layer (Isotropic)***	***Empty Space Layer (Transversely Isotropic)***
E_{rr}	*4.84 TPa*[†]	$E_{rr}(\varepsilon)$**
$E_{\theta\theta}$	*4.84 TPa*[†]	*1.14 MPa**
Ezz	*4.84 TPa*[†]	*1.14 MPa**
$\nu_{r\theta}$	*0.19*[†]	*0.19*
ν_{rz}	*0.19*[†]	*0.19*
$\nu_{\theta z}$	*0.19*[†]	*0.19*
$G_{r\theta}$	*2.03 TPa**	*0.48 MPa*[††]
G_{rz}	*2.03 TPa**	*0.48 MPa*[††]
$G_{\theta z}$	*2.03 TPa**	*0.48 MPa*[††]

[†] *Pantano et al., (2003, 2004a, 2004b).*

[††] *Cummings and Zettl (2000).*

* substitute E and ν for g-layer and G and ν for s-layer in Equation 2.25c

** see Equation 2.29

Next, we plot several curves (Figures 2.12 to 2.17) by substituting the elastic properties for the graphene and the space layers into the final material constant equations (Equations 2.27a to 2.27f). Figures 2.12 to 2.14 show the variation of the global elastic properties as a function of number of concentric shell tubes, where f_g assumes the global form, $f_g(N)$. Figures 2.15 to 2.17, on the other hand, show the variation of the elastic properties of individual set of layers as a function of radial location (R^i) within an MWCNT, where f_g assumes the local form $f_g(R^i)$; the individual set of layers includes a single space and its adjacent graphene layer. All the shell tubes in Figures 2.12 to 2.17 have armchair (n, n) chirality with the innermost radius of 0.34 *nm* and n = 5, 10, ...

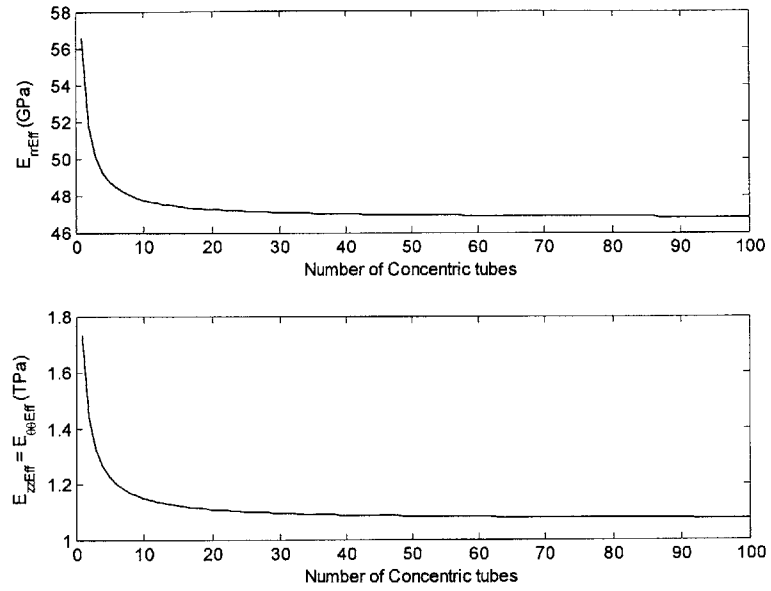

Figure 2.12: Variation of E_{rrEff}, $E_{\theta\theta Eff}$, and E_{zzEff} of the representative volume element of the equivalent orthotropic representation model with number of concentric tubes in an MWCNT, $R_{innermost} = 0.34\ nm$.

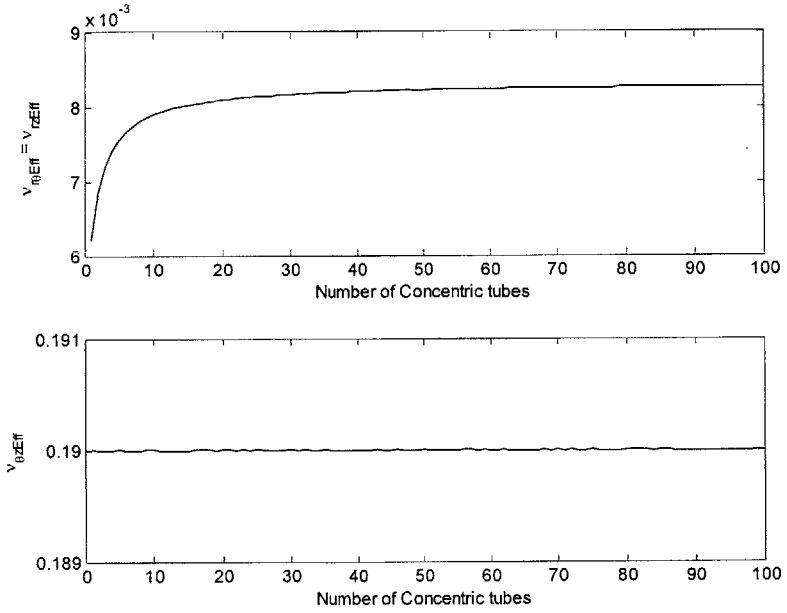

Figure 2.13: Variation of $\nu_{r\theta Eff}$, ν_{rzEff}, and $\nu_{\theta zEff}$ of the representative volume element of the equivalent orthotropic representation model with number of concentric tubes in an MWCNT, $R_{innermost} = 0.34\ nm$.

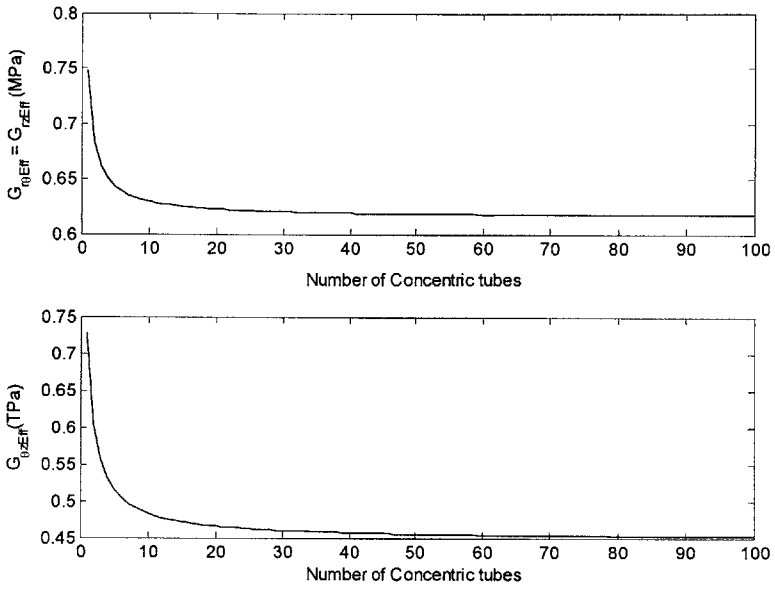

Figure 2.14: Variation of $G_{r\theta Eff}$, G_{rzEff}, and $G_{\theta zEff}$ of the representative volume element of the equivalent orthotropic representation model with number of concentric tubes in an MWCNT, $R_{innermost} = 0.34\ nm$.

Figures 2.12 to 2.14 show that the global elastic properties for the RVE of the EOR model assumes constant values for more than 10 walls; conversely the EOR-based MWCNT models may not be able to capture the nonlinear behavior for less than 10 walls. However, for CNTs having more than 10 walls, the EOR model based on the global form of volume fraction may capture the nonlinear mechanics of MWCNT deformation. The global elastic properties of the MWCNT can be treated as constant for higher number of concentric tubes where the influence of the inner layers diminishes. For CNTs with less than 10 walls we can consider the local form of f_g, which allows the elastic properties of the individual layer to vary with its location inside the MWCNT, as shown in Figures 2.15 to 2.17.

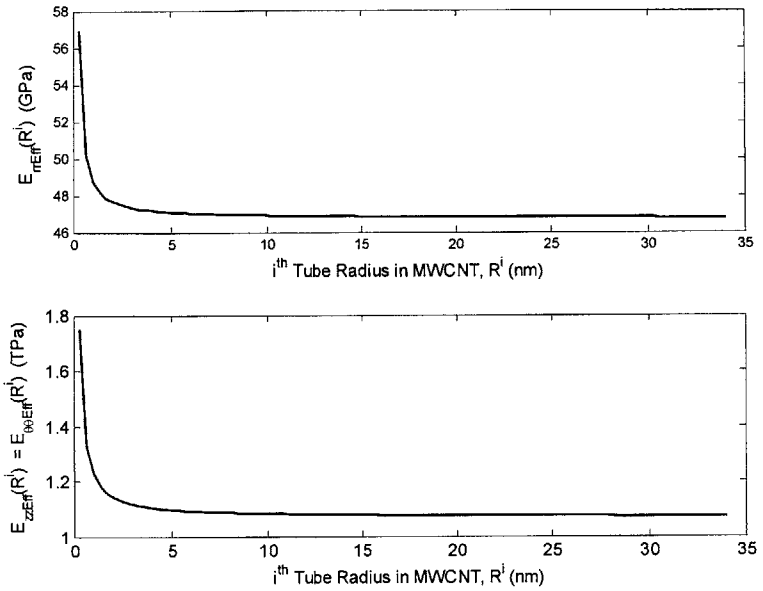

Figure 2.15: Variation of E_{rrEff}, $E_{\theta\theta Eff}$, and E_{zzEff} of the representative volume element consisting of single layer of graphene and space layer of the EOR model with radial location in an MWCNT, R_i = 0.34 *nm*.

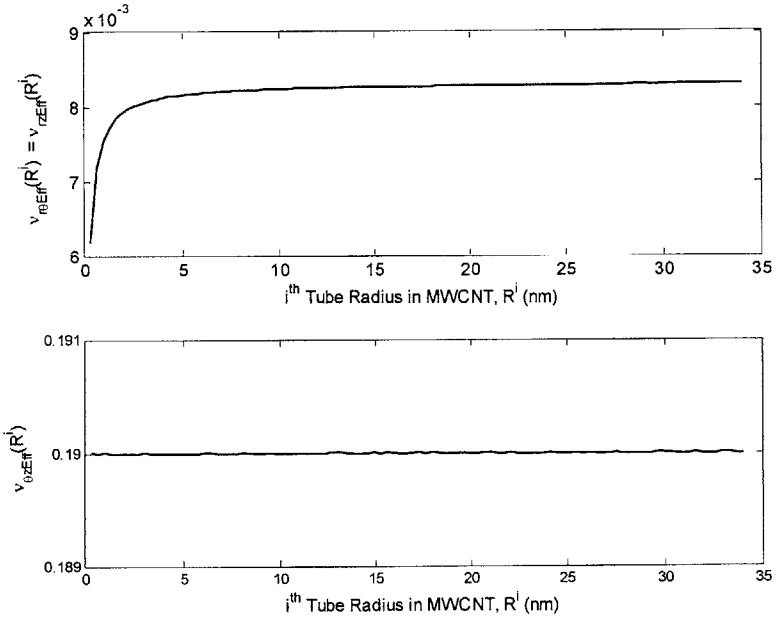

Figure 2.16: Variation of $\nu_{r\theta Eff}$, ν_{rzEff}, and $\nu_{\theta zEff}$ of the representative volume element consisting of single layer of graphene and space layer of the EOR model with radial location in an MWCNT, R_i = 0.34 *nm*.

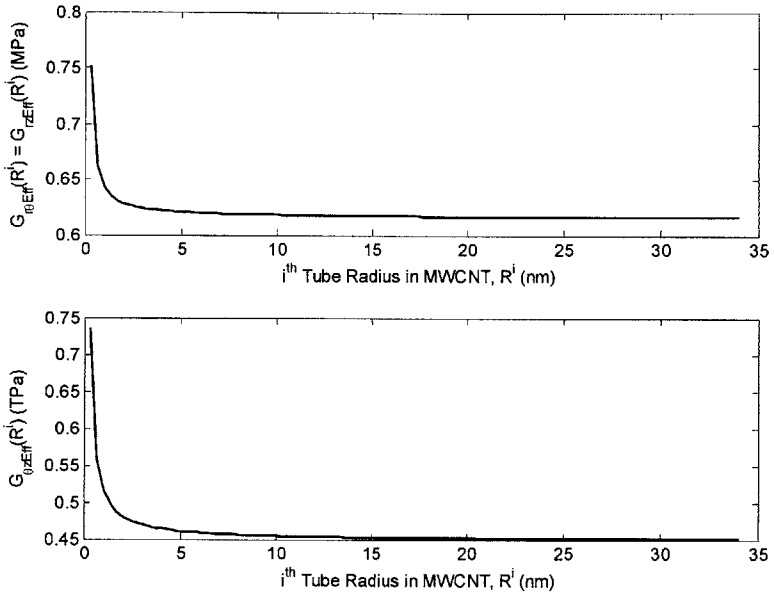

Figure 2.17: Variation of $G_{r\theta Eff}$, G_{rzEff}, and $G_{\theta zEff}$ of the representative volume element consisting of single layer of graphene and space layer of the EOR model with radial location in an MWCNT, $R_i = 0.34\ nm$.

Figures 2.13 and 2.16 show that $v_{r\theta}$ (= v_{rz}) is negligible for any number of concentric tubes when compared to $v_{\theta z}$, which is constant (= 0.19) and independent of the number of tubes or the location. The reason $v_{\theta z}$ is independent of the number of concentric tubes is because the EOR model has locally transverse symmetry. Contrary to $v_{r\theta}$ (= v_{rz}), strain in the axial or the tangential direction results in strain in the radial direction of MWCNTs. Yakobson et al., (1996) concluded from their MD simulation results for SWCNT subjected to tension that the Poisson ratio is equal to 0.19.

Next, we write the constitutive equations in the matrix form for a material point with locally transverse isotropy with the axis of symmetry in the r-direction and in terms of engineering normal and shear strains. Notice that the coordinate system used throughout our analysis is cylindrical.

$$\begin{Bmatrix} \sigma_{rr} \\ \sigma_{\theta\theta} \\ \sigma_{zz} \\ \sigma_{r\theta} \\ \sigma_{rz} \\ \sigma_{\theta z} \end{Bmatrix} = \begin{bmatrix} C_{11} & C_{12} & C_{12} & 0 & 0 & 0 \\ C_{12} & C_{22} & C_{23} & 0 & 0 & 0 \\ C_{12} & C_{23} & C_{22} & 0 & 0 & 0 \\ 0 & 0 & 0 & C_{44} & 0 & 0 \\ 0 & 0 & 0 & 0 & C_{44} & 0 \\ 0 & 0 & 0 & 0 & 0 & C_{66} \end{bmatrix} \begin{Bmatrix} \varepsilon_{rr} \\ \varepsilon_{\theta\theta} \\ \varepsilon_{zz} \\ \gamma_{r\theta} \\ \gamma_{rz} \\ \gamma_{\theta z} \end{Bmatrix}$$

$$C_{11} = \frac{E_{rrEff}\left(1-\nu_{\theta zEff}^2\right)}{\Delta}; \qquad C_{22} = C_{33} = \frac{E_{\theta\theta Eff}\left(1-\nu_{rzEff}\nu_{zrEff}\right)}{\Delta}$$

$$C_{44} = C_{55} = G_{r\theta Eff} = G_{rzEff}; \qquad C_{66} = \frac{C_{11}-C_{12}}{2}; \; G_{\theta zEff} = \frac{E_{\theta\theta Eff}}{2\left(1+\nu_{\theta zEff}\right)}; \; \nu_{\theta zEff} = \nu_g = \nu_{\theta zs}$$

$$C_{12} = \frac{E_{rrEff}\left(\nu_{\theta rEff}+\nu_{\theta rEff}\nu_{\theta zEff}\right)}{\Delta}; \quad C_{23} = \frac{E_{\theta\theta Eff}\left(\nu_{\theta zEff}+\nu_{r\theta Eff}\nu_{\theta rEff}\right)}{\Delta}$$

$$\Delta = 1-\nu_{\theta zEff}^2 - 2\nu_{r\theta Eff}\nu_{\theta rEff} - 2\nu_{\theta zEff}\nu_{r\theta Eff}\nu_{\theta rEff} \tag{2.30}$$

The stiffness matrix in Equation 2.30 is symmetric and requires only five independent elastic constants (C_{11}, C_{22}, C_{44}, C_{12} and C_{23}) as is required for transversely isotropic materials.

Since from Figures 2.12 to 2.14, the effective engineering constant values stabilize for more than 10 walls, we extrapolated the asymptotic effective engineering constant values from Equations 2.27a to 2.27f and substituted them into Equations in 2.30 to find the elastic constants (C_{11}, C_{22}, C_{44}, C_{12} and C_{23}). These elastic constants are then compared with those for graphite (e.g., Blakslee et al., 1970, Zhao and Spain, 1989) and used by (Liu et al., 2001, 2003, Wang and Wang, 2004, Wang et al., 2004, and Wang et al., 2005) in their orthotropic solid beam model. Elastic constants for both the graphite and 100-walled CNT are listed and compared in Table 2.2.

Table 2.2: Elastic constants of graphite and 100-walled CNT using current EOR model, represented in cylindrical coordinate system at equilibrium.

Elastic Constant	***Basal Plane of Graphite****	***EOR Model***
C_{11}	*36.50±0.1 GPa*	*46.88 GPa*
$C_{22} = C_{33}$	*1.06±0.02 TPa*	*1.12 TPa*
$C_{12} = C_{13}$	*15±5 GPa*	*2.45 GPa*
C_{23}	*180±20 GPa*	*212.80 GPa*
C_{44}	*4.5±0.05 GPa*	*0.62 MPa*
C_{66}	*440 GPa*	*453.40 GPa*

* (Blakslee et al., 1970; Zhao and Spain, 1998).

Values of C_{22} and C_{33} are 1.12 *TPa* which agrees well with the planar Young's modulus of graphene sheet (1.06±0.02 *TPa*). Both simulations and research indicate similar values for C_{22} and C_{33} as discussed earlier in Chapter 1. Similarly, elastic constants C_{11}, C_{12}, C_{13}, C_{23}, and C_{66} for the EOR model are also close to the graphite elastic constants. However, C_{44} for the layered structure vary from bulk graphite primarily because of the shear modulus, $G_{\theta z}$, value assumed in Table 2.1. Recall that Pantano et al., (2004b) assumed zero shear modulus in their NSSR model so that the adoption of actual C_{44} value in our EOR model will result in difference between the two models. Adopting the higher value of shear modulus, $G_{\theta z}$ (= 4.5 *GPa*), will result in graphite property-based EOR model to deviate from the NSSR model; to support the argument, we have compared the simulation results obtained from the two approaches towards the end of this chapter.

Next, we will see how the LJ potential's (Equation 2.29) dependence on radial normal strain is manifested in the stiffness matrix components for a 100-walled CNT; this is done by varying the radial normal strain, as shown in Figures 2.18 to 2.20. The tubes in Figures 2.18 to 2.20 have an innermost radius and an outermost radius of 0.34 *nm* and 34 *nm*, respectively and have armchair chirality (n, n), where n = 5, 10, ... The variations in stiffness matrix components show that assuming a constant value for the LJ potential like Liu et al., (2001, 2003), Wang and Wang (2004), Wang et al., (2004), and Wang et al., (2005) yields unsatisfactory results. This is especially the case in the post-buckling

regime where radial strain could increase significantly or when the MWCNT is subjected to lateral compression, as will be discussed in the subsequent sections.

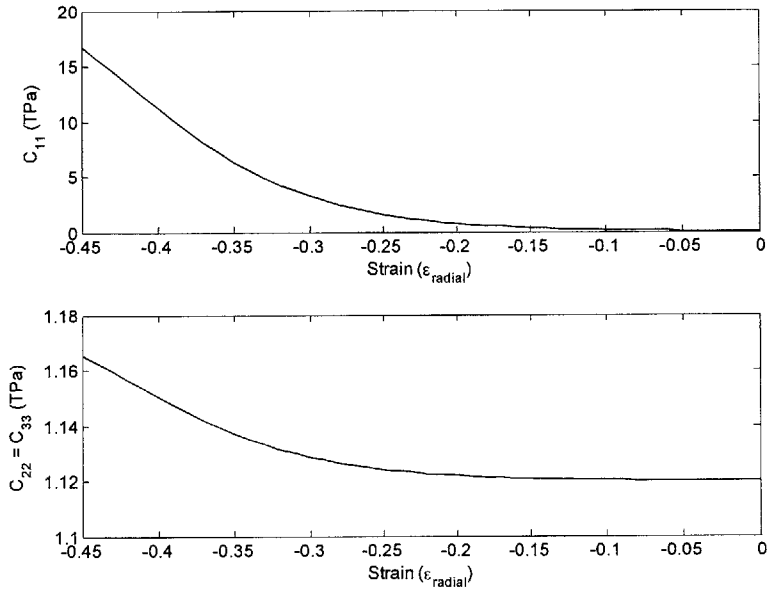

Figure 2.18: Variation of C_{11}, C_{22} and C_{33} material constants with radial strain applied to the representative volume element of the EOR model.

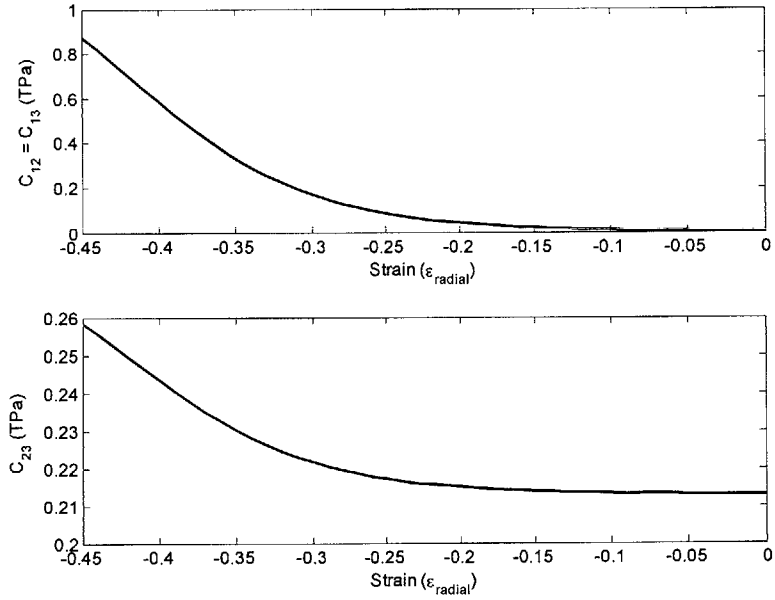

Figure 2.19: Variation *of* C_{12}, C_{13} and C_{23} material constants with radial strain applied to the representative volume element of the EOR model.

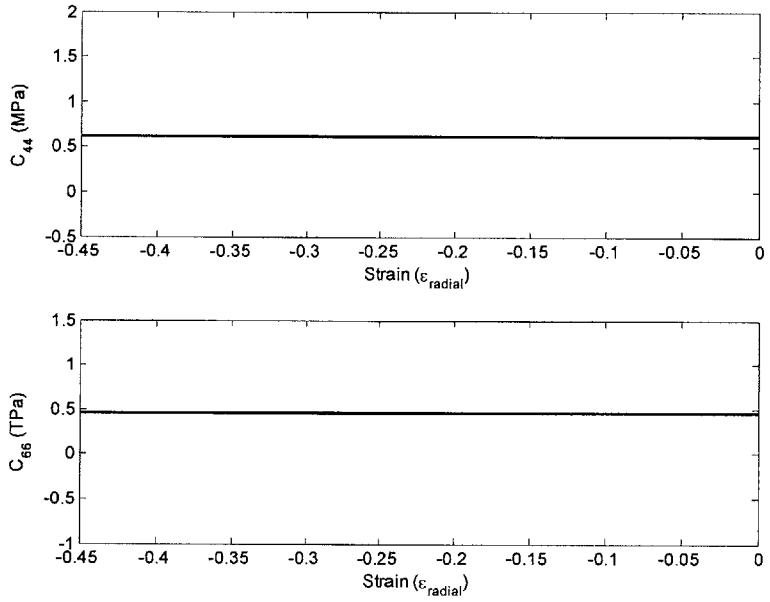

Figure 2.20: Variation of C_{44} and C_{66} material constants with radial strain applied to the representative volume element of the EOR model.

Figures 2.18 and 2.19 show that material constants in the transverse direction (C_{11} and $C_{12} = C_{13}$) change drastically as compared to the in-plane material constants ($C_{22} = C_{33}$ and C_{23}). Figure 2.20, on the other hand, shows that elastic constants (C_{44} and C_{66}) affecting the shear properties of the RVE remain constant with the incremental strain. Hence, we can conclude that taking into account the LJ potential's dependence on strain is critical in the modeling of MWCNT for simulations where strain in the radial direction might be expected, as is the case of lateral compression.

Based on the effective equivalent engineering constants in Table 2.1, the EOR model will be shown to provide good predictions of the elastic behavior in a variety of loading situations prior to any instabilities such as buckling. For predicting the buckling and post-buckling regime, the element size in the FE simulations will be shown to play a major role. Finally, a commercially available advanced finite element software package (*ABAQUS*) was used to model several MWCNTs. The solid elements were assigned a local cylindrical material coordinate system, as shown in Figure 2.21; the user defined material properties were solved in terms of the stiffness matrix components in Equations 2.30.

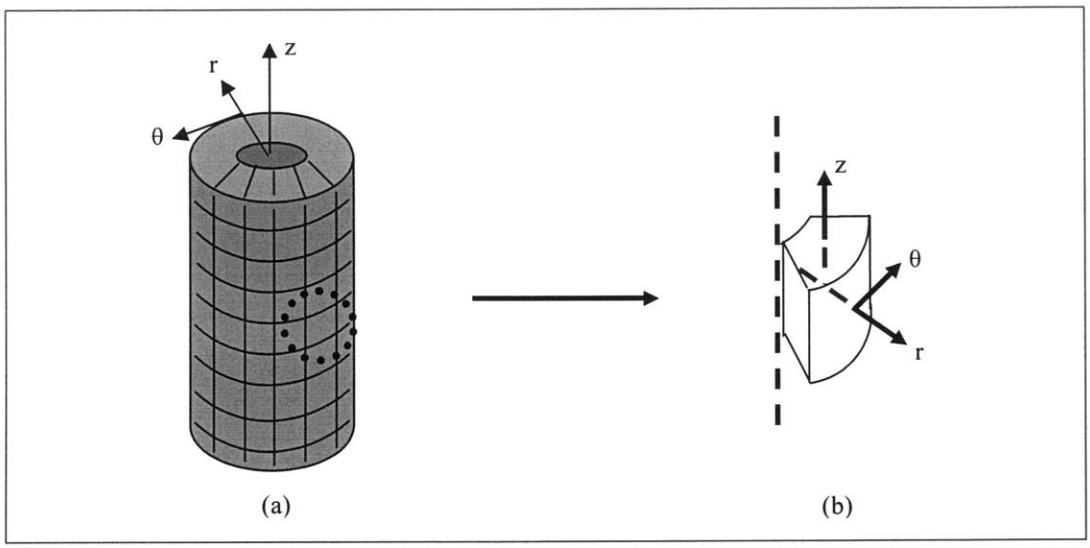

Figure 2.21: MWCNT model using EOR model divided into small 8-node solid elements along with global cylindrical coordinate system (a). Local cylindrical material coordinate system assigned to solid element in an MWCNT (b).

2.4 Results and Discussion

In this section, we will apply the new FE-based modeling approach to simulate the nonlinear mechanical behavior of MWCNTs of various aspect ratios subjected to bending, axial compression, and lateral compression. We have used the finite element software package, *ABAQUS*, for modeling and simulating MWCNTs. The results obtained from simulation of the above three loading conditions are then verified by comparing them to those of the nested structural shell representation (NSSR) (Pantano et al., 2003, 2004a). The lateral compression simulation results are also compared with the MD simulations and experimental results (e.g., Palaci et al., 2005, Guo et al., 2004, Yu et al., 2000a, Shen et al., 2000, Hertel et al., 1998, and Lordi and Yao, 1998).

This section is divided into three main subsections and begins with the study of mesh sensitivity for the EOR model for simulating MWCNTs subjected to bending, axial compression and lateral compression. Thereafter in the second subsection, FE simulation results using the EOR and the NSSR models are compared for MWCNTs of different

aspect ratios subjected to the above loading conditions. Finally in the last subsection, the EOR model elastic properties will be replaced with the bulk graphite elastic properties to monitor how the graphite assumption affects the simulation results.

2.4.1 Mesh (element size) Sensitivity Study

According to the shell theory, in a thin cylindrical shell tube, the onset of buckling is determined by the shell diameter, thickness and Young's modulus. Using the EOR model without the outer shell discretely modeled, the onset of buckling is difficult to predict when compared to the nested shell model in which buckling propagates from the outermost shell to the innermost. In their FE-based nested shell model, Pantano et al., (2004b) noticed that the MWCNT model depends on the mesh size and agrees well if an element size of 0.24 *nm* is used – the dimension equivalent to the hexagonal lattice. Similarly, for the EOR model, smaller elements might erroneously capture a rippling wavelength that cannot be accommodated by the carbon lattice structure; too large an element dimension might miss the buckling wavelength. This introduces a mesh sensitivity issue in the EOR model, which we investigate by subjecting FE-based EOR model of a 14-walled CNT to bending, axial compression, and lateral compression.

2.4.1.1 Bending

Here we repeat the bending simulations by Pantano et al., (2003) by constructing a 14-walled CNT of length (L) 15 *nm* of the armchair (n, n) type MWCNT and with n = 5, 10, …, 70, which gives an outer tube radius R_o of 4.76 *nm*. The CNT is then rigidly fixed at one end (symmetry plane) and rotated at the other end where the radial and circumferential displacements are constrained. The free end is rotated by 0.2 *radians* imposing a bending angle θ of 0.4 *radians* for an equivalent beam length L of 30 *nm*. The θ and the L yields a maximum global curvature κ ($= \theta/L$) of 0.0133 nm^{-1}. The bending moment versus the global curvature diagram from the NSSR model, along with the EOR model of different element sizes, are shown in Figure 2.24. Figures 2.22 and 2.23 show the initial and the final deformed 14-walled CNT model from the NSSR and EOR models, respectively. Figure 2.24 shows that regardless of the element size, the EOR

model captures the pre-buckling behavior of the 14-walled NSSR CNT model. However, the buckling initiation point and the post-buckling behavior are strongly dependent on element size and are only properly captured when the element size is specifically set to a proper initial wavelength (5*0.24 *nm* = 1.2 *nm*) of ~2.15 nm, predicted by the NSSR model of a similar MWCNT (Pantano et al., 2003). The buckling point and post-buckling behavior is different for both small- (0.96 *nm*) and large- (1.44 *nm*) mesh linear 8-node solid elements. The EOR model fails to capture the steady state buckling wavelength of ~4.80 nm shown by the NSSR model; the wavelength for the EOR model decreases as the amplitude increases.

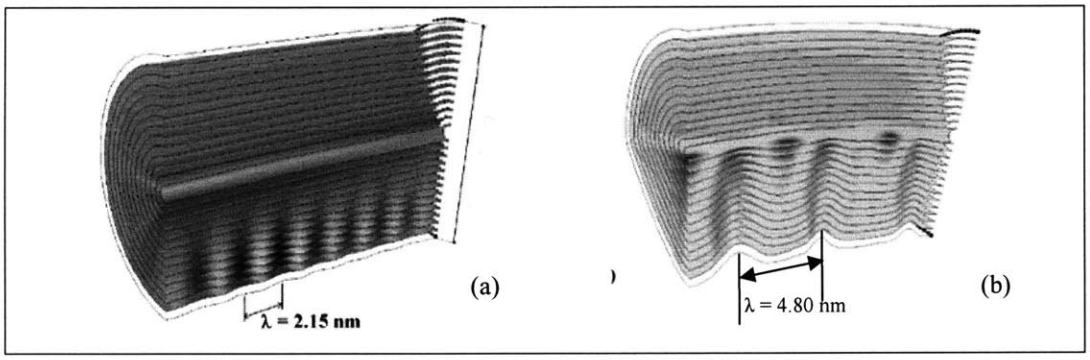

Figure 2.22: FE bending simulation of a 14-walled CNT nested shell model (a) (Pantano et al., 2003) and EOR model (b). L = 30 *nm* and 15 *nm* for nested shell and EOR models, respectively. Initial wavelength for the nested shell and EOR models are ~2.15 nm.

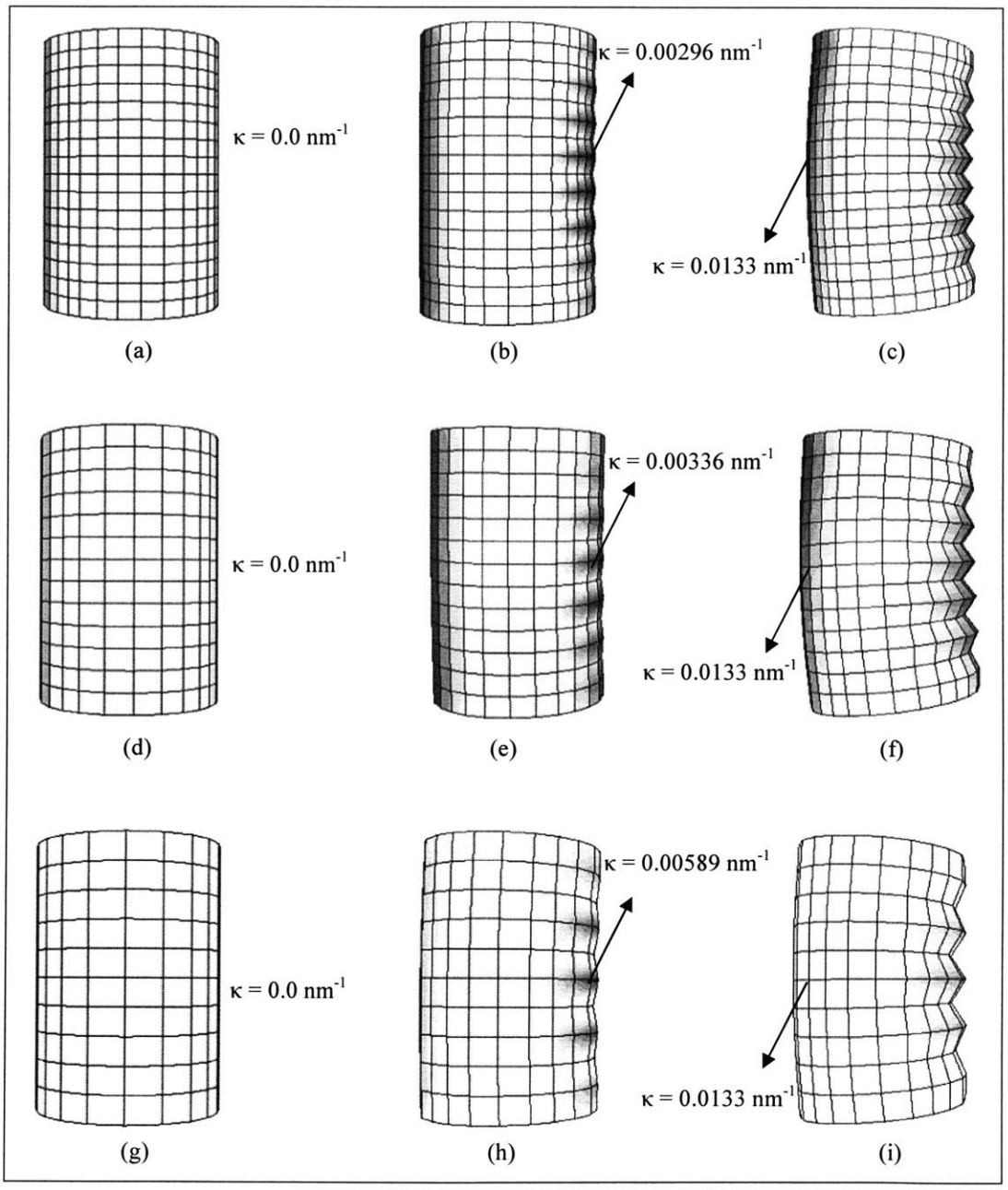

Figure 2.23: FE bending simulation of EOR-based 14-walled CNT with different element size of L=15 *nm* R_o = 4.76 *nm*, showing the initial, buckling point, and final configuration of the MWCNT. Element size = 0.96 *nm* (a, b, and c), = 1.2 *nm* (d, e, and f), and = 1.44 *nm* (g, h, and i). The initial buckling wavelength is ~1.92 *nm* (b), ~2.4 *nm* (e), and ~2.88 *nm* (h).

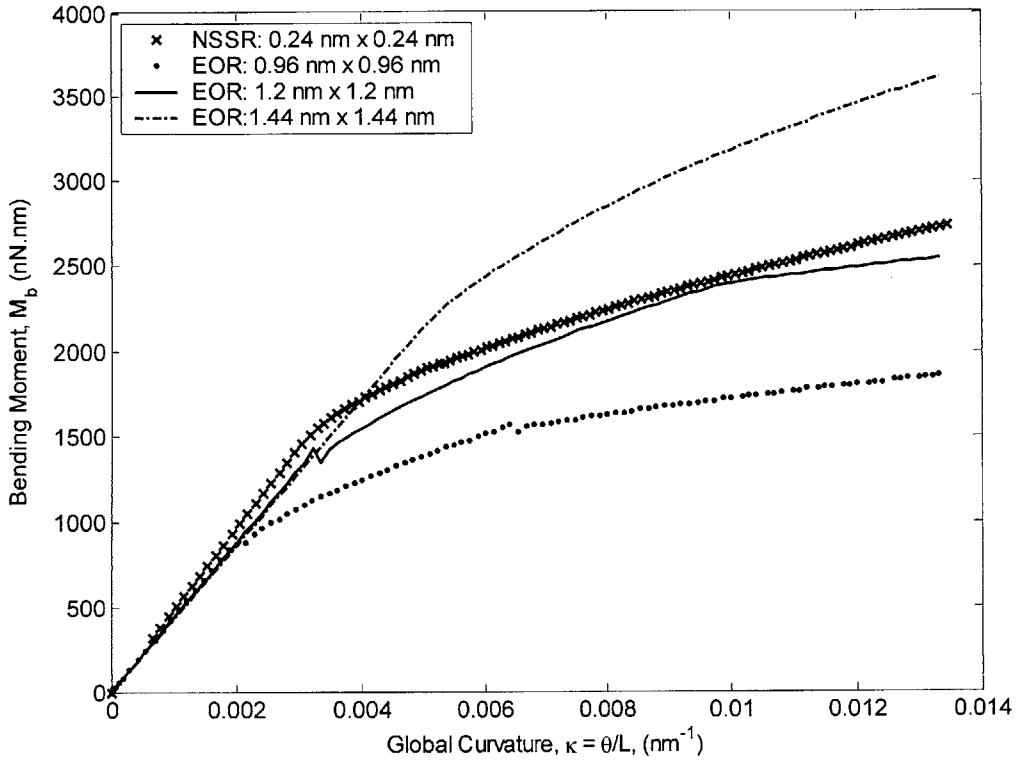

Figure 2.24: FE bending simulation of 14-walled CNT of L = 15 *nm* and outer radius of R_o = 4.76 *nm*. The tube is armchair type (*n, n*) with n = 70 (Pantano et al., 2003).

From results presented in Figure 2.24, we reach a conclusion that the pre-buckling behavior is insensitive to mesh size; mesh sizes other than 1.2 *nm* for a 14-walled CNT results in a different initial buckling λ. However, for a mesh size of 1.2 *nm*, the initial buckling wavelength is very close to the approximate value of 2.15 *nm*, and the corresponding moment-curvature plot in Figure 2.24 is in agreement with the results presented by Pantano et al., (2003).

2.4.1.2 Axial Compression

Next, the effect of mesh size on the axial compression behavior a 14-walled CNT is studied using the EOR model. The MWCNT FE-based model here is similar to the one constructed in the bending simulation earlier. To our advantage, Pantano et al., (2003) presented NSSR FE-based simulation results for a 14-walled CNT under axial

compression, as shown in Figures 2.25 and 2.27. Here one end of the MWCNT is fully constrained, while only radial and circumferential displacements are constrained on the other. The free end is then gradually displaced (δ) by a distance of 1 *nm* in the axial direction towards the fixed end to give a macroscopic axial compressive strain ($\varepsilon_z = \delta/L$) of 0.666 *nm*. The axial force versus the compressive strain diagram computed from the NSSR model and EOR model of different element sizes, are shown in Figure 2.27. Similar to bending simulations earlier, EOR-based FE models are also simulated for mesh sizes of 0.96 *nm*, 1.2 *nm*, and 1.44 *nm*; Figure 2.26 shows snapshots taken from the FE simulations before, during, and after buckling occurs in the FE-based MWCNT.

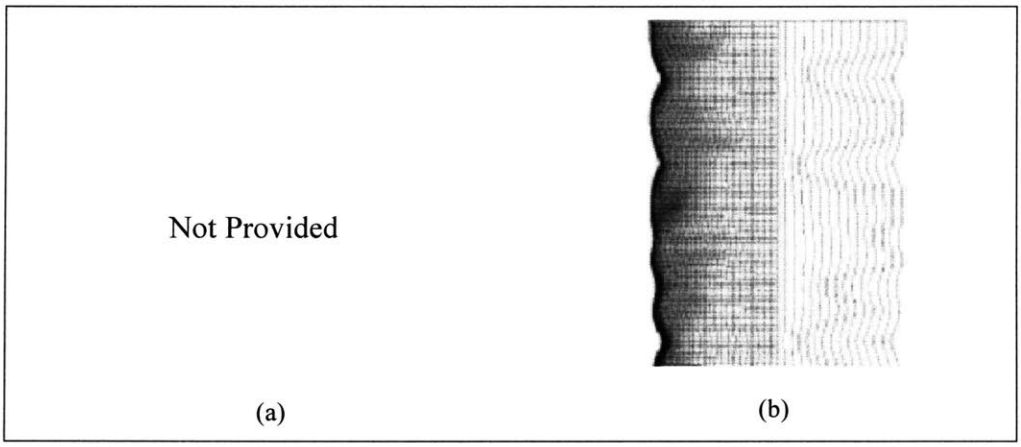

Figure 2.25: Axial compression of a 14-walled CNT; the nested shell model (Pantano et al., 2003). The mesh size for the nested shell model is 0.24 *nm* x 0.24 *nm*. Maximum compressive strain of 0.04 was applied by displacing one end by 0.6 *nm*.

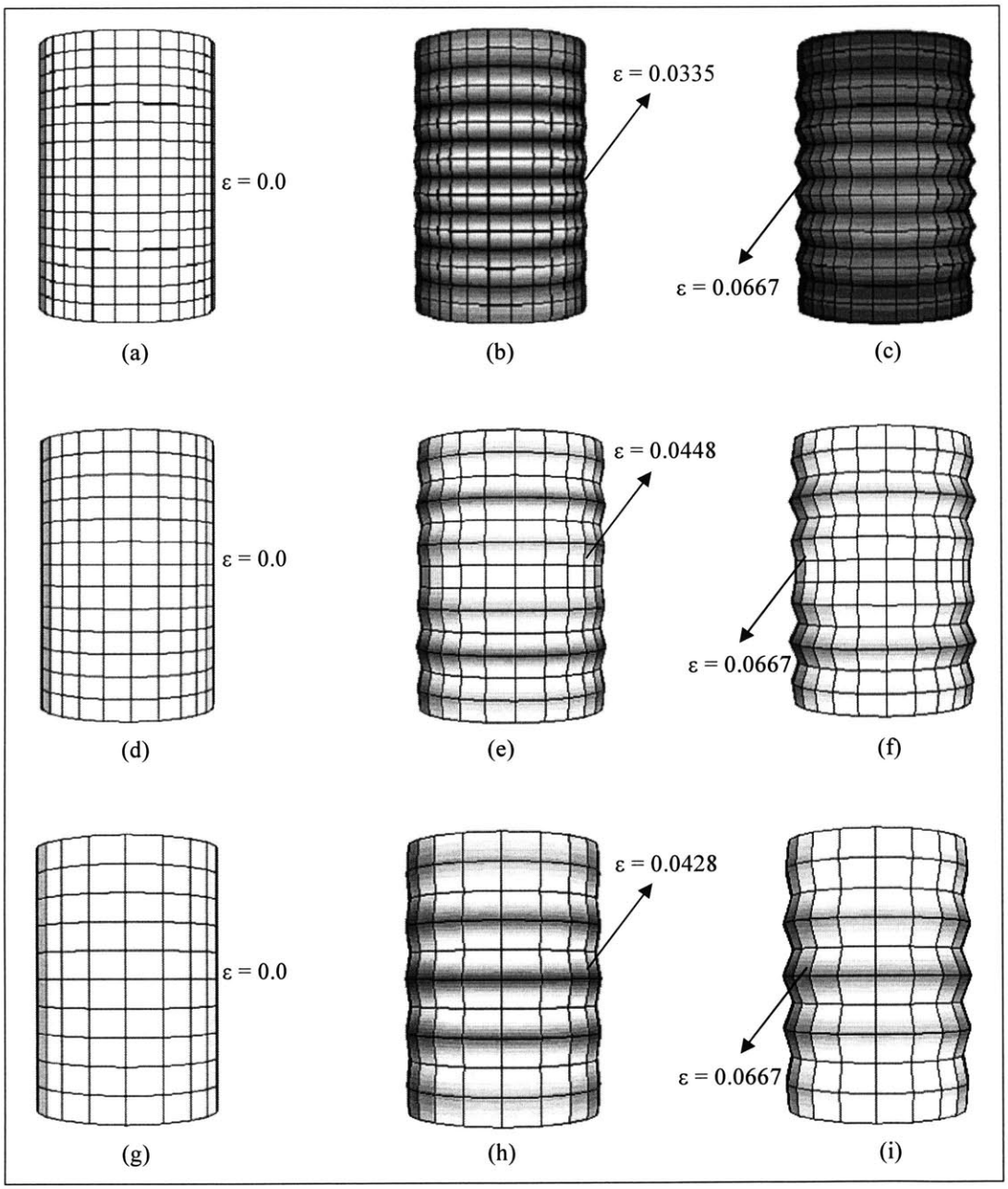

Figure 2.26: FE compression simulation of EOR-based 14-walled CNT with different element size of L=15 *nm* R_o = 4.76 *nm*, showing the initial, buckling point, and final configuration of the MWCNT. Element size = 0.96 *nm* (a, b, and c), = 1.2 *nm* (d, e, and f), and = 1.44 *nm* (g, h, and i). The initial buckling wavelength is ~1.92 *nm* (b), ~2.4 *nm* (e), and ~2.88 *nm* (h).

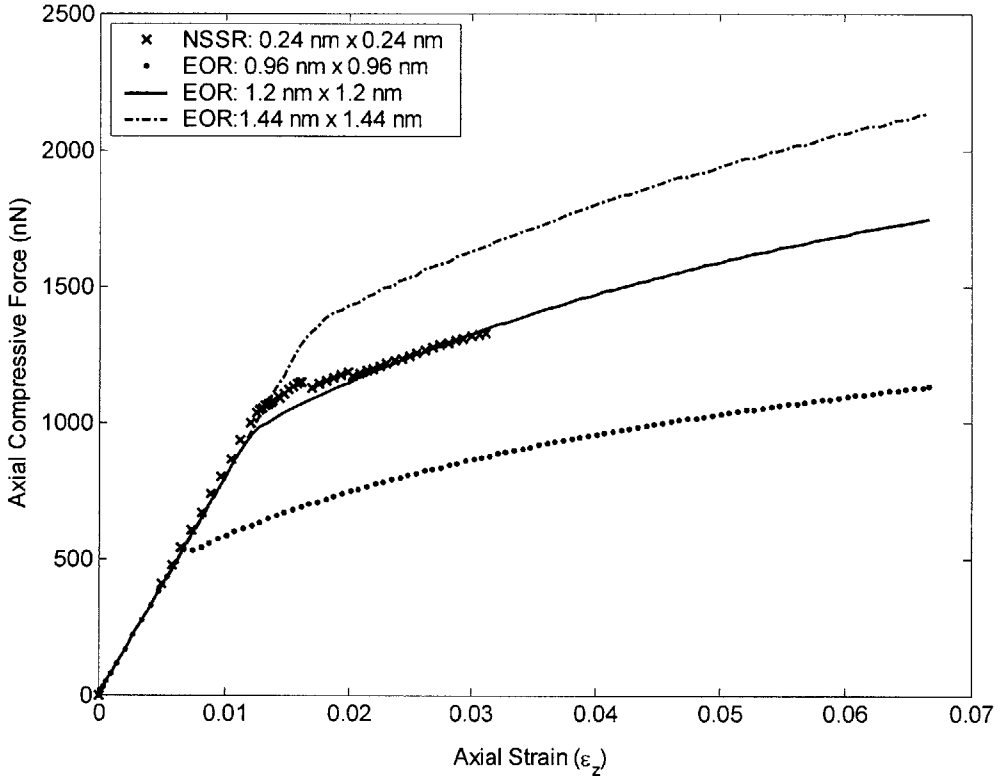

Figure 2.27: Axial compression of 14-walled CNT of L = 15 *nm* and outer radius of R_o = 4.76 *nm*. The tube is armchair type (*n, n*) with n = 70 (Pantano et al., 2003).

Similar to the bending simulation results in Figure 2.24, the axial force versus strain curves for different mesh sizes show that the EOR model captures the pre-buckling behavior of the 14-walled CNT modeled using the NSSR model, as shown in Figure 2.27. Also, similar to the bending simulations, the proper buckling initiation point is only captured when element size is 1.2 *nm* – buckling being sooner for smaller elements (0.96 *nm*) and delayed for larger (1.44 *nm*) element sizes. Therefore, both the buckling point and the post-buckling behavior are sensitive to mesh size in axial compression FE simulations.

Results from Figure 2.24 and 2.27 show that the bending and compressive behavior of an MWCNT can only be captured if the proper element size is selected, based on the initial buckling wavelength. Pantano et al., (2003) reported that buckling progression under axial compression and bending is similar for MWCNTs of the same

size. However, Figure 2.26 shows that the EOR models again fails to capture the steady state buckling of the MWCNT for all element sizes. The EOR model only captures the initial buckling wavelength, thereafter, only the amplitude of the buckling wavelength increases with further compression.

Unlike the NSSR model, where Pantano et al., (2003, 2004a) reported that the buckling wavelength doubles as the MWCNT is further bent or compressed without any significant change in amplitude; on the contrary, the EOR model simulation shows a decrease in buckling wavelength with increases in amplitude. Therefore, the EOR based FE models cannot be used for simulating situations where precise surface deformation studies are important.

2.4.1.3 Lateral Compression

Next, the effect of mesh size on the lateral compression behavior is studied for a 10-walled CNT (armchair type (n, n); n = 25, 30,..., 70). The EOR based FE model of CNT has L of 1.2 *nm*, inner radius R_i of 1.7 *nm*, and outer radius R_o of 4.76 *nm*. A hollow tube is chosen because the van der Waals forces can be extremely high when the interlayer spacing decreases upon lateral compression of the MWCNT; this often leads to convergence problems in achieving a solution for FE models in *ABAQUS*. To our knowledge there is no data available in the literature for lateral compression of a NSSR based FE model for large MWCNTs; Pantano et al., (2003, 2004b) did not present any results for three-dimenstional lateral compression of large MWCNTs. Therefore, we simulated a lateral compression of a MWCNT using the NSSR model. We constructed a 10-walled CNT of L = 1.2 *nm*, R_i of 1.7 *nm*, and R_o of 4.76 *nm* with linear 4-node shell elements (S4 in *ABAQUS*), as shown in Figure 2.28. Here, taking advantage of the symmetry conditions, only one-half of the CNT is constructed. The element size for the NSSR model is taken to be 0.24 *nm* and the user defined interlayer interactions elements were modeled according to Pantano et al., (2004b). Figures 2.28-a, -b, and -c show snapshots at 0 nm, 1.0 nm, and 2.0 nm lateral displacements, respectively.

Two 2-dimensional rigid planar plates are placed on the outermost shell diagonally opposite to each other, as shown in Figure 2.28. The lower rigid plate is fully constrained while the upper plate is gradually displaced towards the other plate by a

distance of 2.0 *nm*. The contacts between the plates and the outermost surface of the MWCNT are modeled to be frictionless. Except for the direction perpendicular to the two-dimensional rigid plane and rotation about the axial direction, all degrees of freedom are constrained for the nodes that constitute the symmetry plane for the shell elements.

Similarly, FE models of EOR based 10-walled CNT are constructed for different mesh sizes and from linear 8-node solid elements (C3D8 in *ABAQUS*) in order to compare the EOR and NSSR models for lateral compression. The CNTs have length, L of 1.2 *nm*, inner radius R_i of 1.7 *nm*, and outer radius R_o of 4.76 *nm*, as shown in Figures 2.29. The interlayer van der Waals force is modeled within the inner surface with the same user defined elements that were used to model the interlayer force in the nested shell model. The lateral force versus lateral displacement results thus obtained from the NSSR and EOR based FE models are shown in Figure 2.30. Mesh sizes of 0.14 *nm*, 0.24 *nm*, and 0.34 *nm* were used in the EOR based FE simulations.

The deformations under the NSSR and EOR models in Figure 2.28 and 2.29 do not indicate any kind of buckling pattern. Figure 2.30 indicate that lateral compressions of MWCNTs are also sensitive to mesh size, with the best element size for lateral compression being 0.24 *nm* – again, equivalent to the height of the hexagonal lattice cell.

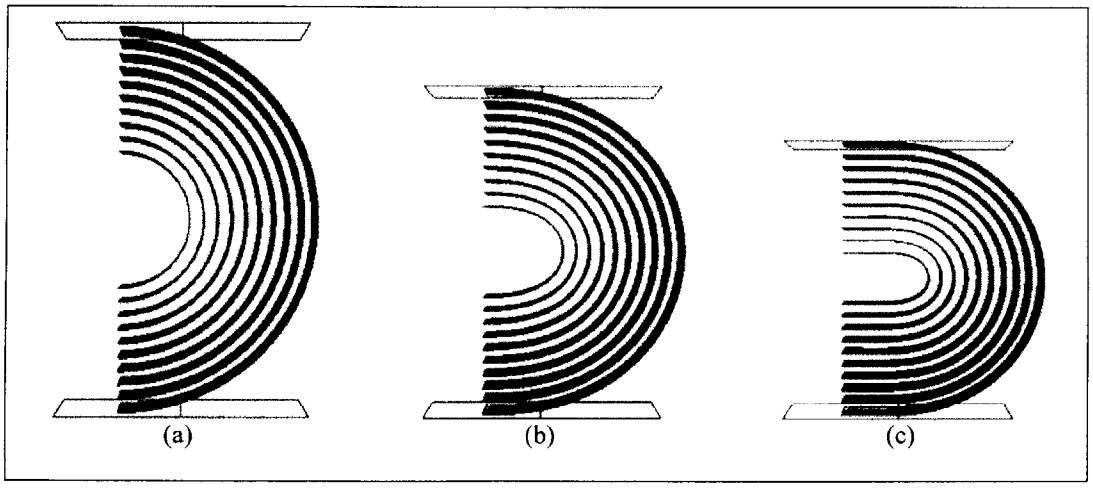

Figure 2.28: Lateral compression of NSSR based 10-walled CNT of L = 1.2 *nm*, inner radius R_i = 1.7 *nm*, and outer radius of R_o = 4.76 *nm* (mesh size = 0.24 *nm*). The tubes are armchair type (*n*, *n*) with *n* = 25,..,70. Snapshots of the FE simulations at lateral displacements of 0 *nm* (a), 1.0 *nm* (b), 2.0 *nm* (c).

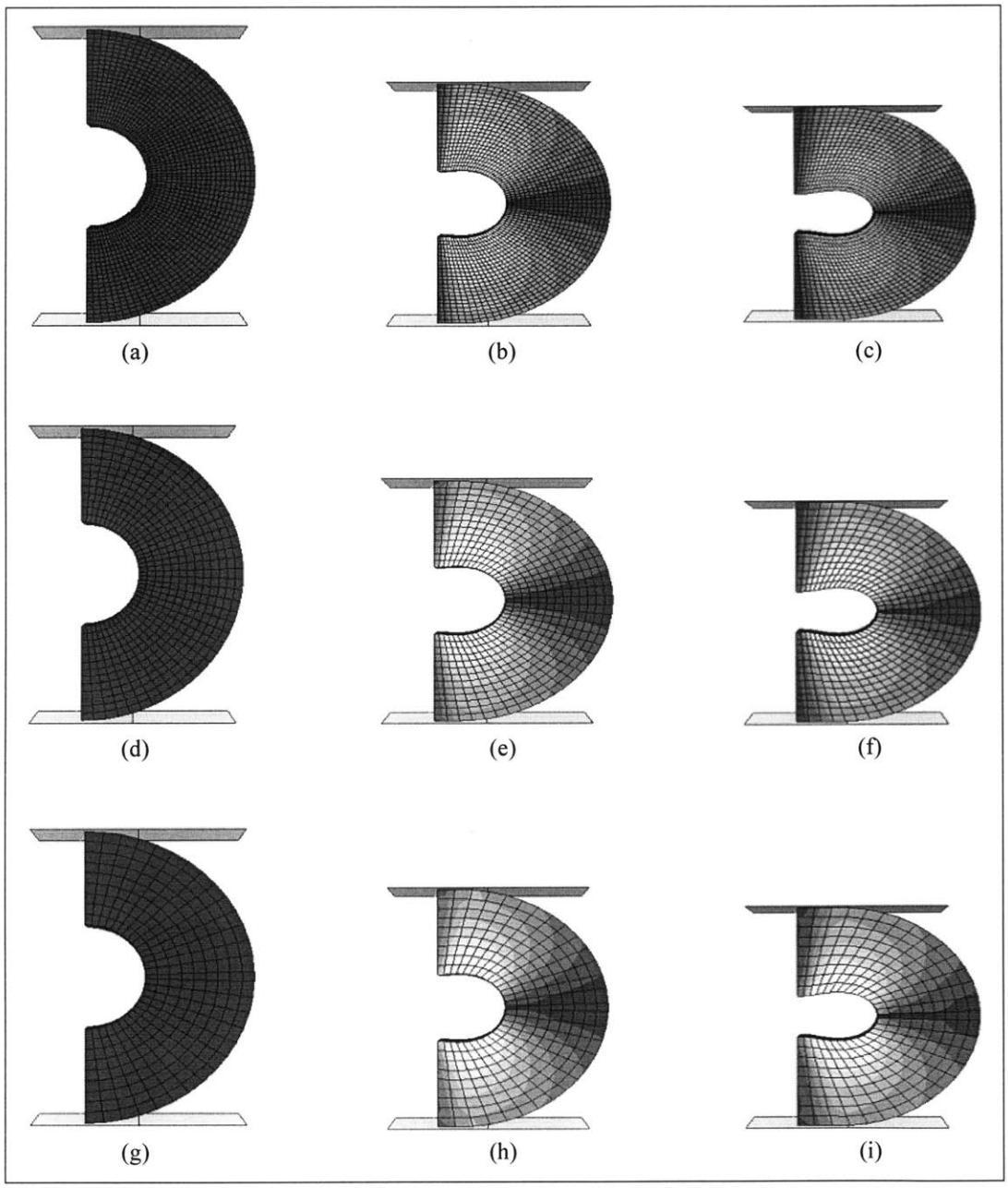

Figure 2.29: FE simulation snapshots where a 10-walled CNT of L = 1.2 *nm*, inner radius R_i = 1.7 *nm*, and outer radius of R_o = 4.76 *nm* is subjected to lateral compression. The tubes are armchair type (*n, n*) with n = 25,..,70. Element size = 0.14 *nm* (a, b, and c), = 0.24 *nm* (d, e, and f), and = 0.34 *nm* (g, h, and i). The FE simulation snapshots are taken at lateral displacement of 0.0 *nm* (a, d, and g), 1.0 *nm* (b, e, and h), and 2.0 *nm* (c, f, and i).

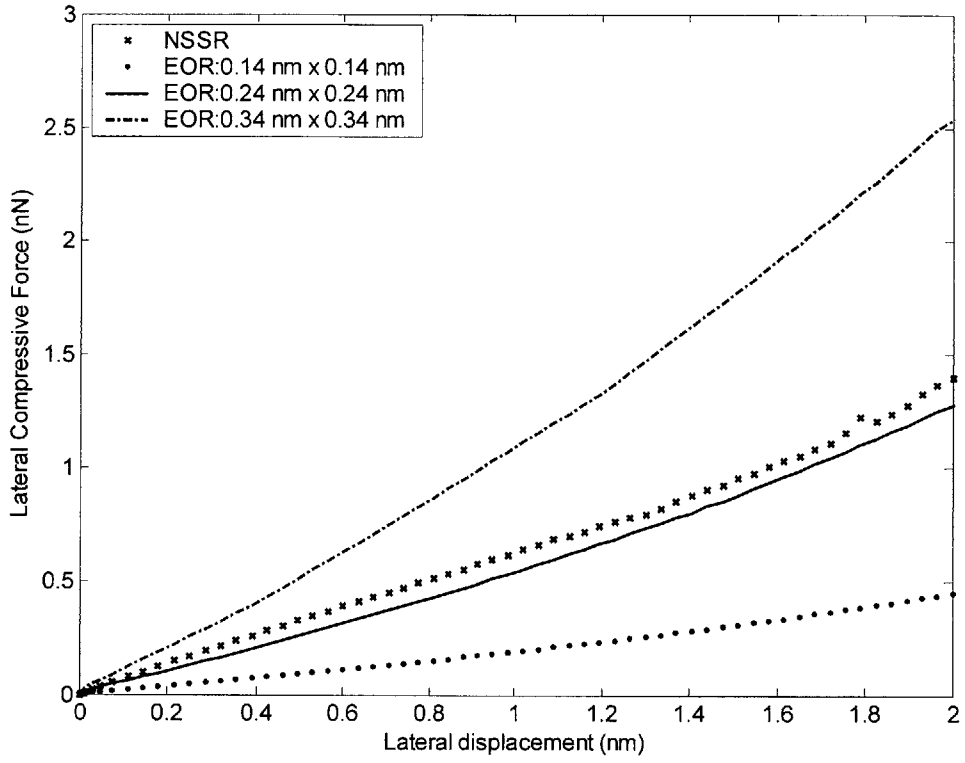

Figure 2.30: Lateral compression of 10-walled CNT of L = 1.2 *nm* R_i = 1.7 *nm*, and R_o = 4.76 *nm*.

From the above simulation results, we see that the period and uniformity of the rippling pattern is affected by the mesh size; therefore, a proper mesh size is very important in EOR-based FE modeling of MWCNTs. For example, a mesh size of 1.2 *nm* (5*0.24 *nm*) is necessary for the 14-walled CNT for simulating bending and axial compression, while that number is 0.24 *nm* for lateral compressions.

Next, since many applications in electric field require the knowledge of how the outermost layer deforms (Pantano et al., 2004c), we next create a 14-walled CNT model with a single discrete shell tube (0.24 *nm* x 0.24 *nm*) around the EOR model (element size 0.24 *nm* x 0.24 *nm* and 1.2 *nm* x 1.2 *nm*), as shown in Figures 2.31, 2.32, 2.34, 2.35, and 2.37. As before, the FE model is then subjected to bending, axial compression, and lateral compression, the results of which are shown in Figures 2.33, 2.36, and 2.38. In all the simulations, the interlayer van der Waals force is incorporated in between the shell tube

and the solid element surfaces incorporating the user defined interaction elements designed by Pantano et al., (2004b).

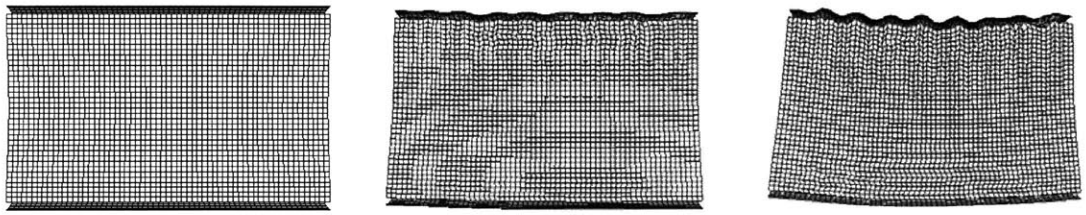

(a) (b) (c)

Figure 2.31: Bending of combined EOR model with a discrete outer shell model. Mesh size of 0.24 *nm* for the EOR model and 0.24 *nm* for the shell model was chosen for 14 -walled CNT. At $k = 0\ nm^{-1}$ (a) $k = 0.00401\ nm^{-1}$ (b), and $k = 0.0134\ nm^{-1}$ (c).

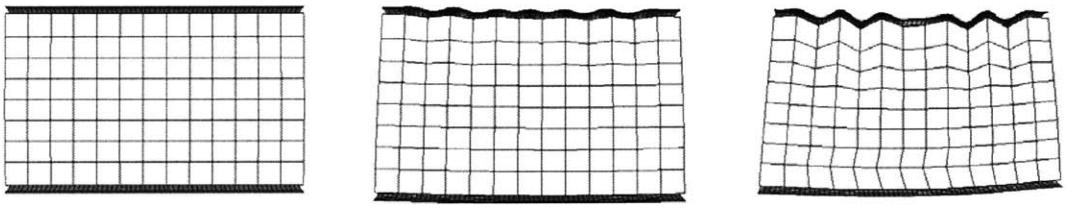

(a) (b) (c)

Figure 2.32: Bending of combined EOR model with a discrete outer shell model. Mesh size of 1.2 *nm* for the EOR model and 0.24 *nm* for the shell model was chosen for 14 -walled CNT. At $k = 0\ nm^{-1}$ (a) $k = 0.00456\ nm^{-1}$ (b), and $k = 0.0134\ nm^{-1}$ (c).

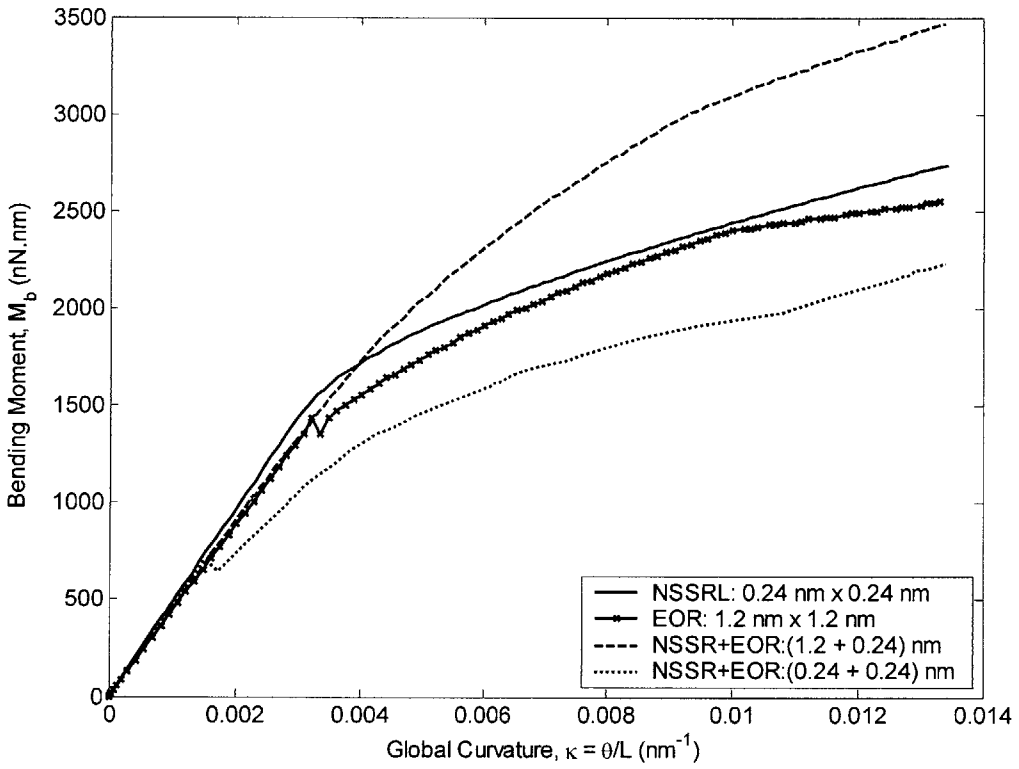

Figure 2.33: FE simulation of 14-walled CNT (EOR model) subjected to bending. The three curves are for the EOR model, nested shell, and a combination of the EOR and nested shell model.

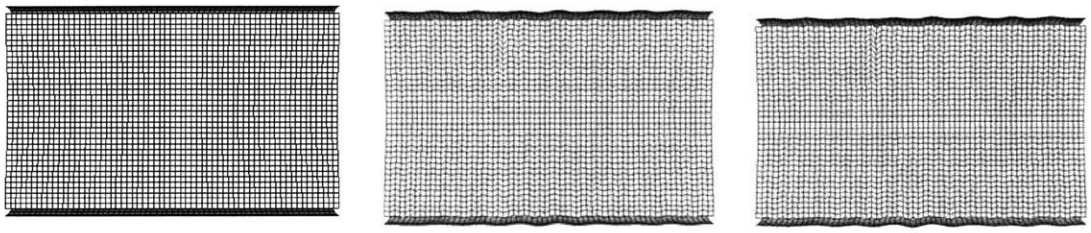

(a) (b) (c)

Figure 2.34: Axial compression of combined EOR model with a discrete outer shell model. Mesh size of 0.24 *nm* for the EOR model and 0.24 *nm* for the shell model was chosen for 14-walled CNT. At $\varepsilon = 0$ (a) $\varepsilon = 0.0176$ (b), and $\varepsilon = 0.0202$ (c).

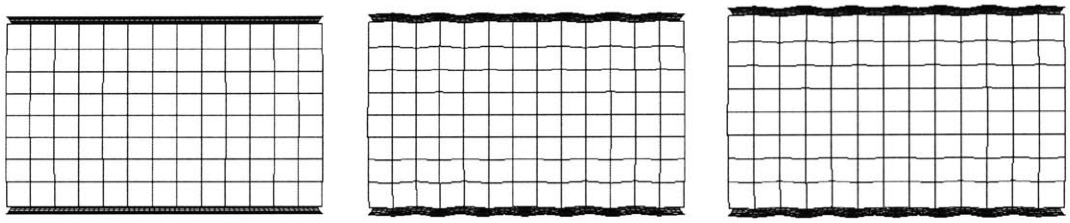

(a) (b) (c)

Figure 2.35: Axial compression of combined EOR model with a discrete outer shell model. Mesh size of 1.2 *nm* for the EOR model and 0.24 *nm* for the shell model was chosen for 14-walled CNT. At $\varepsilon = 0$ (a) $\varepsilon = 0.0213$ (b), and $\varepsilon = 0.0535$ (c).

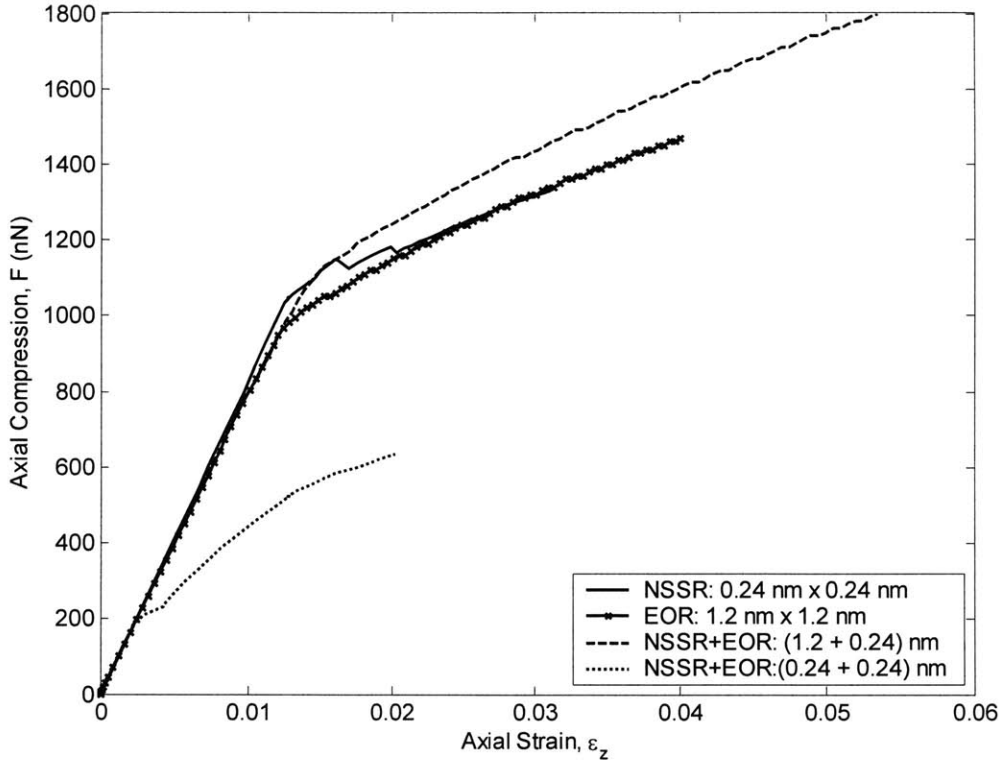

Figure 2.36: FE simulation of 14-walled CNT (EOR model) subjected to axial compression. The three curves are for the EOR model, nested shell, and a combination of the EOR and nested shell model.

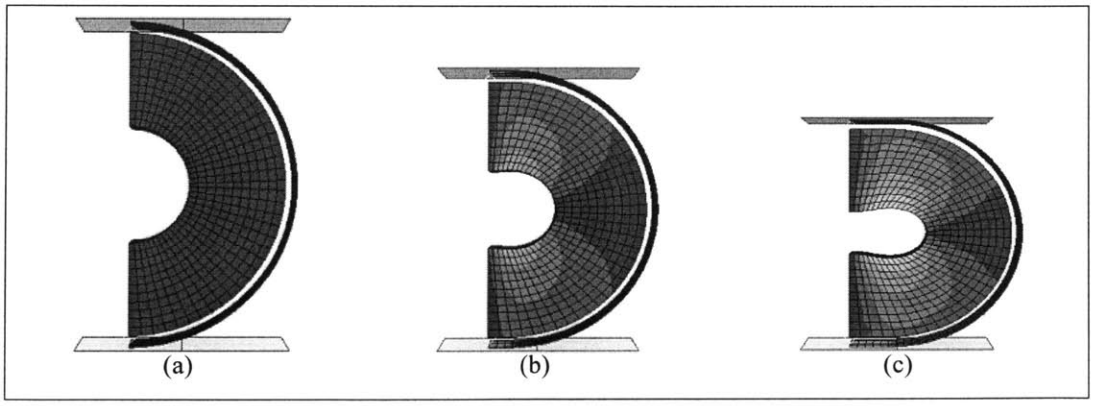

Figure 2.37: Lateral compression of combined EOR and NSSR model. Mesh size of 0.24 *nm* for both the EOR and NSSR model for 14-walled CNT at lateral compression (δ) of 0.0 nm (a), 1.0 nm (b), and 2.0 nm (c).

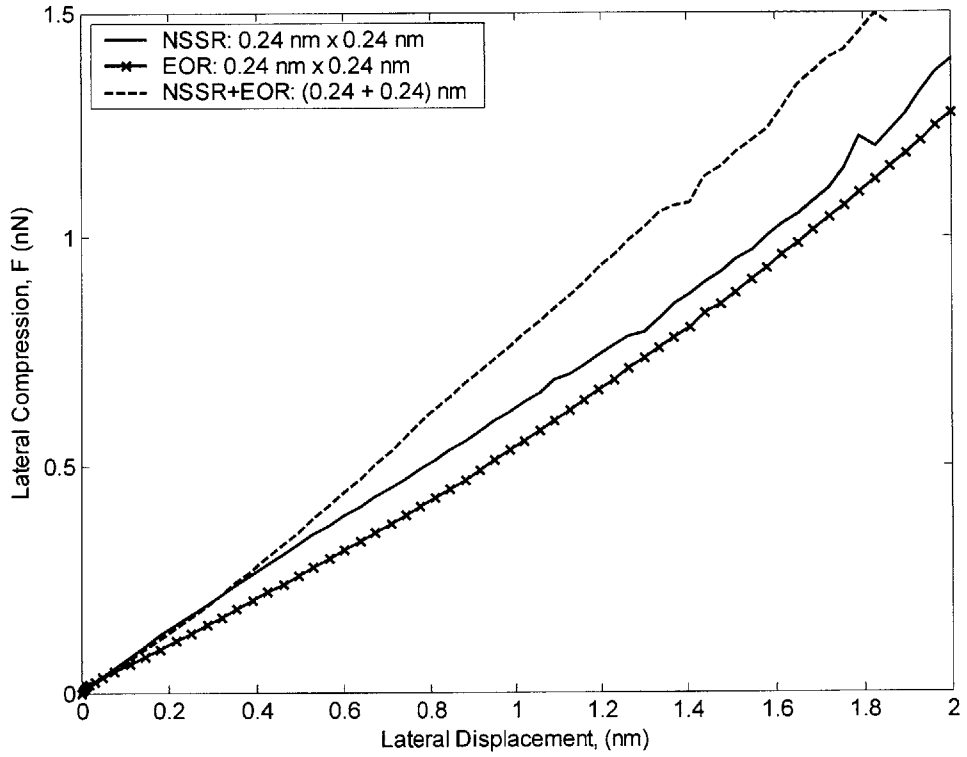

Figure 2.38: FE simulation of 14-walled CNT (EOR model) subjected to lateral compression. The three curves are for the EOR model, nested shell, and a combination of the EOR and nested shell model.

Clearly, Figures 2.33 to 2.37 show that EOR-NSSR combined element model results agree well with the nested shell model results if a proper element size is chosen. The EOR-NSSR based FE model results agree well for the pre-buckling and the buckling initiation regimes, but not the post-buckling in Figure 2.33. Figures 2.31-b, 2.32-b, 2.34-b, and 2.35-b visually show that combined EOR-NSSR models are able to capture the initial buckling wavelength and the rippling pattern irrespective of the element size chosen for the EOR model; the initial buckling wavelength predicted by the NSSR model is ~2.15 nm. However, Figures 2.33 and 2.36 show that selecting an element size equal to 0.24 *nm* x 0.24 *nm* results in premature buckling. Figure 2.36 indicate that the combined model under axial compression gives reasonable results for pre- and post-buckling and even the buckling point. Although the initial buckling wavelength of the combined model

is similar to the nested shell and the EOR models, the steady state buckling wavelength did not increase with deformation, as was reported by Pantano et al., (2003); the wavelength was observed to decrease and amplitude to increase with further deformation. The difference in the mesh sizes of the solid and shell elements in the combined FE model is the major source of difference in the post-buckling behavior. The difference in mesh size magnifies the errors for this highly nonlinear deformation mechanics and geometry of the CNT. For lateral compression simulations for the combined EOR-NSSR model show a slight increase in the lateral compression force with lateral displacement, as shown in Figure 2.38. Nonetheless, the difference is negligible and therefore can be applied to model MWCNTs in the FE analysis.

Next, we apply our observations from the above simulations to model MWCNTs of different aspect ratios. We subject these CNTs to bending, axial compression and lateral compression.

2.4.2 Comparison of EOR Model to NSSR Model and Experiments

We found from the FE simulation results presented in the previous section that in order to properly capture the deformation behavior of MWCNTs, a proper element size needs to be assigned to the EOR-based FE models. Before we simulate the EOR-based MWCNT models of different aspect ratios under different loading conditions, there is a need for an adequate method that estimates the proper element sizes. Recall that for a 14-walled CNT, the best simulation results were obtained when an element size of 1.2 *nm* was used. This element size is approximately half of the initial buckling wavelength predicted by the NSSR-based MWCNT model and thin shell theory. Therefore, in the subsequent subsections, we will estimate the element size based on thin shell theory (Equation 2.5) and round the result to an integer multiple of 0.24 nm.

2.4.2.1 Bending

EOR based FE bending simulations are performed on MWCNTs of L = 15 *nm* and for 4-, 8-, 14-, and 19-walled CNTs. All of the tubes in the MWCNT are of armchair (n, n) chirality, with n = 5, 10,..., 95, and with R_o = 1.36 *nm*, 2.72 *nm*, 4.76 *nm*, and 6.46

nm, respectively, for 4-, 8-, 14-, and 19-walled CNTs. The bending simulation procedures for these MWCNTs are the same as that for the14-walled CNT, modeled earlier. The bending moment versus global curvature results obtained by simulating MWCNTs are shown in Figure 2.39. In Figure 2.40 we compare the total simulation time versus the number of walls for the EOR and the NSSR FE models.

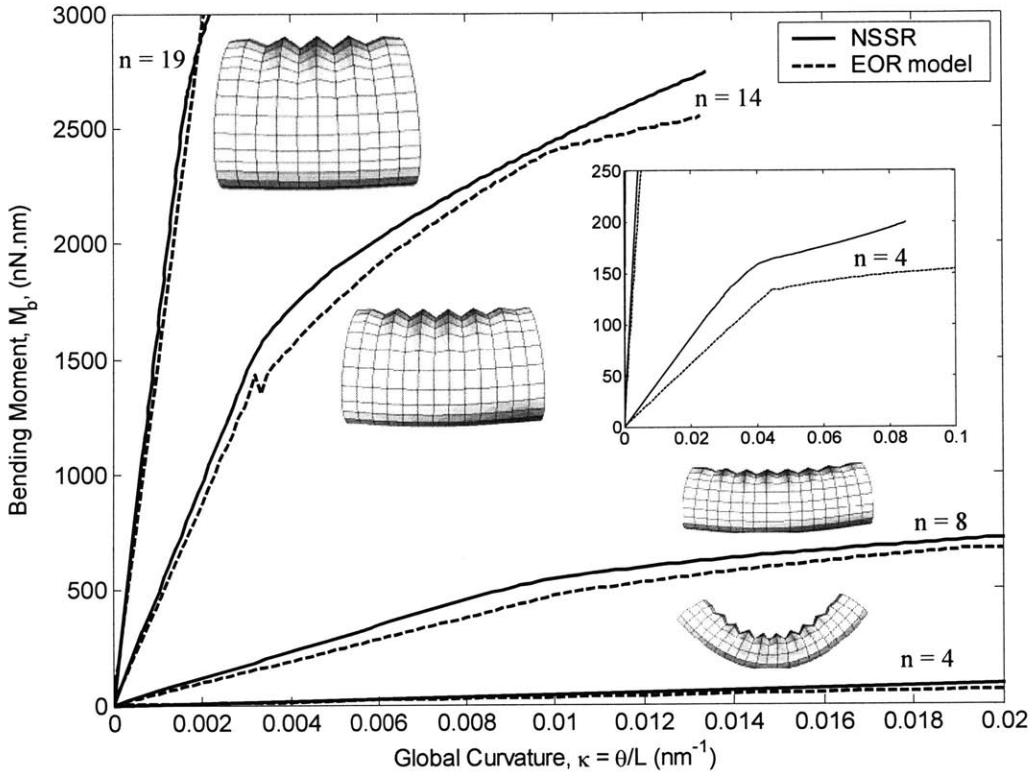

Figure 2.39: Comparison of the EOR model with the nested shell model. Comparison of bending moment of 4, 8, 14 and 19-walled CNT of L = 15 *nm* for the EOR and the nested shell models (Pantano et al., 2003).

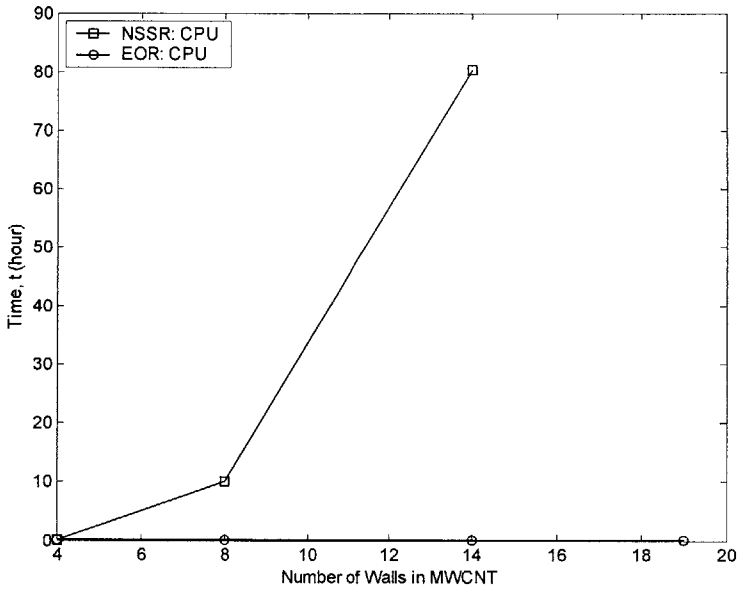

Figure 2.40: Simulation time comparison of Nested shell and EOR model to run a job in ABAQUS for Bending of different MWCNTs.

The best fit with the nested shell model was obtained by using element sizes of 0.72 *nm* (3*0.24 *nm*), 0.96 *nm* (4*0.24 *nm*), 1.2 *nm* (5*0.24 *nm*), and 1.44 *nm* (6*0.24 *nm*) for 4-, 8-, 14-, and 19-walled CNTs, respectively. Recall that we estimated the element size for the EOR-based FE simulations as half the initial buckling wavelength predicted by thin shell theory (Equation 2.5a) and as an integer multiple of 0.24 *nm*, as shown below:

$$element\,size = 1.7\sqrt{R_o t_g} \quad nm; \tag{2.31}$$

where, R_o is outermost radius of the MWCNT and t_g = 0.075 *nm* is the shell tube thickness. If the solution from Equation 2.31 is not a multiple of 0.24, then the element size is rounded to a higher multiple of 0.24 as follows:

$$element\,size = round\left(\frac{element\,size}{0.24}\right). \tag{2.32}$$

Figure 2.39 shows how the EOR model is able to satisfactorily capture the nonlinear mechanics of the pre- and the post-buckling including the buckling point of the MWCNTs. For the 4- and 8-walled CNT, the difference in the slopes of bending moment versus global curvature between the two models can be attributed to the use of global volume fraction $f_g(N)$ by the EOR model. We found earlier in Section 2.3.1 that for MWCNT with less than 10 walls, the properties for the concentric layers vary significantly with radial location; the differences in mechanical properties become negligible as the number of walls increases in an MWCNT. Figure 2.40, on the other hand, highlights the computational advantage of FE simulation with the EOR model over the nested shell model.

2.4.2.2 Axial Compression

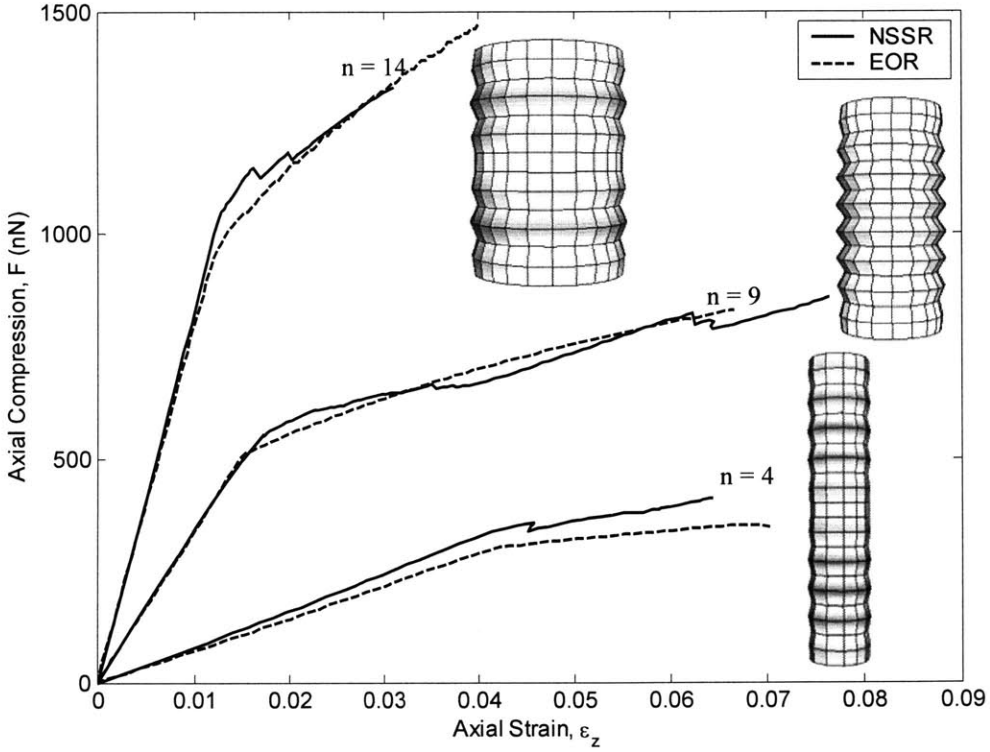

Figure 2.41: Comparison of the results from the EOR model and the nested shell model. Comparison of axial compression of 4, 9 and 14-walled CNT of L = 15 *nm* fixed at one end and compressed at the other with the nested shell model results (Pantano et al., 2003).

We next repeat the EOR-based FE simulations for MWCNTs of 4-, 9-, and 14 walls in a manner similar to the axial compression simulations presented earlier in Section 2.4.1.2. The mesh sizes are same as those found earlier for MWCNTs in the previous section. Applying Equations 2.31 and 2.32, the element size for the 9-walled CNT was found to be the same as that for the 8-walled CNT. The results of axial compressive force versus strain are shown in Figure 2.41 and simulation time for the EOR and the nested shell models in Figure 2.42, respectively.

Figure 2.41 shows that the EOR model of MWCNTs capture remarkably the nonlinear mechanics of pre- and post-buckling including the buckling point. Similar to the bending simulations, a slight deviation from the NSSR model is visible in the pre-buckling regime for the 4-wall CNT. The deviation again becomes negligible as the number of walls increases in the MWCNT. Again the axial compression simulations with the EOR model are also computationally efficient, much like in the bending simulations (Figure 2.42).

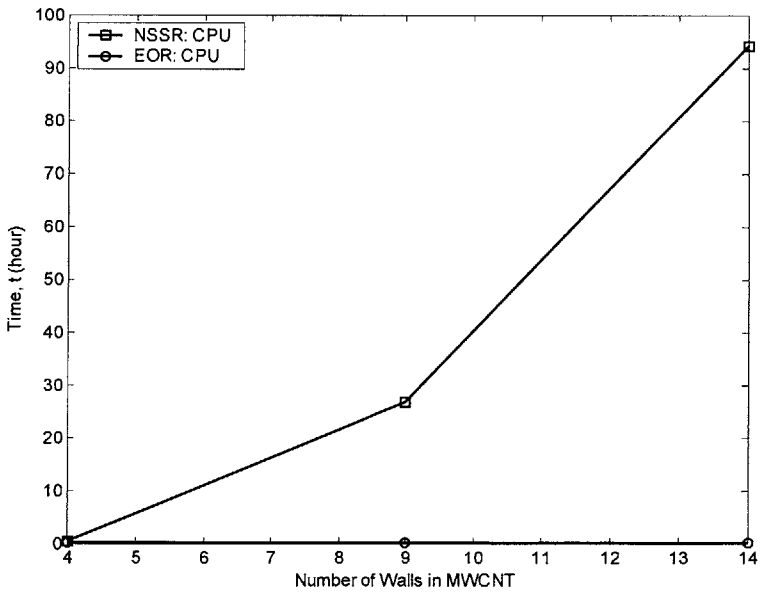

Figure 2.42: Simulation time comparison of Nested shell and EOR model to run a job in ABAQUS for compression of different MWCNTs.

2.4.2.3 Lateral Compression

Lateral compression of a MWCNT is now examined. Although little simulation data exist for large MWCNTs subjected to lateral compression, the availability of some experimental data by Shen et al., (2000) allows us to check the applicability of the EOR model. In their experiment, MWCNTs were indented from above with a tetrahedron-shaped diamond tip with an apex radius of about 25 *nm*. They suggested that the major mechanics of deformation comes from changes in the cross-section from a circular one to an elliptic one, with the innermost shell deforming the most. The average R_o for their MWCNTs is approximately10 *nm*; however, the number of shell tubes, the innermost radius, and the length are unknown. Using the MD simulations of 2- and 4-walled CNTs by Guo et al., (2004) as a guideline, we estimated the innermost radius to be approximately 1.7 *nm*.

We next simulate the lateral compression of a 10-walled CNT with a rigid sphere of radius 25 *nm*, as shown in Figure 2.43. The MWCNT FE model constructed from both linear 4-node shell (0.24 nm x 0.24 nm) and linear 8-node solid (0.72 nm x 0.72 nm) elements has dimensions as follows: R_i = 1.7 *nm*, R_o = 5.1 *nm* and L = 50 *nm*. A large length of 50 *nm* was chosen to minimize the end effects. The tangential and the axial displacements were constrained on both ends while the rigid tip is gradually compress the MWCNT laterally. The van der Waals interlayer interactions were applied at two locations – between the shell and the solid elements, and within the inner surface of the shell tube.

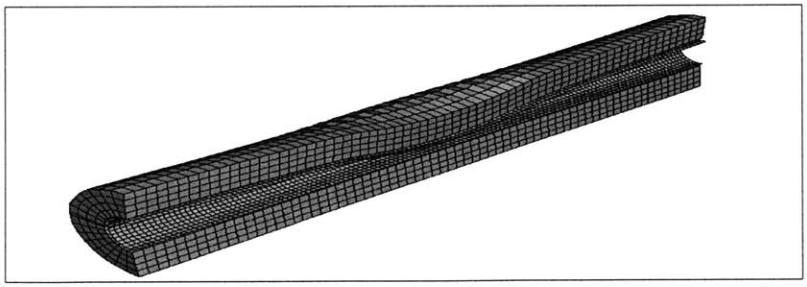

Figure 2.43: Lateral compression of the combined EOR model with a discrete inner shell model. Mesh size of 0.72 *nm* for the EOR model and 0.24 *nm* for the shell model was chosen for 14-walled CNT. R_i = 1.7 *nm*, R_o = 5.1 *nm* and L = 50 *nm*. The radius of the rigid spherical tip (not shown) is 25 *nm*.

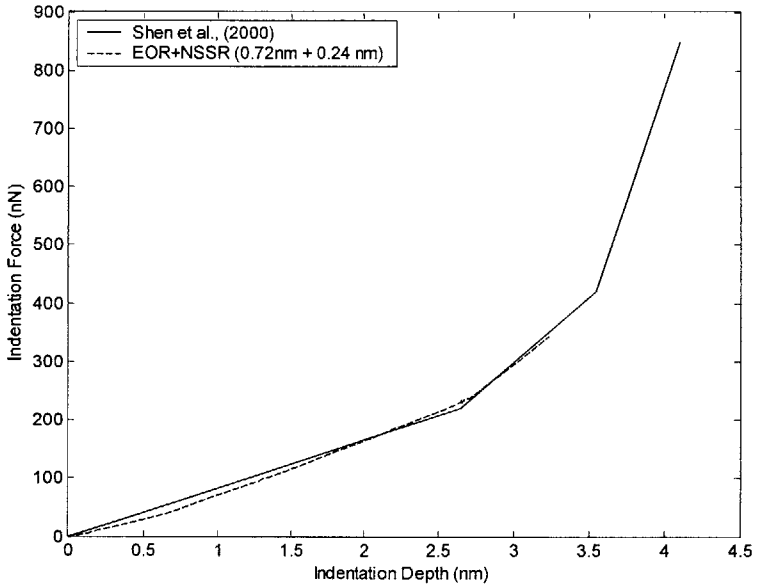

Figure 2.44: Lateral compression of the FE-based model of MWCNT using combined solid and shell elements (Shen et al., 2000).

Figure 2.43 shows how the combined EOR-NSSR model of a 10-walled CNT is able to capture the lateral compression of an MWCNT. The initial slope of the combined FE MWCNT model in Figure 2.44 matches with that of the experimental curve. However, as suggested by the MD simulation results (Guo et al., 2004), the steep slope beyond a lateral displacement of ~2.5 *nm* is due to the interlayer separation decreasing below the equilibrium spacing.

2.4.3 Comparison of EOR properties with Bulk Graphite Properties

Liu et al., (2001, 2003), Wang and Wang (2004), Wang et al., (2004), and Wang et al., (2005) performed FE simulations in which a two- and three-dimensional MWCNT beam model was subjected to bending; the solid beam FE model had bulk graphite properties listed in Table 2.2. The bending moment-curvature results were presented in a diagram as normalized quantities. In order to study the difference, if any, between the two approaches, we simulated the bending, axial and lateral compression of a 14-walled CNT modeled using the bulk graphite elastic constants listed in Table 2.2. The

simulations conditions are the same as those in Subsections 2.4.1.1 to 2.4.1.3 with the exception of element sizes – 0.96 *nm* and 1.2 *nm*. The results thus obtained from the simulations are compared with the results from the NSSR and the EOR models in Figures 2.45 to 2.47. For simulations using graphite elastic constants, an element size of 0.96 *nm*, different than that of the EOR model was required in order to match the results from the NSSR model.

Figure 2.45 shows that only the pre-buckling deformation behavior is matched by the 1.2 *nm* case, whereas both the pre- and post buckling are matched reasonably well by the 0.96 *nm* element size case. However, when FE models of MWCNTs are constructed from linear 8-node solid elements of size 0.96 *nm*, the initial buckling wavelength is constrained to less than 1.92 *nm* (2*0.96 *nm*) as opposed to the 2.15 *nm* wavelength as predicted by the NSSR model.

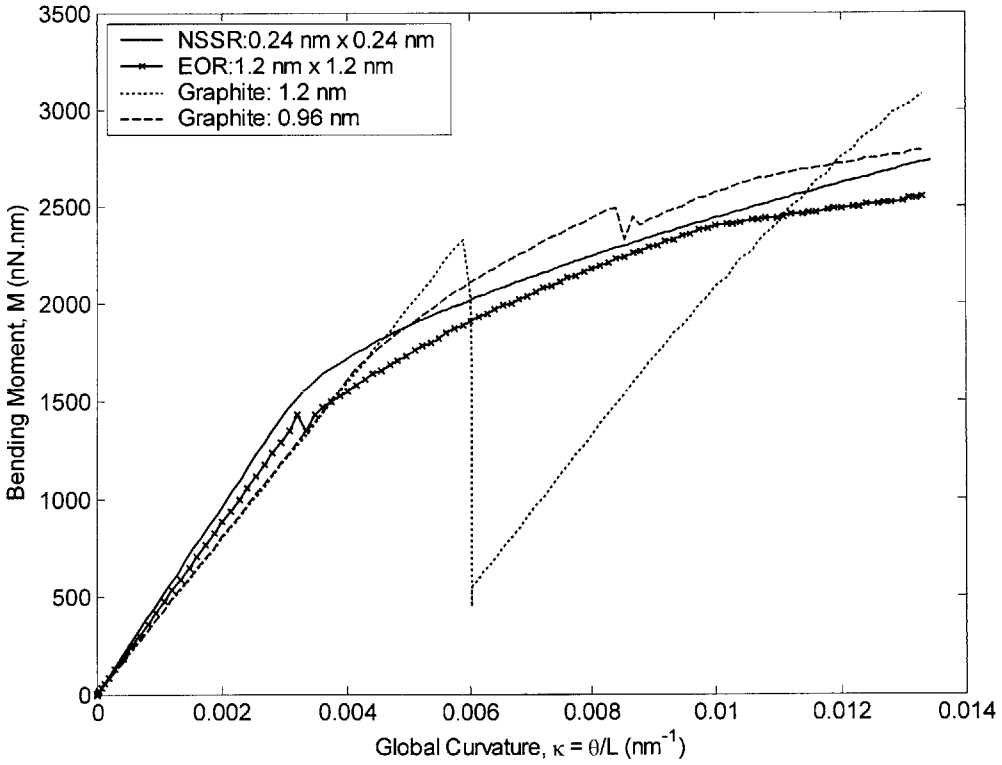

Figure 2.45: Bending of 14-walled CNT. The three curves are from the nested shell, the EOR, and graphite properties in the EOR models of the FE-based MWCNT model.

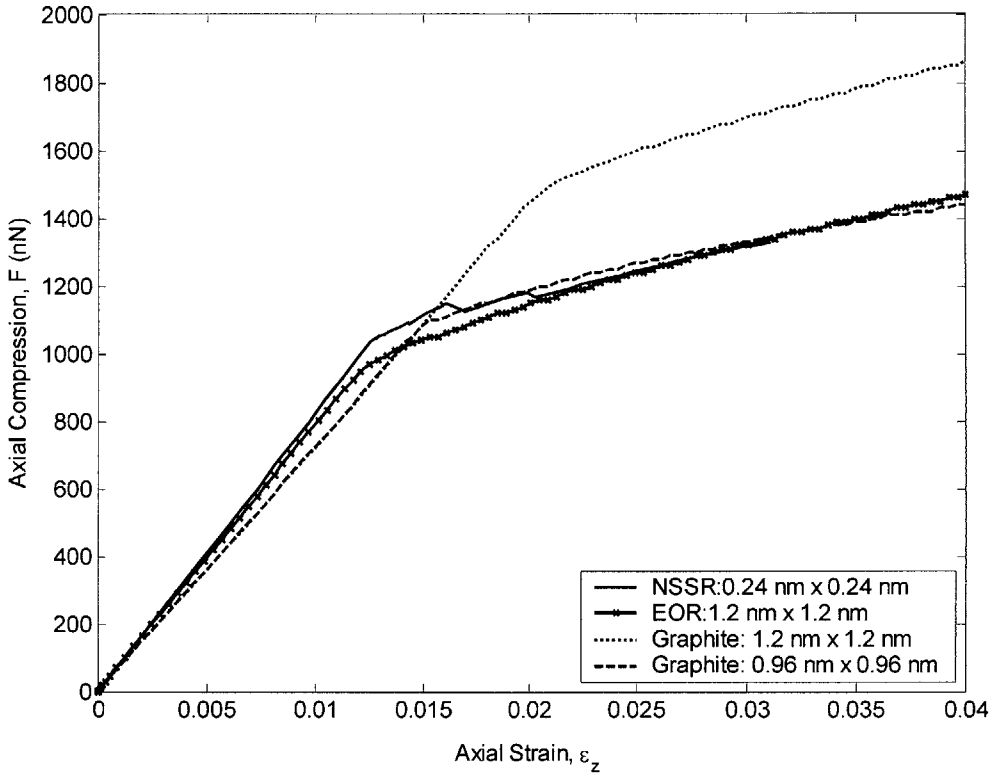

Figure 2.46: Axial compression of 14-walled CNT. The three curves are from the nested shell, the EOR, and graphite properties in the EOR of the FE-based MWCNT model.

For the compressive simulations, Figure 2.46 also shows that only the pre-buckling deformation behavior is matched by the 1.2 *nm* case, whereas both the pre- and post buckling are matched reasonably well by the 0.96 *nm* element size case. However, by the same argument provided earlier, a smaller element size of 0.96 *nm* limits the initial buckling wavelength to less than 1.92 *nm*.

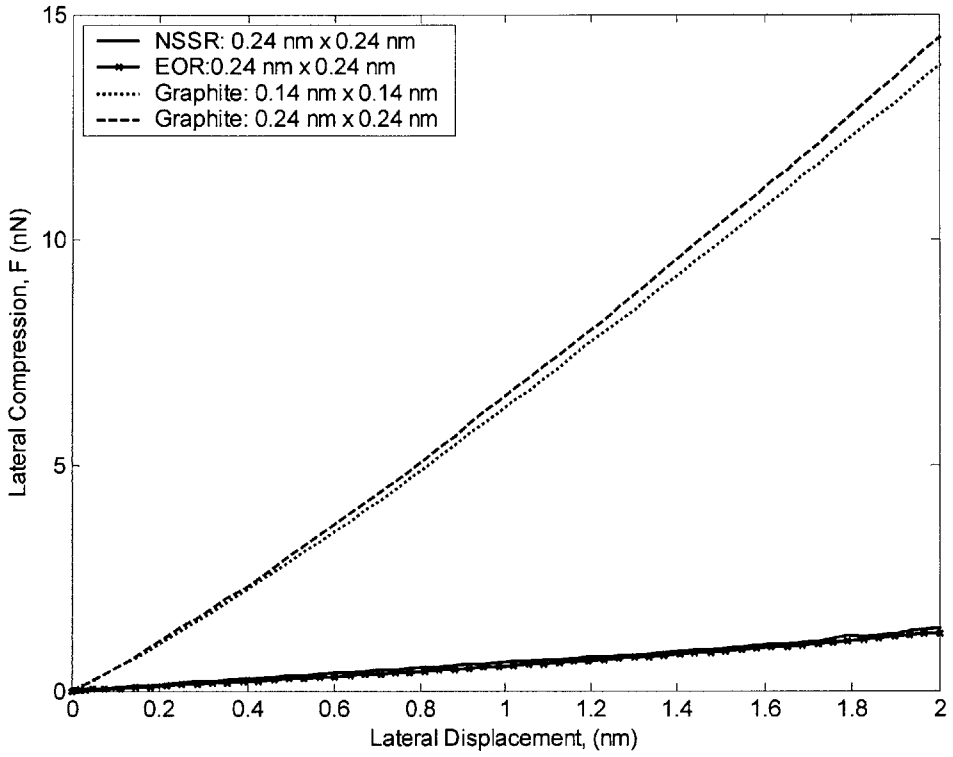

Figure 2.47: Lateral compression of 10-walled CNT. The three curves are for nested shell, EOR, and graphite of the FE-based MWCNT model.

Figure 2.47 shows the lateral compression simulation results of a 10-walled CNT with R_i = 1.7 *nm*, R_o = 4.76 *nm*, and L = 1.2 *nm*; with the graphite elastic constants listed in Table 2.2; and element sizes of 0.24 *nm* and 0.14 *nm*. Unlike the EOR-based MWCNT model, element size does not affect appreciably MWCNT models that are based on the graphite properties. Figure 2.53 also shows that the lateral compression behavior predicted by the MWCNT model with graphite properties does not match the behavior predicted by the NSSR model. In fact, for lateral compression simulations, the results obtained using graphite properties fail to match the results from the nested shell or the EOR models by an order of magnitude.

Based on Figures 2.45 to 2.47, graphite properties-based MWCNT FE models seem to capture the complete deformation behavior for bending and axial compression simulations; the model, however, fails to capture the deformation behavior in lateral

compression simulations. In addition, the model fails to capture the initial buckling wavelength when the MWCNT is subjected to bending and axial compression.

Before we conclude this chapter, in order to verify the Poisson ratio trend in MWCNTs, we conducted FE-based compression and tension simulations for 4- and 14-walled CNTs. The FE-based MWCNTs were costructed from the EOR and NSSR models. The NSSR-based 4-walled model had an innermost tube radius R_i of 0.34 *nm*, an outermost tube radius R_o of 1.36 *nm* and a length L of 15 *nm*, while the 14-walled CNT model had R_i of 0.34 *nm*, R_o of 4.76 *nm* and L of 15 *nm*. The tubes modeled are of armchair (n, n) chirality, i.e., $n = 5, 10, \ldots 70$. The EOR-based 4-walled model had similar dimensions as their NSSR-based CNT counterparts; the innermost radius is zero for the EOR-based MWCNT models. During the simulation, one end was fully constrained, while the other end was gradually displaced axially to simulate compression and tension, accordingly. The results obtained from the compression and tension of 4- and 14-walled CNTs are shown in Figures 2.48 to 2.53.

FE simulation results in Figures 2.48 and 2.49 show that the EOR model captures remarkably the deformation mechanics of the MWCNTs under axial compression and tension. In addition to the compressive and tensile forces, Poisson ratio $\nu_{z\theta}$ (= $-(\delta R/R)/(\delta L/L)$) versus strain was calculated as shown in Figures 2.50 and 2.51. According to both figures, the Poisson ratio obtained from the EOR model is approximately 0.17 while that from the NSSR model is 0.19. The compression simulations of 4-walled FE-based CNTs (Figure 2.50) indicate that Poisson ratio is more or less invariant of axial strain for both the NSSR and EOR models. However, for the EOR-based 14-walled CNT, the Poisson ratio varies nonlinear behavior with respect to axial strain as can be seen in Figures 2.50 and 2.51; this effect does not have any appreciable consequences, as suggested by the overlapping force versus strain curves from the two models in Figures 2.48 and 2.49. We expected the Poisson ratio to drop with the increase in number of concentric tubes and van der Waals forces; however, the results in Figure

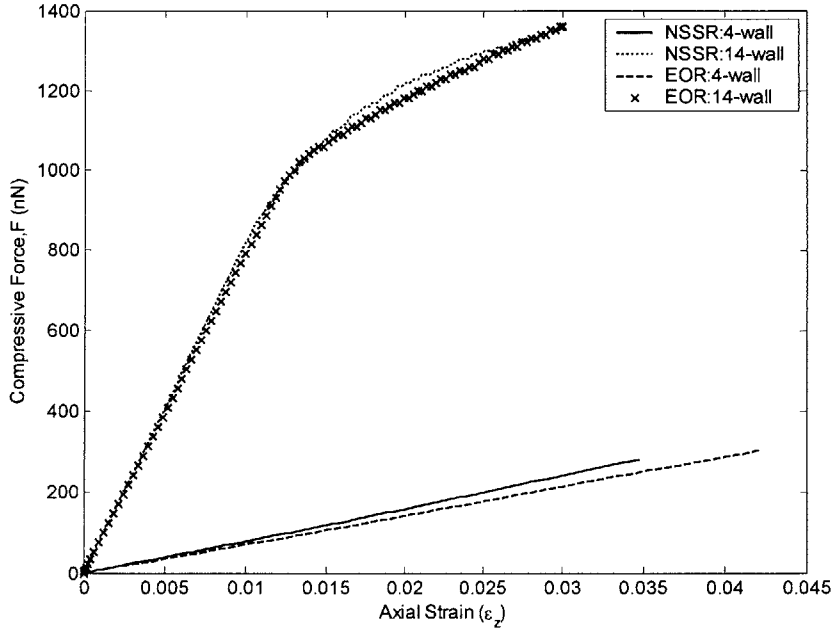

Figure 2.48: Compressive force versus axial strain for 4- and 14-walled nested shell and EOR model.

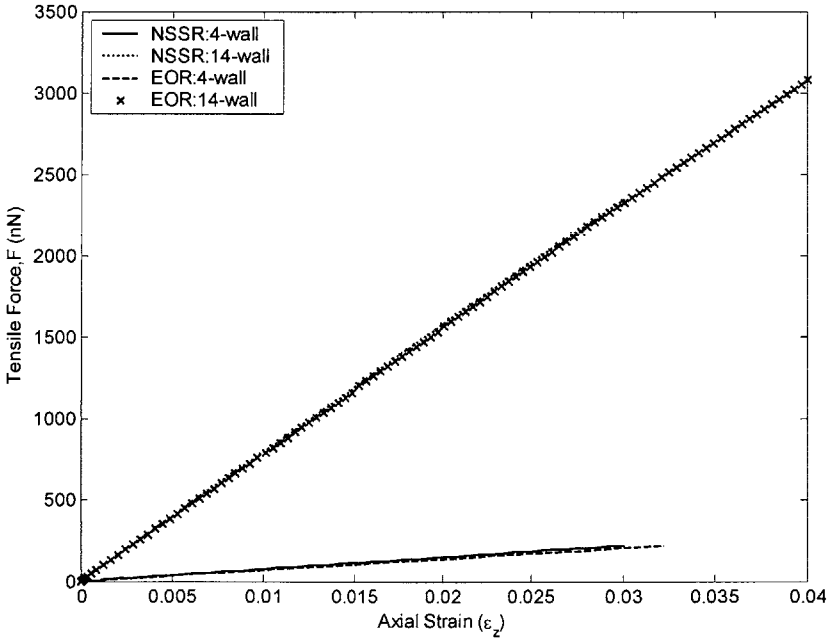

Figure 2.49: Tension force versus axial strain for 4- and 14-walled nested shell and EOR model used to derive Poisson curves.

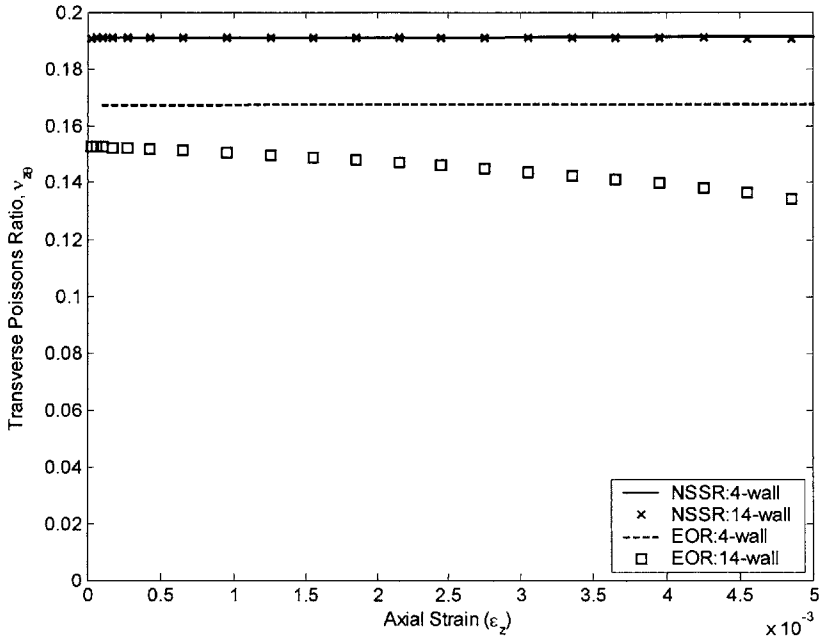

Figure 2.50: Compression test for 4- and 14-walled CNT using the nested shell and the EOR model $v_{z\theta} = [-(\delta R/R)/(\delta L/L)]$.

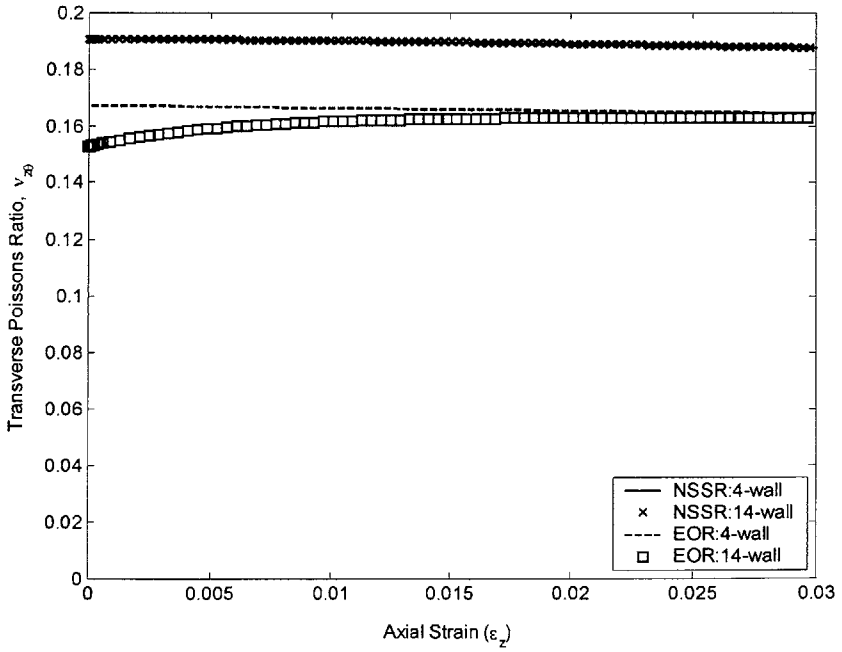

Figure 2.51: Tension test for 4- and 14-walled CNT using the nested shell and the EOR model $\nu_{z\theta} = [-(\delta R/R)/(\delta L/L)]$.

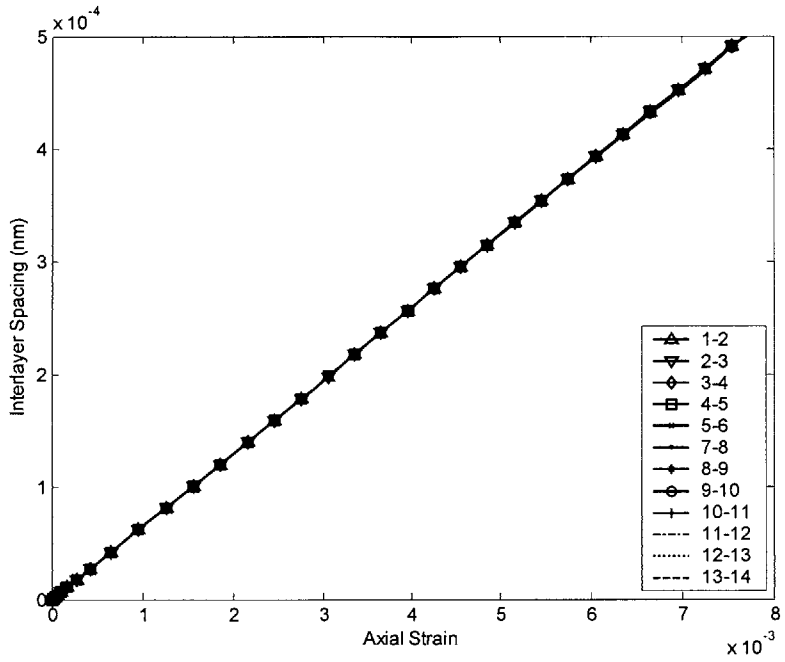

Figure 2.52: Interlayer spacing between adjacent walls versus compressive axial strain for 14-walled CNT. Innermost shell = 1 and outermost shell = 14.

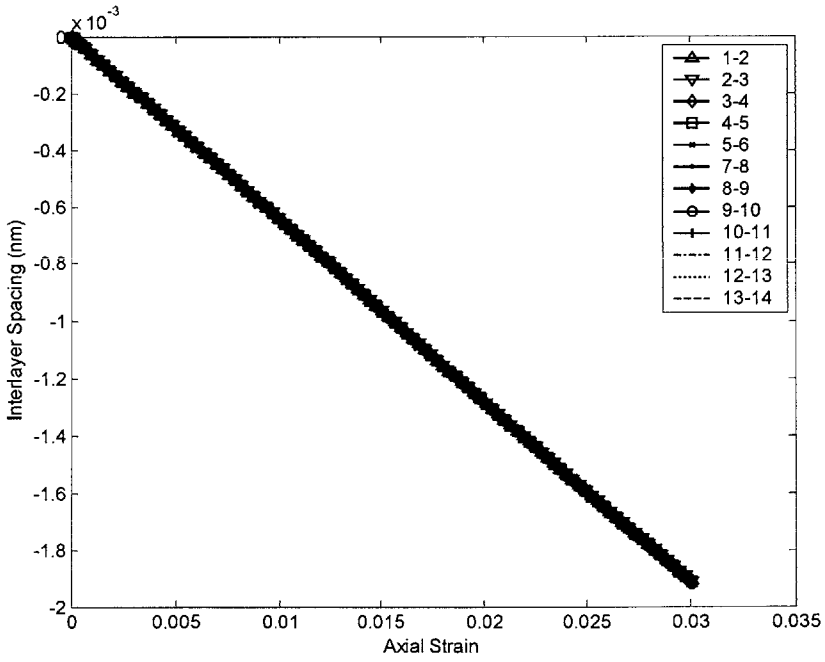

Figure 2.53: Interlayer spacing between adjacent walls versus tensile axial strain for 14-walled CNT. Innermost shell = 1 and outermost shell = 14.

We expected the Poisson ratio to drop with the increase in number of concentric tubes; however, the results for NSSR-based MWCNTs in Figures 2.50 and 2.51 show that the Poisson ratio is same for both 4- and 14-walled CNTs. This suggests that the interlayer spacing change linearly with axial strain, which is verified from the curves in Figures 2.51 and 2.52 for the 14-walled CNT. The interlayer spacing between the adjacent shell tubes changes linearly and similarly for all tubes within the 14-walled CNT.

2.5 Conclusions

In dealing with FE simulations of layered carbon nanotubes, a novel and time-efficient equivalent orthotropic solid model has been suggested. The proposed model is a compromise between computational efficiency and accuracy, and can be used for any number of concentric tubes in an MWCNT. The equivalent orthotropic material properties were derived from the material properties of the individual layers in the nested shell model (Pantano et al., 2004b). The properties for the isotropic graphene layer are taken to be E = 4.84 *TPa* and υ = 0.19. On the other hand, the space layer, whose effective modulus in the radial direction is derived from the LJ potential, is assumed to be anisotropic. Since the EOR model is based on the layered nested structure of thin shells, we assumed a negligible but finite shear modulus for the space layer of 0.48 *MPa* and υ = 0.19 – same as the graphite sheet. When actual shear modulus values (4.5 *GPa*) of graphite were used, the EOR model was observed to fail for the post buckling regime under buckling and bending. Because of the difference in the solid and shell elements used in FE simulations, the mesh size for the EOR model varies from that suggested by Pantano et al., (2004b) – 0.24 *nm*; as a result, the EOR model fails to predict the buckling of MWCNTs. However, when an appropriate element size is chosen based on thin shell theory, the EOR model is able to capture the complete deformation of the MWCNT. When compared with the nested shell models, the results indicated that the EOR models can be used to successfully simulate large MWCNTs subjected to bending, axial, and lateral compressions. Although the initial buckling wavelength was found to be

equivalent to that predicted by the nested shell model and experimental observations, the EOR model fails to capture the steady state buckling wavelength. For the EOR model, the buckling wavelength and amplitude were found to decrease and increase, respectively with deformation; Pantano et al., (2004b) reported otherwise. Since the steady state buckling of the EOR model is different than that of the NSSR model, the EOR model is inadequate when deformation of external surface features is important such as in electron transport theory in carbon nanotubes Pantano et al., (2004c). However, the proposed model could work very well in modeling such processes as nano-indentation and nano-scratching of vertically aligned carbon nanotubes (VACNT) forests with an AFM tip.

In brief, the equivalent orthotropic solid MWCNT model is a compromise between the computational efficiency and the accuracy of the results. The model is reliable when a quick structural behavioral study of MWCNTs is required.

Chapter 3

Vertically aligned carbon nanotubes (VACNT) have been a recent subject of intense investigation due to the numerous potential applications of VACNTs ranging from field emission and vacuum microelectronic devices, to the creation of super-hydrophobic surfaces, and as a source of well defined CNTs. Qi et al., (2003) suggested the nano-indentation process to estimate the effective mechanical properties of VACNTs and their constituent CNTs. The study of nano-indentation reveals a process whereby nanotubes are consecutively bent during the penetration of the indentor. Therefore, the resistance of a VACNT forest to penetration comes from the successive bending of nanotubes as the indentor encounters nanotubes. Qi et al., (2003) first proposed a micro-mechanical model that captures the nano-indentation process; using their model, the effective bending stiffness of the constituent nanotubes in the VACNT array was deduced from nano-indentation force-penetration depth curves. In this chapter, we propose a similar analytical method for nano-indentation tests to determine the mechanical properties of VACNTs and their constituent nanotubes. We proposed two micro-mechanical contact models: one that accounts for large deformations and another that simulates the buckling of nanotubes. The effectiveness of the analytical model of the MWCNT in predicting nonlinear deformations is then examined by comparing the results with nano- and macro-scale experiments and EOR-based finite element (FE) simulations of the previous chapter. Macro-scale experiments and FE-based models are used to check whether the proposed model captures the nonlinear deformation of MWCNTs. Thereafter, EOR-based FE models are used to include the buckling of nanotubes in the proposed micro-mechanical model. After including the critical observations from other researchers (e.g., Yakobson et al., 1996; Wong et al., 1997; and Pantano et al., 2003, 2004a, 2004b) and the FE-based models to the contact model, it was found that the micro-mechanical model adequately captures the buckling effects in the nano-indentation process. The proposed model was observed to capture the force-penetration curve of the constituent nanotubes in a VACNT sample obtained via nano-indentation. The proposed contact models are able to provide excellent predictions of such complex deformations, since it accounts for the nonlinear deformation and buckling of the MWCNTs. This new

technique requires no special treatment of the samples, making it possible to apply this method to a large number of tests to determine the statistical properties of CNTs, and as a potential quality control method in mass production (Qi et al., 2003).

3.1 Introduction

Currently the process of nano-indentation is being explored as a reliable means of determining the mechanical properties of carbon nanotubes and the constituent tubes of vertically aligned carbon nanotubes forests. Under indentation, each nanotube can be modeled as a cantilevered beam subjected to deflection from the penetration of the indentor. The resistance to indentation is the result of the cumulative bending of the VACNTs. Using beam theory, the effective bending stiffness is determined by fitting the mechanical model to the indentation force-penetration curves. Qi et al., (2003) used a sharp tip AFM tip to perform several nano-indentations on the VACNT forests and large-deflection beam theory to analytically model the nano-indentation process. In the past, many experimentalists (Wong et al., 1997, Salvetat et al., 1999) used the classic beam theory approach to determine mechanical properties of carbon nanotubes despite the fact that most experiments deflect the cantilevered CNTs to large deflections. On the other hand, Qi et al., (2003) in their nano-indentation contact model used large deformation beam theory that accounted for both the axial and lateral components of the load applied via the indentor tip; however, the second order curvature effects were ignored. The absence of any standardization in the use of various beam theories in the study of carbon nanotube mechanics motivated us to check the applicability of theory in the nano-indentation process.

This chapter first reviews beam theories including theoretical analysis of linear and of nonlinear deflections of cantilevered beams. Second, the analytical results from linear and nonlinear deflection theories are compared to experimental results for an MWCNT fixed at one end and deflected to large angles. Third, the appropriate beam theory is applied to nano-indentation of VACNT arrays, forest-like samples, as shown in

Figure 3.1. A discussion of the relevance of large deflection theory of cantilevered beams then concludes the chapter.

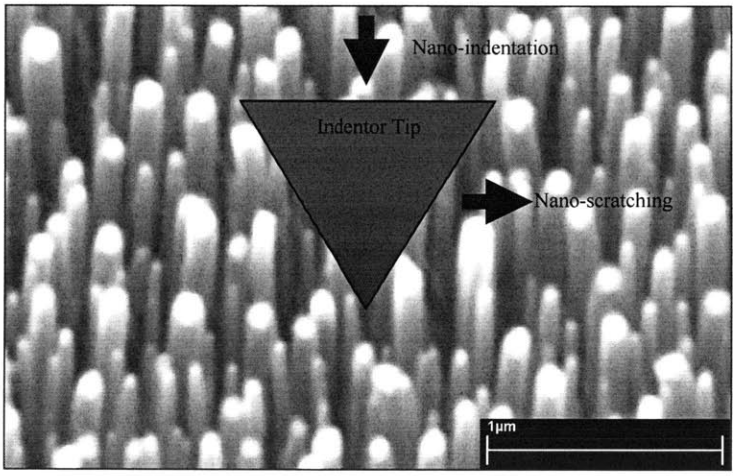

Figure 3.1: Indentor tip nano-indenting (down arrow) and nano-scratching (right arrow) in a vertically aligned carbon nanotubes (VACNT) sample (Qi et al., 2003).

3.2 Theoretical Analysis of Beam Bending

When investigating the deflections of a beam of bending stiffness (EI), an analysis usually begins with the Bernoulli-Euler law. According to this law, the curvature ($1/\rho$) at any point x along the length of the beam is proportional to the bending moment (M_b) at that section.

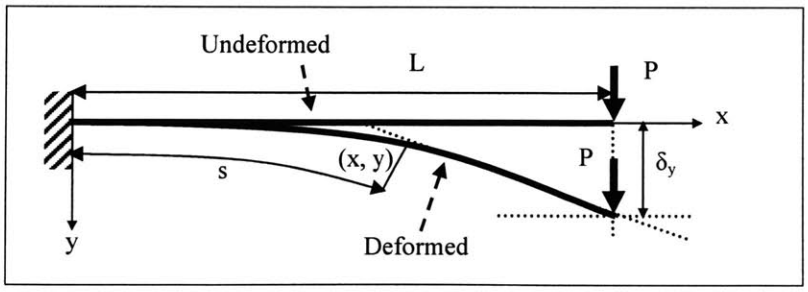

Figure 3.2: Cantilever beam loaded with an external concentrated load at the free end and parameters used for small deflections of the beam.

The mathematical representation

$$\frac{1}{\rho} = \frac{M_b}{EI} = \frac{d\phi}{ds} \tag{3.1}$$

is immediately applicable when the equation of the deflection curve is given in the intrinsic form $s = f(\varphi)$ where s is measured along the length of the arc and φ is the slope at s, as shown in Figure 3.2. In rectangular coordinates, the curvature is expressed as

$$\frac{1}{\rho} = -\frac{d^2y/dx^2}{\left[1+(dy/dx)^2\right]^{3/2}} \tag{3.2}$$

The negative sign can be explained by the fact that in assuming downward deflections as positive, an increase in x means a decrease in φ. The combination of Equations 3.1 and 3.2 results in a second order nonlinear differential equation when solved for the deflection y as a function of bending moment

$$\frac{d^2y/dx^2}{\left[1+(dy/dx)^2\right]^{3/2}} = -\frac{M_b}{EI}. \tag{3.3}$$

In classic beam theory, which assumes small deflections, the relationship between bending moment and curvature is linearized by neglecting the square of the slope, $(dy/dx)^2$, in comparison with unity in Equation 3.2. The governing linear equation that relates the M_b to the transverse displacement then takes the following form:

$$\frac{d^2y}{dx^2} = -\frac{M_b}{EI}. \tag{3.4}$$

Neglecting $(dy/dx)^2$, however, is not permissible for slender beams when the deflections are appreciable compared to the length. The second order term allows for the shortening of the lever arm during the deflection when a load is applied at the free end of a

cantilever beam. The classic theory is therefore not applicable for the calculation of large deflections. Moreover, the classic beam theory gives no solution for deflections in any direction other than the one normal to the original shape of the beam.

For the case of inclined load, P, applied to a cantilevered beam of length L at the free end such that tip deflection $\delta << L$, the moment contribution due to the horizontal component of the load (P_x) is ignored, as shown in Figure 3.3. This is because the equations are formulated considering fixed geometry (i.e., the moments are determined with respect to the original geometry and thus the moment from P_x is zero. However, as the beam deflects due to the bending moment at any x induced by P_y, the lateral deflection then also provides a moment contribution from P_x (Equation 3.5). Therefore, in the case of large deflection, two nonlinearities arise, one due to the curvature-deflection relation (Equation 3.2) and another due to the additional moment due to

$P_x(M_b = -P_x(\delta - y))$, as well as that due to $P_y\,(M_b = -P_y(L - x))$. (3.5)

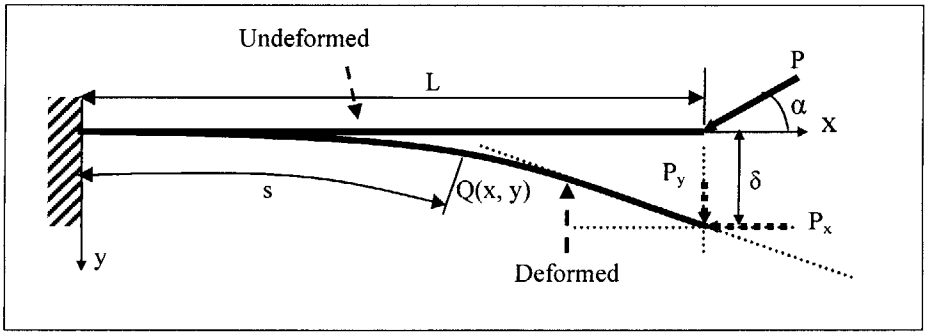

Figure 3.3: Cantilever beam loaded with an external concentrated load at the free end and parameters used for small deflections of the beam.

In this section, we compare and contrast linear versus nonlinear analysis of beam bending for the case of a cantilevered beam subjected to an inclined point load at the free end. Figure 3.4 shows a cantilever beam of length L with a concentrated load P inclined at an angle α, applied at the free end of the beam in undeformed and deformed configurations. In this figure δ_x and δ_y are the horizontal and vertical displacements at the free end, respectively, and ψ_o is the maximum slope of the beam at the free end. Also in

Figure 3.4, θ is the sum of ψ and α. Let the origin of the Cartesian coordinate system be at the fixed end of the beam, and let (x, y) be the coordinates of point Q, and s the arc length. Next, we present four cases where a concentrated load is applied normal or inclined at the free end of the cantilever beam considering small and large tip deflection.

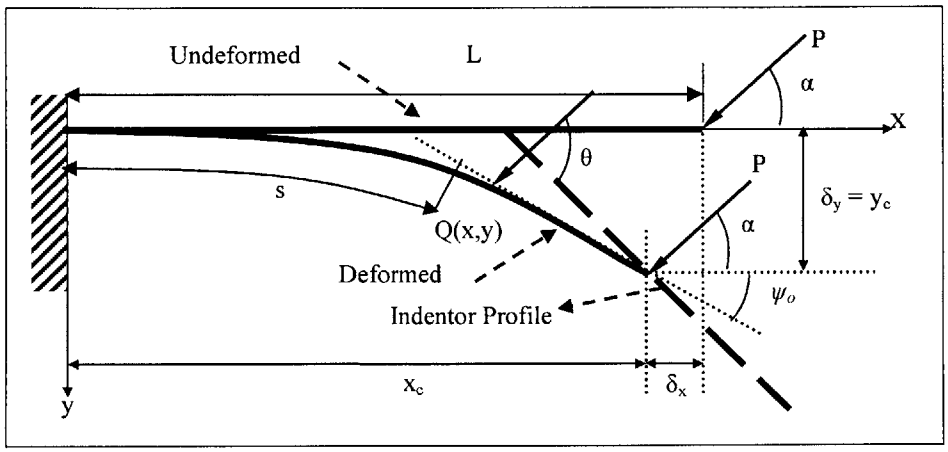

Figure 3.4: Cantilever beam loaded with an external concentrated inclined load at the free end and related parameters for large deflections.

3.2.1 Equations for Small Deformation of A Cantilevered Beam with A Concentrated Normal Load Applied at The Free End

For the case of small deformation, lateral tip deflection, bending moment, and stored strain energy (U) for a cantilever beam are derived by integrating the governing linear relationship, Equation 3.4, and geometric boundary conditions (Crandall et al., 1976). The load considered here is applied normal to the neutral axis ($\alpha = 90°$), as shown in Figure 3.2. The geometric boundary condition for the cantilevered beam are given by the following two conditions

$$y\big|_{x=0} = 0$$

$$\left.\frac{dy}{dx}\right|_{x=0} = 0. \tag{3.6}$$

The bending moment as a function of x is:

$$M_b = -P(L-x), \tag{3.7}$$

and then integrating Equation 3.4 and applying the boundary conditions in Equation 3.6 gives the following relationship for vertical tip deflection and slope:

$$\delta_y = \frac{PL^3}{3EI} \tag{3.8}$$

$$\frac{1}{\rho} = \frac{PL}{EI}. \tag{3.9}$$

Since the bending energy in a beam is given as

$$U = \int_0^L \frac{M_b^2}{2EI} dx. \tag{3.10}$$

Substituting Equation 3.7 in Equation 3.10 and solving the integral gives the required bending energy relation as follows:

$$U = \frac{P^2 L^3}{6EI}. \tag{3.11}$$

3.2.2 Equations for Large Deflection of A Cantilever Beam with A Concentrated Normal Load Applied at The Free End

The relevant equations for this case can be obtained by considering first a situation where a concentrated inclined load is applied at an angle α to the axis of the beam, as shown in Figure 3.5, and then substituting $\alpha = 90°$ (Fay, 1962).

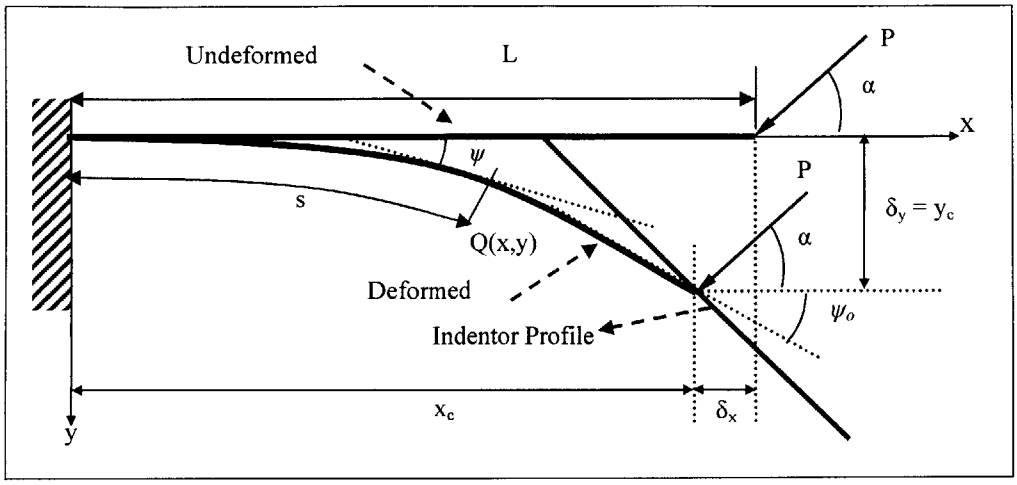

Figure 3.5: Cantilever beam loaded with an external concentrated inclined load at the free end and related parameters for large deflections; for normal load $\alpha = 90°$ in the above figure.

The Bending Moment at Q(x,y)

$$M_b = EI\frac{d\psi}{ds} = P\sin\alpha(x_c - x) + P\cos\alpha(y_c - y)\,. \tag{3.12}$$

Let,

$$\theta = \psi + \alpha\,. \tag{3.13}$$

Differentiating Equation 3.12 with respect to s and substituting Equation 3.13, we get

$$EI\frac{d^2\psi}{ds^2} = -P\sin\alpha\cos\psi - P\cos\alpha\sin\psi = -P\sin\theta \tag{3.14}$$

$$\sin\theta = \sin(\psi + \alpha) = \sin\alpha\cos\psi + \cos\alpha\sin\psi$$

Now let,

$$u = \frac{s}{L} \tag{3.15}$$

$$\therefore du = \frac{ds}{L}, \text{ and } d\theta = d\psi \tag{3.16}$$

$$\therefore \frac{d\theta}{du} = L\frac{d\psi}{ds} \tag{3.17}$$

$$\frac{d}{du}\left[\frac{d\psi}{ds}\right]L = \frac{d}{ds}\left[\frac{d\psi}{ds}\right]L\frac{ds}{du} = \frac{d^2\psi}{ds^2}L^2 \tag{3.18}$$

$$\frac{d^2\psi}{ds^2} = \frac{1}{L^2}\frac{d^2\theta}{du^2}. \tag{3.19}$$

Substituting Equation 3.19 into Equation 3.14 gives

$$\frac{EI}{L^2}\frac{d^2\theta}{du^2} + P\sin\theta = 0. \tag{3.20}$$

Next let

$$k^2 = \frac{P}{EI}, \text{ and} \tag{3.21}$$

$$c = \frac{PL^2}{EI} = L^2k^2. \tag{3.22}$$

Rearranging Equation 3.20 and substituting into Equations 3.21 and 3.22 gives

$$\frac{d^2\theta}{du^2} + c\sin\theta = 0. \tag{3.23}$$

Boundary Conditions

$$(\psi)_{s=0} = 0 \qquad \text{(or)} \qquad (\theta)_{u=0} = \alpha \tag{3.24}$$

$$\left(\frac{d\psi}{ds}\right)_{s=L} = 0 \qquad \text{(or)} \qquad \left(\frac{d\theta}{du}\right)_{\theta=\psi_0+\alpha} = 0 \tag{3.25}$$

Multiplying both sides of Equation 3.23 by $2d\theta$ and integrating, we get

$$\int\left[2\frac{d^2\theta}{du^2}d\theta + 2c\sin\theta.d\theta\right] = 0 \tag{3.26}$$

$$\left[\frac{d\theta}{du}\right]^2 = 2c\left[\cos\theta - \cos(\psi_0 + \alpha)\right] \tag{3.27}$$

$$\therefore \left[\frac{d\theta}{du}\right] = \left[2c\{\cos\theta - \cos(\psi_0 + \alpha)\}\right]^{\frac{1}{2}}. \tag{3.28}$$

Now solving for du in Equation 3.17 and equating to Equation 3.16, and then substituting Equation 3.28 gives

$$du = \frac{ds}{L} = \frac{d\psi}{\left(d\theta/du\right)} = \frac{d\theta}{\left[2c\{\cos\theta - \cos(\psi_0 + \alpha)\}\right]^{\frac{1}{2}}}. \tag{3.29}$$

Solving Equation 18 for ds, we get

$$ds = \frac{Ld\theta}{\left[2c\{\cos\theta - \cos(\psi_0 + \alpha)\}\right]^{\frac{1}{2}}}. \tag{3.30}$$

Integrating both sides of Equation 3.30 and taking limits from α to $(\psi_0 + \alpha)$, we get

$$\int_{\alpha}^{(\psi_0+\alpha)} ds = \frac{L}{2c}\int_{\alpha}^{(\psi_0+\alpha)} \frac{d\theta}{\left[\cos\theta - \cos(\psi_0 + \alpha)\right]^{\frac{1}{2}}}. \tag{3.31}$$

Solving the above equation, we get

$$L = \frac{L}{2c}\int_{\alpha}^{(\psi_0+\alpha)} \frac{d\theta}{\left[\cos\theta - \cos(\psi_0 + \alpha)\right]^{\frac{1}{2}}}. \tag{3.32}$$

Applying integration limit property, we write Equation 3.32 as

$$1=\frac{1}{\sqrt{2c}}\left\{-\int_{0}^{\alpha}\frac{d\theta}{[\cos\theta-\cos(\psi_0+\alpha)]^{\frac{1}{2}}}+\int_{0}^{(\psi_0+\alpha)}\frac{d\theta}{[\cos\theta-\cos(\psi_0+\alpha)]^{\frac{1}{2}}}\right\}. \tag{3.33}$$

Next, using trigonometric identities, we rewrite the above equation as,

$$1=\frac{1}{2\sqrt{c}}\left\{-\int_{0}^{\alpha}\frac{d\theta}{[\sin^2\{(\psi_0+\alpha)/2\}-\sin^2\{\theta/2\}]^{\frac{1}{2}}}+\int_{0}^{(\psi_0+\alpha)}\frac{d\theta}{[\sin^2\{(\psi_0+\alpha)/2\}-\sin^2\{\theta/2\}]^{\frac{1}{2}}}\right\} \tag{3.34}$$

Next let,

$$p=\sin\{(\psi_0+\alpha)/2\}, \text{ and} \tag{3.35}$$

$$p\sin\phi=\sin\{\theta/2\}. \tag{3.36}$$

Now differentiating both sides of Equation 3.36, we get

$$p\cos\phi d\phi=\frac{1}{2}\cos(\theta/2)d\theta. \tag{3.37}$$

Rearranging Equation 3.37 and using trigonometric identities, we get

$$d\theta=\frac{2p\cos\phi d\phi}{\cos(\theta/2)}=\frac{2p\cos\phi d\phi}{\sqrt{1-\sin^2(\theta/2)}}=\frac{2p\cos\phi d\phi}{\sqrt{1-p^2\sin^2\phi}}. \tag{3.38}$$

Since,

$$\theta\big|_{x=0}=\alpha \tag{3.39}$$

else,

$$\theta\big|_{x=L} = \psi_0 + \alpha\,, \tag{3.40}$$

substituting Equation 3.39 into Equation 3.36, and assuming it to be equal to a variable m, we get

$$m = \phi = \sin^{-1}\left[\frac{\sin(\alpha/2)}{p}\right]; \text{ for } x = 0\,. \tag{3.41}$$

Alternatively, substituting Equations 3.35 and 3.40 yields

$$\phi = \sin^{-1}\left[\frac{\sin\{(\psi_0 + \alpha)/2\}}{p}\right] = \frac{\pi}{2}\,. \tag{3.42}$$

Next, substituting Equations 3.35, 3.36, 3.38, 3.41, and 3.42 in Equation 3.34, we get

$$1 = \frac{1}{2\sqrt{c}}\left\{-\int_0^m \frac{\left(\frac{2p\cos\phi d\phi}{\sqrt{1-p^2\sin^2\phi}}\right)}{\left[p^2 - p^2\sin^2\phi\right]^{\frac{1}{2}}} + \int_0^{\frac{\pi}{2}} \frac{\left(\frac{2p\cos\phi d\phi}{\sqrt{1-p^2\sin^2\phi}}\right)}{\left[p^2 - p^2\sin^2\phi\right]^{\frac{1}{2}}}\right\}. \tag{3.43}$$

Simplifying Equation 3.43 further gives

$$1 = \frac{1}{\sqrt{c}}\left\{\int_0^{\frac{\pi}{2}} \frac{d\phi}{\left[1-p^2\sin^2\phi\right]^{\frac{1}{2}}} - \int_0^m \frac{d\phi}{\left[1-p^2\sin^2\phi\right]^{\frac{1}{2}}}\right\}. \tag{3.44}$$

Now applying trigonometric identity and Equation 3.38, we write Equation 3.30 as

$$ds = \frac{L\left[\dfrac{2p\cos\phi d\phi}{\sqrt{1-p^2\sin^2\phi}}\right]}{2\sqrt{c}\left[\sin^2\{(\psi_0+\alpha)/2\}-\sin^2\{\theta/2\}\right]^{\frac{1}{2}}}. \tag{3.45}$$

Substitute Equations 3.35 and 3.36 in Equation 3.45 to get

$$ds = \frac{L\left[\dfrac{2p\cos\phi d\phi}{\sqrt{1-p^2\sin^2\phi}}\right]}{\sqrt{c}\left[p^2-p^2\sin^2\phi\right]^{\frac{1}{2}}}. \tag{3.46}$$

Substituting Equation 3.22 into Equation 3.46 and simplifying, we write *ds* as

$$ds = \frac{d\phi}{k\left[1-p^2\sin^2\phi\right]^{\frac{1}{2}}}. \tag{3.47}$$

From Figure 3.4,

$$\frac{dx}{ds} = \cos\psi \text{ , and } \frac{dy}{ds} = \sin\psi . \tag{3.48}$$

Substitute Equations 3.13 and 3.47 in left equation in Equation 3.48 to get

$$dx = \frac{\cos(\theta-\alpha)d\phi}{k\sqrt{1-p^2\sin^2\phi}}. \tag{3.49}$$

Recall the trigonometric identity,

$$\cos(\theta-\alpha) = \cos\theta\cos\alpha + \sin\theta\sin\alpha . \tag{3.50}$$

Then, using Equations 3.35 and 3.36, we get

$$\sin\theta = 2\sin(\theta/2)\cos(\theta/2) = 2\sin(\theta/2)\sqrt{1-\sin^2(\theta/2)} = 2p\sin\phi\sqrt{1-p^2\sin^2\phi}\,, \quad (3.51)$$

$$\cos\theta = 1-2\sin^2(\theta/2) = 1-2p^2\sin^2\phi\,. \quad (3.52)$$

Now, substitute Equations 3.50, 3.51, and 3.52 in Equation 3.49 to get

$$dx = \frac{(\cos\theta\cos\alpha + \sin\theta\sin\alpha)d\phi}{k\sqrt{1-p^2\sin^2\phi}}, \quad (3.53)$$

$$dx = \frac{(1-2p^2\sin^2\phi)\cos\alpha d\phi}{k\sqrt{1-p^2\sin^2\phi}} + \frac{2p\sin\phi\sqrt{1-p^2\sin^2\phi}\sin\alpha d\phi}{k\sqrt{1-p^2\sin^2\phi}}. \quad (3.54)$$

Simplifying Equation 3.54 further, we get

$$dx = \frac{\cos\alpha}{k}\left[\frac{d\phi}{\sqrt{1-p^2\sin^2\phi}} - \frac{2p^2\sin^2\phi d\phi}{\sqrt{1-p^2\sin^2\phi}}\right] + \frac{\sin\alpha}{k}2p\sin\phi d\phi\,. \quad (3.55)$$

Integrating both sides of the above equation and taking the limit from m to n, we get

$$x = \frac{1}{k}\left[\cos\alpha\{F(p,m) - F(p,n) + 2E(p,n) - 2E(p,m)\} + 2p\sin\alpha(\cos m - \cos n)\right] \quad (3.56)$$

where, m is from Equation 3.41, and

$$n = \sin^{-1}\left[\frac{\sin\{(\psi+\alpha)/2\}}{p}\right], \quad (3.57)$$

$$F(p,m) = \int_0^m \frac{d\phi}{\left[1-p^2\sin^2\phi\right]^{\frac{1}{2}}}, \quad (3.58)$$

$$F(p,n)=\int_0^n \frac{d\phi}{\left[1-p^2\sin^2\phi\right]^{\frac{1}{2}}}, \tag{3.59}$$

$$E(p,m)=\int_0^m \left[1-p^2\sin^2\phi\right]^{\frac{1}{2}} d\phi, \tag{3.60}$$

$$E(p,n)=\int_0^n \left[1-p^2\sin^2\phi\right]^{\frac{1}{2}} d\phi. \tag{3.61}$$

Since at the free end of the cantilever beam, $\psi=\psi_0 \Rightarrow n=\frac{\pi}{2}$, Equation 3.56 becomes,

$$x_c = L-\delta_x = \frac{1}{k}\left[\cos\alpha\{F(p,m)-K(p)+2E(p)-2E(p,m)\}+2p\sin\alpha\cos m\right] \tag{3.62}$$

where,

$$K(p)=\int_0^{\frac{\pi}{2}} \frac{d\phi}{\left[1-p^2\sin^2\phi\right]^{\frac{1}{2}}}, \tag{3.63}$$

$$E(p)=\int_0^{\frac{\pi}{2}} \left[1-p^2\sin^2\phi\right]^{\frac{1}{2}} d\phi, \tag{3.64}$$

Note: $F(p,m), F(p,n), K(p)$ are 'complete elliptic integrals of the first kind,' whereas, $E(p,m), E(p,n), E(p)$ are the 'complete elliptic integrals of the second kind.'

Next, using Equations 3.48 and 3.50 to 3.52 and simplifying, we get

$$dy=\frac{(\sin\theta\cos\alpha-\cos\theta\sin\alpha)d\phi}{k\sqrt{1-p^2\sin^2\phi}}, \tag{3.65}$$

$$dy = \frac{2p\sin\phi\sqrt{1-p^2\sin^2\phi}\cos\alpha.d\phi}{k\sqrt{1-p^2\sin^2\phi}} - \frac{(1-2p^2\sin^2\phi)\sin\alpha.d\phi}{k\sqrt{1-p^2\sin^2\phi}}, \tag{3.66}$$

$$dy = \frac{\cos\alpha}{k}2p\sin\phi d\phi - \frac{\sin\alpha}{k}\left[\frac{d\phi}{\sqrt{1-p^2\sin^2\phi}} - \frac{2p^2\sin^2\phi d\phi}{\sqrt{1-p^2\sin^2\phi}}\right]. \tag{3.67}$$

Integrating both sides of Equation 3.67 and taking the limit from m to n as in Equation 3.56, we get

$$y = \frac{1}{k}[2p\cos\alpha(\cos m - \cos n) - \sin\alpha\{F(p,m) - F(p,n) + 2E(p,n) - 2E(p,m)\}]. \tag{3.68}$$

Again for the free end of the cantilever beam, $\psi = \psi_0 \Rightarrow n = \frac{\pi}{2}$; therefore, Equation 3.68 becomes

$$y_c = \delta_y = \frac{1}{k}[2p\cos\alpha\cos m - \sin\alpha\{F(p,m) - K(p) + 2E(p) - 2E(p,m)\}]. \tag{3.69}$$

Rearranging Equations 3.22, 3.44, 3.58, and 3.63, we get the following relation,

$$L = \frac{1}{k}[K(p) - F(p,m)]. \tag{3.70}$$

Bending Moment and Curvature at the fixed end

We can solve for bending moment at any point Q in the beam by first solving for $(d\psi/ds)$ from Equations 3.17 and 3.28, and then substituting the result into Equation 3.12

$$M_b = \frac{EI}{L}\sqrt{2c(\cos\theta - \cos(\psi_o + \alpha))}. \tag{3.71}$$

Next, bending moment at the fixed end of the beam can be evaluated by substituting Equation 3.13 in the above equation as

$$M_b\big|_{\substack{x=0\\ \psi=0}} = \frac{EI}{L}\sqrt{2c\left(\cos\alpha - \cos(\psi_o + \alpha)\right)}\,. \tag{3.72}$$

Also substituting Equation 3.72 in Equation 3.1, we get the curvature at the fixed end as

$$\frac{1}{\rho}\bigg|_{\substack{x=0\\ \psi=0}} = \frac{1}{L}\sqrt{2c\left(\cos\alpha - \cos(\psi_o + \alpha)\right)}\,. \tag{3.73}$$

Next, substitute Equations 3.21 and 3.22 into both Equations 3.72 and 3.73, to get

$$M_b\big|_{\substack{x=0\\ \psi=0}} = EI\sqrt{\frac{2P}{EI}\left(\cos\alpha - \cos(\psi_o + \alpha)\right)} \tag{3.74}$$

$$\frac{1}{\rho}\bigg|_{\substack{x=0\\ \psi=0}} = \sqrt{\frac{2P}{EI}\left(\cos\alpha - \cos(\psi_o + \alpha)\right)}\,. \tag{3.75}$$

Strain Energy due to Bending

Substitute $M_b = (EI)/\rho$ from Equation 3.1 into Equation 3.10, to get

$$dU = \frac{EI}{2\rho^2}ds\,. \tag{3.76}$$

Substitute Equations 3.21, 3.70 and 3.75 into 3.76 and rewrite as follows

$$dU = P\{\cos\theta - \cos(\psi_o + \alpha)\}ds \tag{3.77}$$

$$U = P\int_{\alpha}^{(\psi_o+\alpha)}\{\cos\theta - \cos(\psi_o + \alpha)\}ds\,. \tag{3.78}$$

Thereafter, substituting Equations 3.20, 3.21, and 3.30 into Equation 3.78, we get

$$U = \frac{P}{k\sqrt{2}} \int_{\alpha}^{(\psi_o+\alpha)} \sqrt{\{\cos\theta - \cos(\psi_o + \alpha)\}}\, d\theta \tag{3.79}$$

$$U = \frac{P}{k\sqrt{2}} \left[\int_{0}^{(\psi_o+\alpha)} \sqrt{\{\cos\theta - \cos(\psi_o + \alpha)\}}\, d\theta - \int_{0}^{\alpha} \sqrt{\{\cos\theta - \cos(\psi_o + \alpha)\}}\, d\theta \right]. \tag{3.80}$$

Applying trigonometry identity, Equation 3.52 into Equation 3.80, we get

$$U = \frac{P}{k} \left[\int_{0}^{(\psi_o+\alpha)} \sqrt{\left\{ \sin^2\left(\frac{(\psi_o + \alpha)}{2}\right) - \sin^2\left(\frac{\theta}{2}\right) \right\}}\, d\theta - \int_{0}^{\alpha} \sqrt{\left\{ \sin^2\left(\frac{(\psi_o + \alpha)}{2}\right) - \sin^2\left(\frac{\theta}{2}\right) \right\}}\, d\theta \right]. \tag{3.81}$$

Substituting Equations 3.35, 3.36, 3.38, 3.41, and 3.42 into Equation 3.81, gives

$$U = \frac{P}{k} \left[\int_{0}^{\pi/2} \sqrt{\{p^2 - p^2 \sin^2\phi\}} \frac{2p\cos\phi}{\sqrt{1 - p^2\sin^2\phi}}\, d\phi - \int_{0}^{m} \sqrt{\{p^2 - p^2 \sin^2\phi\}} \frac{2p\cos\phi}{\sqrt{1 - p^2\sin^2\phi}}\, d\phi \right]. \tag{3.82}$$

Simplifying using basic trigonometric identity $\sin^2\theta + \cos^2\theta = 1$, we get

$$U = \frac{2P}{k} \left[\int_{0}^{\pi/2} \frac{(p^2 - p^2\sin^2\phi)}{\sqrt{1 - p^2\sin^2\phi}}\, d\phi - \int_{0}^{m} \frac{(p^2 - p^2\sin^2\phi)}{\sqrt{1 - p^2\sin^2\phi}}\, d\phi \right] \tag{3.83}$$

$$U = \frac{2P}{k} \left[\int_{0}^{\pi/2} \frac{\{(1 - p^2\sin^2\phi) - 1 + p^2\}}{\sqrt{1 - p^2\sin^2\phi}}\, d\phi - \int_{0}^{m} \frac{\{(1 - p^2\sin^2\phi) - 1 + p^2\}}{\sqrt{1 - p^2\sin^2\phi}}\, d\phi \right] \tag{3.84}$$

$$U = \frac{2P}{k} \left[\int_{0}^{\pi/2} \sqrt{1 - p^2\sin^2\phi}\, d\phi - (1 - p^2) \int_{0}^{\pi/2} \frac{d\phi}{\sqrt{1 - p^2\sin^2\phi}} \right.$$

$$\left. - \int_{0}^{m} \sqrt{1 - p^2\sin^2\phi}\, d\phi + (1 - p^2) \int_{0}^{m} \frac{d\phi}{\sqrt{1 - p^2\sin^2\phi}} \right]. \tag{3.85}$$

Next, substituting Equations 3.58, 3.60, 3.63, and 3.64 in Equation 3.85, we get

$$U = \frac{2P}{k}\left[\{E(p) - E(p,m)\} - \left(1 - p^2\right)\{K(p) - F(p,m)\}\right]. \tag{3.86}$$

Finally, substitute α = 90° in Equations 3.41, we get the required equations for a cantilever beam subjected to large deflection on applying a transverse load at the free end

$$m = \sin^{-1}\left(\frac{1}{p\sqrt{2}}\right). \tag{3.87}$$

From Equation 3.87 and trigonometric identity $\sin^2\theta + \cos^2\theta = 1$, we get

$$\cos m = \sqrt{\frac{2p^2 - 1}{2p^2}}, \tag{3.88}$$

and substituting Equation 3.88 and α = 90° into Equation 3.62, to get

$$x_c = L - \delta_x = \left[\frac{2EI\left(2p^2 - 1\right)}{P}\right]^{\frac{1}{2}}. \tag{3.89}$$

Similarly, substituting α = 90° in Equation 3.69 gives

$$y_c = \delta_y = \frac{1}{k}\left[K(p) - F(p,m) - 2E(p) + 2E(p,m)\right]. \tag{3.90}$$

Now, using trigonometric identity $\sin(a+b) = \sin a\cos b + \cos a\sin b$ in Equation 3.35

$$p = \sin\left(\frac{\left(\psi_o + \alpha\right)}{2}\right) = \frac{1}{\sqrt{2}}\left(\sin\left(\frac{\psi_o}{2}\right) + \cos\left(\frac{\psi_o}{2}\right)\right). \tag{3.91}$$

Squaring both sides of Equation 3.91, then using trig. identity $\sin^2\theta + \cos^2\theta = 1$, we get

$$p = \sqrt{\frac{(1+\sin\psi_o)}{2}}. \tag{3.92}$$

The bending moment (M_b), the curvature ($1/\rho$), and the corresponding strain energy (U) can also be solved for the case where load is applied normally at the end of the beam by substituting $\alpha = 90°$ in Equations 3.74, 3.85, and 3.86 as

$$M_b\Big|_{\substack{x=0\\ \psi=0}} = EI\left[\frac{2P\sin\psi_o}{EI}\right]^{\frac{1}{2}} \tag{3.93}$$

$$\frac{1}{\rho}\Big|_{\substack{x=0\\ \psi=0}} = \left[\frac{2P\sin\psi_o}{EI}\right]^{\frac{1}{2}} \tag{3.94}$$

$$U = \frac{2P}{k}\left[\{E(p)-E(p,m)\}-(1-p^2)\{K(p)-F(p,m)\}\right]. \tag{3.95}$$

Next, we will show that Equations 3.93 and 3.94 reduce to Equations 3.7 and 3.9 at $x = 0$, respectively, when we assume small tip deflections ($\delta_x \approx 0$). First Equation 3.93 can be written as

$$M_b\Big|_{\substack{x=0\\ \psi=0}} = P\left[\frac{2EI\sin\psi_o}{P}\right]^{\frac{1}{2}} \tag{3.96}$$

Equation 3.96 then can be written as

$$M_b\Big|_{\substack{x=0\\ \psi=0}} = P\left[\frac{2EI}{P}\left(2\left(\frac{1+\sin\psi_o}{2}\right)-1\right)\right]^{\frac{1}{2}}. \tag{3.97}$$

Thereafter, substitute Equation 3.92 in Equation 3.97 and simplifying gives

$$M_b\Big|_{\substack{x=0\\ \psi=0}} = P\left[\frac{2EI}{P}\left(2p^2-1\right)\right]^{\frac{1}{2}}. \tag{3.98}$$

Substituting Equation 3.89 in Equation 3.98, we get

$$M_b\Big|_{\substack{x=0\\ \psi=0}} = PL. \tag{3.99}$$

Equation 3.99 is same as Equation 3.7 for zero axial deflection ($\delta_x \approx 0$). Now, since Equation 3.94 is obtained by dividing Equation 3.93 by *EI*, we obtain Equation 3.9 by dividing Equation 3.99 by *EI*, we get

$$\frac{1}{\rho}\Big|_{\substack{x=0\\ \psi=0}} = \frac{PL}{EI}. \tag{3.100}$$

Next, we compare the linear and nonlinear numerical solutions of a cantilever beam with a concentrated load applied normal to the beam in order to determine whether the difference is appreciable.

The difference between the analytical solutions of linear and nonlinear deflection equations for concentrated load applied normal to the axis of the beam is presented graphically in non-dimensional terms as PL^2/EI as a function of (δ_y/L), as shown in Figure 3.5. In order to present the non-dimensionalized diagrams, linear and nonlinear equations are rearranged as follows:

$$\frac{PL^2}{EI} = 3\left(\frac{\delta_y}{L}\right) \text{ for the linear case and} \tag{3.101}$$

$$\frac{PL^2}{EI} = \left(\frac{\delta_y}{L}\right)^{-2}\left[K(p)-F(p,m)-2E(p)+2E(p,m)\right]^2 \text{ for the nonlinear case.} \tag{3.102}$$

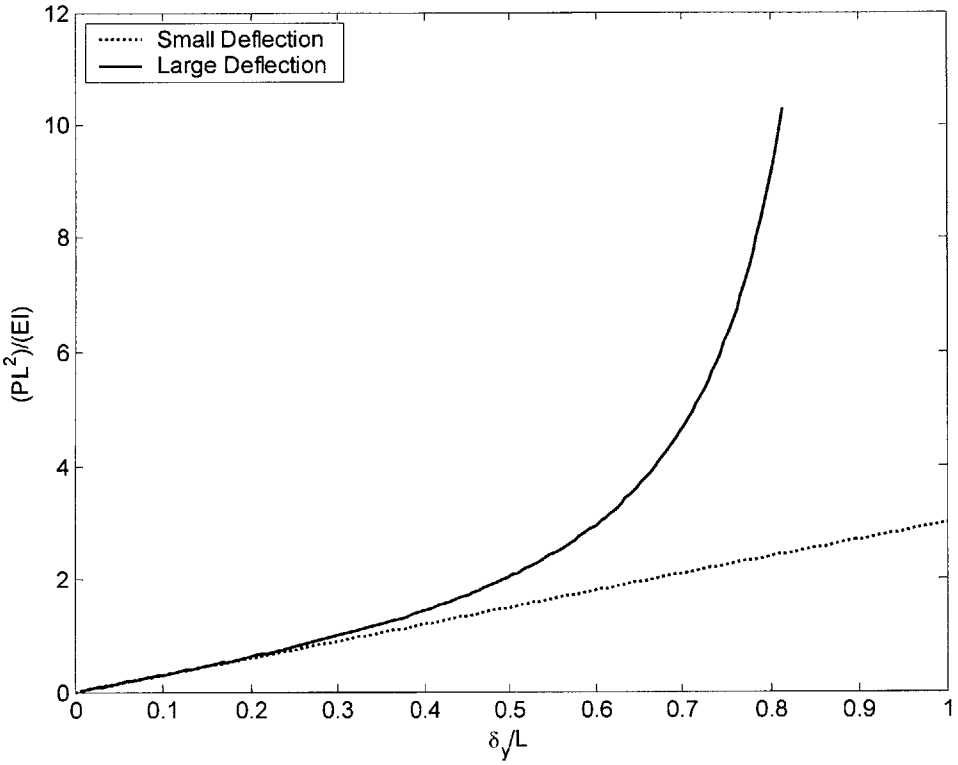

Figure 3.6: Non-dimensional load versus non-dimensional lateral tip displacement for cantilevered beam loaded with an external concentrated normal load at the free end.

Figure 3.6 clearly show the difference between the results of the classic beam theory for small deformation of a cantilevered beam to the large deformation, where a concentrated normal load is applied at the free end; the classic beam theory show linear behavior even for large deflections while the nonlinear curve starts to deviate for lateral tip deflection, δ_y, is greater than $0.6*L$.

We next present the nonlinear large deflection equations one that accounts both the axial and vertical components of load in the deformed configuration (Qi et al., 2003) and the other that also accounts for the nonlinear differential relationship between curvature and deflection (Fay, 1962).

3.2.3 Equations for Large Deformation of A Cantilevered Beam with A Concentrated Inclined Load at The Free End – (Qi et al., 2003)

Qi et al. (2003) solved the governing differential equation (Equation 3.4) of the beam theory and related the bending deflection to the axial and lateral force components of the inclined load applied by the indentor tip, as shown in Figure 3.7. In Qi et al., (2003), the applied load is always normal to the indentor surface since there is no friction between the CNT and the indentor. Therefore, the relationship between the x and y load components is develop: $F_x / F_y = P.tan(\theta_{indentor})$. Qi et al., (2003) applied this relation in their derivation of the nonlinear equations, as shown below.

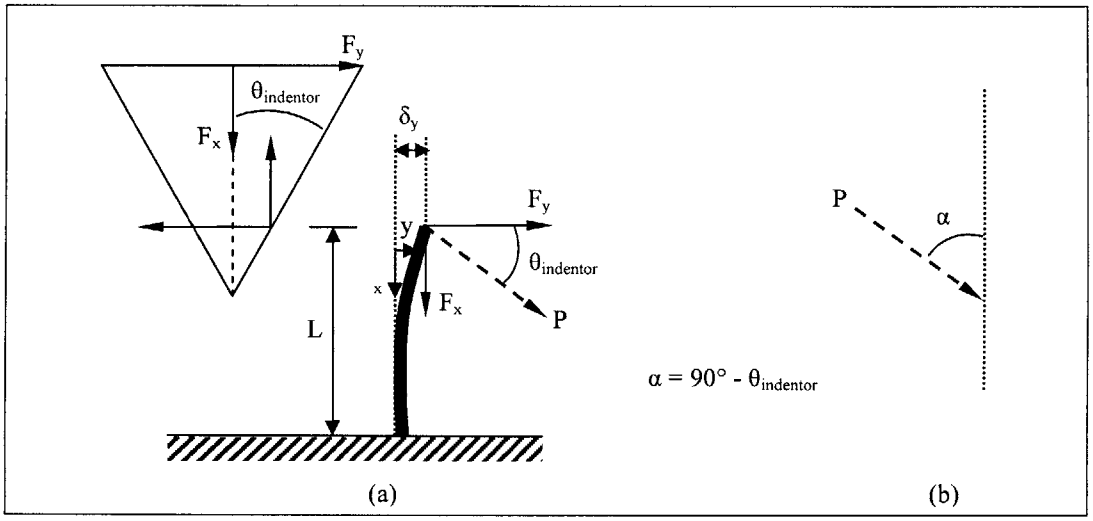

Figure 3.7: Cantilever beam loaded with an external concentrated inclined load at the free end and related parameters for small deflections (a) (Qi et al., 2003). To be consistent with the previous notation, applied inclined load can be represented as shown in (b).

The bending moment at any point x along the beam in Figure 3.7-a is

$$M_b = -F_y x - F_x(\delta_y - y) \tag{3.103}$$

Now substitute Equation 3.103 in Equation 3.4, to obtain the relationship between moment and curvature as follows

$$(EI)\frac{d^2y}{dx^2} = F_y x + F_x(\delta_y - y). \tag{3.104}$$

This differential equation is thus formulated in the deformed configuration and thus accounts for the effect of large deflections on the bending moment represented by the beam; however, it does not account for the nonlinear differential relationship between curvature and deflection.

$$y\big|_{x=L} = 0 \quad \text{and} \quad \left.\frac{dy}{dx}\right|_{x=L} = 0. \tag{3.105}$$

Next, assuming $k^2 = F_x/(EI)$ and $Y = \delta_y - y$, Equations 3.104 and 3.105 can be written as

$$\frac{d^2Y}{dx^2} + k^2 y = -\frac{F_y x}{EI}, \tag{3.106}$$

with boundary conditions

$$Y\big|_{x=0} = 0 \quad \text{and} \quad \left.\frac{dY}{dx}\right|_{x=L} = 0. \tag{3.107}$$

The general solution to Equation 3.106 is

$$Y = A\cos kx + B\sin kx - \frac{F_y}{F_x}x, \tag{3.108}$$

where A and B are constants determined from Equation 3.108 as follows

$$A = 0 \quad \text{and} \quad B = \frac{F_y}{F_x k\cos kL}. \tag{3.109}$$

Therefore,

$$y = \delta_y - \frac{F_y}{F_x k \cos kL} \sin kx + \frac{F_y}{F_x} x . \tag{3.110}$$

Since $y\big|_{x=L} = 0$,

$$\delta_y = \frac{F_y}{F_x}\left(\frac{\tan kL}{k} - L\right), \tag{3.111}$$

and Equation 3.110 is rewritten as

$$y = \frac{F_y}{F_x k \cos kL}(\sin kL - \sin kx) - \frac{F_y}{F_x}(L - x). \tag{3.112}$$

The slope of the beam deformation is $-y'$, and

$$y' = \frac{F_y}{F_x}\left(1 - \frac{\cos kx}{\cos kL}\right). \tag{3.113}$$

The fact that the slope y' cannot exceed the slope of the indentor's side surface (Figure 3.10-a), or

$$-y' < \tan\theta_{indentor} . \tag{3.114}$$

Since there is no friction between the CNT and the indentor, the horizontal and vertical components of the inclined load P can be written as

$$F_x = P \sin\theta_{indentor} = P \cos\alpha \tag{3.115}$$

$$F_y = P\cos\theta_{indentor} = P\sin\alpha\,. \tag{3.116}$$

Therefore, Equation 3.104 can be written as

$$\delta_y = \tan\alpha\left(\frac{\tan kL}{k} - L\right), \tag{3.117}$$

where k then becomes

$$k = \sqrt{\frac{P\cos\alpha}{EI}}\,. \tag{3.118}$$

Next, the expression for strain energy due to bending is obtained by substituting the bending moment equation (Equation 3.103) into the integral bending energy formula

$$U = \left[\frac{\sin^2\alpha}{4kL\cos\alpha}\right]\left[\frac{kL - \sin(kL)\cos(kL)}{\cos^2(kL)}\right]. \tag{3.119}$$

Recall that this approach accounts for the axial component of the inclined load P; however, the higher order term in Equation 3.2 is assumed negligible. Therefore, there is a need for a set of nonlinear equations that takes both the axial component of the applied load P and the second order term in Equation 3.2 into account.

3.2.4 Equations for Large Deformation of A Cantilevered Beam with A Concentrated Inclined Load at The Free End – (Fay, 1962)

For large cantilevered beam deflections with an inclined load P, as shown in Figure 3.8, the differential equations can be solved and expressed in terms of elliptic integrals. The required expressions were derived earlier in Section 3.2.2, where Equations 3.62 and 3.69 are solved for the axial (δ_x) and lateral tip deflections (δ_y), respectively, and

Equations 3.70, 3.21, 3.35, and 3.41 are other relevant parameters required in solving Equations 3.62 and 3.69 (Fay, 1962).

$$L = \frac{1}{k}[K(p) - F(p,m)], \tag{3.120}$$

$$\delta_x = L - \frac{1}{k}[\cos\alpha\{F(p,m) - K(p) + 2E(p) - 2E(p,m)\} + 2p\sin\alpha\cos m], \tag{3.121}$$

$$\delta_y = \frac{1}{k}[2p\cos\alpha\cos m - \sin\alpha\{F(p,m) - K(p) + 2E(p) - 2E(p,m)\}], \tag{3.122}$$

where

$$k = \sqrt{\frac{P}{EI}} = \frac{1}{L}[K(p) - F(p,m)], \tag{3.123}$$

$$p = \sin\{(\psi_0 + \alpha)/2\}, \tag{3.124}$$

$$m = \sin^{-1}\left[\frac{\sin(\alpha/2)}{p}\right]. \tag{3.125}$$

The bending moment at the fixed end, the curvature, and the strain energy stored in the beam is given by Equations 3.74, 3.75, and 3.86

$$M_b\big|_{\substack{x=0\\ \psi=0}} = EI\sqrt{\frac{2P}{EI}(\cos\alpha - \cos(\psi_o + \alpha))}, \tag{3.126}$$

$$\frac{1}{\rho}\bigg|_{\substack{x=0\\ \psi=0}} = \sqrt{\frac{2P}{EI}(\cos\alpha - \cos(\psi_o + \alpha))}, \tag{3.127}$$

$$U = \frac{2P}{k}\left[\{E(p) - E(p,m)\} - (1 - p^2)\{K(p) - F(p,m)\}\right]. \tag{3.128}$$

The horizontal and vertical components of load P are given by Equations 3.115 and 3.116, respectively.

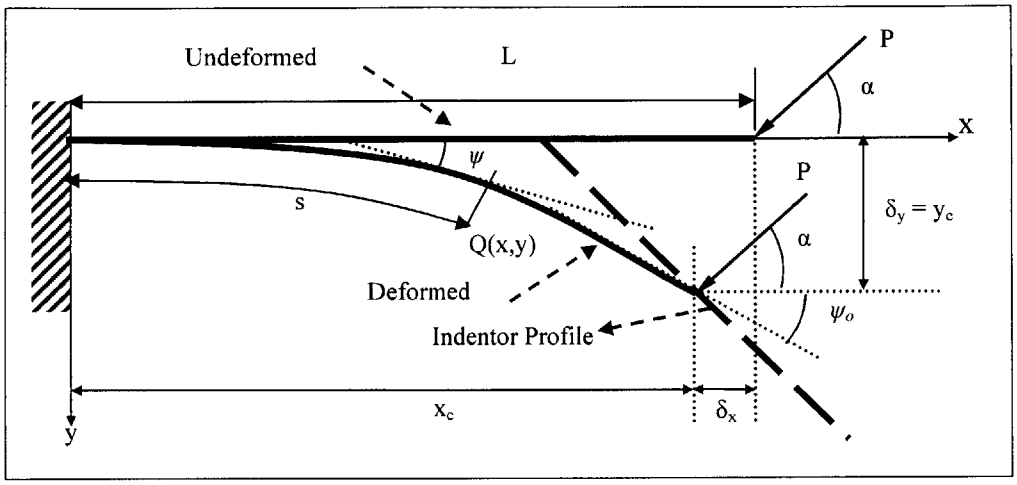

Figure 3.8: Cantilever beam loaded with an external concentrated inclined load at the free end and related parameters for large deflections; for normal load α = 90° in the above figure.

Now, the difference between the analytical solutions from nonlinear deflection equations is presented graphically in non-dimensional terms as PL^2/EI as a function of (δ_y/L), as shown in Figure 3.9. In order to present the non-dimensionalized diagrams, nonlinear equations from both theories are rearranged as follows:

$$\frac{\delta_y}{L} = \tan\alpha\left[\frac{\tan(kL)}{kL} - 1\right], \tag{3.129}$$

where

$$kL = \sqrt{\frac{PL^2}{EI}\cos\alpha} \quad \text{Qi et al., (2003).} \tag{3.130}$$

The current nonlinear approach can be rewritten as,

$$\frac{PL^2}{EI} = \left(\frac{\delta_y}{L}\right)^{-2}\left[2p\cos\alpha\cos m - \sin\alpha\{F(p,m) - K(p) + 2E(p) - 2E(p,m)\}\right]^2. \tag{3.131}$$

Figure 3.9 was plotted assuming the inclined load is applied with an indentor tip similar to the one Qi et al., (2003) used that had a semi-apex angle or face angle, $\theta_{indentor}$, of 21.6° that implies α = 68.4° (α = 90° - $\theta_{indentor}$). A similar process was repeated for $\theta_{indentor}$, of 65.35° that implies α = 24.65° and the results were plotted in Figure 3.10. Both Figures 3.9 and 3.10 clearly show that the two approaches start to deviate considerably beyond the tip deflection to length ratio (δ_y/L) of 0.6. The difference between the two approaches is because Qi et al., (2003) ignored the higher second order term in the bending curvature (Equation 3.2); this limits their (Qi et al., 2003) the lateral tip deflections, δ_y, to less than 0.6*L, or for approximate tip deflection angle, ψ_o, < 31°.

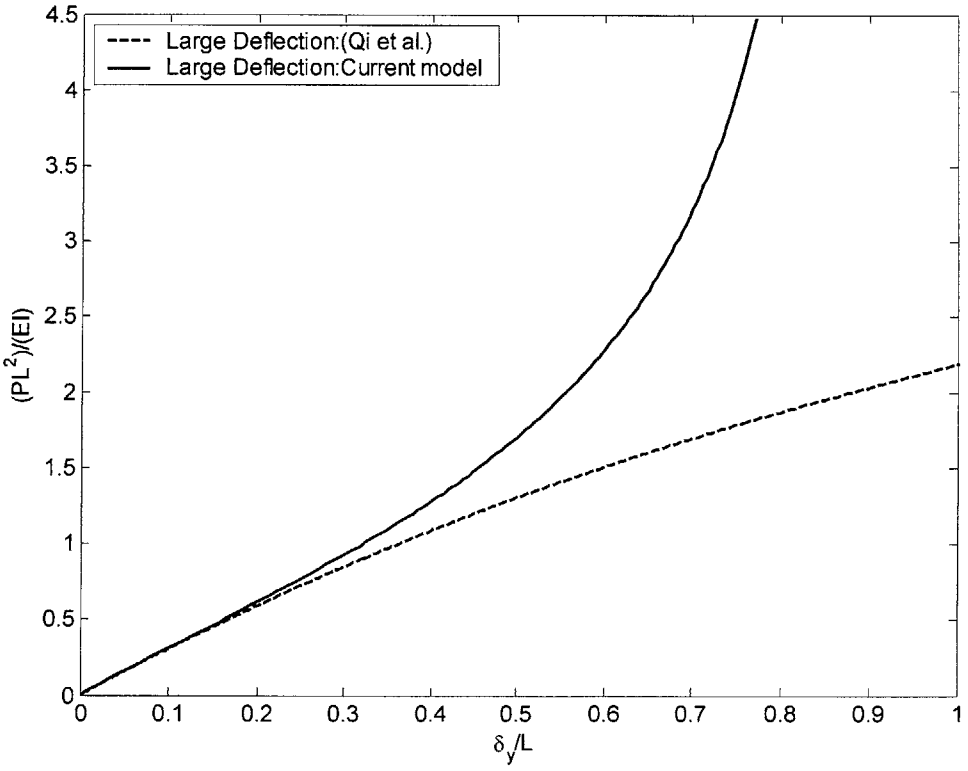

Figure 3.9: Non-dimensional load versus non-dimensional lateral tip displacement for cantilevered beam loaded with an external concentrated inclined load at the free end (α = 68.4°; sharp indentor tips).

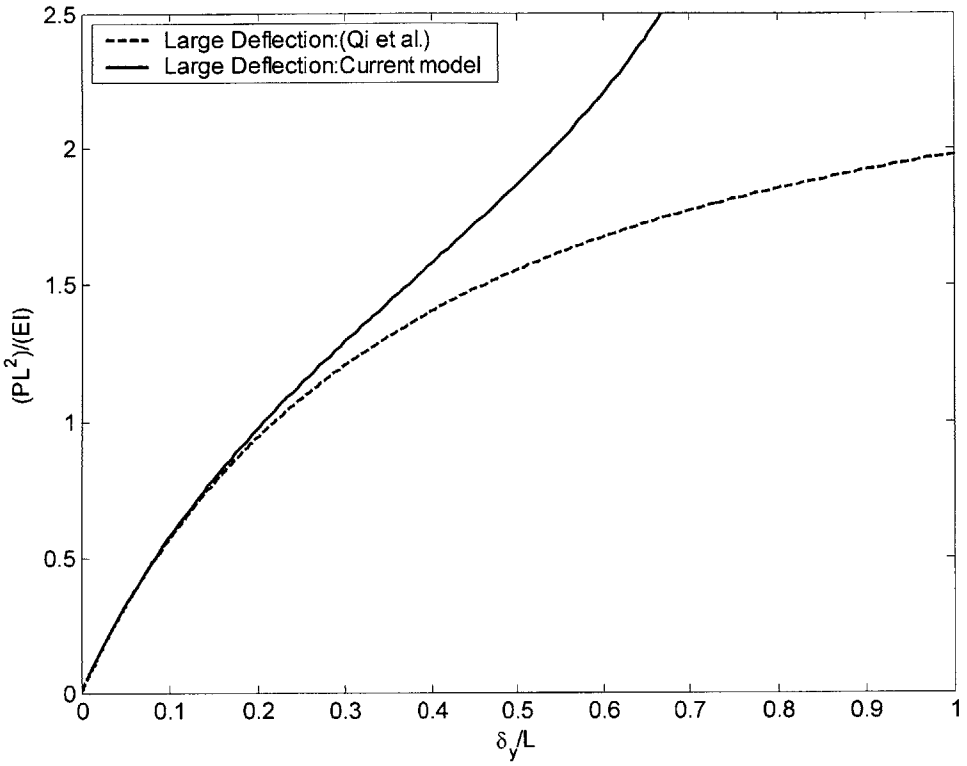

Figure 3.10: Non-dimensional load versus non-dimensional lateral tip displacement for cantilevered beam loaded with an external concentrated inclined load at the free end (α = 24.65°; wide indentor tips).

After comparing the analytical solutions for large deflection of a cantilevered beam in Figures 3.9 and 3.10, we next compare the analytical solutions from all four beam theories with experimental data from Wong et al., (1997), Ebeling, (2004), and Qi et al., (2003). We first compare the linear and nonlinear beam theories from Sections 3.2.1 and 3.2.2 with the experimental results from Wong et al., (1997) and thereafter, beam theories from Sections 3.2.3 and 3.2.4 with macro-scale experiments (Ebeling, 2004). In order to compare the nonlinear beam theories in Sections 3.2.3 and 3.2.4, we will first present and formulate a micro-mechanical contact model similar to the contact model presented by Qi et al., (2003) for simulating the indentation process. The contact model will be based on the nano-indentation of VACNT forest-like samples, and will then be applied to macro-scale beam experiments performed by Ebeling (2004).

3.3 Mechanics of Experiment – Wong et al., (1997)

Comparing the analytical solutions for small and large deflection of the tip of a cantilevered beam in Figure 3.6, we next compare the analytical solutions from both theories with the experimental results of Wong et al., (1997). In order to compare the analytical solutions with the experimental data, two plots with lateral force and strain energy are plotted against the lateral tip displacement.

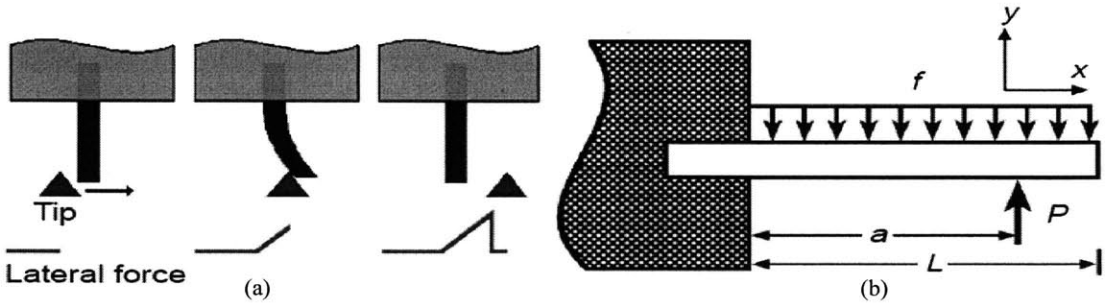

Figure 3.11: A schematic of the experiment where a MWCNT was fixed at one end and bent at the free end with an AFM tip moved laterally (Wong et al., 1997). Schematic of the top-view of the experimental setup (a); schematic that shows forces acting on the beam. Notice that the AFM tip here applies a lateral load and not an inclined load relative to the beam longitudinal axis (b).

Wong et al., (1997) used an AFM tip to locate and characterize the dimensions of the MWCNT to be 32.9 *nm* in diameter and nearly 1000 *nm* in length. Thereafter, we assumed that they applied a lateral force at a distance of 813 *nm* from the fixed end with the AFM tip. Since the AFM tip touches the nanotube at a point along the longitudinal axis before the free end, we assume a point contact between the nanotube and the AFM tip. The assumption of point contact leads us to believe that load applied by the AFM tip was normal to the axis of the beam. A schematic of their experiment is shown in Figure 3.11. Three different sets of data were recorded: force versus lateral tip displacement data, strain energy versus lateral tip displacement data, and force constant (K) versus distance data. The distance in the last data set is the distance of the tip from the fixed end of the MWCNT. A curve obtained from classical beam theory was then curved fitted to the last to estimate effective bending modulus E_b from the experimental data set (Wong et al., 1997):

$$K = \frac{\partial P}{\partial y} = \frac{3\pi r^4}{4a^3} E_b ,$$

where $\pi r^4 / 4$ is I (moment of inertia) for a solid cylinder of radius r, and a is the distance between the fixed end and the applied lateral load, as shown in Figure 3.11-b. The friction forces were assumed negligible and the effective bending modulus was thus approximated to be 1.26 *TPa* (Wong et al., 1997).

Based on linear and nonlinear beam theories, the lateral force and the stored strain energy versus lateral displacement curves were plotted in Figures 3.12-a and 3.12-b, respectively. In order to match the analytical results with the experimental results, the beam in both beam theories is taken to have a cylindrical shape with length of 813 *nm*, diameter of 32.9 *nm*, and effective bending modulus of 1.26 *TPa*.

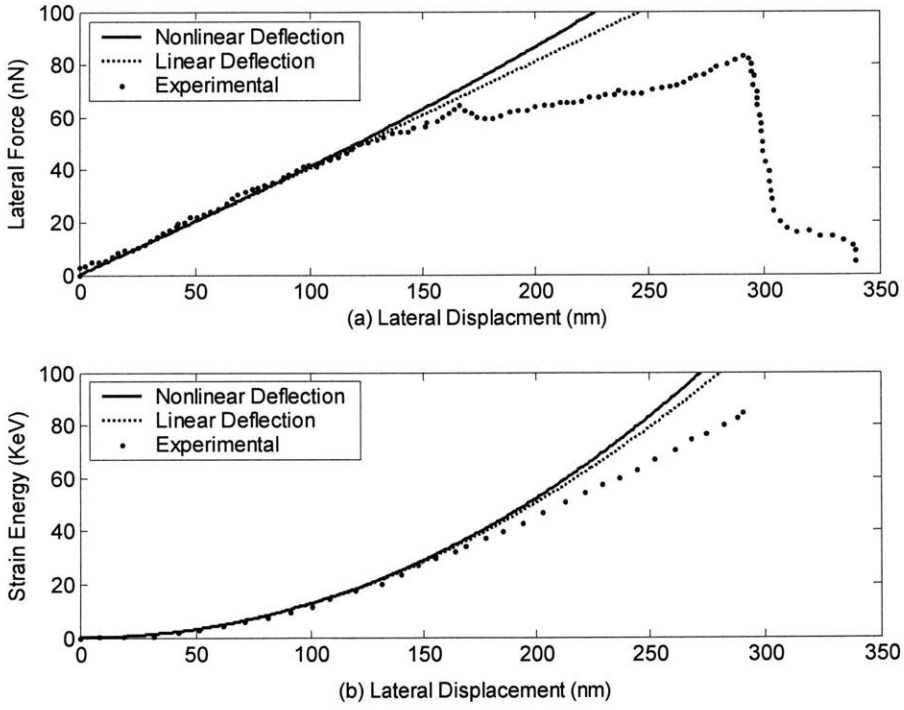

Figure 3.12: Comparison of lateral force versus lateral tip displacement for linear and nonlinear beam theories, and experimental data (Wong et al., 1997) (a). Comparison of strain energy versus lateral tip displacement for linear and nonlinear beam theories, and experimental data (b). The graphs were obtained for MWCNT of L = 813 *nm*, D = 32.9 *nm* and effective E_b = 1.26 *TPa*.

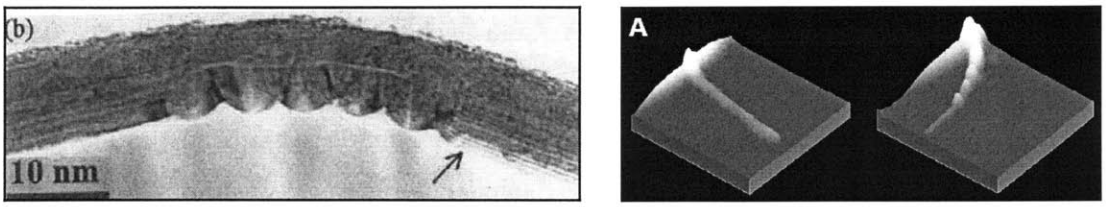

(a) (b)

Figure 3.13: Local buckling in a MWCNT (a) (Poncharal et al., 1999). Periodic buckling (bumps on the far right figure) observed while bending MWCNT to undergo large deflections with an AFM tip (b) (Wong et al., 1997).

Figure 3.12 show that both beam theories match the experimental results up until where there is a sudden drop in the slope at a lateral displacement of approximately 170 *nm*. Wong et al., (1997) reported that the sudden drop in the curves is because the MWCNT underwent buckling at approximately deflection angle of 10°, as shown in Figures 3.13. The process of buckling was first observed by Iijima et al., (1996) and later by Poncharal et al., (1999) and Falvo et al., (1997); the MWCNTs were observed to regain their original shape even after large deformations. Both beam theories are able to capture the quadratic behavior of the experimental energy curve in Figure 3.12-b before the CNT buckles; thereafter the experimental curve shows a linear behavior.

Both beam theories show similar behavior when compared with the experimental data. The beam in Wong et al., (1997) buckles beyond the tip deflection of approximately 170 *nm*, and from the analytical comparison earlier we showed that the two beam theories deviate beyond tip deflection of $0.6*L$ (approx. 0.6*813.0 *nm*= 487.8 *nm*), renders the comparison of the analytical results with the experimental results inconclusive.

3.4 Mechanics of Nano-Indentation of Nanotube Arrays

Qi et al., (2003) probed the mechanical behavior of Vertically Aligned Carbon Nanotube (VACNT) arrays, also known as nano grass and nano forests via nano-indentation, as shown in Figure 3.14. Thereafter, they used the force-penetration results to determine the effective mechanical properties of the constituent CNTs, including

bending stiffness and effective bending modulus. The key structural features of the VACNT are CNT diameter, length and areal density. Observation of nano-indentation reveals a process whereby nanotubes are consecutively bent during the penetration of the indentor. In the micro-mechanical model of the indentation process (Qi et al., 2003), the effective bending stiffness $(EI)_{eff}$ of constituent CNTs in the VACNT array is deduced from nano-indentation force-penetration depth curves. The obtained average $(EI)_{eff}$ of CNTs is then used to interpret an average effective bending modulus E_b, effective axial modulus E_a, and a wall modulus E_w of an MWCNT. The E_b, the E_a, and the E_w of MWCNTs reported by Qi et al., (2003) ranged between 0.91 and 1.24 *TPa*, 0.90 and 1.23 *TPa,* and 4.14 and 5.61 *TPa*, respectively. The MWCNT walls were each assumed to have a mechanical shell thickness of 0.075 *nm* and shell spacing of 0.34 *nm*.

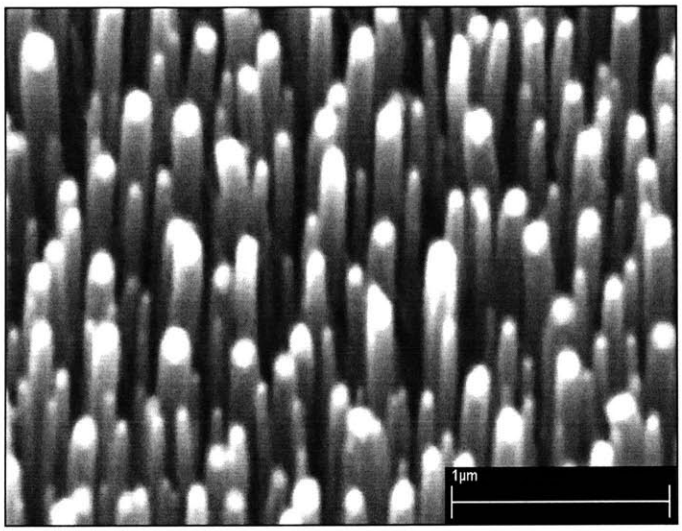

Figure 3.14: A SEM image of a 25° tilted view of a Vertically Aligned Carbon Nanotubes sample reveals the forest like landscape (Qi et al., 2003).

This section presents micro-mechanical models of the nano-indentation process for two indentor geometries, a sharp tip with a semi-apex angle or face angle of 21.6° and a Berkovich tip with face angle of 65.35°. The micro-mechanical model presented here includes various stages of CNT indentor interaction and also includes CNT buckling during indentation.

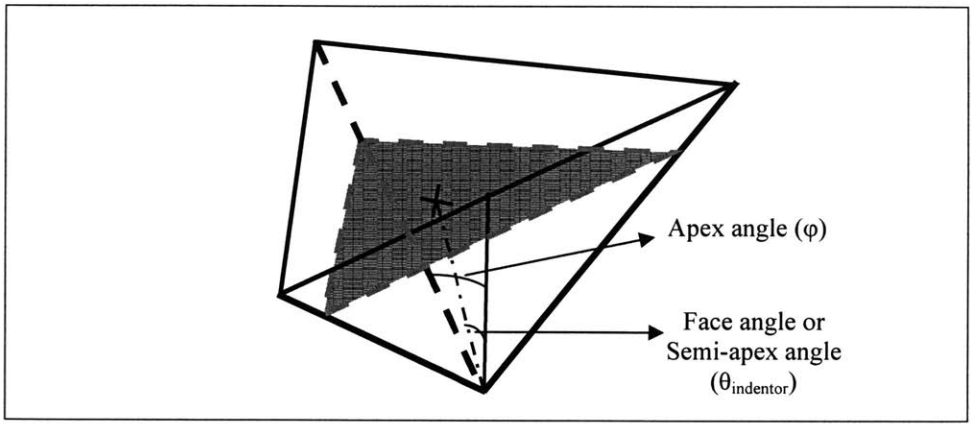

Figure 3.15: A schematic of indentor tip.

Qi et al., (2003) used an AFM diamond tip for nano-indentations on the VACNT sample; the AFM tip had an apex angle, φ, of 60° and a semi-apex angle, $\theta_{indentor}$, of 21.6°, as shown in Figure 3.15. Deep indentation of a VACNT sample with this AFM tip results in large deflection of the nanotubes; a two-dimensional representation of nano-indentation is shown in Figure 3.16. Qi et al., (2003) used the nonlinear beam theory presented in Section 3.2.3 to formulate the mechanical contact model to simulate nano-indentation that accounted for the lateral and axial components of load by the AFM tip formulated in the deformed configuration. When the contact model results were compared with the experimental data, the average effective bending modulus values (0.91 *TPa* to 1.24 *TPa*) agreed well with other experimental values found for CNTs in literature.

The nonlinear contact model that Qi et al., (2003) presented is expected to agree well for modest indentations upto 0.6 or so of the average height of the VACNT array, as was concluded from Figures 3.9 and 3.10. The results however are not expected to capture the entire force-penetration curve behavior for deep indentations with CNT deflections beyond $0.6*L_{CNT}$, and also will not capture buckling of CNTs. Wong et al., (1997) reported that the CNT in their experiment buckled at a lateral tip deflection of approximately 170 *nm*. The flatness of the Berkovich tip increases the ratio of axial to lateral loading of the CNT, decreasing the overall deflection and load at which the CNT will buckles during indentation. In addition, Qi et al. (2003) noted that CNTs transition from making a point contact to a line contact with the AFM tip. The line contact occurs

when a CNT tip deflection reaches $\theta_{indentor}$ of the AFM tip and this changes the end loading conditions for the CNT from there on. Figures 3.16-c and 3.16-d show a two-dimensional schematic representation of the point contact and the line contact of a CNT with an indentor tip, respectively.

In the following sections, we propose two micro-mechanical contact models for nano-indentation with a pyramidal shape indentor tip that build upon the model presented by Qi et al., (2003); both sharp and Berkovich tips are considered. The first proposed micro-mechanical contact model considers only the large deflection problem associated with deep indentations or Berkovich tips. The second model uses an approximate approach for capturing the influence of buckling of CNTs on indentation force-displacement curves. Both of these models apply the more complete nonlinear analysis presented in Section 3.2.4.

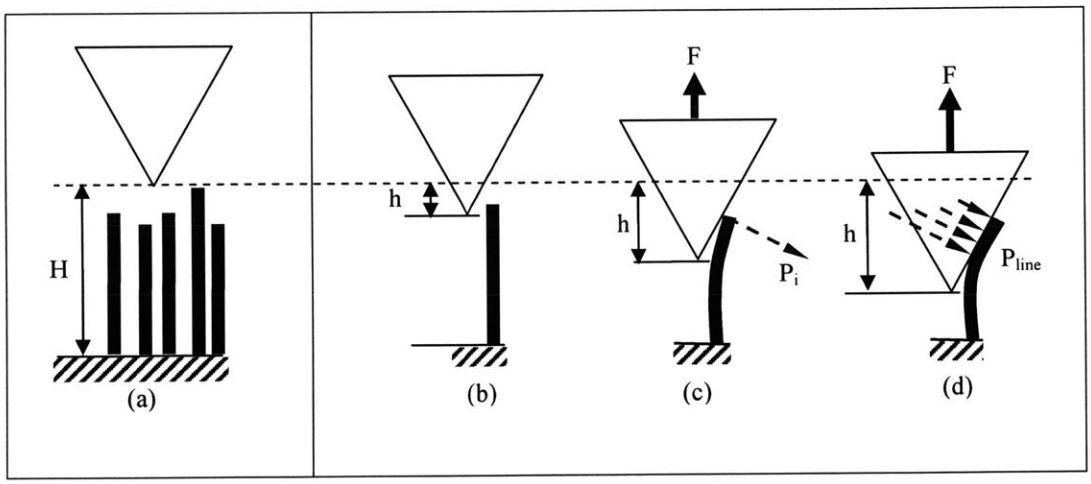

Figure 3.16: Schematic of nano-indentation of a VACNT forest (a). The indentor tip is about to make contact with the CNT (b). The tip and CNT make a point contact (c). The tip and the CNT make a line contact (d). The point contact load and the line contact load are normal to the indentor's face (b and c).

3.4.1 Micro-Mechanical Contact Model (without buckling)

The proposed three-dimensional micro-mechanical contact model is based on the large deflection nonlinear equations. The model is divided into two phases: point contact between CNT and indentor, and line contact between CNT and indentor. The point contact phase indicates the regime of deformation where the load is applied as an inclined point force at the free end of the nanotube; the line contact phase indicates the regime of deformation where the load is distributed nonuniformly over the line segment of the nanotube, as shown in Figures 3.16-c and 3.16-d, respectively. The contact between the CNTs and the indentor face is assumed frictionless. In addition, any interaction between the CNTs is ignored in our contact model.

In the following subsections, we first formulate the theoretical contact model for each phase without including the buckling effect. Second, the micro-mechanical contact model is then verified against the results from macro-scale experimentation (Ebeling, 2004) and finite element models based on the macro-scale experimentation.

3.4.1.1 Point Contact Phase ($\psi_{oi} < \theta_{indentor}$)

In the point contact phase, a point load P_i is applied to the free end of a nanotube of length L_i and diameter D_i at an angle α with the vertical (normal to the indentor's face). Here the slope of the CNT at the free end, ψ_{oi}, remains less than the indentor semi-apex angle $\theta_{indentor}$, as shown in Figure 3.17-b. When the slope equals $\theta_{indentor}$, the CNT enters the line contact phase, discussed in the next subsection.

The model in this phase begins with the indentor tip initially located at a height, H above the VACNT forest, as shown in Figures 3.16-a and 3.17-a. The VACNT forest is generated randomly using a Gaussian distribution for CNT locations and heights. During the nano-indentation simulation, the indentor tip sequentially encounters and bends nanotubes as the depth of penetration, h, is increased, as shown in Figure 3.16. Considering an i^{th} nanotube encountered as, CNT_i; the indentor touches CNT_i and subjects it to a point load P_i. The load P_i is applied normal to the indentor face, as shown in Figure 3.17-b.

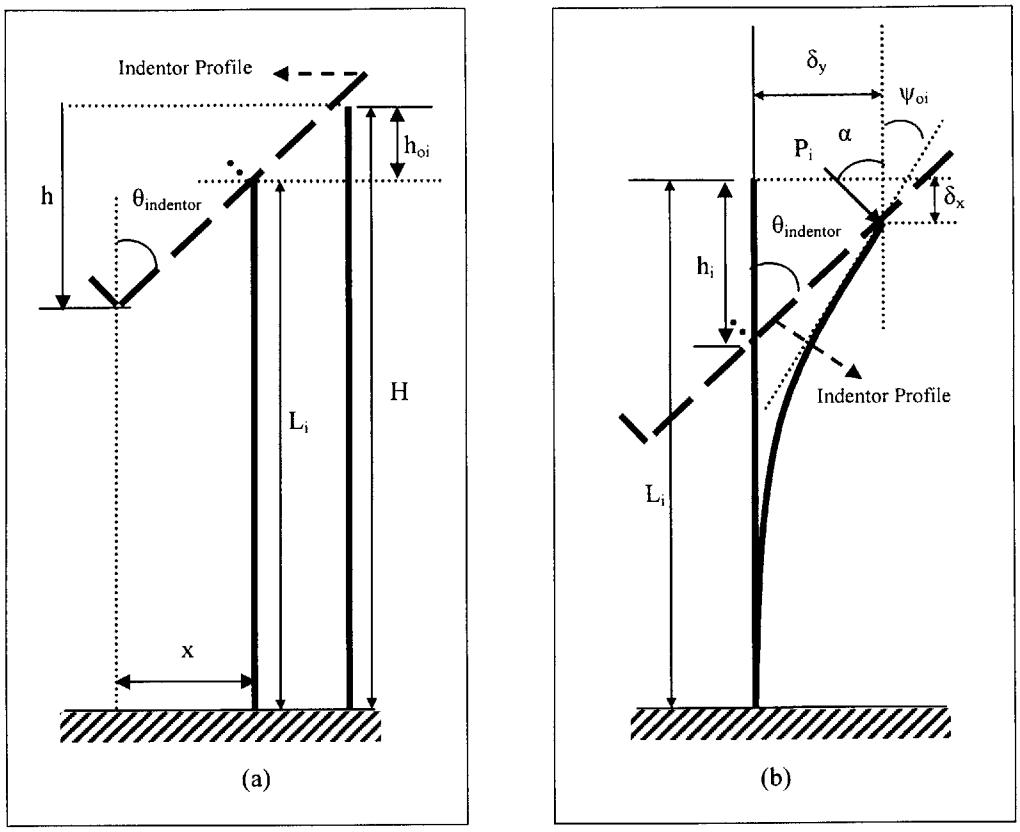

Figure 3.17: Schematic to find the relation between h_i and h (a). Point contact between a CNT and an indentor profile at the free end (b).

Unlike the contact model presented by Qi et al., (2003), nonlinear equations (Section 3.2.4) used in our contact model cannot be arranged to find a direct relation between P_i and h. For clarity, the nonlinear equations are given as (see Section 3.2.2 for the formulation):

$$\delta_x = L_i - \frac{1}{k_i}\left[\cos\alpha\{F(p,m) - K(p) + 2E(p) - 2E(p,m)\} + 2p\sin\alpha\cos m\right] \tag{3.132}$$

$$\delta_y = \frac{1}{k_i}\left[2p\cos\alpha\cos m - \sin\alpha\{F(p,m) - K(p) + 2E(p) - 2E(p,m)\}\right] \tag{3.133}$$

where

$$k_i = \sqrt{\frac{P_i}{(EI)_{Eff}}} = \frac{1}{L_i}[K(p) - F(p,m)] \tag{3.134}$$

$$p = \sin\{(\psi_0 + \alpha)/2\} \tag{3.135}$$

$$m = \sin^{-1}\left[\frac{\sin(\alpha/2)}{p}\right]. \tag{3.136}$$

Rearranging Equation 3.134, we get

$$P_i = (EI)_{Eff}\left[\frac{\{K(p) - F(p,m)\}}{L_i}\right]^2. \tag{3.137}$$

$(EI)_{Eff}$ in Equations 3.134 and 3.137 is the average effective bending stiffness of a CNT in the VACNT forest. Also, in Equations 3.132 to 3.134 and 3.137, *K(p)* and *F(p, m)* are the complete elliptic integrals of the first kind, while *E(p)* and *E(p, m)* are the complete elliptic integrals of the second kind; the expanded form of these first and second kind elliptic integrals are given as

$$K(p) = \int_0^{\frac{\pi}{2}} \frac{d\phi}{\left[1 - p^2 \sin^2\phi\right]^{\frac{1}{2}}}; \qquad F(p,m) = \int_0^{m} \frac{d\phi}{\left[1 - p^2 \sin^2\phi\right]^{\frac{1}{2}}}$$

$$E(p) = \int_0^{\frac{\pi}{2}} \left[1 - p^2 \sin^2\phi\right]^{\frac{1}{2}} d\phi; \qquad E(p,m) = \int_0^{m} \left[1 - p^2 \sin^2\phi\right]^{\frac{1}{2}} d\phi.$$

Because no direct relation between P_i and h exists, we use geometry and an iterative method to approach a solution. First, δ_x and δ_y in Equations 3.132 and 3.133 are solved for a particular ψ_{oi}; here the deflection angle varies as $0° < \psi_{oi} < \theta_{indentor}$. Thereafter, h_i is solved by substituting δ_x and δ_y in Equation 3.138; the relation in Equation 3.138 is found by relating the deflection of CNT_i to the geometry of the indentor, as shown in Figure 3.17-b; it is given by

$$L_i - \delta_x = (L_i - h_i) + \delta_y \tan\left[\frac{\pi}{2} - \theta_{indentor}\right],$$

$$\text{(or) } h_i = \delta_x + \delta_y \tan(\alpha), \tag{3.138}$$

$$\text{where } \alpha = \frac{\pi}{2} - \theta_{indentor}. \tag{3.139}$$

The process is repeated for several ψ_{oi} ranging from 0° to $\theta_{indentor}$, which gives several discrete points (ψ_{oi}, h_i). A sixth order polynomial is then curve fitted on these discrete points; the polynomial thus obtained, ψ_{oi}, is a function of h_i, where h_i is found by sequentially increasing the h ($h_i = h - h_{oi}$; $h_{oi} = H - L_i$), as shown in Figure 3.17-a. Thereafter, simply substituting ψ_{oi} into Equation 3.137, gives the required load P_i that the indentor tip applies upon reaching an indention depth, h_i.

For all the nanotubes that come into contact with the indentor tip at a given particular indentation depth h, values of P_i are found and then added together; thereafter, the net indentation force F (see Figure 3.16) is expressed as

$$F = \sum_{i=1}^{n} \gamma_i P_i \cos\alpha \tag{3.140}$$

where $\gamma_i = 0$ when CNT_i is not in contact, and $\gamma_i = 1$ otherwise. The value of γ_i can be determined from geometry inequality as follows (see Figure 3.17-a):

$$(H - h) + x\tan\left(\frac{\pi}{2} - \theta_{indentor}\right) \le L_i, \tag{3.141}$$

where x is the known relative distance between CNT_i and the indentor tip that comes into contact when the inequality in Equation 3.141 is satisfied. The value of h_i ($= h - h_{oi}$) for an individual nanotube sequentially increases once CNT_i makes contact with one of the faces of the indentor tip.

On continuing the indentation, the deflection angle increases as the indentation depth increases, and some of the CNTs reach the $\theta_{indentor}$ of the tip. The CNT closest to the center or peak point of the inverted pyramid tip reaches the line contact phase before the other outer CNTs come into contact. The inclined force P_i is calculated for CNT_i until it reaches the equal angle condition. Once CNT_i reaches the line contact phase, it goes through a different iterative process discussed in the next section.

3.4.1.2 Line Contact Phase ($\psi_{oi} = \theta_{indentor}$)

Once the CNT_i deflection angle reaches the $\theta_{indentor}$ of the indentor, it enters the line contact phase. Here the load at an angle α with the vertical is distributed nonuniformly over the contact length near the free end of the CNT_i, as shown in Figures 3.18 and 3.19-a by the curved dotted lines. Unlike the point contact phase, here ψ_{oi} remains constant and is equal to $\theta_{indentor}$. As a result, p and m become constants in Equations 3.135 and 3.136, respectively, and k_i, δ_x, δ_y, P_i, and h_i, functions of L_i rather than ψ_{oi}. Here, L_i is defined as the length of CNT_i from the fixed end to the point of application of P_i.

An iterative method, similar to the one in the point contact phase, is then used to find a solution. First, for an initial L_i equal to L_{oi}, we solve for δ_x and δ_y from Equations 3.132 and 3.133 and substitute the values in Equation 3.138_2 to solve for corresponding h_i. Notice that the point of application of the equivalent load P_i on CNT_i continually changes as indentation progresses; this results in the shortening of the effective length L_i of the beam, as shown in Figure 3.18. L_i decreases by about $1/3^{rd}$ of the line contact length ($L_{oi} - L_i$) with each incremental increase in h_i (Figure 3.19-b) and is used to repeat the iterative process for the next indentation depth. Several discrete points (L_i, h_i) are found on which a sixth order polynomial is curve fitted; the polynomial is then a direct relation between h_i and L_i. Finally, h_i is solved from the known indentation depth h of the indentor tip by subtracting the initial separation distance h_{oi} (= H - L_i) between CNT_i and the indentor ($h_i = h - h_{oi}$). Thereafter, by substituting h_i in the polynomial, we solve for L_i; this L_i gives the required equivalent load P_i when substituted in Equation 3.137. P_i is then the required 'equivalent load' that the indentor tip applies to CNT_i in line contact with the indentor surface at a relative indentation depth h_i.

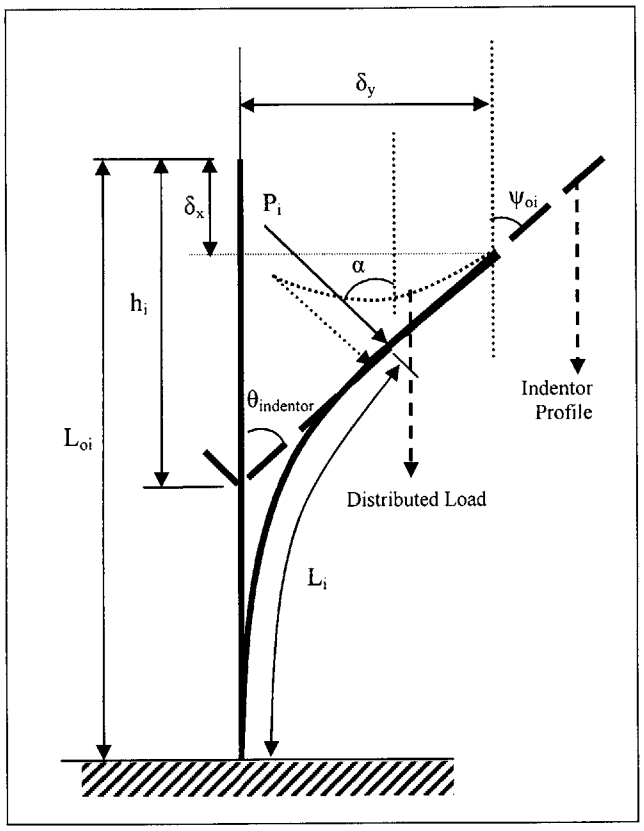

Figure 3.18: Line contact between a CNT and an indentor that occurs for $\psi_o \geq \theta_{indentor}$ (b). Also shown in figure, an equivalent concentrated load P_i near the free end and the nonuniform load (curved dotted line).

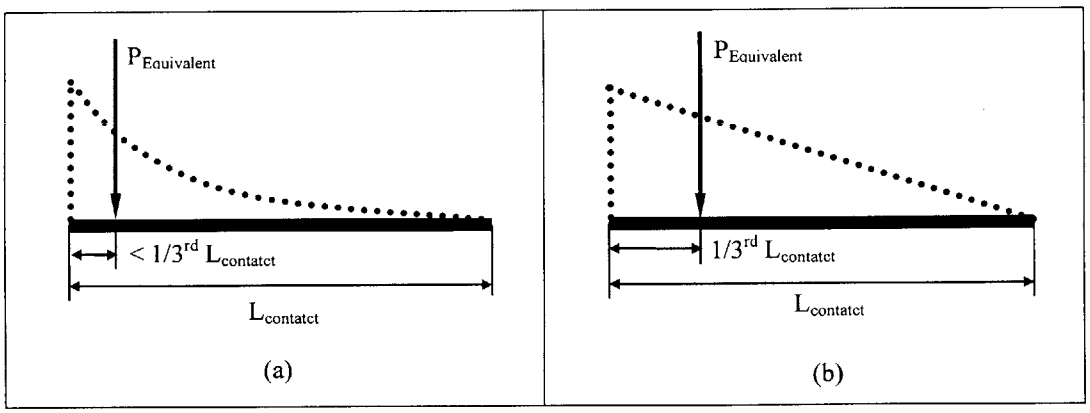

Figure 3.19: Expected nonuniform load distribution pattern with approximate location of the equivalent load (a). Assumed linearly varying uniformly distributed load pattern with the location of equivalent load (b). The thick solid line represents the region of CNT that makes line contact with the indentor surface.

A similar process is repeated for all the CNTs that make a line contact with the indentor tip; the sum of all the equivalent inclined loads for a particular indentation depth h is then added to the inclined loads of the CNTs still in the point contact phase. The sum is finally substituted in Equation 3.140 to get the net indentation force F at h, as shown in Figure 3.16-d.

Next, numerical solutions obtained from the above micro-mechanical contact model are compared with macro-scale experimental (Ebeling, 2004) and finite element simulation data for a single Teflon beam subjected to indentation. Thereafter, we will attempt to capture the complete deformation behavior with buckling of CNTs in our micro-mechanical model.

3.4.2 Results (without buckling)

In order to verify the model, theoretical results are first compared to macro-scale indentation experiments on a single Teflon cylinder (Ebeling, 2004). Theoretical results are then compared to finite element indentation simulations. Both a sharp ($\theta_{indentor}$ = 21.6°) and a Berkovich ($\theta_{indentor}$ = 65.35°) indentor tips are examined.

3.4.2.1 Macro-Scale Experiments

In order to verify the micro-mechanical contact model, two macro-scale experiments were performed. First, a Teflon solid cylindrical tube having a diameter of 9.53 *mm* and length of 124.0 *mm* was indented with a large scale sharp indentor tip, as shown Figure 3.20-a. Second, a similar Teflon solid cylindrical tube having a diameter of 9.53 *mm* and length of 184.0 *mm* was indented with a large scale Berkovich indentor tip, as shown in Figure 3.20-d. The factory-rated Young's modulus of Teflon is ~0.7 *GPa*. The solid tubes were threaded on one end and were fitted on an Aluminum base plate, as shown in Figure 3.20. The indentor tips were made of Aluminum sheet metal, as shown in Figure 3.20. The contact between the Teflon cylinder and the indentor surface was assumed frictionless; to minimize the effect further, a fine layer of lubricant was applied on the indentor surface.

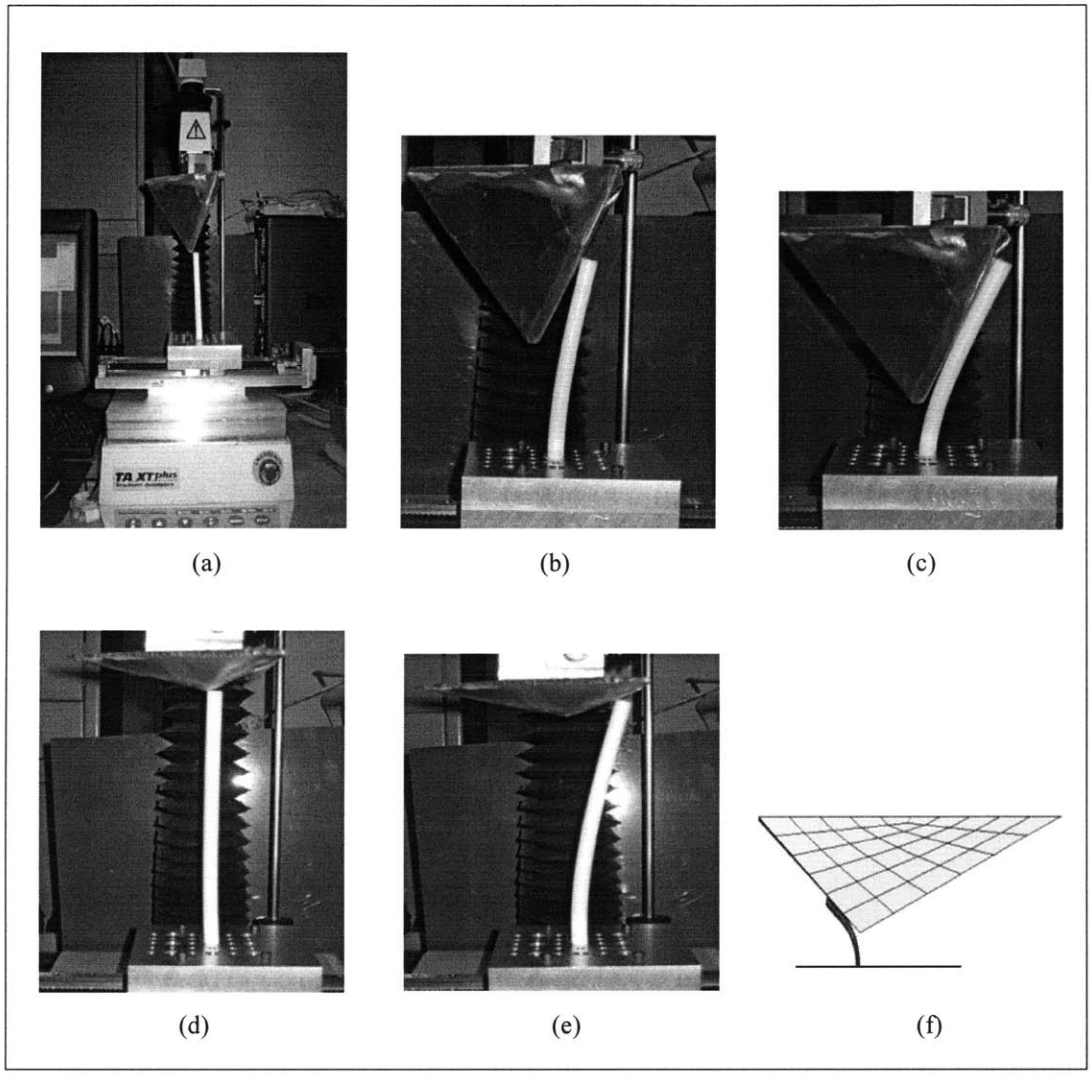

Figure 3.20: Macro-scale experimental setup for indentation of solid Teflon tube rigidly fixed at one end. Sharp indentor tip deflecting a single solid Teflon tube of L = 124.0 *mm* and D = 9.53 *mm*, shown in initial position, δ = 0 *mm* (a), point contact phase, δ = 50 *mm* (b), and line contact phase, δ =110 *mm* (c). Berkovich indentor tip deflecting solid Teflon tube of L = 184 *mm* and D = 9.53 *mm*, shown in initial position, δ = 0 *mm* (d), point contact phase, δ = 10 *mm* (c), and line contact phase, δ = 140 *mm* (f).

A texture analyzer (see Figure 3.20-a) from *Stable Micro Systems* (Model # *TA.XT.plus*) was then used to deflect the Teflon cylinder via an Aluminum indentor. Here the indentor tip was displaced by 115.0 *mm* downwards for the sharp tip and 21.0 *mm* for the Berkovich tip at the rate of 6.0 *mm/sec*. Because of the limitation imposed by the texture analyzer, the Aluminum Berkovich tip was designed to be smaller in dimension, which limited the indentation depth in our experiment. Figures 3.20-a, b and c, and d, e and f show three snapshots at the initial, the point contact, and the line contact phases, respectively, for both types of indentor tips. The vertical component of the indentation force and the penetration depth was directly obtained from the texture analyzer software; the data was then compared with the results from our theoretical and finite element simulations, as will be discussed next.

3.4.2.2 Macro-Scale Finite Element Simulations

Next, two three-dimensional Finite Element (FE) contact models were constructed and their solutions compared to those of the micro-mechanical model and experiments from the previous section. A commercial FE software package, *ABAQUS,* was used to model the experiments in the previous section. The FE-based models consist of a deformable solid cylindrical beam rigidly fixed at one end and displaced at the other by an indentor tip, modeled as a rigid body. In the first FE simulation, the cylindrical beam has a diameter of 9.53 *mm* and length of 124.0 *mm* with indentor tip having an apex angle φ of 60° and a semi-apex angle $\theta_{indentor}$ of 21.6° (sharp tip), as shown in Figure 3.21-a. In the second FE simulation, the cylindrical beam has a diameter of 9.53 *mm* and length of 184.0 *mm* with indenter tip having φ of 142.4° and $\theta_{indentor}$ of 65.35° (Berkovich tip), as shown in Figure 3.21-d. The cylindrical beam was assigned 0.24 x 0.24 *nm* linear 8-node solid elements (C3D8) with linear elastic material properties of Teflon (Young's modulus of 0.7 *GPa* and Poisson ratio of 0.46). Initially the free end of the cylindrical beam FE model is in contact with the indentor tip. In both simulations, all degrees of freedom for the indentor tip except the vertical displacement were fixed. During the simulation, the indentor tip was displaced such that it deflects the Teflon tube on indentation. The indentor tip is displaced enough to make a point contact and a line contact during the simulation, as shown in Figures 3.21. Figures 3.21-b and 3.21-e show the beams making

a point contact with the indentor surface for the sharp and the Berkovich tips, respectively. On the other hand, Figures 3.21-c and 3.21-f show the snapshots of the FE simulation where the beams make a line contact with the sharp and the Berkovich tips, respectively. The indentation force and vertical displacement were measured at a reference point on the tip. Similar to the experiment, the tips were specified to displace downwards by 115.0 *mm* and 180.0 *mm* for the sharp and the Berkovich tip simulations, respectively.

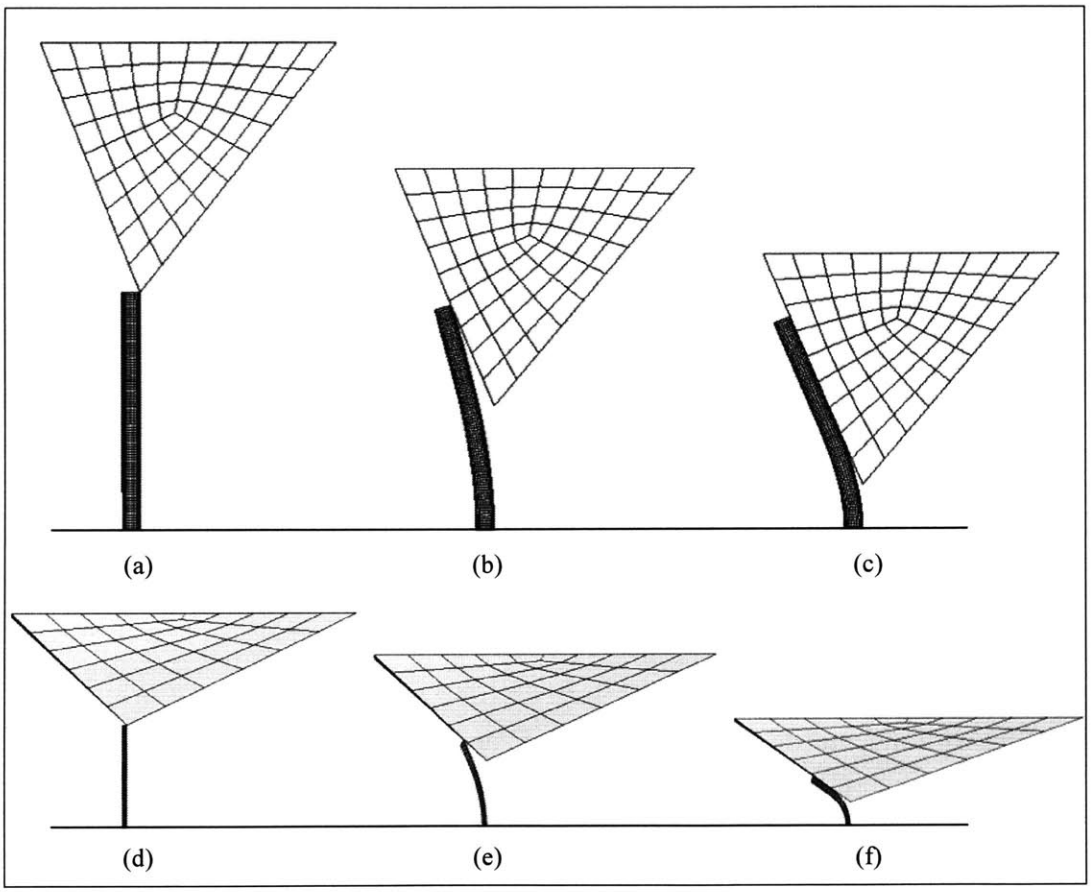

Figure 3.21: Macro-scale finite element simulation for indentation of solid Teflon tube rigidly fixed at one end. Sharp indentor tip deflecting a single Teflon solid tube of L = 124.0 *mm* and D = 9.53 *mm* shown in initial position, δ = 0 *mm* (a), point contact phase, δ = 60 *mm* (b), and line contact phase, δ = 110 *mm* (c). Berkovich indentor tip deflecting solid Teflon solid tube of L = 184.0 *mm* and D = 9.53 *mm* shown in initial position, δ = 0 *mm* (d), point contact phase, δ = 30 *mm* (e), and line contact phase, δ = 140 *mm* (f).

Next, the experimental, FE simulation and contact model results are compared together in Figures 3.22 and 3.23 for sharp and Berkovich tips, respectively. Figure 3.22, in addition to the results from our contact model, shows the results from contact model proposed by Qi et al., (2003). The numerical solutions from FE and mechanical contact model are in excellent agreement throughout the force-displacement curve, while they both differ slightly from the experimental results (see Figures 3.22 and 3.23). Results from the FE and contact model match and show linear behavior for initial indentation, as shown in the Figure 3.22 inset view. The initial linear behavior is observed until an indentation depth of 80 *mm* where the Teflon beam and the indentor tip surface make a point contact; thereafter, the beam makes line contact with the indentor, as shown in Figure 3.21-c and by black arrow in Figure 3.22. The initial linear segment is the small deflection region where linear beam theory can be applied with reasonably good approximation to the experimental data. The *f-p* results from Qi et al., (2003) contact model shows remarkably good fit to the experimental data throughout the point contact phase. Figure 3.23 inset view, on the other hand, shows that for indentation with the Berkovich tip, the initial force-displacement curve is not linear. The initial curve behavior in Figure 3.21-e is nonlinear because even the small indentation results in large deflection of the beam. In addition, the results for the Berkovich tip in Figure 3.23 shows that transition from point contact to line contact phase occurs at an indentation depth of approximately 120 *mm*.

Even though the contact model and the FE simulations capture the force-displacement behavior from the experimental results in Figures 3.22 and 3.23, they deviate slightly in the inset views and they transition to the line contact phase sooner (see Figure 3.22). The inset views differ mainly because of the machining error of the Aluminum indentor tips. The edges of the indentor tips used in the experiment have chamfer because of the folding of Aluminum sheets, while the contact and the FE models have sharp edges. In addition, the actual $\theta_{indentor}$ for the experimental sharp and Berkovich tips are approximately 23° and 66°, respectively.

The Teflon beams deflect more with small indentation because of chamfer on the edges; this results in a change in slope of the experimental curve in the inset view of Figure 3.22. The slope of the curve outside of the chamfer region is similar to the

simulation results. In addition, the force values in Figure 3.22 are slightly higher than the simulation results mainly because of the higher $\theta_{indentor}$, which also results in the delay in transition of the beam from point contact to line contact.

Because of the size limitation of the Texture Analyzer instrument, complete indentation of the Teflon beam with the macro-scale Berkovich tip was not possible; therefore, data showing the transition from point to line contact is missing in Figure 3.23.

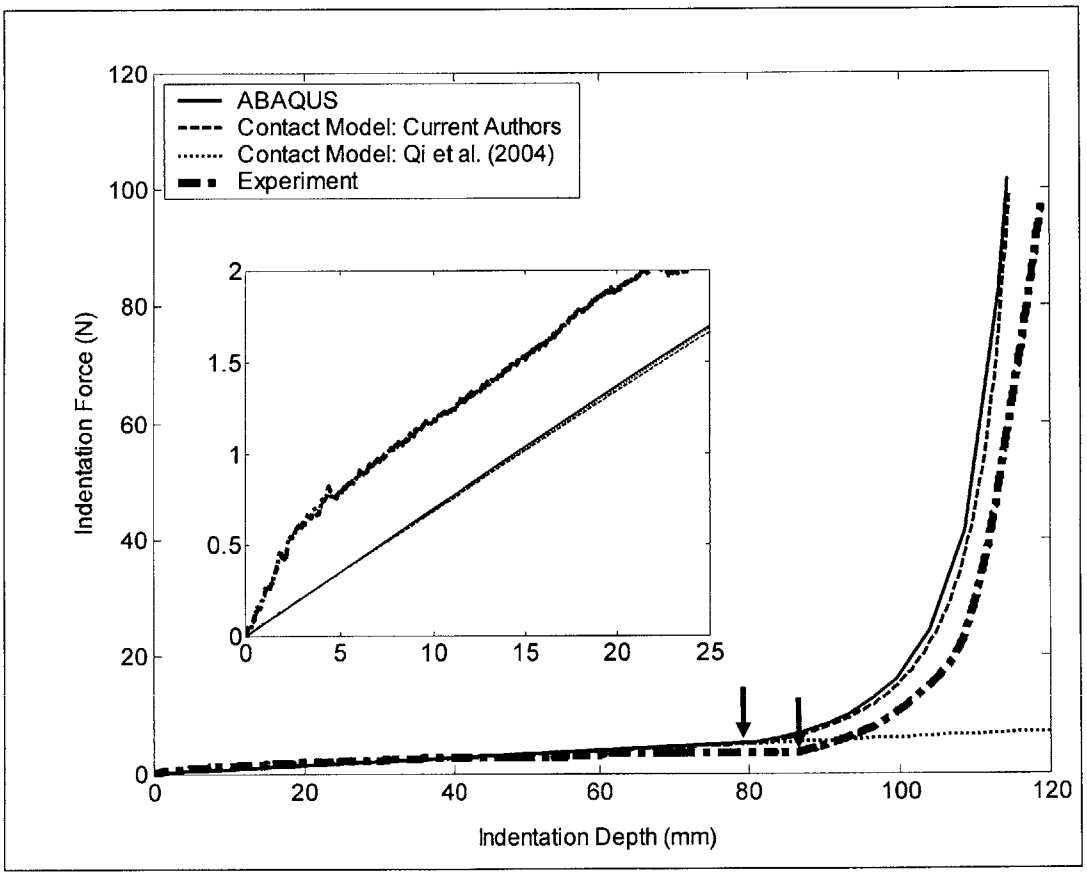

Figure 3.22: Force versus penetration depth curves from finite element, contact model, and experimentation of macro scale model. Single Teflon solid tube (L = 124.0 *mm*, D = 9.53 *mm*, E = 0.7 *GPa*, υ = 0.46) indented with a sharp indentor tip ($\theta_{indentor}$ = 21.6°). The inset picture is the close-up view of the beginning portion of the curves showing the linear relation between force and penetration depth. The black-arrow indicates the end of the point contact phase.

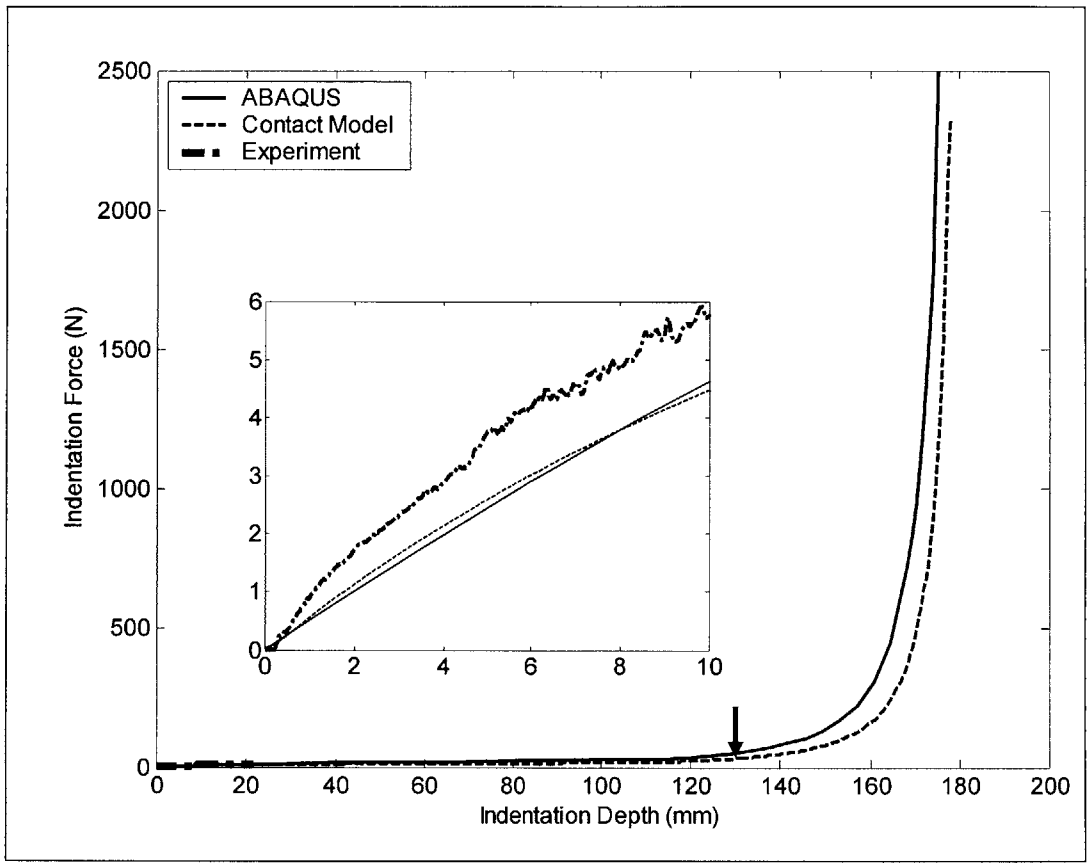

Figure 3.23: Force versus penetration depth curves from finite element, contact model, and experimentation of macro scale model. Single Teflon solid tube (L = 184.0 *mm*, D = 9.53 *mm*, E = 0.7 *GPa*, υ = 0.46) was indented with a Berkovich indentor tip ($\theta_{indentor}$ = 65.35°). The inset picture is the close-up view of the beginning portion of the curves showing the linear relation between force and penetration depth. The black-arrow indicates the end of the point contact phase.

3.4.3 Micro-Mechanical Contact Model (with buckling)

The three-dimensional micro-mechanical contact model based on large deformation was proposed earlier. The micro-mechanical model was found to be in good agreement with the experimental and FE model results. The contact model, however, does not account for the local buckling observed on the compressive side of the bend in CNTs subjected to bending.

In this section, we will incorporate the local buckling phenomenon in our contact model and attempt to approximate the penetration force-displacement curve behavior by comparing the results obtained from nano-indentation FE simulations of EOR-based MWCNT models. But first, we will show how equations presented by Timoshenko (1936) and later used by Yakobson et al., (1996) for buckling phenomenon in thin shell tubes could be used in our contact model for adequately predicting the onset of rippling in MWCNTs.

Onset of Rippling

The CNTs that are bent to large curvatures undergo local elastic buckling as was observed experimentally by Poncharal et al., (1993), and Falvo et al., (1997) and in numerical simulations by Iijima et al., (1996), Yakobson et al., (1996), Liu et al., (2001, 2003), Wang and Wang (2004), Wang et al., (2004), and Wang et al., (2005), Pantano et al., (2003, 2004a, 2004b), and others. The effective bending modulus of the CNT decreases with the emergence of a local rippling mode – a mode where local buckling initiates on the compressive side of the bend. In the case of nano-indentation, the rippling occurs locally and gives a hinge-like effect that results in an overall reduced stiffness of the CNT. To simplify this complex problem, we will attempt to capture a critical load/displacement at which localized buckling occurs and a subsequent reduction in effective tube stiffness post-buckling.

Buckling of MWCNTs is a complex problem where interlayer van der Waals forces play a major role as shown by Pantano et al., (2004a). However, the initiation of the buckling during bending of an MWCNT can be approximated from the buckling of the outermost shell, as shown in Pantano et al., (2003). In Chapter 2, we estimated the element size of an MWCNT, based on the initial buckling wavelength of the outermost shell predicted by thin shell theory (see Equation 2.5) (Timoshenko, 1936); here we also propose to use thin shell theory to predict the critical buckling point for a MWCNT subjected to bending. To estimate the critical point for the emergence of the rippling bending mode for a MWCNT, the local critical curvature κ_{cr} is estimated from the equation suggested by Timoshenko (1936) and later used by Yakobson et al., (1996):

$$\kappa_{cr} = \frac{2\varepsilon_{cr}}{D} \tag{3.142}$$

where

$$\varepsilon_{cr} = \frac{2t_w}{D\sqrt{3(1-\nu^2)}}. \tag{3.143}$$

In Equation 3.143, ε_{cr}, t_w, D, and ν are the critical strain, shell wall thickness, outermost diameter of the shell tube, and Poisson ratio, respectively. Substituting $t_w = 0.075$ *nm* and $\nu = 0.19$ into Equation 3.143 and then result into Equation 3.142, we get the required approximate critical curvature for the outermost shell wall in a MWCNT as

$$\kappa_{cr} = \frac{0.1764}{D^2}\ nm^{-1}. \tag{3.144}$$

We will next incorporate Equations 3.144 in our contact model and later verify the results with FE models.

In our micro-mechanical contact model for nano-indentation, we calculate the curvature at the fixed end of CNT_i where it is highest and is given by the following relation (see Section 3.2.2 for the formulation):

$$\left.\frac{1}{\rho}\right|_{\substack{x=0\\ \psi=0}} = \sqrt{\frac{P}{EI}(\cos\alpha - \cos(\psi_o + \alpha))}. \tag{3.145}$$

The curvature is calculated for every CNT that comes in contact with the indentor tip and is deflected from 0° to $\theta_{indentor}$.

3.4.3.1 Point Contact Phase

During the nano-indentation, the curvature of CNT_i can exceed the expected critical curvature calculated from Equation 3.144. Since, Yakobson et al., (1996) and

Iijima et al., (1996) in their MD simulations for SWCNT and DWCNT and Wong et al., (1997) in their experimental result for MWCNT observed that the bending force decreases significantly once buckling occurs, we assume the load P_i stays constant after the beam deflects beyond the critical curvature and until CNT_i transitions to the line contact phase. The constant force assumption can be inappropriate for cases when the deflection is small – indentation with sharp tip, for example; Wong et al., (1997) reported a 30% drop in force that nearly remained constant after buckling. However, for large deflections (indentation with sharp tips) nanotubes can buckle sideways to result in a hinge-like effect and show greater drop in bending force. We will verify the constant load approximation later from finite element simulations of an MWCNT. Next, rearranging Equation 3.134 as

$$(EI)_{Eff} = \frac{P_i L_i^2}{[K(p) - F(p,m)]^2} \tag{3.146}$$

shows that the effective bending stiffness $(EI)_{Eff}$ decreases for larger denominators, with P_i and L_i being constants in the point contact phase. This behavior supports the argument that the effective bending modulus decreases at the onset of the rippling bending mode.

3.4.3.2 Line Contact Phase

Once the slope ψ_{oi} of CNT_i at the tip reaches $\theta_{indentor}$, ψ_{oi} remains constant throughout the line contact phase and produces negligible change in the curvature of the nanotube. Thus the effective stiffness $(EI)_{eff}$ of CNT_i can be assumed to remain constant and equal to the last $(EI)_{eff}$ value solved for at the end of the point contact phase (Equation 3.146). The process then can be thought to be similar to the one discussed earlier in Section 3.4.1.2.

Next, we verify if the proposed changes in the micro-mechanical contact model capture the indentation force-displacement curve behavior when beams buckle. We will verify the validity of the modified contact model by comparing the results from EOR-based MWCNT FE models and experimental data obtained from a VACNT sample indentation.

3.4.4 Results (with buckling)

Here, we first compare the indentation force-displacement results from two FE-based models of a MWCNT; one is able to capture only the pre-buckling behavior, while the other the pre-buckling, the buckling point, and the post-buckling behavior of MWCNTs. Thereafter, we compare the FE model results with our proposed contact models. Lastly, the numerical solutions obtained from nano-indentation of randomly generated MWCNTs are compared with the experimental results obtained from nano-indentation of VACNT samples. The experiments were carried out with both a sharp and a Berkovich AFM tip.

3.4.4.1 Nano-Scale Finite Element Contact Model: Single MWCNT

In this section, we present two FE models simulating the nano-indentation process. In the first model, a MWCNT is constructed from 8-node solid elements (mesh size = 20x20 *nm*) assigned isotropic material properties (E_b = 1.127 *TPa* and v = 0.19); the second model is also constructed in a similar fashion (mesh size = 1.68 *nm* x 1.68 *nm*), but assigned locally orthotropic material properties. The material properties for the second FE model were found via the EOR method proposed in Chapter 2. The MWCNTs constructed in both FE models have length L = 204.96 *nm* and diameter D = 20.4 *nm* and are indented 180.0 *nm* with sharp and Berkovich indentor tips, as shown in Figures 3.24 and 3.25, respectively. The indentor tips in both FE simulations are modeled using rigid elements. The contact between the MWCNT and the indentor is modeled to be frictionless. Next, the boundary conditions are defined to be similar to those applied earlier for macro-scale Teflon tube FE models in Section 3.4.2.2.

The local isotropic material properties for the MWCNT (E_b = 1.127 *TPa* and v = 0.19) in our model were estimated from beam theory. Here an effective bending stiffness $(EI)_{Eff}$ is measured and the bending modulus E_b is determined by assuming an effective moment of inertia $I_{Eff} = \pi(D^4)/64$, where D is the outer diameter. E_b is then computed to be (Qi et al., 2003),

$$E_b \approx \frac{(EI)_{Eff}}{I_{Eff}}, \tag{3.147}$$

where $(EI)_{Eff}$ is estimated from

$$(EI)_{Eff} = E_w \sum_{i=1}^{N} I_i,$$

$$I_i = \frac{\pi}{4}\left[\left(R_i + \frac{t}{2}\right)^4 - \left(R_i - \frac{t}{2}\right)^4\right]. \tag{3.148}$$

In Equation 3.148_1, E_w is the effective wall modulus of the graphite sheet and is taken to be 4.84 *TPa* (Pantano et al., 2004b), and in Equation 3.148_2, I_i, R_i, and t are the moment of inertia, radius and thickness of the wall of the i^{th} tube, respectively; the thickness = 0.075 *nm*. Considering the shear interactions/stiffness between walls to be very low as observed by Cummings and Zettl (2000) and Yu et al., (2000c), we can approximate $(EI)_{Eff}$ of the MWCNT through the sum of the bending stiffness of each tube with Equation 3.148_1 (e.g., Govindjee and Sackman 1999 and Qi et al., 2003).

Figures 3.24 and 3.25 show the FE indentation simulation snapshots at three stages (initial, point contact, and line contact) for MWCNTs having isotropic and locally orthotropic properties for sharp and Berkovich indentor tips, respectively. The corresponding indentation force-displacement results from both FE models are shown in Figures 3.26 to 3.29.

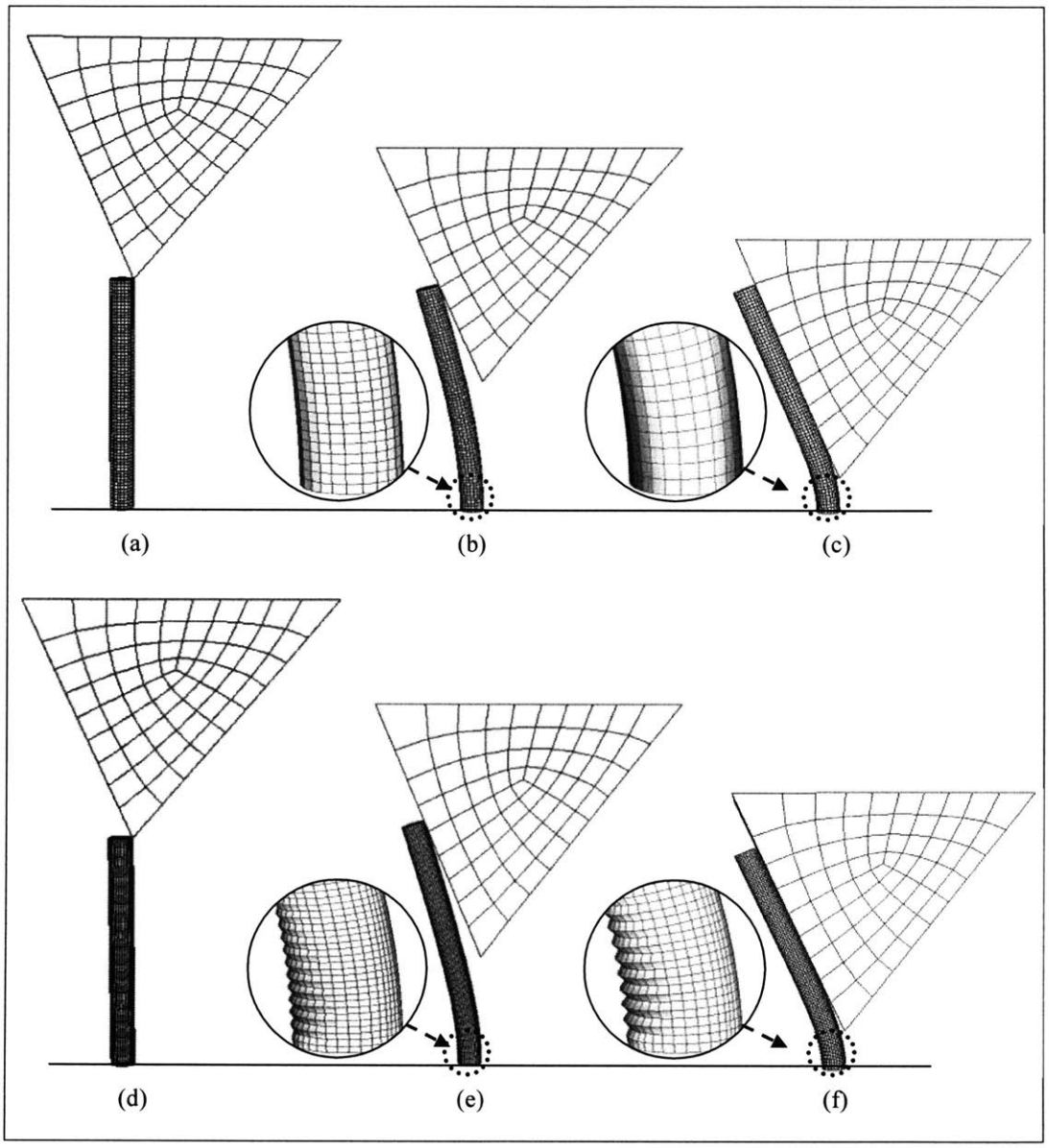

Figure 3.24: Nano-scale finite element simulation for indentation of a MWCNT rigidly fixed at one end. Sharp indentor tip deflecting a single MWCNT beam with isotropic properties (E = 1.127 TPa, v = 0.19) of L = 204.96 nm and D = 20.4 nm shown in initial position, δ = 0 mm (a), point contact phase, δ = 155 mm (b), and line contact phase, δ = 180 mm (c). Sharp indentor tip deflecting a single MWCNT beam with orthotropic properties of L = 204.96 nm and D = 20.4 nm shown in initial position, δ = 0 mm (d), point contact phase, δ = 127 mm (e), and line contact phase, δ = 158 mm (f). The inset view in Figures b, c, e, and f show the rippling occurring in orthotropic model and missing in isotropic model.

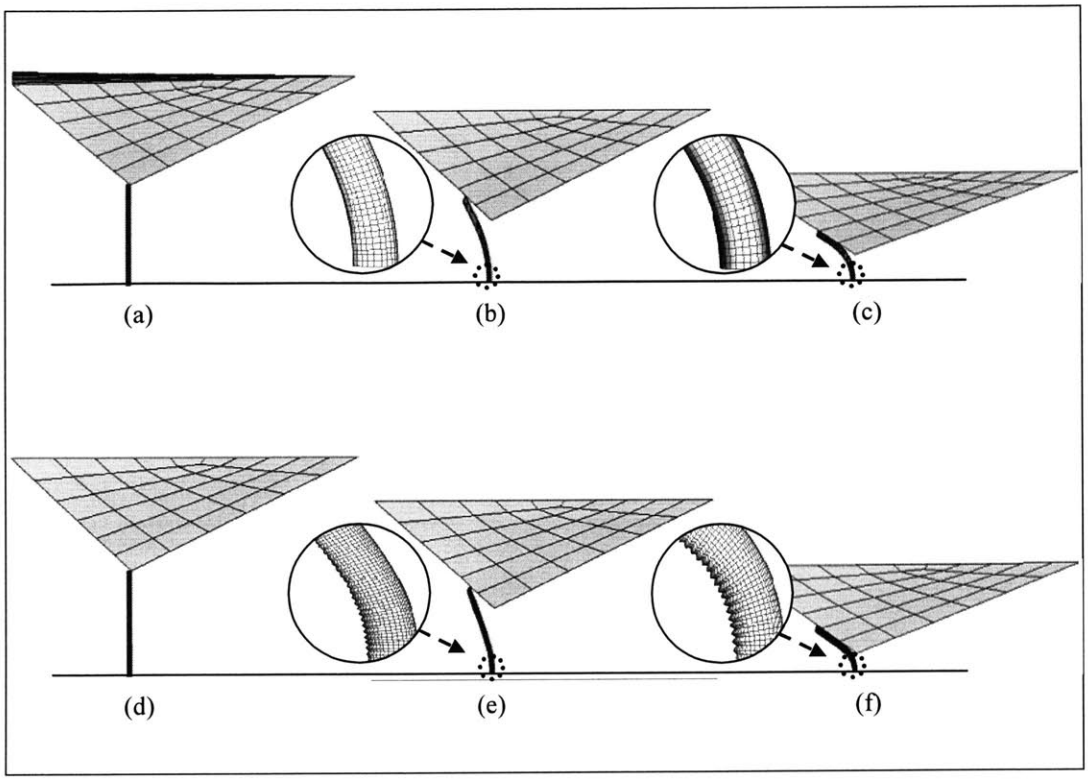

Figure 3.25: Nano-scale finite element simulation for indentation of a MWCNT rigidly fixed at one end. Berkovich indentor tip deflecting single MWCNT beam with isotropic properties of L = 204.96 *nm* and D = 20.4 *nm* shown in initial position, δ = 0 *mm* (a), point contact phase, δ = 50 *mm* (b), and line contact phase, δ = 140 *mm* (c). Berkovich indentor tip deflecting a single MWCNT beam with orthotropic properties of L = 204.96 *nm* and D = 20.4 *nm* shown in initial position, δ = 0 *mm* (d), point contact phase, δ = 50 *mm* (e), and line contact phase, δ = 160 *mm* (f). The inset view in Figures b, c, e, and f show the rippling occurring in orthotropic model and missing in isotropic model.

Figures 3.24 and 3.25 show that the net macroscopic deformations of EOR-based beams as a whole (a, b, c in Figures 3.24 and 3.25), do not differ when compared with their isotropic counterparts (d, e, f in Figures 3.24 and 3.25). However, the inset views in Figures 3.24 (e and f) and 3.26 (e and f) clearly show both models to differ, in that the EOR-based FE model of the MWCNT is able to capture the buckling of the MWCNT on indenting, while the isotropic version of a similar beam fails to do so, as shown in Figures 3.24 (b and c) and 3.25 (b and c).

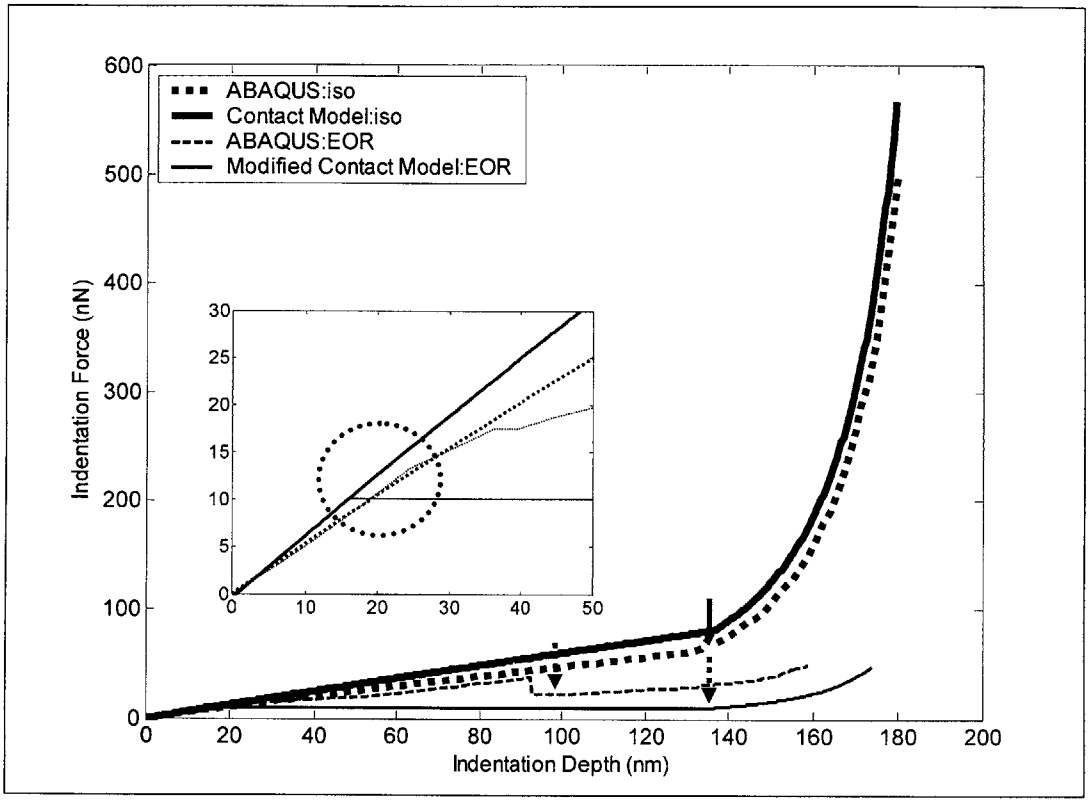

Figure 3.26: Force versus penetration depth curves from finite element and contact models of nano-scale model. Single MWCNT tube (L = 204.96 *nm*, D = 20.4 *nm*, E = 1.127 *TPa*, υ = 0.19) was indented with a sharp indentor tip ($\theta_{indentor}$ = 21.6°). The inset picture is the close-up view of the beginning portion of the curves. The solid- and dotted-arrows indicate the beginning of the line contact phase for isotropic and EOR models, respectively. The dotted black circle in the inset view represents the buckling point.

Figures 3.26 and 3.27, and Figures 3.28 and 3.29 respectively show the indentation force-penetration (*f-p*) depth results obtained from the FE nano-indentation simulations for both tips. Figures 3.26 to 3.29 show that the proposed contact model captures remarkably the *f-p* curve behavior for the MWCNT constructed from elements with isotropic material properties; however, that is not the case for the EOR-based model. The first change in slope of the *f-p* curves obtained from EOR FE models in Figures 3.26 and 3.29 suggest that the overall load for buckling is higher than that predicted from outer wall only and is affected by the inner walls; the sudden change in slope indicates the point when the innermost tube buckles. Applying thin shell theory buckling criteria

(Equation 3.144), the modified contact model is able to predict the pre-buckling behavior as well as the buckling initiation point, as shown in the inset views in Figures 3.26 and 3.28. When the buckling initiates, several kinks occur at discrete locations on the compressive side of the MWCNT, as shown in Figure 3.30-a; this is equivalent to the formation of a single kink in a SWCNT, as shown in the FE simulations by Pantano et al., (2004b). On further indenting, the kinks propagate and become distributed on the entire compressive side of the MWCNT, as shown in Figure 3.30-b; this is equivalent to the propagation and the development of multiple kinks due to van der Waals forces when a SWCNT is bent further (Pantano et al., 2004b). For actual MWCNTs we suggest that the

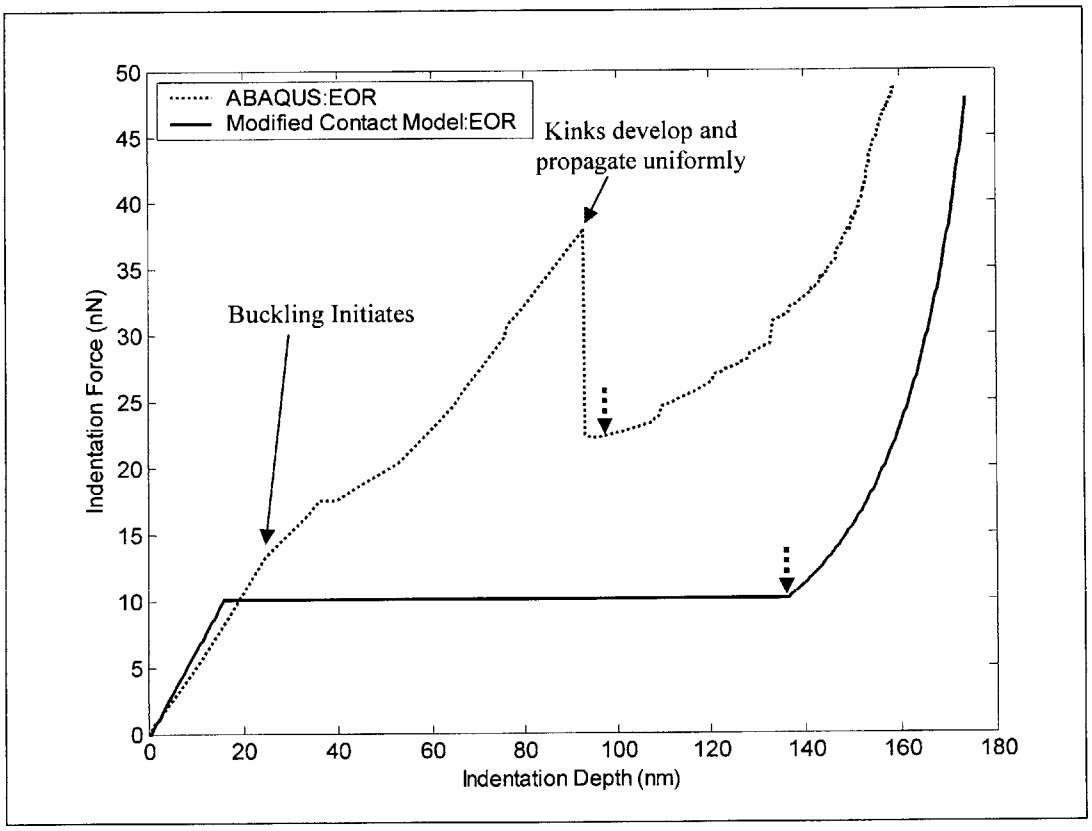

Figure 3.27: Force versus penetration depth curves from finite element and contact models of nano-scale model. Single EOR-based MWCNT tube (L = 204.96 *nm*, D = 20.4 *nm*) was indented with a sharp indentor tip ($\theta_{indentor}$ = 21.6°). The dotted-arrow indicates the beginning of the line contact phase.

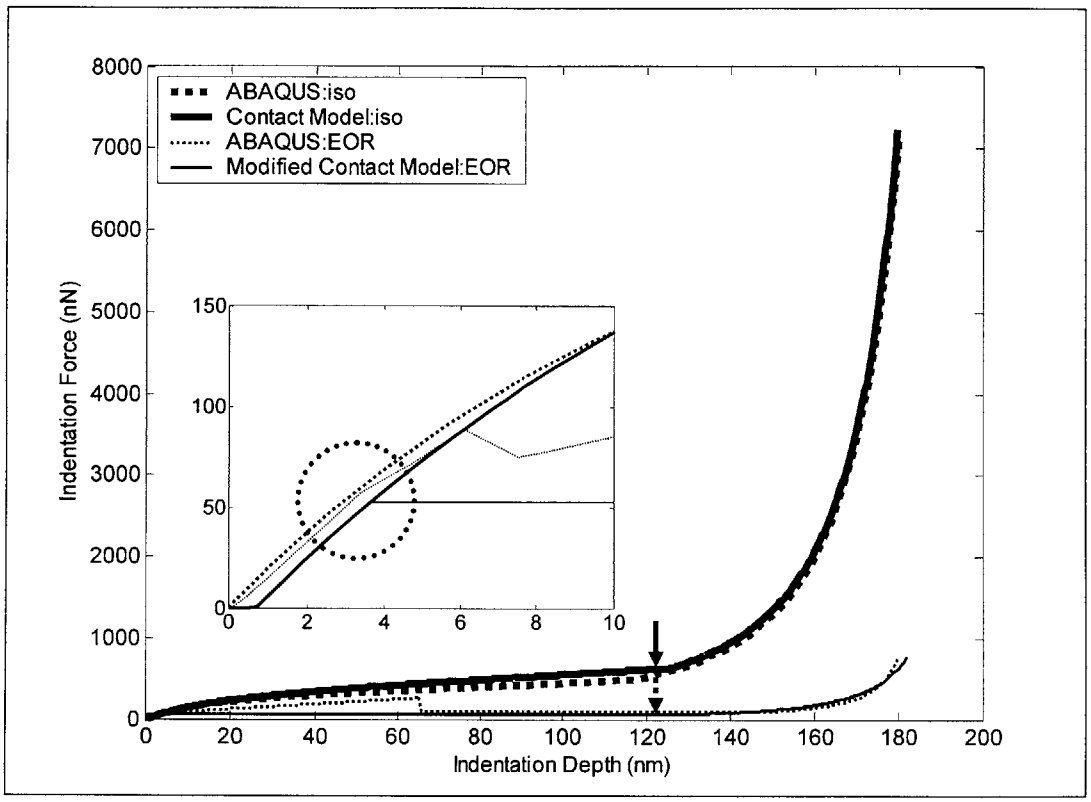

Figure 3.28: Force versus penetration depth curves from finite element and contact models of nano-scale model. Single MWCNT tube (L = 204.96 *nm*, D = 20.4 *nm*, E = 1.127 *TPa*, υ = 0.19) was indented with a Berkovich indentor tip ($\theta_{indentor}$ = 65.35°). The inset picture is the close-up view of the beginning portion of the curves. The solid- and dotted-arrows indicate the beginning of the line contact phase for isotropic and EOR models, respectively. The dotted black circle in the inset view represents the buckling point.

Unlike the pre-buckling and buckling point behavior, the post-buckling behavior of the *f-p* curves differ widely throughout for the sharp tip case and initially for the wide tip case. The dotted arrows in Figures 3.28 and 3.30 indicate the transition point during the indentation when the MWCNT transitions from point contact to line contact phase for EOR-based and isotropic-based MWCNT models, respectively. The arrows reveal that buckling in the EOR-based MWCNT model causes the transition to the line contact phase to lead for the sharp tip (by approx. 40 *nm*), and lag (by approx. 10 *nm*) for the Berkovich tip when compared to their respective isotropic-material MWCNT models. The transition point, however, remains unchanged in the *f-p* curves from the modified contact model.

The change in transition point depends on the occurrence of the hinge effect, which takes place when buckling is distributed everywhere. The hinge effect occurs because the local nanotube flattening causes a sudden change in the curvature of the nanotube, further resulting in a sudden collapse in indentation force. Recall that the plateau region of the *f-p* curve is the regime where the effective bending stiffness of MWCNT decreases with the emergence of the rippling bending mode.

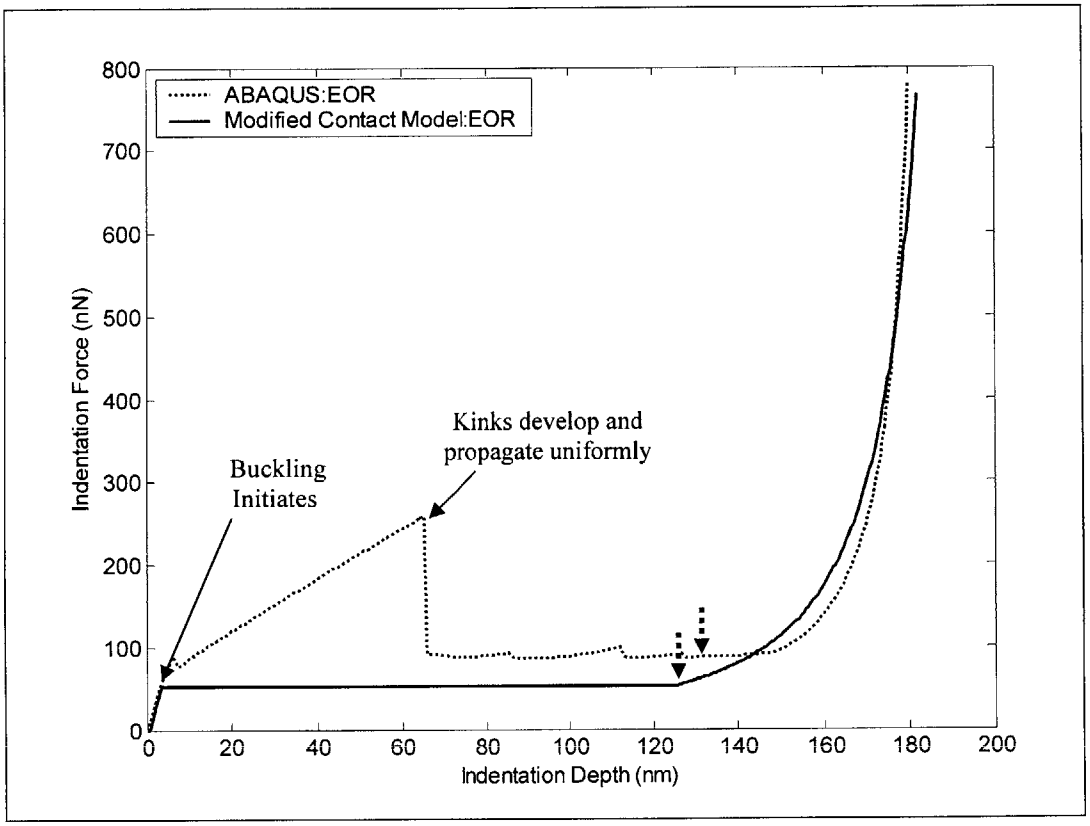

Figure 3.29: Force versus penetration depth curves from finite element and contact models of nano-scale model. Single EOR-based MWCNT tube (L = 204.96 *nm*, D = 20.4 *nm*) was indented with a Berkovich indentor tip ($\theta_{indentor}$ = 65.35°). The dotted –arrows indicates the beginning of the line contact phase.

The plateau region in Figure 3.30 is larger than in Figure 3.28; this indicates that the constant force assumption after buckling in our modified contact model for the sharp tip case is not valid, and better results may be expected with our unmodified contact

model. For the Berkovich tip, our proposed modified contact model seems to reasonably capture the overall *f-p* curve behavior obtained from simulating the indentation of the EOR-based MWCNT model.

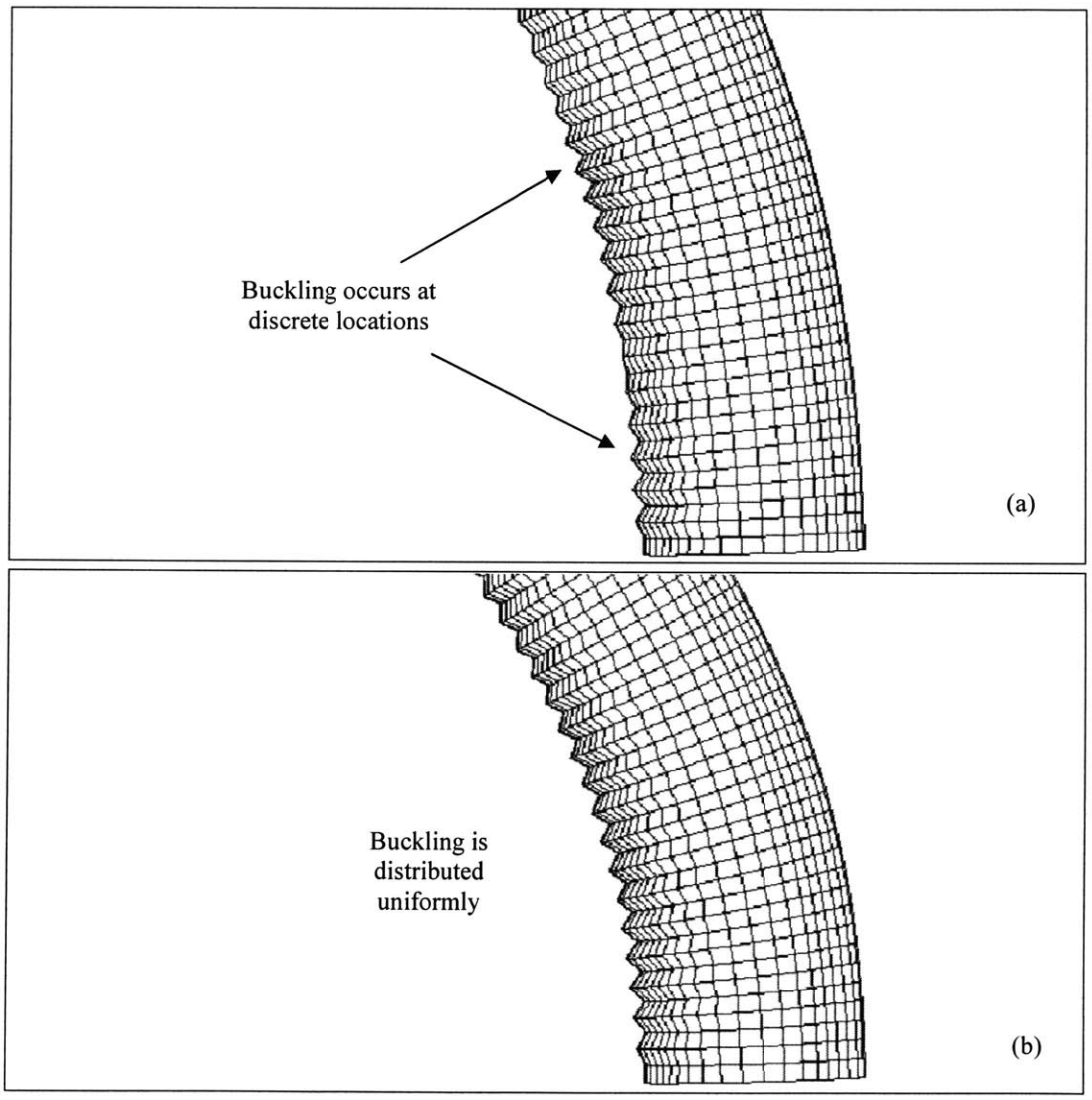

Figure 3.30: Enlarged snapshot view of the EOR-based FE model of MWCNT in rippling bending mode from Figure 3.25-e and -f. Buckling occurs at discrete location when buckling initiates ($\delta = 40\ nm$) (a). Buckling progresses and is distributed uniformly ($\delta = 70\ nm$) (b).

Based on comparison of the two contact models with FE simulations, we propose to use the contact model (without buckling) for sharp tips and the modified contact model (with buckling) for the Berkovich tips. However, ignoring the buckling in simulations with a sharp tip will result in a slight over-estimation of the effective bending stiffness for VACNTs having high areal density. The error will be small for low density VACNT samples because of the shape of the indentor tip; only a few of the CNTs will deflect to extreme angles. Similarly, ignoring the complex buckling mechanics in our modified contact model for the Berkovich tip will result in a slight over-estimation of the effective bending stiffness. Using a better set of equations that capture the proper buckling mechanics can fix this problem in future.

By modeling the mechanics of MWCNTs subjected to large deflections and buckling, we compare the modified contact model for randomly generated VACNT with experimental data.

3.4.4.2 Nano-Scale Contact Model: VACNT Forests

In order to check the validity of our modified contact model, we conducted nano-indentations experimentally on two VACNT samples and compared the results with our numerical solutions.

Experimentations

Two VACNT forest samples were prepared at the University of Cambridge with the PECVD (Plasma Enhanced Chemical Vapor Deposition) method (Chhowalla et al., 2001) with different nickel catalyst thicknesses (ranging from 3.5 to 7 *nm*) and growth time. The samples were then studied under a JOEL SEM, with the samples tilted at 0° (observed from top), 15°, and 25° relative to the vertical. Figure 3.31 shows images of the samples tilted at 25° clearly revealing the forest-like landscapes of the VACNTs (Qi et al., 2003).

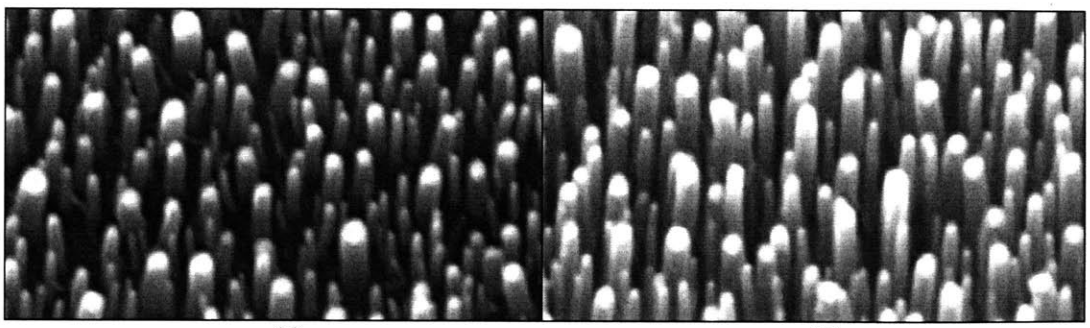

(a) (b)

Figure 3.31: Vertically aligned carbon nanotubes: sample A (a); sample B (b). The samples are tilted by 25° to reveal the forest-like landscapes.

The areal density (number of tubes per μm^2 of substrate) measurement for each sample was measured by counting the number of nanotubes in the image, then dividing the total number of nanotubes by the total area of the image. Measurements were made on images with the sample tilted at 25°. The diameter and the length were measured from images with the samples tilted at 0° (for diameter only), 15°, and 25°, respectively. For each image, at least 30 nanotubes were randomly selected for measurements. The length and diameter measurements were further verified by measuring nanotubes that had been laid flat on the substrate. The average and deviation of diameter and length, and the areal density for each of the two samples are listed in Table 1.

Table 1: Dimensions of the two VACNT samples (Qi et al., 2003).

Sample	**Outer diameter**		**Length**		**Areal density**	
	Average D_o (nm)	Deviation σ_D (nm)	Average L (nm)	Deviation σ_L (nm)	m (μm^{-2})	Percentage of area covered by CNTs (%)
A	90	15	1100	160	26	17
B	139	38	1380	233	19	15

Nano-indentation tests on VACNT forests with a sharp tip were conducted with Digital Instrument Dimension 3100 SPM (Scanning Probe Microscopy), while a Hysitron TriboIndenter was used for the Berkovich tip. The sharp diamond tip cantilever in Dimension 3100 SPM is made of stainless steel. The working resonant frequency is about

55 to 60 *kHz* in the tapping mode. According to the specification from the sharp tip supplier, the radius of the diamond tip is less than 25 *nm*. The TriboIndenter uses a diamond Berkovich tip with a half angle reported to be 65.35° by the supplier. The unique design of the TriboIndenter does not require a cantilever beam design.

The standard procedure for nano-indentation tests within an AFM was followed. The tapping mode is first engaged to scan the surface and the area of interest is located. When nano-indentation is initiated, the tip is lifted slightly (typically about 100-300 nm) above the surface. As the nano-indentation is executed, the tip is driven by the piezo-scanner toward the surface until a pre-set reaction force is reached. The tip is then retracted back to its initial position. The procedure for the TriboIndentor is similar, except that the area of interest is located visually by avoiding any scratches on the sample surface. Thereafter, indentation force versus indentor tip displacement data points are collected by nano-indenting the VACNT sample; each indentation was performed at a different location, separated by nearly 800 *nm*. For better quality of results, 30 indentations on each sample, and *f-p* curve data were collected; the data obtained from 10 such nano-indentations on a VACNT with the both tips are shown in Figures 3.32 and 3.33, respectively.

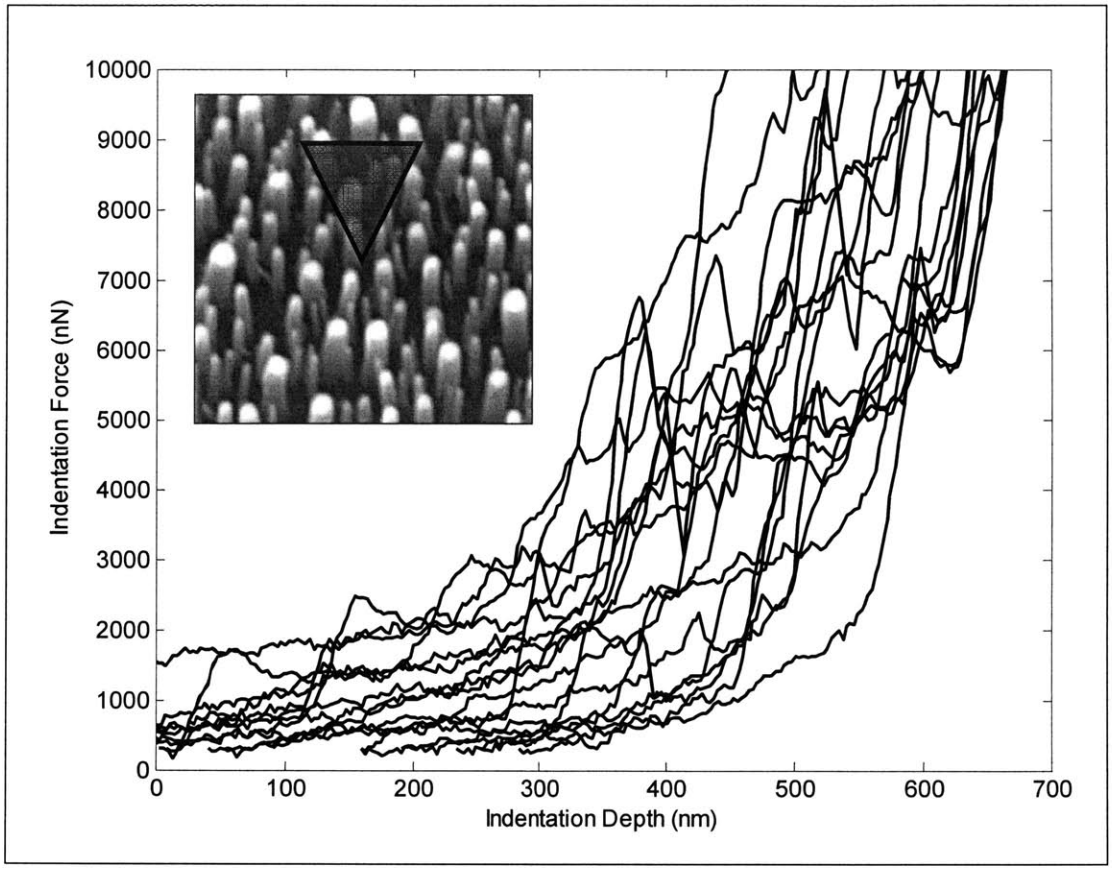

Figure 3.32: The indentation force-displacement curves obtained on random nano-indentations on a VACNT forest with a sharp tip. The inset view shows the SEM image of sample A along with a schematic of a sharp tip indentor.

The inset views in Figures 3.32 and 3.33 show the SEM image of the respective samples with a schematic of the two indentor tips. The data taken via AFM is noisy compared to that taken from TriboIndenter. Inset-B view in Figure 3.33 show a sudden rise and then drop in the indentation force in the beginning of the curves; this sudden drop behavior is expected due to the buckling of CNTs on indenting with a virtually flat Berkovich indentor tip, as was observed from finite element simulations earlier.

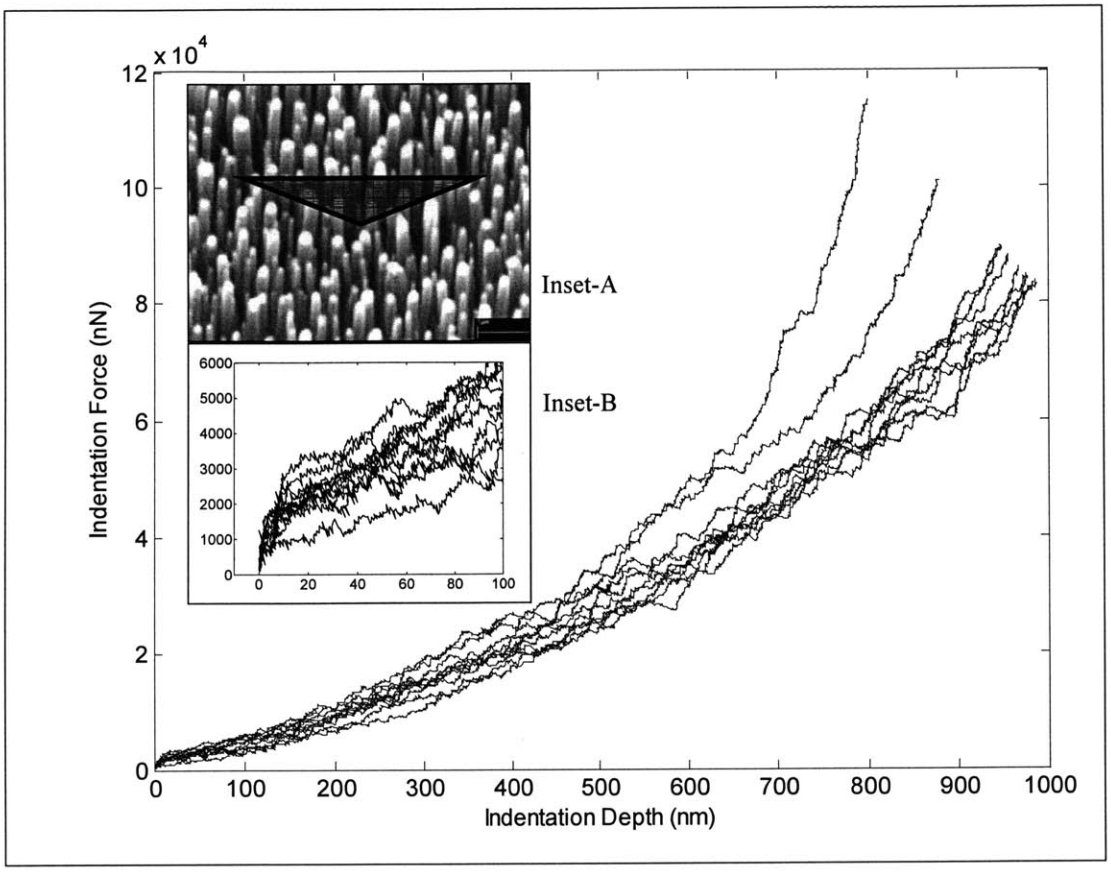

Figure 3.33: Random nano-indentation on a VACNT forest with a Berkovich tip. The corresponding indentation force-displacement curves. Inset-A shows the SEM image of sample B along with a schematic of a Berkovich tip indentor. Inset-B shows the closeup-view of the indentation force-displacement curves.

Simulations

Here we applied the modified micro-mechanical contact model to randomly generated MWCNTs of various length and diameter; a Gaussian distribution method is applied in conjunction with the data in Table 1 to generate the MWCNTs (Qi et al., 2003). The randomly generated MWCNTs mimic the VACNT samples used for nano-indentation experimentation (see the inset views of Figures 3.34 and 3.35). Several *f-p* curves similar to the experimental ones are obtained from the simulations (Figures 3.34 and 3.35). An average of several *f-p* curves from the simulations and the

experimentations are then compared. The nano-indentation simulations were repeated by changing the average effective bending stiffness until the two average *f-p* curves match. The process is completed twice: first with a sharp tip and second with a Berkovich tip; the final average *f-p* curves are shown in Figures 3.36 and 3.37.

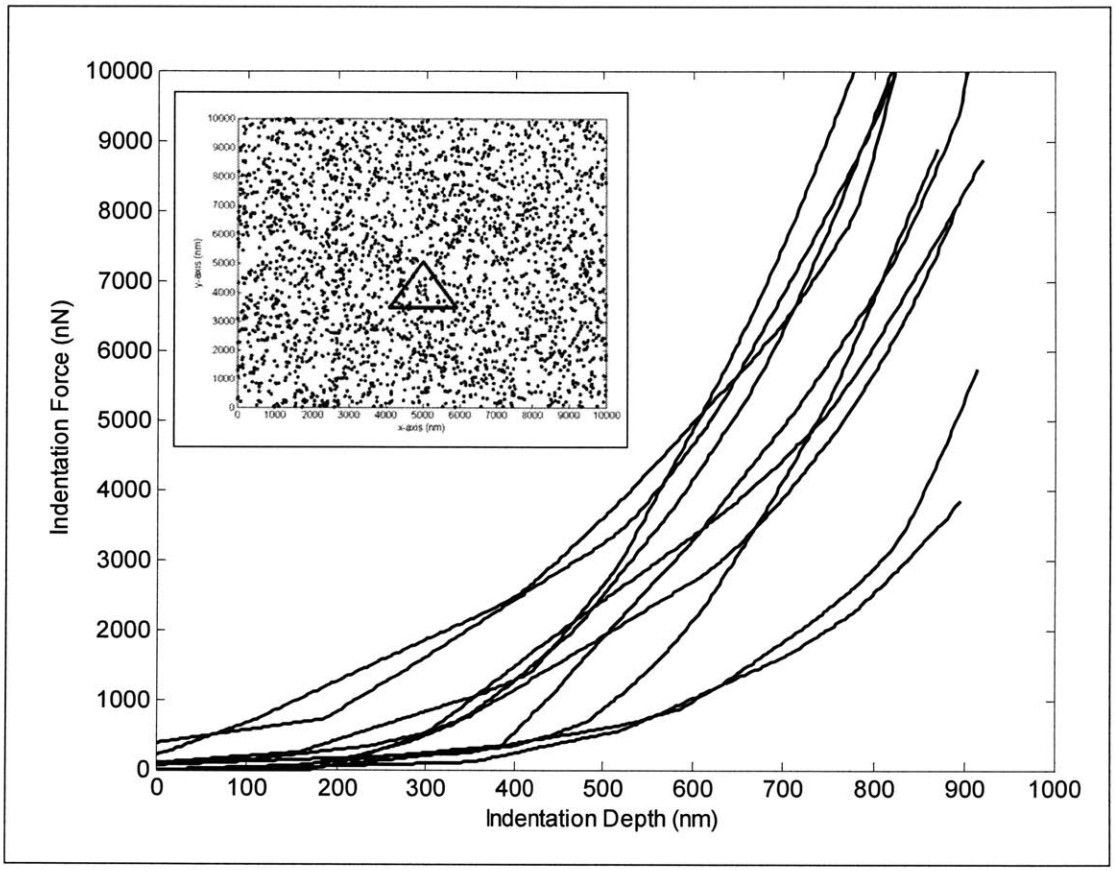

Figure 3.34: Random nano-indentation with sharp tip on a VACNT forest. Nanotubes are randomly distributed using Gaussian distribution method. The corresponding indentation force-displacement curves. Inset view shows the simulated sample A.

Indentation force-penetration data in Figures 3.34 and 3.35 obtained from the simulations show behaviors similar to their experimental counterparts in Figures 3.32 and 3.33, respectively. The curves in Figure 3.34 are somewhat linear during the initial indentation depth while that in Inset-B in Figure 3.35 show a sudden drop due to buckling, observed earlier in Inset-B in Figure 3.33. Recall that in our modified contact model for simulating nano-indentations with a Berkovich tip, we ignored the real

buckling phenomenon in which buckling gradually propagates inwards; on the other hand, the modified contact model captures it in a more abrupt way because the buckling of all the inner tubes coincides with the buckling of the outermost tube .

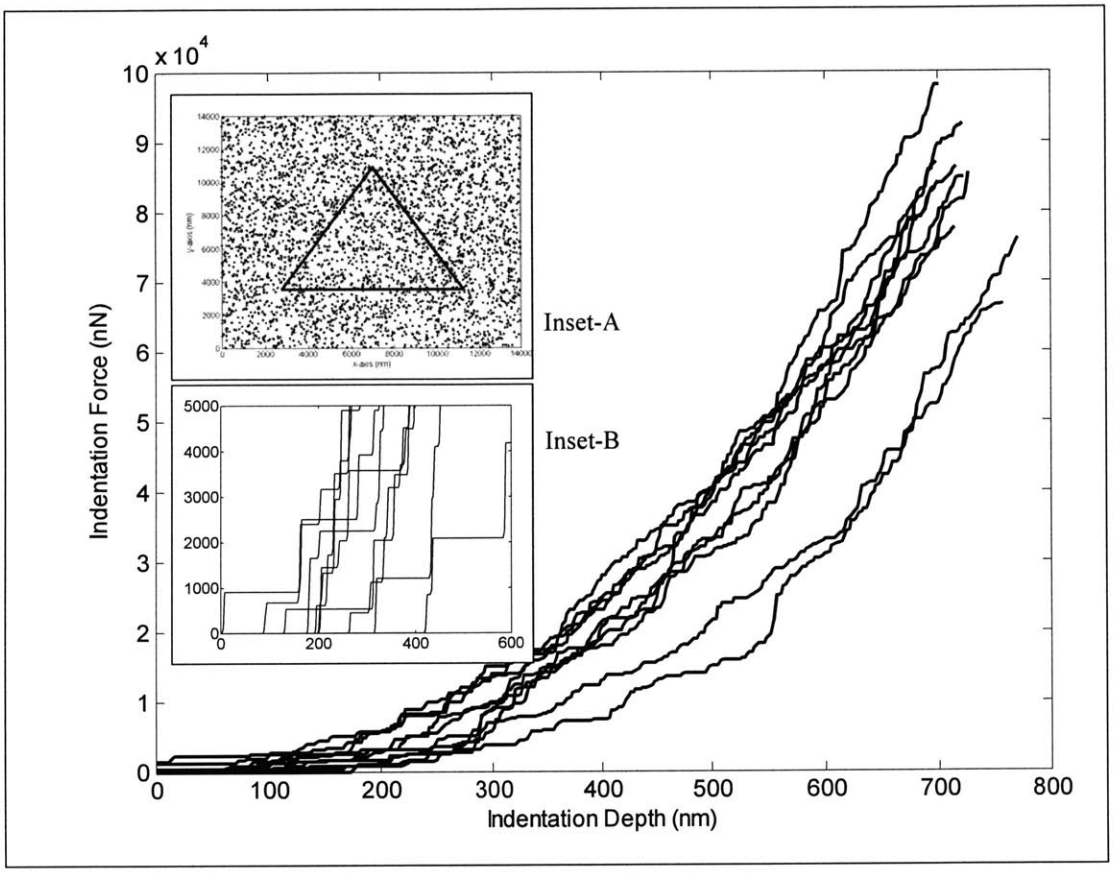

Figure 3.35: Random nano-indentation with Berkovich tip on a VACNT forest. Nanotubes are randomly distributed using Gaussian distribution method. The corresponding indentation force-displacement curves. Inset-A shows the SEM image of simulated sample B along with a schematic of a Berkovich tip indentor. Inset-B shows the closeup-view of the indentation force-displacement curves.

To our surprise, the average simulation curve in Figure 3.36 is able to capture the average experimental curve behavior to higher indentation load values; the average effective bending stiffness $(EI)_{Eff}$ thus found was approximately 4.4 $N.nm^2$. Thereafter, substituting the average length and diameter values of sample A CNTs along with the average $(EI)_{Eff}$ into Equation 3.147, we get the effective bending modulus E_{bEff} to be 1.1

TPa. The predicted average E_{bEff} of approximately 1.1 *TPa* matches the average reported value of CNTs in the literature. Similarly, the average simulation curve in Figure 3.37 is able to capture the average experimental *f-p* curve to extremely high load values and indentation depth; the average $(EI)_{Eff}$ for Sample B was found to be approximately 25.7 $N.nm^2$. Repeating the above calculations, the average E_{bEff} was found to be approximately1.08 *TPa*. Because of the inability of our modified contact model to completely capture the buckling mechanics, the average E_{bEff} value of 1.08 *TPa* can be slightly overestimated. Nonetheless, both micro-mechanical contact models seem to provide reasonable average E_{bEff} values, while capturing the *f-p* curve behavior.

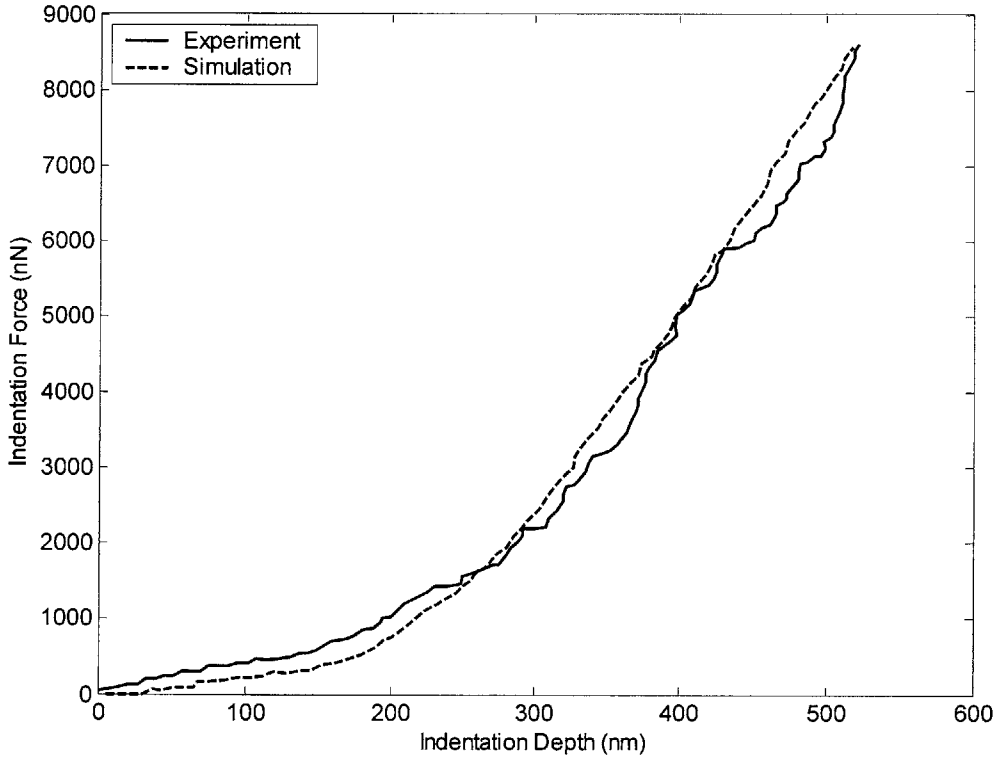

Figure 3.36: Average force versus penetration depth curves from modified micro-mechanical contact model and experimentation using sharp AFM tip. The average tube length and diameter are 1100.0 *nm* and 90.0 *nm*, respectively. VACNT sample of average tube L = 1100.0 *nm*, D = 90.0 *nm* was indented with a sharp tip indentor (semi-apex angle = 21.6°). $EI = 4.4\ N.nm^2$ and E_b = 1.1 *TPa*.

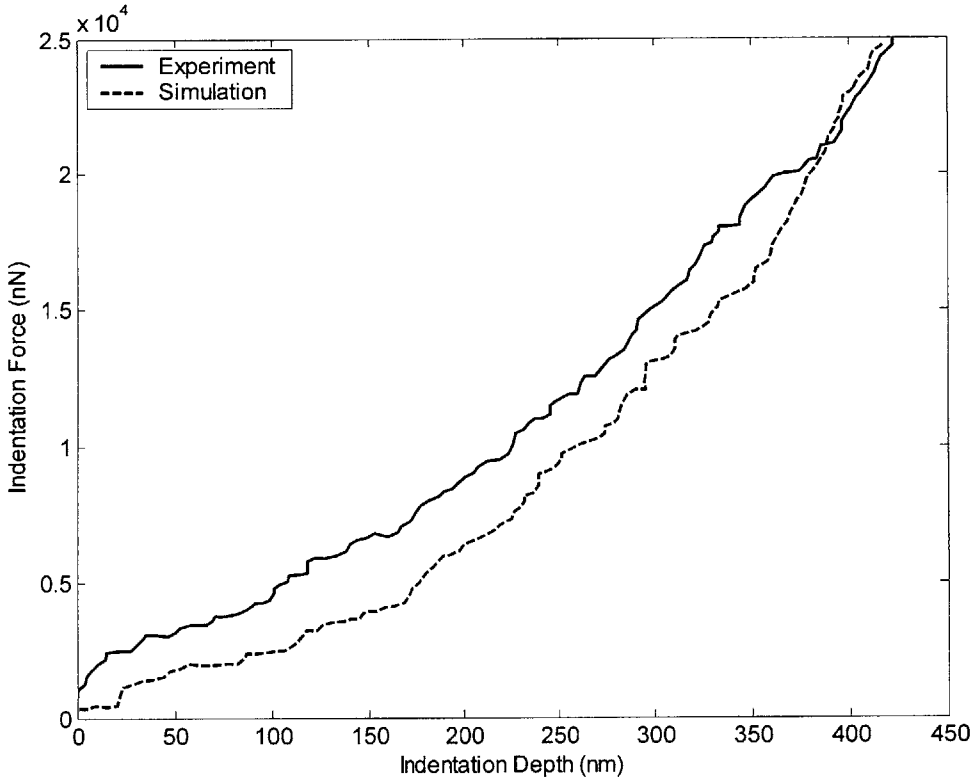

Figure 3.37: Force versus penetration depth curves from modified micro-mechanical contact model and experiment using Berkovich AFM tip. VACNT sample of average tube L = 1380.0 *nm*, D = 139.5 *nm* was indented with a Berkovich tip indentor (semi-apex angle = 65.35°). EI = 25.7 $N.nm^2$ and E_b = 1.08 *TPa*.

3.5 Mechanics of Nano-Scratching of Nanotube Arrays

In the preceding section, we proposed two micro-mechanical contact models: one accounting for large nonlinear deformation of MWCNTs, and another, for the initial buckling of the MWCNTs. Here, we propose a process, nano-scratching, whereby nanotubes are bent to extremely large deflections by laterally displacing an AFM indentor tip perpendicular to the longitudinal axis of the nanotube. A schematic diagram of nano-scratching on a VACNT sample is shown in Figure 3.38. In addition to the same flexibilities provided by nano-indentation, including adaptable three-sided pyramidal

indentor tips and variable indentation depths, nano-scratching also provides the benefit of reducing experimental effort. Whereas several nano-indentations are necessary to acquire a statistical average of mechanical properties, such may not the case for nano-scratching, whereby local averages can be obtained via a single experiment. The challenge involved in formulating such a complex model was another impetus for pursuing nano-scratching. Because of this complexity, and in order to capture the basic physics of the model, we ignored the interactions between the nanotubes (Figure 3.38) and assume negligible friction between the nanotubes and the indentor.

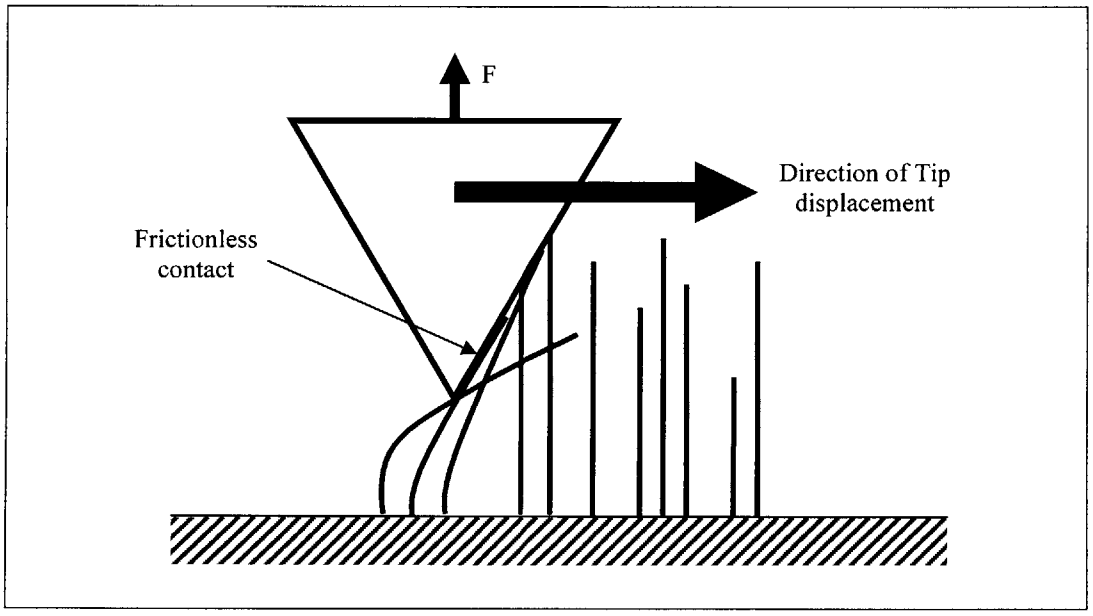

Figure 3.38: Schematic of nano-scratching of a VACNT sample with an AFM tip.

In the following sections, we propose two micro-mechanical contact models for the nano-scratching with a sharp and Berkovich shaped indentor tips. The first proposed contact model considers only large deflections resulting from the lateral displacement of the indentor tip. The second model incorporates an approximate approach for capturing the influence of buckling of CNTs on vertical force-lateral displacement (*f-d*) curves.

3.5.1 Micro-Mechanical Contact Model (without buckling)

We propose a micro-mechanical contact model by extending the three-dimensional contact model for nano-indentation and dividing the scratching contact model into three phases: end-point contact, line contact and point contact. The end-point contact phase indicates the regime where the indentor makes a point contact with the free end of the CNT to apply a point load on the nanotube, as shown in Figure 3.39-a. The line contact phase indicates the regime where the indentor makes a line contact with the CNT to apply a nonuniform distributed load, as shown in Figure 3.39-b. Lastly, the point contact phase indicates the regime of deformation where a point load is applied at a point somewhere perpendicular on the longitudinal axis of the CNT, as shown in Figure 3.39-c. In the last phase, only the edge of the indentor tip comes in contact with a point on the axis of the CNT. Notice that the end-point contact and line contact phases in the nano-scratching process, with the exception of the tip displacement direction, appear similar to the nano-indentation process.

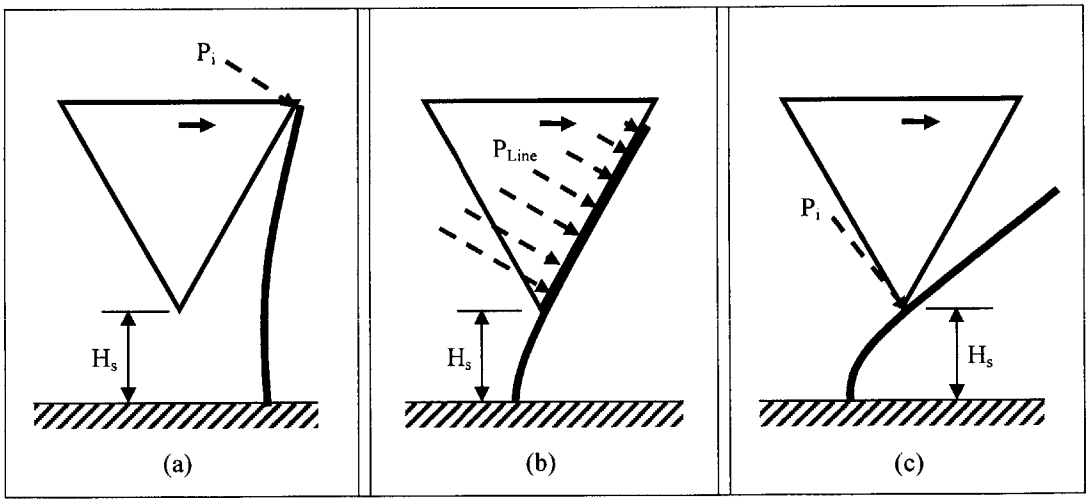

Figure 3.39: Schematic reveals three phases of nano-scratching process: end-point contact phase (a), line contact phase (b), and point contact phase (c).

Although a typical scratching experiment initiates with the vertical displacement of the indentor tip, which is followed by lateral displacement, we ignore the nano-indentation part in our contact model. If desired, both nano-indentation and nano-

scratching contact models could be combined with ease in the end to capture the complete scratching process. Here it should be noted that upon indentation, the CNTs initially come into contact on all three indentor tip surfaces, i.e., two sides and the back, as shown in Figure 3.40. Upon lateral displacement, the CNTs in contact with the back surface start to unbend, after which, only the side surfaces of the indentor make contact with the CNTs.

In the following two subsections, we first formulate the theoretical contact model for each phase. Second, the micro-mechanical contact model is verified against the results from macro-scale experiments (Ebeling, 2004) and finite element models based on the macro-scale experiments.

3.5.1.1 End-Point Contact Phase ($\psi_{oi} < \theta_{indentor}$)

Figure 3.39-a shows that, at any given instance, the end point contact phase in nano-scratching is similar to the point contact phase for nano-indentation. See Section 3.4.1.1. Because in nano-scratching, the indentor tip displaces laterally rather than vertically, the lateral motion can be transformed into an equivalent vertical displacement, such that the existing point contact phase of the nano-indentation model can be adopted.

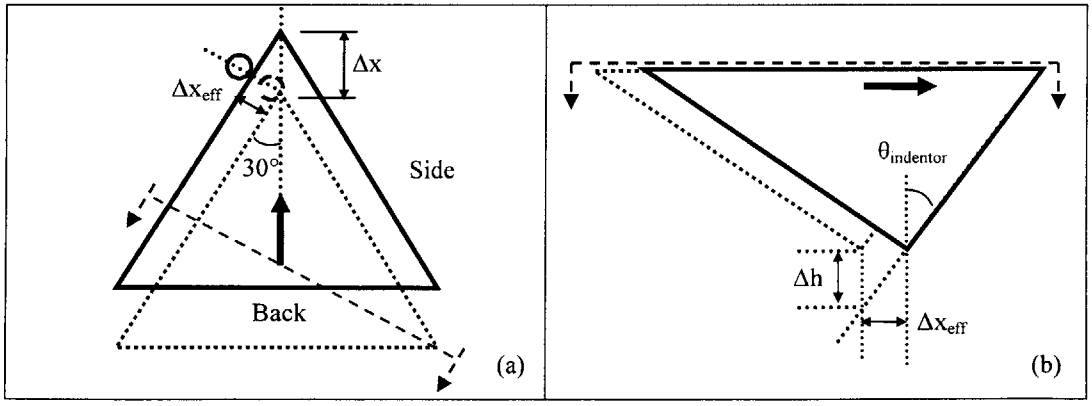

Figure 3.40: Two-dimensional geometrical representation of the indentor tip used to convert the lateral increment into the vertical depth increment; top-view (a), side-view (b). Red dash line indicates direction of the view for side view.

The difference in the direction of the indentor displacement is accounted for with the help of a conversion factor found from geometry, as shown in Figure 3.40; this factor converts the lateral scratch increment (Δx) into a vertical depth increment (Δh) and is given by

$$\Delta x_{eff} = \Delta x \sin(30°), \tag{3.149}$$

$$\Delta h_{sides} = \Delta x_{eff} / \tan \theta_{indentor}, \tag{3.150}$$

$$\Delta h_{back} = \Delta x / \tan \theta_{indentor}. \tag{3.151}$$

Equations 3.150 and 3.151 are applied to the side and the back surfaces of the indentor tip, respectively. Thereafter, applying the conversion factor to the nano-indentation contact model at a known lateral displacement $X_{Lateral}$ yields the point load P_i applied by the indentor to CNT_i; $X_{Lateral}$ is the sum of all lateral displacement increments Δx. Similarly P_i is found for all CNTs that come in contact with the indentor tip. Then, P_i values for all CNTs are added together and substituted into Equation 3.140 to solve for the net vertical component of the force F, applied by the indentor located at $X_{Lateral}$. The value for γ in Equation 3.140 is still found from the inequality in Equation 3.141. Substituting the separation distance between the indentor tip and the base of the VACNT sample, H_s for H - h in Equation 3.141 changes the inequality and yields (see Figure 3.39):

$$H_s + x \tan\left(\frac{\pi}{2} - \theta_{indentor}\right) \leq L_i. \tag{3.152}$$

When ψ_{oi} is equal to $\theta_{indentor}$, CNT_i transitions to the line contact phase.

3.5.1.2 Line Contact Phase ($\psi_{oi} = \theta_{indentor}$)

Like the previous phase, the line contact phase in the nano-scratching model is also similar to the line contact phase in nano-indentation; a two-dimensional representation of the line contact phase in nano-scratching is shown in Figure 3.39-b. In

this phase, ψ_{oi} equals $\theta_{indentor}$. Because of the similarity between the two line contact phases in nano-indentation and scratching, we apply Equations 3.150 and 3.151 to the theoretical model formulated in Section 3.4.1.2 to convert the horizontal increment of the indentor tip into the vertical increment in the nano-indentation contact model. Thereafter, the load P_i for CNT_i is added to the load values for CNTs in the point and line contact phase, and substituted into Equation 3.141 to obtain the net vertical force F.

3.5.1.3 Point Contact Phase ($\psi_{oi} > \theta_{indentor}$)

The point contact phase in nano-scratching refers to the regime where CNT_i makes a point contact with the indentor edge, rather than the indentor surface; a two-dimensional schematic of the point contact phase is shown in Figure 3.39-c. In addition, the resisting concentrated load on the indentor as a result of deflecting CNT_i acts in such a way that it is always perpendicular to the edge of the indentor and the longitudinal axis of the CNT_i; this point contact between the CNT_i and the indentor edge results in α to vary, as shown in Figure 3.41. Notice that in this phase, the ψ_{oi}, α, and the effective length L_i of CNT_i are all variables and that the sum of α and ψ_{0i} is always fixed at 90°; this means that while the tip moves laterally, if angle α decreases then ψ_{0i} increases. The effective length of CNT_i increases because the contact point between the indentor's edge and CNT_i moves closer to the free end continuously until it detaches from CNT_i, as shown in Figure 3.41.

To deal with a number of unknowns in this phase, we first find a relation between the inclination angle α and scratch location Δx in terms of Δh in Equation 3.154. The relation is found by first solving for discrete points (Δh, α) based on the last known L_i from the previous line contact phase, and then increasing ψ_{oi} beyond $\theta_{indentor}$ to approximately 145° in beam theory equations listed in Section 3.2.4. Thereafter, a sixth order polynomial is fitted through the discrete points to obtain the required relation between α and Δh. The iterative process is repeated whenever L_i changes. In this phase, we approximate the incremental change in L_i, (δL_i) by using the following relation derived from the two-dimensional geometry shown in Figures 3.42-a and 3.42-b.

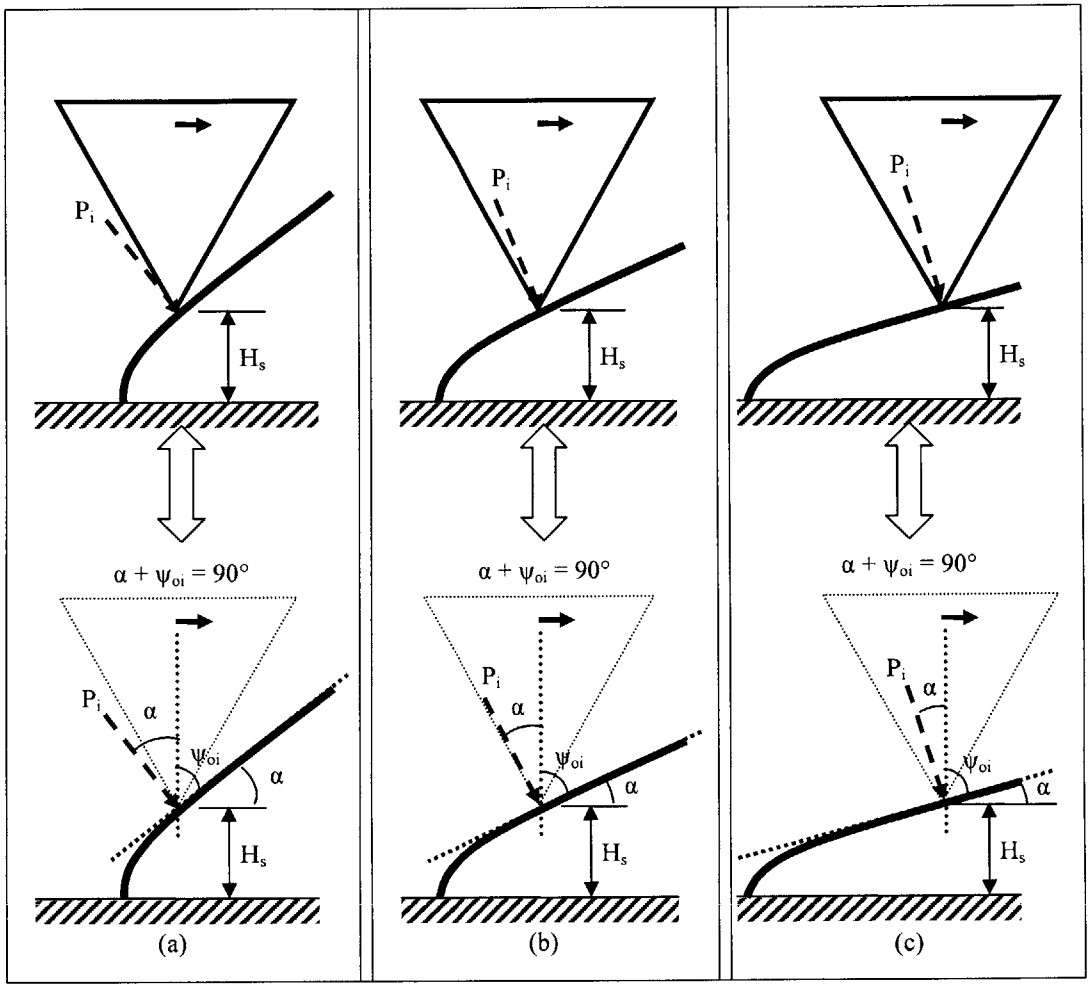

Figure 3.41: Two-dimensional geometrical representation of the indentor tip used to convert the lateral increment into the vertical depth increment; top-view (a), side-view (b). Red dash line indicates direction of the view for side view.

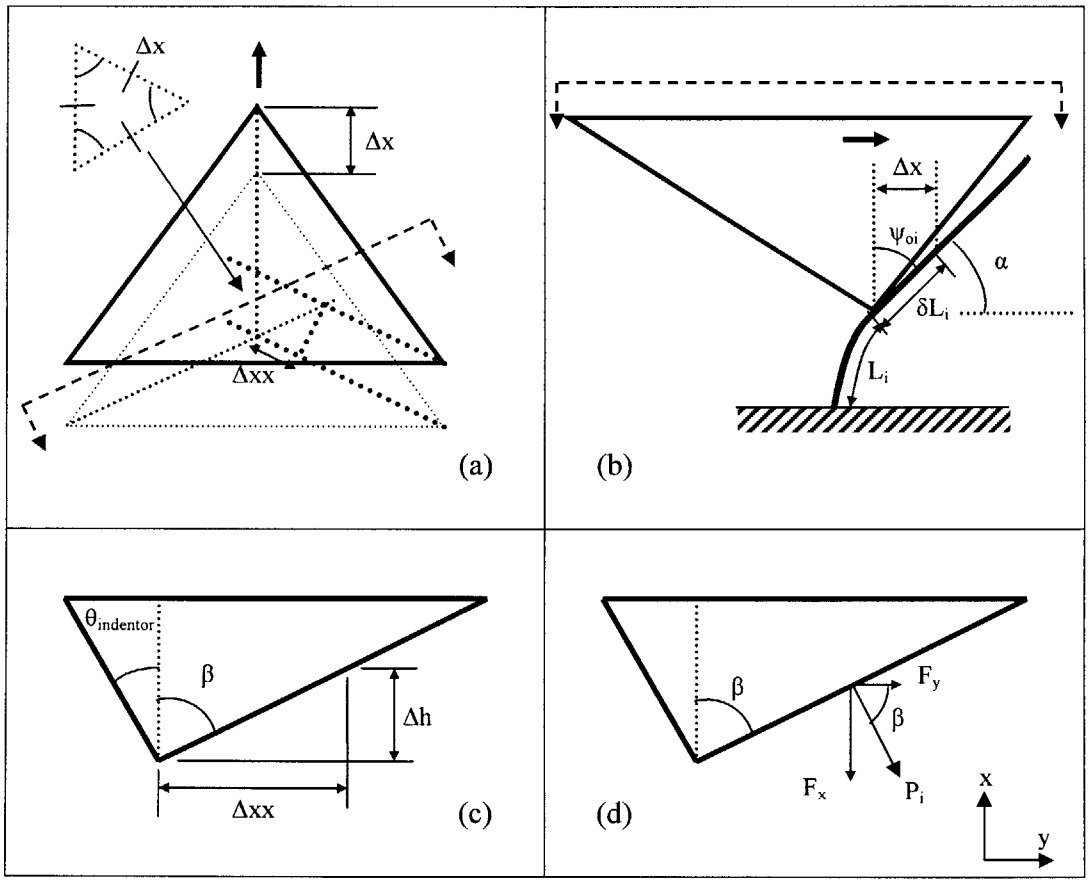

Figure 3.42: Two dimensional geometrical representation of the indentor tip used to find the approximate effective length increment of the CNT in point contact phase. Top view of the indentor tip (a) and side of the indentor tip with CNT in point contact phase (b, c, and d).

$$\delta L = \frac{\Delta x}{\cos\alpha} \tag{3.153}$$

$$\Delta xx = \Delta x \cos(60°) = \frac{\Delta h}{\tan(\beta)}. \tag{3.154}$$

In Equation 3.154, β ($= \varphi$ - $\theta_{indentor}$) is 38.4° and 77.08° for sharp and Berkovich indentor tips, respectively (Figures 3.42-c and 3.42-d). Since CNT_i comes into contact with the edge of the indentor tip in this phase, the point load (P_i) components are calculated from the following equations (Figure 3.42-d).

$$F_y = P_i \cos(\beta) \tag{3.155}$$

$$F_x = P_i \sin(\beta) \tag{3.156}$$

A similar process is repeated at each lateral displacement of the indentor tip and for every CNT_i that makes a point contact with the indentor edge. Then, the vertical component of force is calculated from Equation 3.156 and added to the vertical component of loads from other CNTs in Equation 3.140; subsequently, the net vertical force F on the indentor at $X_{Lateral}$ is obtained.

Next, numerical solutions obtained from the above micro-mechanical contact model are compared with macro-scale experimental (Ebeling, 2004) and FE simulation data for a single Teflon beam subjected to scratching.

3.5.2 Results (without Buckling)

In order to verify the model, theoretical results are first compared to macro-scale scratching experiments on a single Teflon cylinder; a sharp tip is used for the process (Ebeling, 2004). Theoretical results are then compared to finite element scratching simulations using both a sharp and a Berkovich indentor tip.

3.5.2.1 Macro-Scale Experiments

To verify the contact model, a single macro-scale experiment was performed. A Teflon solid cylindrical tube having a diameter of 9.53 *mm* and length of 124.0 *mm* was scratched with a large scale sharp indentor tip, as shown in Figure 3.43. The experimental setup is similar to the setup of macro-scale indentation discussed earlier in Section 3.4.2.1. Since the texture analyzer can only displace the indentor tip in the vertical direction, a linear translational stage and a motion controller were added to the experimental setup to displace the Teflon tube laterally. The lateral motion of the Teflon tube helped us replicate the lateral motion of the indentor. The linear translational stage is a *Servo Systems* model # *LPS-8-20-0.5* and the motion controller is an *IMS* model # *MDrive23*.

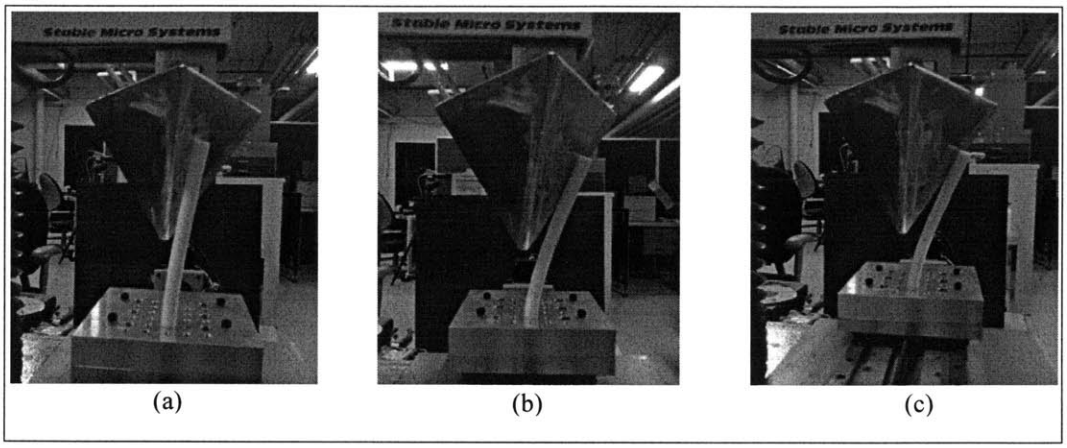

Figure 3.43: Macro scale experimental setup for sharp tip and solid Teflon Tube. The Teflon solid tube dimensions are $L = 124$ *mm* and $D = 9.53$ *mm*. The three figures show the end-point contact phase (a), line contact phase (b), and the point contact phase (c).

The experiment begins with the indentor tip displacing 70 *mm* downwards without making contact with the Teflon tube. Then, the stage is moved laterally at a constant rate of 10 *mm/s*; Figures 3.43-a, b, and c show three snapshots at the end-point contact, line contact, and point contact phases, respectively. The vertical component of the scratch force and the time interval data are directly obtained from the texture analyzer software; the time interval is then multiplied by the rate of motion to convert it into lateral displacement. Lastly, the vertical force versus lateral displacement data are compared with the results from our theoretical and finite element simulations.

3.5.2.2 Macro-Scale Finite Element Simulations

Next, two three-dimensional FE contact models were constructed, and their solutions compared to those of the micro-mechanical model and experiment from the previous section. The FE models were constructed in a method similar to the macro-scale FE models for the indentation earlier in Section 3.4.2.2. During the simulations, the indentor tip was displaced laterally, while keeping the vertical separation between the base of the Teflon tube and the tip of the indentor at 54 *mm*. Figure 3.44-a and d, b and e, and c and f show snapshots of the model beams making an end-point contact, line contact, and point contact with the indentor tips, respectively.

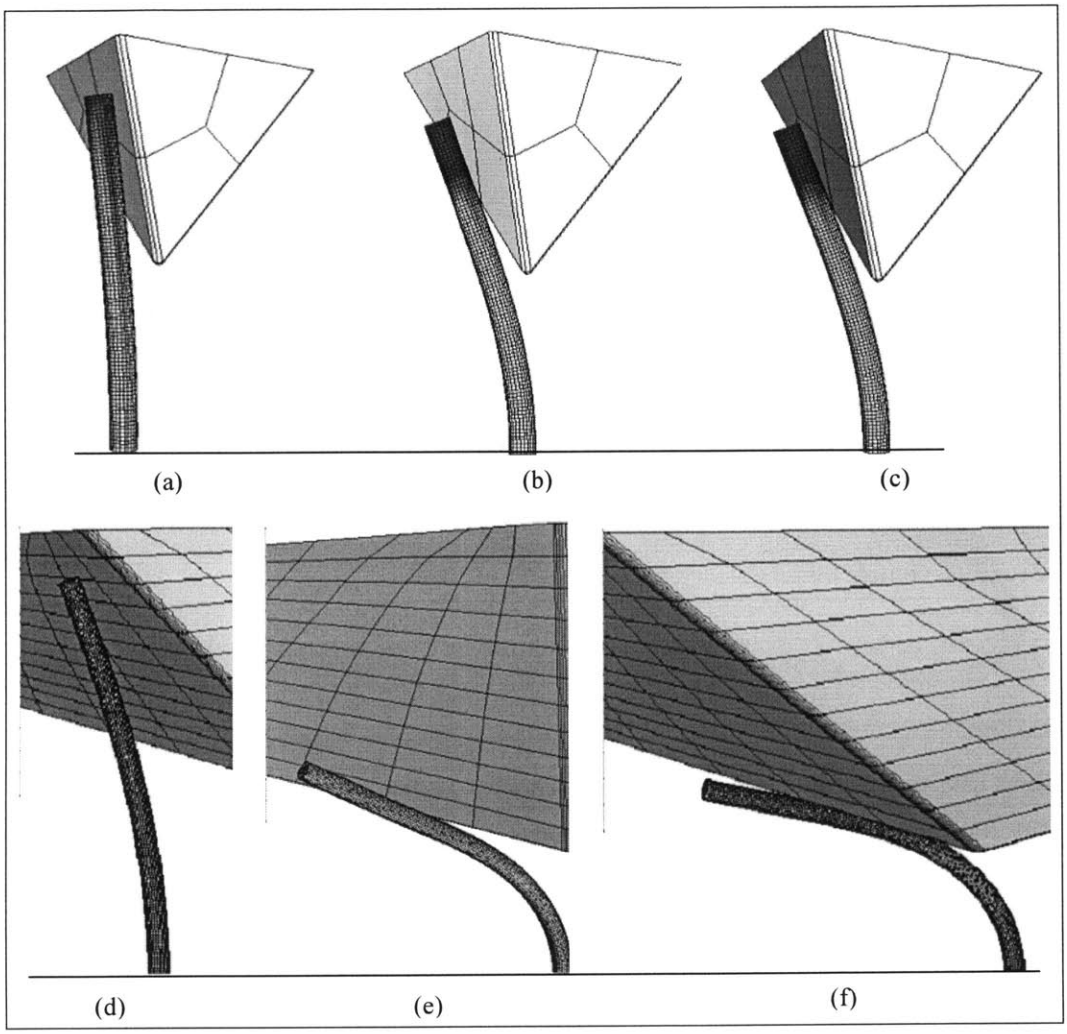

Figure 3.44: Macro-scale finite element simulation for scratching of solid Teflon tube rigidly fixed at one end. Sharp indentor tip deflecting a single Teflon solid tube of L = 124.0 *mm* and D = 9.53 *mm* shown in end-point contact phase, δ = 28.3 *mm* (a), line contact phase, δ = 80.2 *mm* (b), and point contact phase, δ = 90.8 *mm* (c). Berkovich indentor tip deflecting solid Teflon solid tube of L = 184.0 *mm* and D = 9.53 *mm* shown in end-point contat phase, δ = 104.9 *mm* (d), line contact phase, δ = 630 *mm* (e), and point contact phase, δ = 646.2 *mm* (f). Vertical separation from the base of the fixed end of the tube and the indentor tip is 54 *mm*.

Next, the experimental, FE simulation and contact model results for a sharp indentor tip are compared together in Figure 3.45, and FE simulation and contact model results for the Berkovich indentor tip in Figure 3.46. These figures show that results from the contact model and FE simulations are in reasonably good agreement throughout the

force-displacement curve, with the exception of the peak heights which differ in magnitude along certain portions of the curve. Roman numerals *I*, *II*, *III*, and *IV* in Figure 3.45 represent the end-point contact, line contact, transition, and point contact phases, respectively. Notice the similarity of the curve represented in *I* and *II* in Figures 3.45 and 3.46 with those obtained from nano-indentation.

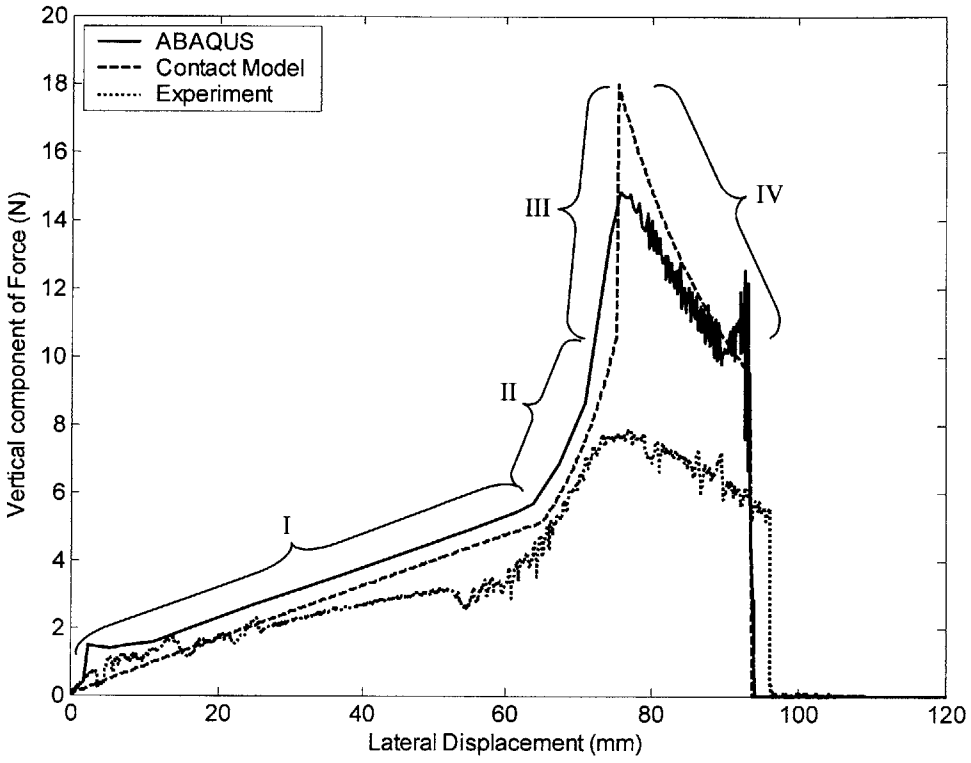

Figure 3.45: Force versus penetration depth curves from mechanical contact, FE and experimentation of macro scale model. Single Teflon solid tube (L = 124 *mm*, D = 9.53 *mm*, E = 0.7 *GPa*, υ = 0.46) was indented with a sharp tip indentor (semi-apex angle = 21.6°). (*I*) refer to the end-point contact phase, (*II*) refers to the line contact phase, (*III*) refers to the transition from line contact to point contact phase and lastly, (*IV*) refers to the point contact phase.

From Figure 3.45, the results from FE and contact model simulations, and the experimental data are in general agreement. It is clear from Figure 3.45 that the contact and FE-based models are able to capture the overall physical behavior of the scratching procedure described in the earlier sections. The main source for the visible difference in

the curves in Figure 3.45 is the chamfered edges of the indentor tip in the experimental setup and in the FE-based model – the chamfer radius is larger in the experimental setup (~40 *mm*) than in the FE-based model (20 *mm*) and zero in the contact model. The higher the chamfer radius, the smaller the deflection of the CNT is; this results in the attenuation of the highest peak in the FE-based and experimental nano-scratching curves. A correlation between the peak height and the chamfer radius can be observed in Figure 3.45; as the chamfer radius decreases, the sharpness and the magnitude of the peak increases, and the slope of the curve in section *IV* increases. Chamfer in the indentor tips also causes the beam to deflect more in a shorter period of time and accounts for the bump in the beginning in both the experimental and FE-based curves. In addition, the slightly higher face angle of the Aluminum indentor (~23°) in the experiment causes the cylindrical tube to transition from the end-point to line contact phase slightly earlier than in the contact model curve. Also, the sudden rise in section *III* of the curve obtained from the contact model in Figure 3.45 can be attributed to the vertical component of the force found from Equation 3.156. In addition, the change in slope from section *II* to *III* in the FE simulation is gradual because of the chamfer. The sudden drop towards the end of the curve corresponds to the point where the beam detaches itself from the indentor tip.

Figure 3.46 on the other hand, shows results obtained from the contact model and FE simulations with the Berkovich indentor tip. Here the chamfer radius of the edge of the Berkovich tip was set to be 10 *mm* and as a result, the bump in section *IV* is very small. As was mentioned in the previous paragraph, the smaller chamfer radius causes the beam to deflect an amount close to that of the contact model. Notice that section *III* of the curve obtained from the contact model shows a drop instead of the rise in Figure 3.45, and it can be attributed to the alternate equation used to find the vertical component of force. The crude method used to approximate the change in length δL in the iterations (Section 3.5.1.3) explains the visible difference of the two curves in section *III* and *IV*. Again, the sudden drop after section *IV* for both curves in Figure 3.46 corresponds to the location where the beam detaches from the indentor tip.

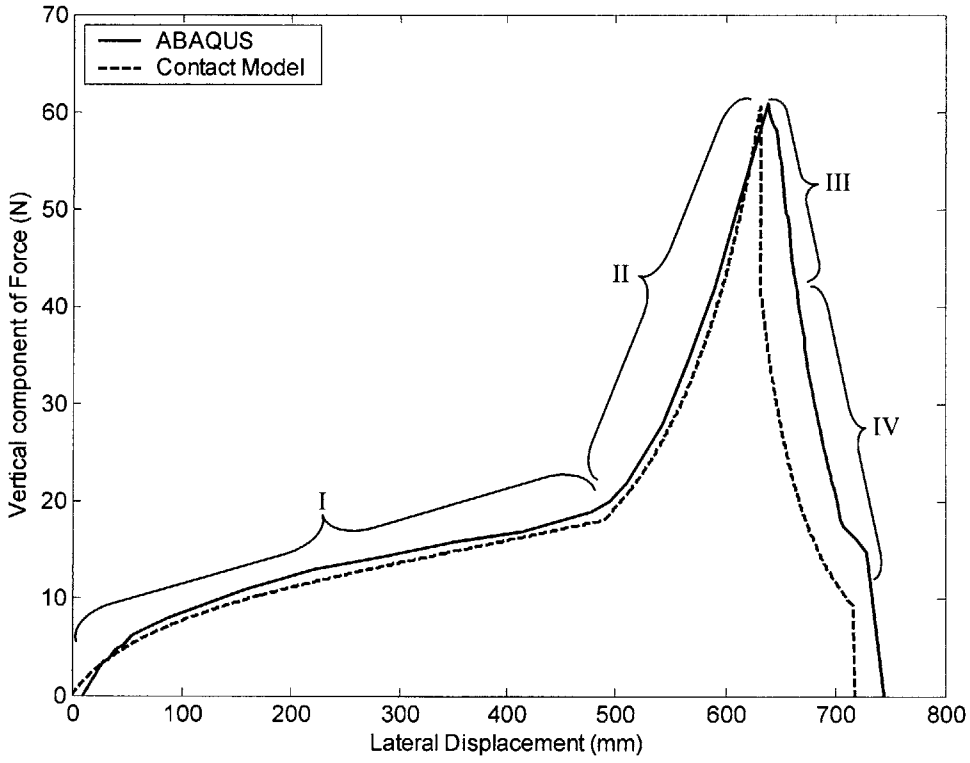

Figure 3.46: Force versus penetration depth curves from mechanical contact, FE and experimentation of macro scale model. Single Teflon solid tube (L = 184 *mm*, D = 9.53 *mm*, E = 0.7 *GPa*, υ = 0.46) was indented with a Berkovich tip indentor. (*I*) refer to the end-point contact phase, (*II*) refers to the line contact phase, (*III*) refers to the transition from line contact to point contact phase and lastly, (*IV*) refers to the point contact phase.

3.6 Conclusions

Nano-indentation tests have been used to determine the mechanical properties of vertically aligned carbon nanotube (VACNT) forests and constituent carbon nanotubes (Qi et al., 2003). A study of the physical process of nano-indentation on VACNT forests reveals a process where nanotubes are consecutively bent during the penetration of the indentor. The resistance of VACNT forests to penetration is a result of superposition of the bending responses of several nanotubes as the indentor successively encounters them.

Qi et al., (2003) first presented nano-indentation tests together with a micro-mechanical contact model that determines the effective bending stiffness of the MWCNT of the VACNT forest. Qi et al., (2003) used nonlinear beam theory to formulate their contact model; in their nonlinear beam theory, both the lateral and axial components of the load from the indentor are considered; however, it does not account for the nonlinear differential elasticity between curvature and deflection. In addition, their model did not include the buckling effects for MWCNTs subjected to bending. Based upon their model, we proposed two models: one that accounts for the nonlinear elasticity between the curvature and the deflection, and another for accounting the buckling phenomenon. The indentation process was divided into two phases: point contact and line contact phases. The two contact models were then compared with nano- and macro-scale experimental and finite element simulation results. We observed from our EOR-based FE simulations that nanotubes buckle when indented with both sharp and Berkovich tips, resulting in a gradual change in slope followed by an abrupt drop in the force-penetration depth curve. The change in slope is gradual because the buckling cascades from the outermost shell tube inwards. This buckling is what results in an order of magnitude lower penetration force when compared with the results from the contact models. In order to capture the reduction in penetration force, we attempted to account for the buckling effect in our contact model using thin shell theory. The results thus obtained from the modified contact model showed reasonable agreement with the simulation results for nano-indentation with Berkovich tips. However, for indentations with a sharp tip, the modified contact model failed to capture most of the force-penetration depth curve behavior; the true behavior of the force-penetration depth curve was better captured by the unmodified contact model.

The contact and the modified contact models were verified against two nano-indentation experiments – one with a sharp tip and another with Berkovich tip. The effective bending modulus obtained from both contact models upon curve fitting the experimental data were found to be 1.10 *TPa* and 1.08 *TPa* for the sharp and Berkovich tips, respectively. These effective bending modulus values matched well with other experimental data available in the literature. We next extended our contact model for nano-indentation to simulate nano-scratching process. In nano-scratching, the indentor tip

is displaced laterally while keeping the vertical distance constant; this results in the loading conditions to change from concentrated to distributed and then back to concentrated while CNTs are subjected to large deflections. In this chapter, we compared results from scratching contact model with those of macro-scale experiment and FE simulations and showed that we were able to capture remarkably the deformation mechanics of a macro-scale beam model. Currently, the proposed scratching model is being worked upon for including buckling in MWCNTs and to collect experimental data similar to that of nano-indentation of VACNT forests.

Chapter 4

Realizing the need to model large multi-walled carbon nanotubes (MWCNTs) with a finite element method (FEM), a computationally efficient model was proposed in Chapter 2. The proposed model is built upon the nested structural shell representation (NSSR) model proposed by Pantano et al., (2004b) – a linear elastic representation based on the orthotropy of the nested tube microstructure. We referred to the new model as an equivalent orthotropic representation (EOR) model where the microstructure is locally orthotropic. The effectiveness of the EOR model in predicting the nonlinear deformation was then examined via comparison with the results of the NSSR model. The EOR method when applied to the FE MWCNT models, replicates the bending, axial and radial compression phenomena seen in the NSSR model and several experimental investigations. In the proposed new model, linear 8-node solid elements are used in the construction of MWCNT models in a commercially available advanced finite element software, *ABAQUS*. The simulation results showed that the EOR-based FE models are able to predict the pre-buckling behavior of MWCNTs irrespective of the element size; however, the model fails to predict the buckling point and post buckling behavior of MWCNTs unless the proper element size is chosen in the construction of the MWCNT models. Fortunately, by using the thin shell theory results for predicting the initial buckling wavelength (Timoshenko,1936), we were able to estimate the required element size and thus predict the buckling and post buckling behavior of MWCNTs. Even with a proper solid element size, the MWCNT models were observed to capture only the initial buckling wavelength but not the steady state buckling wavelength, as predicted by the NSSR model in Pantano et al., (2003, 2004a). Thereafter, we proposed a technique where both the EOR and the NSSR models were combined to model MWCNTs; here the discrete outermost tube and the remaining inner tubes are constructed using the NSSR and the EOR models, respectively. Although less precise, the new combined technique gave results similar to that of EOR models when compared with the NSSR results for the three different loading conditions. After successfully capturing the deformation behavior of MWCNTs with a compromise between the accuracy and computational efficiency of

the NSSR models, we applied the EOR model to formulate an analytical model that simulates the nano-indentation of vertically aligned carbon nanotube (VACNT) forests.

A micro-mechanical contact model for simulating the nano-indentation process was first proposed by Qi et al., (2003). The model, however, did not account for the nonlinear differential relationship between curvature and deflection, and the buckling of MWCNTs at large deflection angles; these two conditions limited their contact model to only simulations with sharp indentor tips. In chapter 3, we proposed a modified contact model based on the one proposed by Qi et al., (2003) where we accounted for the nonlinear differential relationship between curvature and deflection in our beam theory, and also the critical conditions that adequately capture the buckling effects of MWCNTs. Thereafter, numerically and experimentally comparing the proposed beam theory with the one formulated by Qi et al., (2003), we found that their theory is only valid for CNT lateral tip deflections less than approximately 0.6 times the length of the CNT. Next, when comparing the results of EOR-based MWCNT FE models, we realized that the bucking behavior is quite complex as it propagates from the outermost shell to the innermost gradually, and that it is not an instantaneous process as modeled in our modified contact model. On comparing the solutions obtained from the modified contact model to that of FE simulations for sharp and Berkovich tips, we concluded that at the present, our contact model without the buckling effects similar to that of Qi et al., (2003) works well for simulating sharp tip indentations. However, for simulating Berkovich tip indentation, our modified contact model works well. This was verified by comparing the simulation results with experimental force-penetration (*f-p*) results obtained from nano-indentions of two separate VACNT samples with a sharp and a Berkovich tip. An average effective bending stiffness $(EI)_{Eff}$ was deduced by fitting the average simulation curve to the average experimental *f-p* curve. Thereafter, a simple method that accounts for the multi-walled structure of MWCNT was used to interpret the $(EI)_{Eff}$ in terms of the effective bending modulus E_b of the average CNT in the VACNT forests. The E_b values of 1.1 *TPa* and 1.08 *TPa* thus found agree well with the bending modulus value of ~1 *TPa,* which is accepted by most researchers. Thereafter, we extended the nano-indentation micro-mechanical contact model to simulate nano-scratching.

Nano-scratching is a process in which an AFM tip displaces laterally and perpendicular to the nanotube's longitudinal axis, and deflect them to extremely large angles. We realized the similarity between the nano-indentation and nano-scratching processes, and extended our micro-mechanical contact model to simulate nano-scratching. We added another phase in our nano-indentation contact model to account for the complex regime in nano-scratching where the longitudinal axis of the CNT comes into a point contact with indentor tip's edge. At the present in our contact model for nano-scratching, we accounted only for the large deflections of the nanotube and compared the results with those of a macro-scale experiment and FE simulations. The proposed model was found to capture the deformation behavior of beams well when subjected to lateral deflection by scratching. The proposed analytical model, however does not account for buckling in nanotubes.

The new proposed contact models for simulating nano-indentations and nano-scratching, and methods for modeling EOR-based FE simulations of MWCNTs are build on the previous work of Pantano et al., (2004b) and Qi et al., (2003). Both methods are time efficient and are able to capture the nonlinear mechanics of MWCNTs with reasonably good approximations. We suggest future work that accounts for the radial variation of the effective MWCNT material properties in the EOR model, and analytical methods that include the complete complex buckling phenomenon in the modified contact models for nano-indentation and nano-scratching. By inferring from results of the EOR model, the current contact models can be extended to include the external interactions of CNTs with each other.

References

Abell, G. C., 1985. Empirical chemical pseudopotential theory of molecular and metallic bonding. Phys Rev. B., 31(10), pp. 6184-6196.

Allinger, N. L., 1977. Conformational-analysis. 130. MM2-Hydrocarbon force-field utilizing v1 and v2 torsional terms. J. Am. Chem. Soc., 99(25), pp. 8127-8134.

Allinger, N. L., Yuh, Y. H., and Lii, J. H., 1989. Molecular mechanics-The MM3 force-field for hydrocarbons. J. Am. Chem. Soc., 111(23), pp. 8551-8566.

Arroyo, M., and Belytschko, T., 2003. Nonlinear mechanical response and rippling of thick multi-walled carbon nanotubes. Phys. Rev. Lett., 91, pp. 215505.

Blakslee, O. L., Proctor, D. G., Seldin, E. J., Spence, G. B., and Weng, T., 1970. Elastic constants of compression-annealed pyrolytic graphite. J. App. Phys., 41(8), pp. 3373-3382.

Bower, C., Rosen, R., Jin, L., Han, J., and Zhou, O., 1999. Deformation of carbon nanotubes in nanotube-polymer composites. Appl. Phys. Lett. 74, 3317-3319.

Brenner, D. W., Shenderova, O. A., Harrison, J. A., Stuart, S. J., Ni, B., and Sinnott, S.B., 2002. A second-generation reactive empirical bond order (REBO) potential energy expression for hydrocarbons. J. Phys.: Condens. Matter, 14, pp. 783-802.

Chhowalla, M., Teo, K. B. K., Ducati, C., Rupesinghe, N. L., Amaratunga, G. A. J., Ferrari, A. C., Roy, D., Robertson, J., Milne, W. I., 2001. Growth process conditions of vertically aligned carbon nanotubes using plasma enhanced chemical vapor deposition. J. Appl. Phys., 90, pp. 5308-5317.

Crandall, S. H., Dahl, N. C., and Lardner, T. J., 1976. An introduction to the mechanics of solids. McGraw-Hill, New York.

Cui, F., Luo, C., and Dong, 2004. J., Dimerization of C60 molecules within the single-walled carbon nanotube. Phys. Lett. A, 327, pp. 55-60.

Cummings, J., and Zettl, A., 2000. Low friction nanoscale linear bearing realized from multiwall carbon nanotubes. Science, 289, pp. 602-604.

Dresselhaus, M.S., Dresselhaus, G., and Avouris, P., 2000. Carbon Nanotubes Synthesis, Structure, Properties, and Applications, Springer, New York.

Ebbesen, T. W., 1997. Carbon Nanotubes Preparation and Properties, CRC Press Inc.,.

Ebeling, G. F., 2004. Macro scale physical model of nanoindentation on vertically aligned carbon nanotube forests. SB Thesis, MIT.

Falvo, M. R., Clary, G. J., Taylor, R. M. II, Chi, V., Brooks, F.P., Washburn, S., and Superfine, R., 1997. Bending and buckling of carbon nanotubes under large strain. Nature, 389 (6651), pp. 582-584.

Fay, F. R., 1962. Flexible bars. Butterworths Inc., London.

Ghosh, S., Gadagkar, V., and Sood, A. K., 2005. Strains induced in carbon nanotubes due to the presence of ions: Ab initio restricted Hatree-Fock calculations. Chem. Phys. Lett., 406, pp. 10-14.

Girifalco, L. A., and Lad, R. A., 1956. Energy of cohesion, compressibility and the potential energy functions of the graphite system. J. Chem. Phys., 25(4), pp. 693-697.

Govindjee, S., and Sackman, J. L., 1999. On the use of continuum mechanics to estimate the properties of nanotubes. Solid State Commun., 110, pp. 227-230.

Guo, W., Zhu., C. Z., Yu, T. X., Woo, C.H., Zhang., B., and Dai, Y.T., 2004. Formation of sp^3 Bonding in Nanoindented Carbon Nanotubes and Graphite. Phys. Rev. Lett., 93, 245502.

Harik, V. M., 2001. Ranges of applicability for the continuum beam model in the mechanics of carbon nanotubes and nanorods. Solid State Comm., 120, pp. 331-335.

He, X. Q., Kitipornchai, S., and Liew, K. M., 2005. Buckling analysis of multi-walled carbon nanotubes: a continuum model accounting for van der Waals interaction. J. Mech. and Phys. of Solids, 53, pp. 303-326.

Hernandez, E., Goze, C., Bernier, P., and Rubio, A., 1998. Elastic Properties of C and $B_xC_yN_z$ Composite Nanotubes. Phys. Rev. Lett., 80, pp. 4502-4505.

Hertel, T., Walkup, R. E., and Avouris, P., 1998. Deformation of carbon nanotubes by surface van der Waals forces. Phys. Rev. B., 58(20), pp. 13870-13873.

Iijima, S., 1991. Helical microtubules of graphitics carbon. Nature (London), 354, pp. 56-58.

Iijima, S., Brabec, C., Maiti, A., and Bernholc, J., 1996. Structural flexibility of carbon nanotubes. J. Chem. Phy., 104, pp. 2089-2092.

Kang, W. P., Davidson, J. L., Wisitsora-at, A., Wong, Y. M., Takalkar, R., Subramania, K., Kerns, D. V., and Hofmeister, W. H., 2005. Diamond and carbon-derived vacuum micro- and nano-electronic devices. Diamond and Related Materials, 14(3-7), pp. 685-691.

Ke, C. –H., Pugno, N., Peng, B., and Espinosa, H. D., 2005. Experiments and modeling of carbon nanotube-based NEMS devices. J. Mech. Phys. of Solids, 53(6), pp. 1314-1333.

Kelly, B., 1981. Physics of Graphite. Applied Science Publishers, London.

Kiang, C. –H., Endo. M., Ajayan, P. M., Dresselhaus, G., and Dresselhaus, M. S., 1998. Size Effects in Carbon Nanotubes. Phys., Rev. Lett., 81, pp. 1869-1872.

Krishnan A., Dujardin, E., Ebbesen T. W., Yianilos P. N, and Treacy MMJ., 1998. Young's modulus of single-walled nanotubes. Phys. Rev. Lett., 58(20), pp. 14013-14019.

Kroto, H. W., Heath, J. R., O'Brien, S. C., Curland, R. F., and Smalley, R. E., 1985. C60: Buckminsterfullerene. Nature, 318, pp. 162.

Lau, K. T., Chipara, M., Ling, H., and Hui, D., 2004. On the effective elastic moduli of carbon nanotubes for nanocomposite structures. Compos.: Part B, 35, pp. 95-101.

Li, C., and Chou, T. W., 2003-a. A structural mechanics approach for the analysis of carbon nanotubes. International Journal of Solids and Structures, 40, pp. 2487-2499.

Li, C., and Chou, T. W., 2003-b. Elastic moduli of multi-walled carbon nanotubes and the effect of van der Waals forces. Composites Science and Technology, 63, pp. 1517-1524.

Liew, K. M., Wong, C. H., He, X.Q., Tan, M. J., and Meguid, S.A., 2004. Nanomechanics of single and multiwalled carbon nanotubes. Phys. Rev. B, 69, 113429.

Liu, Y. J., and Chen, X. L., 2003. Continuum Models of Carbon Nanotubes-Based Composites Using the Boundary Element Method. Electronic Journal of Boundary Elements, 1(2), pp. 316-335.

Liu, J. Z., Zheng, Q., and Jiang, Q., 2001. Effect of a Rippling Mode on Resonances of Carbon Nanotubes. Phys. Rev. Lett., 86, pp. 4843-4846.

Liu, J. Z., Zheng, Q., and Jiang, Q., 2003. Effect of bending instabilities on the measurements of mechanical properties of multiwalled carbon nanotubes. Phys. Rev. B., 67, 075414.

Lordi, V., and Yao, N., 1998. Radial compression and controlled cutting of carbon nanotubes. J. Chem. Phys., 109(6), pp. 2509-2512.

Lourie, O., Cox, D.M., Wagner, H.D., 1998. Buckling and collapse of embedded carbon nanotubes. Phys. Rev. Lett. 81 (8), pp.1638-1641.

Mayo, S. L., Olafson, B. D., and Goddard, W. A., 1990. Dreiding-A generic force-field for molecular simulations, J. Phys. Chem., 94(26), pp. 8897-8909.

Odegard, G. M., Gates, T. S., Nicholson, L. M., and Wise, K. E., 2002. Equivalent continuum modeling of nano-structured materials. Comp Sci. Technol., 62, pp. 1869-1880.

Palaci, I., Fedrigo, S., Brune, H., Klinke, C., Chen, M., and Riedo, E., 2005. Radial elasticity of multiwalled carbon nanotubes. Phys. Rev. Lett., 94, 175502.

Pantano, A., Boyce, M. C., and Parks, D. M., 2004-a. Mechanics of Axial Compression of Single and Multi-Wall Carbon Nanotubes. J. Eng. Mat. Tech., 126, pp. 279-284.

Pantano, A., Parks, D.M., and Boyce, M.C., 2003. Nonlinear structural mechanics based modeling of carbon nanotube deformation. Phys. Rev. Lett., 91(14), 145504.

Pantano, A., Parks, D. M., and Boyce M. C., 2004-b. Mechanics of deformation of single- and multi-wall carbon nanotubes. J. Mech. Phys. Solids, 52, pp. 789-821.

Pantano, A., Parks, D. M., Boyce, M. C., and Nardelli, M. B., 2004-c. Mixed finite element-tight-binding electromechanical analysis of carbon nanotubes. J. App. Phys., 96(11), pp. 6756-6760.

Pettifor, D. G., and Oleinik, I. I., 1999. Analytic bond-order potentials beyond Tersoff-Brenner. I. Theory. Phys. Rev. B, 59(13), pp. 8487-8499.

Poncharal, P., Wang, Z. L., Ugarte, D., and de Heer, W. A., 1999. Electrostatic deflections and electromechanical resonances of carbon nanotubes. Science, 283(5407), pp. 1513-1516.

Popov, V. N., Van Doren, V. E., and Balkanski, M., 2000. Elastic properties of crystals of single-walled carbon nanotubes. Solid State Commun., 114, pp. 395-339.

Qi, H. J., Teo, K. B. K., Lau, K., Boyce, M. C., Milne, W. I ., Robertson, J., and Gleason, K. K., 2003. Determination of mechanical properties of carbon nanotubes and vertical aligned carbon nanotubes forests using nanoindentation. J. Mech. Phys. Solids, 51, pp. 2213-2237.

Qian, D., Wagner, G.J., Liu, W.K., Yu, M.-F., and Ruoff, R.S., 2002. Mechanics of carbon nanotubes. Appl. Mech. Rev., 55, pp. 495-532.

Robertson, D. H., Brenner, D. W., and Mintmire, J. W., 1992. Energetics of nanoscale graphitic tubules. Phys. Rev. B, 45(21), pp. 12592-12595.

Ru, C. Q., 2000-a. Column buckling of multiwalled carbon nanotubes with interlayer radial displacements. Phy. Rev. B., 62(24), pp. 16962-16967.

Ru, C. Q., 2001. Degraded axial buckling strain of multiwalled carbon nanotubes due to interlayer slips. J. App. Phys., 89(6), pp. 3426-3433.

Ru, C. Q., 2000-b. Effective Bending Stiffness of Carbon Nanotubes, Phy. Rev. B, 62(15), pp. 9973-9976.

Ru, C. Q., 2000-c. Effect of Van der Waals Forces on Axial Buckling of a Double-Walled Carbon Nanotbue. J. App. Phys., 87(10), pp. 7227-7231.

Ruoff, R. S., Qian, D., and Liu, W. K., 2003. Mechanical properties of carbon nanotubes: theoretical predictions and experimental measurements., C. R. Physique, 4, pp. 993-1008.

Saito, Y., and Yoshikawa, T., 1993. Bamboo-shaped carbon tube filled partially with nickel, J. Cryst. Growth, 134(1-2), pp. 154-156.

Saito, R., Dresselhaus, G., and Dresselhaus, M.S., 2001. Physical Properties of Carbon Nanotubes, Imperial College Press, London.

Salvetat, J. P., Bonard, J. M., Thomson, N. H., Kulik, A. J., Forro, L., Benoit, W., and Zuppiroli, L., 1999. Mechanical properties of carbon nanotubes. Appl. Phys. A, 69, pp. 225-260.

Sears, A., and Batra, R. C., 2004. Macroscopic properties of carbon nanotubes from molecular-mechanics simulations. Phys. Rev. B., (69), 235406.

Shen, L., and Li, J., 2004. Transversely isotropic elastic properties of single-walled carbon nanotubes. Phys. Rev. B., 69, 045414.

Shen, W., Jiang, B., Han, B. S., and Xie, S., 2000. Investigation of the Radial Compression of Carbon Nanotubes with a Scanning Probe Microscope. Phys. Rev. Lett., 84(16), pp. 3634-3637.

Solecki, R., and Conant, R. J., 2003. Advanced mechanics of materials. Oxford University Press, New York.

Sun, X., and Zhao, W., 2005. Prediction of stiffness and strength of single-walled carbon nanotubes by molecular-mechanics based finite element approach. Materials Science and Engineering A, 390, pp. 366-371.

Tersoff, J., and Ruoff, R. S., 1994. Structural Properties of a Carbon-Nanotube Crystal, Phys.Rev. Lett., 73, pp. 676-679.

Thess, A., Lee, R., Nikolaev, P., Hongje, D., Pierre, P., Robert, J., Chunhui, X., Lee, Y. H., Kim, S. G., Rinzler, A. G., Colbert, D. T., Scuseria, G. E., Tomanek, D., Fischer, J. E., and Smalley, R. E., 1997. Crystalline ropes of metallic carbon nanotubes. Science, 273(5274), pp. 483-487.

Thostenson, E. T., Ren, Z., and Chou, T. W., 2001. Advances in the science and technology of carbon nanotubes and their composites: a review, Composites Science and Technology, 61, pp. 1899-1912.

Timoshenko, S., 1936. Theory of Elastic Stability. McGraw-Hill, New York.

Tombler, T. W., Zhou, C. W., Alexseyev, L., Kong J., Dai, H. J., Lei, L., Jayanthi, C. S., Tang, M. J., and Wu, S-Y., 2000. Reversible electromechanical characteristics of carbon nanotubes under local-probe manipulation. Nature (London), 405(6788), pp.769-772.

Treacy, M.M., Ebbesen, T.W., and Gibson, J.M., 1996. Exceptionally high Young's modulus observed for individual carbon nanotubes. Nature, 381, pp. 678-680.

Tserpes, K. I., and Papanikos, P., 2005. Finite element modeling of single-walled carbon nanotubes, Composites: Part B, 36, pp. 468-477.

Valavala, P. K., and Odegard, G. M., 2005. Modeling Techniques for Determination of Mechanical Properties of Polymer Nanocomposites. Rev. Adv. Mater. Sci., 9, pp. 34-44.

Wang, C. Y., Ru, C. Q., and Mioduchowski, A., 2003. Axially compressed buckling of pressured multiwall carbon nanotubes. International J. Solids and Structures, 40, pp. 3893-3911.

Wang, X. Y., and Wang, X., 2004. Numerical simulation for bending modulus of carbon nanotubes and some explanations for experiment. Compos. Part B, 35, pp. 79-86.

Wang, X., Wang, X. Y., and Xiao, J., 2005. A non-linear analysis of the bending modulus of carbon nanotubes with rippling deformations. Compos. Struct., 69, pp. 315-321.

Wang, X., Zhang, Y. C., Xia, X. H., and Huang, C. H., 2004. Effective bending modulus of carbon nanotubes with rippling deformation. J. Solids and Structures, 41, pp. 6429-6439.

Wang, Y., Tomanek, D., and Bertsch, G. F., 1991. Stiffness of a solid composed of c60 clusters. Phys. Rev. B, 44(12), pp. 6562-6565.

Wong, E. W., Sheehan, P. E., and Lieber, C. M., 1997. Nanobeam mechanics: Elasticity, strength, and toughness of nanorods and nanotubes. Science, 277(5334), pp. 1971-1997.

Xiao, J. R., Gama, B. A., and Gillespie, J. W. Jr., 2005. An analytical molecular structural mechanics model for the mechanical properties of carbon nanotubes. International Journal of Solids and Structures, 42, pp. 3075-3092.

Yakobson, B. I., Brabec, C. J., and Bernholc, J., 1996. Nanomechanics of carbon tubes: instabilities beyond linear range. Phys. Rev. Lett., 76, pp. 2511-2514.

Yu, M. F., Kowalewski, T., and Ruoff, R., 2000-a. Investigation of the Radial Deformability of Individual Carbon Nanotubes under Controlled Indentation Force. Phys. Rev. Lett., 85(7), pp. 1456-1459.

Yu, M. F., Yakobson, B. I., and Ruoff, R. S., 2000-b. Controlled sliding and pullout of nested shells in individual multiwalled carbon nanotubes. J. Phys. Chem. B, 104, pp. 8764-8767.

Zhao, X., Liu, Y., Inoue, S., Suzuki, T., Jones, R. O., and Ando, Y., 2004. Smallest Carbon Nanotube is 3 $\AA$ in Diameter. Phys. Rev. Lett., 92(12), pp. 122502.

Zhao, Y. X., and Spain, I. L., 1989. X-ray-differection data for graphite to 20 *GPa*. Phys. Rev. B, 40(2), pp. 993-997.

Zhou, X., Zhou, J. J., and Ou- Yang, Z. C., 2000. Strain energy and Young's modulus of single-wall carbon nanotubes caculated from electronic energy-band theory. Phys. Rev. B, 62(20), pp. 13692-13696.